

# UNIVERSITÀ DEGLI STUDI DI TRIESTE

Sede Amministrativa del Dottorato di Ricerca:  
UNIVERSITÀ DEGLI STUDI DI TRIESTE

XXII CICLO DELLA SCUOLA DI DOTTORATO DI RICERCA IN FISICA

## NEUTRON INDUCED FISSION CROSS SECTION MEASUREMENTS AIMED AT NUCLEAR TECHNOLOGY DEVELOPMENT



DIRETTORE DELLA SCUOLA: **Prof. Gaetano Senatore**

RELATORE: **Dott. Paolo Maria Milazzo**

TUTORE: **Prof. Rinaldo Rui**

DOTTORANDO: **Francesca Belloni**

**ANNO ACCADEMICO 2008/2009**

# Abstract

Neutron induced fission cross sections of  $^{233}\text{U}$ ,  $^{238}\text{U}$ ,  $^{241}\text{Am}$ ,  $^{243}\text{Am}$  and  $^{245}\text{Cm}$  in the energy range between 500 keV and 20 MeV obtained at the n\_TOF Neutron Time of Flight facility at CERN (Genève) are presented. Fission fragments had been detected by a gas counter with good discrimination between nuclear fission products and background events. A comparison between the extracted cross sections, previous experimental results and evaluated libraries is reported.

*Keywords:* neutron, fission, n\_TOF, fission ionization chamber

# Sommario

In questa tesi sono presentate le sezioni d'urto indotte da neutroni di energia compresa tra 500 KeV e 20 MeV su  $^{233}\text{U}$ ,  $^{238}\text{U}$ ,  $^{241}\text{Am}$ ,  $^{243}\text{Am}$  e  $^{245}\text{Cm}$  ottenute alla facility di tempo di volo n\_TOF al CERN (Genève). I frammenti di fissione sono stati rivelati da un contatore a gas con una buona capacità di discriminare i prodotti di fissione dagli eventi di background. La tesi riporta un paragone tra le sezioni estratte, i dati sperimentali ottenuti in passato da altri gruppi e le principali librerie valutative.

*Parole chiave:* neutroni, fissione, n\_TOF, camera di fissione a ionizzazione

*Alla mia famiglia*

# Acknowledgments

## *Trieste sottosopra*

"Trieste sottosopra" (i.e. Trieste upside-down) is a short book by Mauro Covacich, associating each place of the town to a story. But for me "Trieste sottosopra" is also something else. It's my feeling, now that I leave the town. It's Trieste itself, with its singularities, which make it so unique. And it's my PhD experience...

As some words sounded incomprehensible, like the famous "volentieri", some concepts were totally new. As the town is a mix of different traditions, languages and cultures, several people contributed to this PhD.

This work would have never been possible without the constant help of Paolo Milazzo, my supervisor. He invited me to ask whatever doubt I could have and always replied both to direct questions and to my (literally thousands of) e-mails. His daily teaching led me deeper into this data analysis. What I strongly thank him for, among all other things, is that each time a problem arose, he set by me explaining. Paolo put many ideas in this work, which actually is more hands made. Moreover he entirely corrected this manuscript. He always let me free to choose how to organize the job, but each time I got blocked he was present for working together. His sense of humor made the working hours fast and pleasant. His kindness in giving all kind of information, his encouraging and his enthusiasm towards work, life and people made everything simpler. Working in n\_TOF Ts was GREAT thanks to him and I will miss it.

I have two main folders on the server. They are "Analisi\_Paolo" and "Analisi\_Nicola". They are my Gospels. Nicola Colonna initiated me to the neutron induced fission data analysis. He put foundations and several ideas in this PhD, and was always available for giving precious explanations. His interest in neutron physics and search for accurate results were a continuous lesson. He made his routines available and never missed to reply to one e-mail. What I strongly appreciate about Nicola is that his goal is that work must be accurately performed. It's a Collaboration, not a challenge. And he makes everything to put people in condition to work.

I thank Rinaldo Rui, for accepting to be my supervisor from Trieste University.

I still remember my first speech with Kaori Fujii. Paolo had just told me to ask him whatever doubt and she proposed the same thing, adding that each question would have remained between us. I had already pre-announced my total ignorance on several topics, but will always thank her for those words. She proved to be a wonderful colleague, extremely valid in her work and always ready to help. Her kindness also outside job contest was really important for me when I moved to this town. I enjoyed her company, both in office and in Trieste and wish her all the best.

My visit to Orsay was really interesting and would have never been possible without Laurent Tassant-Got and Sylvie Pierre. Thank you for precious explanations and complete availability to show me  $\alpha$  spectrometry, as well as for your kindness and warm welcome. I strongly appreciated the opportunity you gave me to learn!

Marco Calviani passed me his routines to download data from Castor. Without those routines, and the first ROOT advice, I would have never been able to initiate (nor finish) this data analysis. I sincerely thank you for this.

My first time in Legnaro it seemed I would have used SAMMY and Javier Praena decided to pass me his files and provided explanations on his initiative, which I really appreciated. Thank you for your help and kindness, for introducing me to "spritz" and to the history of the Spanish monarchy. I enjoyed many evenings with you!

Cristian Massimi was my personal teacher of the first steps of  $^{56}\text{Fe}(n,\gamma)$  data analysis and of billiards table (where - I know - I still have to improve a lot). Thank you for your patience, explanations and kindness. I enjoyed soccer table with you in n\_TOF vs CLOUDS matches.

Many thanks to Claudia Lederer, the organizer of those evenings. I appreciated all the time spent in your company, both working and having fun. Thank you for sharing job information and for saying what was new in the shifters' rules each time I arrived in CERN.

I sincerely thank Giuseppe Tagliente and Pierfrancesco Mastinu for their availability in providing accurate explanations and for their kindness. The possibility Pierfrancesco gave me to spend more time in CERN was great for learning. Thanks a lot! Eric Berthoumieux was my reference point when in CERN. Thank you for your help! I shared many days with Moinul Meaze. Thank you for your good attitude to people.

I'm grateful to Franz Käppeler for his precious advice and kindness. When I had my first presentation inside the Collaboration, he was wonderful to me!

Finally thanks to the whole n\_TOF Collaboration, and especially the young n\_TOF guys I shared many days with.

In Trieste the whole group III of INFN was really kind, making the atmosphere friendly and easy-going. I want to thank especially Stefano Piano, for the time he spent helping me my first months of PhD, and Raffaele Grosso, for his precious Linux advice. Thank you also to Renzo Rosei, for all interesting conversations during tea pauses. I learnt several things from you all.

Enrico Cattaruzza and Marina De Bon literally saved my life. You are wonderful! Marina, I enjoyed being your home-mate and wish you all the best with Michele!

There are two kind of people in my eyes, the ones who look for personal achievement to prove they are experts and the ones who -being experts - work with dedication, interest and help other people, also belonging to different groups. For this reason and for the example he gives me, outside as inside n\_TOF I sincerely thank Francesco Cerutti. He helped me since the times of my master thesis and was always available for explanations, corrections, advice, good words and encouraging. Grazie di cuore!

A special thought to him, Dmitri Vladimirovich Kamanin, the FOBOS staff, Ettore Gadioli and Ileana Iori, because thanks to them 3 years ago I decided not to leave physics. Вы все в моём сердце.

Thanks to my family and my dearest friends, sempre vicini anche quando lontani.



# Preface

*"Remember your humanity, and forget the rest"*

(Józef Rotblat)

This thesis reports on experimental determination of neutron induced fission cross sections of  $^{233}\text{U}$ ,  $^{238}\text{U}$ ,  $^{241}\text{Am}$ ,  $^{243}\text{Am}$  and  $^{245}\text{Cm}$  in the energy range between 500 keV and 20 MeV. The work has been performed within the n\_TOF collaboration.

Data had been collected in 2004 at the neutron Time Of Flight facility at CERN (Genève) in the frame of a research project involving isotopes relevant for nuclear astrophysics and nuclear technologies.

Precise and consistent  $\sigma_{(n,f)}$  of actinides are required for the design of systems based on the Th/U fuel cycle, for Accelerator Driven Systems (ADS), and the so called Generation-IV (Gen-IV) nuclear reactors. More accurate fission cross-sections are required - among other physical parameters - to reach higher fuel burn-up, thus increasing the efficiency of the fuel cycle, and to improve the safety of future systems, which aim at a higher actinide fraction in the fuel mix. Discrepancies between data from previous measurements performed at other facilities reach 15% for some isotopes in the fast energy region of the incident neutron spectrum. The n\_TOF Collaboration aimed at adding its own contribution in order to reduce such discrepancies. Obtained results are extremely precise, meeting - for some isotopes - the required standard established by the Nuclear Energy Agency (NEA, a specialized agency within the Organization for Economic Co-operation and Development - OECD) nuclear science committee.

Fission fragments had been detected by a gas counter with good discrimination between nuclear fission products and background events. Neutron induced fission cross-sections are determined relative to  $^{235}\text{U}$ , which is a standard for (n,f) reactions from thermal energies up to 200 MeV. This isotope experienced the same neutron flux as the investigated samples, being housed inside the same detector. Corrections for dead-time are included and Monte Carlo simulations performed in order to take into account the thickness of the samples. In this work the extracted neutron induced fission cross sections are provided with an uncertainty representing only the statical one.

The thesis is organized in the following way: Chapter 1 reports on the need of  $\sigma_{(n,f)}$  for uranic and transuranic elements. In Chapter 2 the n\_TOF facility is presented, while in Chapter 3 the employed detector is described. In Chapter 4 some information about the data acquisition and storage systems is given. The main chapter, containing the analysis procedure, follows. Finally the results are presented in Chapter 6 and discussed in Chapter 7.

# Contents

|          |  |           |
|----------|--|-----------|
| <b>1</b> | <b>Introduction</b>  | <b>1</b>  |
| 1.1      | The need of electricity . . . . .  | 1         |
| 1.2      | The nuclear option . . . . .   | 2         |
| 1.3      | The need of nuclear data . . . . .   | 7         |
| 1.3.1    | Burning efficiency . . . . .   | 7         |
| 1.3.2    | Alternative fuel cycles . . . . .  | 8         |
| 1.3.3    | Waste production and weapon proliferation . . . . .                            | 12        |
| 1.4      | Nuclear libraries and experimental data . . . . .                              | 14        |
| <b>2</b> | <b>The n_TOF facility</b>  | <b>17</b> |
| 2.1      | Description . . . . .  | 19        |
| 2.1.1    | Proton extraction line . . . . .   | 19        |
| 2.1.2    | Spallation module . . . . .  | 19        |
| 2.1.3    | Neutron beam optics . . . . .  | 23        |
| 2.1.4    | Experimental Area . . . . .  | 26        |
| 2.1.5    | Beam dump . . . . .  | 26        |
| 2.2      | Beam characteristics . . . . .   | 27        |
| 2.2.1    | Neutron flux . . . . .   | 27        |
| 2.2.2    | Energy resolution . . . . .  | 29        |
| 2.3      | Background . . . . .   | 31        |
| 2.4      | Performance summary . . . . .  | 32        |
| <b>3</b> | <b>The detector</b>  | <b>33</b> |
| 3.1      | Working principle . . . . .  | 33        |
| 3.2      | Design of FIC 1 . . . . .  | 34        |
| 3.3      | Detector characteristics . . . . .   | 36        |
| 3.3.1    | Maximum safety . . . . .   | 36        |
| 3.3.2    | Fast charge collection time . . . . .  | 36        |
| 3.3.3    | Maximization of the energy range of operation . . . . .                        | 36        |
| 3.3.4    | Minimization of neutron interaction with the material of the chamber . . . . . | 38        |
| <b>4</b> | <b>FIC Front-end electronics and DAQ</b>                                       | <b>39</b> |
| 4.1      | Front-end electronics . . . . .  | 39        |
| 4.2      | DAQ . . . . .  | 41        |
| 4.3      | The n_TOF singularity . . . . .  | 42        |
| <b>5</b> | <b>Analysis</b>  | <b>43</b> |

|          |  |           |
|----------|--|-----------|
| 5.1      | Experimental cross-section determination . . . . .               | 45        |
| 5.1.1    | Reading raw data . . . . .                                       | 45        |
| 5.1.2    | Time Of Flight (TOF) . . . . .                                   | 46        |
| 5.1.3    | Data treatment . . . . .   | 47        |
| 5.1.4    | Cross section extraction . . . . .                               | 49        |
| 5.2      | Corrections to the the cross-section determination . . . . .     | 50        |
| 5.2.1    | Dead time correction . . . . .                                   | 50        |
| 5.2.2    | Thickness correction . . . . .                                   | 51        |
| 5.3      | Uncertainties analysis . . . . .                                 | 54        |
| 5.3.1    | Uncertainty on neutron energy . . . . .                          | 54        |
| 5.3.2    | Cross section uncertainty . . . . .                              | 55        |
| <b>6</b> | <b>Experimental results</b>                                      | <b>59</b> |
| 6.1      | $^{235}_{92}\text{U}$ . . . . .                                  | 59        |
| 6.1.1    | Pulse shape analysis . . . . .                                   | 59        |
| 6.1.2    | FFs histogram . . . . .  | 61        |
| 6.1.3    | Dead Time Correction . . . . .                                   | 62        |
| 6.1.4    | Thickness Correction . . . . .                                   | 63        |
| 6.2      | $^{238}_{92}\text{U}$ . . . . .                                  | 66        |
| 6.2.1    | Pulse shape analysis . . . . .                                   | 66        |
| 6.2.2    | FFs histogram . . . . .  | 68        |
| 6.2.3    | Dead Time Correction . . . . .                                   | 68        |
| 6.2.4    | Thickness Correction . . . . .                                   | 68        |
| 6.2.5    | Results . . . . .  | 70        |
| 6.3      | $^{233}_{92}\text{U}$ . . . . .                                  | 75        |
| 6.3.1    | Pulse shape analysis . . . . .                                   | 75        |
| 6.3.2    | FFs histogram . . . . .  | 76        |
| 6.3.3    | Dead Time Correction . . . . .                                   | 77        |
| 6.3.4    | Thickness Correction . . . . .                                   | 77        |
| 6.3.5    | Results . . . . .  | 79        |
| 6.4      | $^{243}_{95}\text{Am}$ . . . . .                                 | 85        |
| 6.4.1    | Pulse shape analysis . . . . .                                   | 85        |
| 6.4.2    | FFs histogram . . . . .  | 87        |
| 6.4.3    | Dead Time Correction . . . . .                                   | 88        |
| 6.4.4    | Thickness Correction . . . . .                                   | 88        |
| 6.4.5    | Results . . . . .  | 89        |
| 6.5      | $^{241}_{95}\text{Am}$ . . . . .                                 | 95        |
| 6.5.1    | Pulse shape analysis . . . . .                                   | 95        |
| 6.5.2    | Preliminary considerations . . . . .                             | 99        |
| 6.5.3    | Offset selection . . . . .                                       | 104       |
| 6.5.4    | Analysis of the charge to amplitude ratio distribution . . . . . | 109       |

|          |  |            |
|----------|--|------------|
| 6.5.5    | Overlap of Charge ditributions . . . . .                         | 112        |
| 6.5.6    | Signal selection . . . . .                                       | 113        |
| 6.5.7    | Calibration . . . . .  | 113        |
| 6.5.8    | Cross section extraction . . . . .                               | 114        |
| 6.5.9    | Results . . . . .  | 115        |
| 6.6      | $^{245}_{96}\text{Cm}$ . . . . .                                 | 121        |
| 6.6.1    | Pulse shape analysis . . . . .                                   | 121        |
| 6.6.2    | Offset selection . . . . .                                       | 123        |
| 6.6.3    | Space-charge equivalence . . . . .                               | 125        |
| 6.6.4    | Analysis of the charge to amplitude ratio distribution . . . . . | 127        |
| 6.6.5    | Cross section extraction . . . . .                               | 127        |
| 6.6.6    | Results . . . . .  | 128        |
| <b>7</b> | <b>Conclusions</b>   | <b>131</b> |
|          | <b>APPENDIX A</b>  | <b>133</b> |
|          | <b>APPENDIX B</b>  | <b>136</b> |
|          | <b>APPENDIX C</b>  | <b>147</b> |
|          | <b>List of Figures</b>   | <b>160</b> |
|          | <b>List of Tables</b>  | <b>168</b> |
|          | <b>References</b>  | <b>169</b> |
|          | <b>Bibliography</b>  | <b>176</b> |



# 1 Introduction

*"The real issue is freedom. We must deal with the energy problem on a war footing."*

J. Carter (15<sup>th</sup> July 1979)

The Earth is the only one Planet of the Solar system and of the known Universe where different factors met and made human life possible. Our society is now the result of the mankind capability to learn from experience, develop ideas and turn them into reality. This allowed the population to grow. But we are now at a point where our development, once in syntony with the environment, is not sustainable anymore.

## 1.1 The need of electricity

It took 50000 years for population to reach 1 billion ( $10^9$ ), a little more than a century to reach 2 billions, 33 years to reach 3 billions, 14 years to reach 4 billions, 13 years to reach 5 billions and 12 years to reach 6 billions. Nowadays there are 6,6 billion people on Earth and by 2050 this number will grow to 9 billions [1; 2]. In such scenario, energy consumption is going to increase (Fig. 1).

Moreover, looking at our world as it is nowadays, a complete unbalanced situation is found. 20% of the population consumes 80% of the natural resources [3]. About 25% of people have no access to electricity today [4] and clean water is a serious issue in several countries. The situation will be even worst as many people populate our planet and as developed and developing countries pollute the environment.

Finally fossil fuels, the most widely used energetic source, are going to finish and the consequently increased contractual power of certain countries without some basic rights or not particularly stable where reserves are located, arises political concerns.

Renewable clean sources are the only way. But, as for now, they would not be sufficient. Nowadays hydroelectric power stations provide 16% of world electricity. One of the main advantage of this energy source (renewable and clean) relies in the possibility of easily stop and start the production process to meet peak-load demand. For this reason it is usually thought as complementary to wind power stations. Other renewable (i.e. solar, wind, biomass and geothermal power) provide only 2.3% of the world electricity generation and, even with subsidy and research support, are foreseen to contribute for no more than 6% by 2030.

Wind energy is in fact intermittent and should be coupled with other solutions (for example hydroelectric power stations). Since regions with strong winds are not

the easiest place to live, the grid efficiency has to be considered.

Geothermal sources (Geysers) are available only in some parts of the world, like in New Zealand. Some other options, like tidal, wave and ocean thermal energy are under study with some pilot projects.

Biofuel seems not to have been a great idea. Land has to be subtracted to agriculture, and the energy inputs for growing, fertilizing and irrigate crops can be greater than the energy gained by the produced fuel.

The most common known method for solar energy exploitation consists in photovoltaic cells. More efficiency can be gained by using their concentrating version, i.e. a sort of parabolic mirror. Though their efficiency (50%) is still far from being comparable with fossil fuels, it must be said that in few years big steps have been made and the hope in further improvements is well reposed.

The cleanest and lowest cost source of electricity remains by the way energy saving. But industry can not base its production on it. Therefore as for now, summarizing, less than 20% of the world electricity generation can be provided by clean and renewable sources (Fig. 2).

## 1.2 The nuclear option

Nowadays we can rely on 13000 reactor years of experience [5]. The first nuclear power plant built for civil purposes and connected to the grid was the AM-1 (Атом Мирный, i.e. peaceful atom) Obninsk Nuclear Power Plant (Russian Federation). It was operative from 27<sup>th</sup> June 1954 up to 29<sup>th</sup> April 2002 and produced around 5 MW (electrical).

Today nuclear power stations generate more electricity than it was produced 50 years ago by all sources. They provide almost 15% of the world electricity and in France the share reaches 75%. In this moment 436 reactors are operative in 30 countries with 372000 MWe of total capacity. Nearly 300 research reactors are used all around the world to study the subatomic structure, improve technology and create radioisotopes for medical applications. Meanwhile about 220 nuclear propelled ships and submarines are sailing our oceans [6].

Nuclear fission generates much more energy than any other process. Typical heat conversion values for different fuels are reported in Table 1. Moreover, though not renewable, this energy source is considered "cleaned", meaning with this word that it doesn't release greenhouse gases in the atmosphere. For these reasons several countries are adopting a pro-nuclear position.

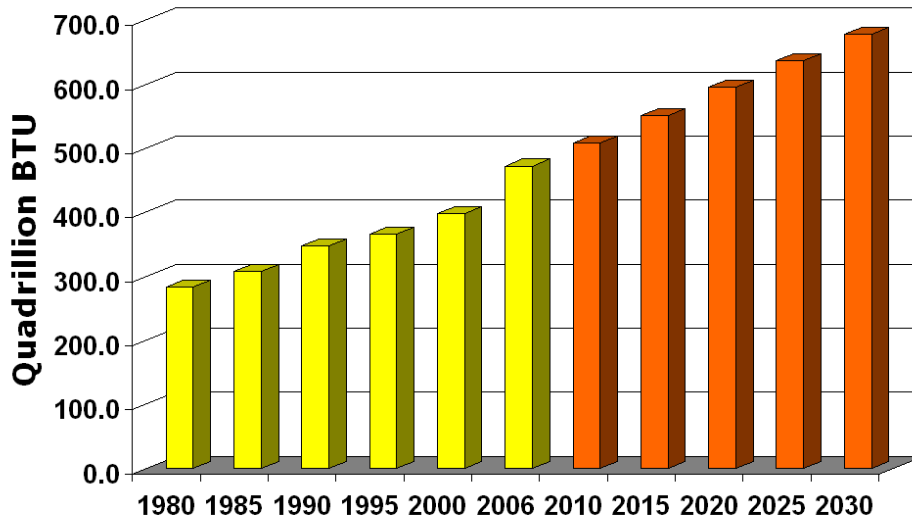


Figure 1: WORLD MARKETED ENERGY CONSUMPTION. YELLOW DATA (HISTORY) FROM [7], ORANGE DATA (PROJECTION) FROM [8].

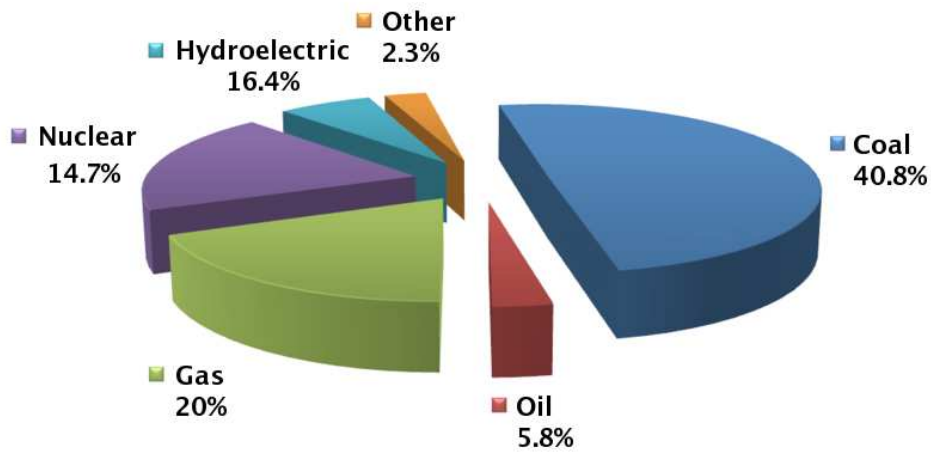


Figure 2: ELECTRICITY GENERATION BY FUEL IN 2008. DATA TAKEN FROM [9] AND REVISED IN A PIE GRAPH.

Without entering into economical and political considerations, where mathematics seems to be an opinion, three facts can not be denied:

- renewable and clean sources are not yet capable to fulfill the world energy demand
- 436 reactors are working, another 52 are in construction, 135 are planned and 295 proposed (See Table 2).
- nuclear reactors (power as well as research) generate waste

Current uranium usage is about 65000 t/yr, which means that at the present exploitation rate easily available reserves <sup>1</sup> are enough to run thermal reactors (i.e. reactors where fission is induced by thermal neutrons) for another 80 years. Trying to disentangle ourselves among optimistic disquisitions about the amount of this major actinide recoverable from stockpiles and weapons, about our limited knowledge of the Earth's crust as well as about the balance between the cost of exploration efforts and the income deriving by the discovery of new mines and pessimistic speeches dealing with the increase in the exploitation rate and with forecast of market prices which would make competitive the now expensive technology to extract uranium from seawater, the only certainty is the finite quantity of this element on our Planet.

Table 1: HEAT CONVERSION VALUES. DATA FROM [6; 10; 11].

| Source                            | Heat Values<br>[MJ/Kg] |
|-----------------------------------|------------------------|
| Firewood                          | 16                     |
| Brown coal                        | 9                      |
| Black coal (low quality)          | 13-20                  |
| Black coal                        | 24-30                  |
| Natural gas                       | 42                     |
| Crude Oil                         | 45-46                  |
| Hydrogen                          | 142                    |
| Uranium* - in light water reactor | 500000                 |

<sup>1</sup>i.e. Reserves of U ore, implying a mineral form that can economically be recovered by dissolution in sulfuric acid. Seawater does not belong to this category.

|                       | NUCLEAR<br>ELECTRICITY<br>GENERATION<br>2008 |      | REACTORS<br>OPERABLE<br>1 Dec. 2009 |       | REACTORS<br>UNDER<br>CONSTRUCTION<br>1 Dec. 2009 |       | REACTORS<br>PLANNED<br>Dec. 2009 |       | REACTORS<br>PROPOSED<br>Dec. 2009 |       | URANIUM<br>REQUIRED<br>2009 |
|-----------------------|--|------|-------------------------------------|-------|--|-------|----------------------------------|-------|-----------------------------------|-------|-----------------------------|
|                       | TWh  | %E   | N                                   | MWe   | N  | MWe   | N                                | MWe   | N                                 | MWe   | Tonnes U                    |
| <b>Argentina</b>      | 6,8  | 6,2  | 2                                   | 935   | 1  | 692   | 1                                | 740   | 1                                 | 740   | 122                         |
| <b>Armenia</b>        | 2,3  | 39,4 | 1                                   | 376   | 0  | 0     | 0                                | 0     | 1                                 | 1000  | 51                          |
| <b>Bangladesh</b>     | 0  | 0    | 0                                   | 0     | 0  | 0     | 0                                | 0     | 2                                 | 2000  | 0                           |
| <b>Belarus</b>        | 0  | 0    | 0                                   | 0     | 0  | 0     | 2                                | 2000  | 2                                 | 2000  | 0                           |
| <b>Belgium</b>        | 43,4   | 53,8 | 7                                   | 5728  | 0  | 0     | 0                                | 0     | 0                                 | 0     | 1002                        |
| <b>Brazil</b>         | 14,0   | 3,2  | 2                                   | 1901  | 0  | 0     | 1                                | 1245  | 4                                 | 4000  | 308                         |
| <b>Bulgaria</b>       | 14,7   | 32,9 | 2                                   | 1906  | 0  | 0     | 2                                | 1900  | 0                                 | 0     | 260                         |
| <b>Canada</b>         | 88,6   | 14,8 | 18                                  | 12652 | 2  | 1500  | 4                                | 4400  | 3                                 | 3800  | 1670                        |
| <b>China</b>          | 65,3   | 2,2  | 11                                  | 8587  | 18   | 19240 | 35                               | 37000 | 90                                | 79000 | 2010                        |
| <b>Czech Republic</b> | 25,0   | 32,5 | 6                                   | 3686  | 0  | 0     | 0                                | 0     | 2                                 | 3400  | 610                         |
| <b>Egypt</b>          | 0  | 0    | 0                                   | 0     | 0  | 0     | 1                                | 1000  | 1                                 | 1000  | 0                           |
| <b>Finland</b>        | 22,0   | 29,7 | 4                                   | 2696  | 1  | 1600  | 0                                | 0     | 0                                 | 1000  | 446                         |
| <b>France</b>         | 418,3  | 76,2 | 58                                  | 63236 | 1  | 1630  | 1                                | 1630  | 1                                 | 1630  | 10569                       |
| <b>Germany</b>        | 140,9  | 28,3 | 17                                  | 20339 | 0  | 0     | 0                                | 0     | 0                                 | 0     | 3398                        |
| <b>Hungary</b>        | 14,0   | 37,2 | 4                                   | 1870  | 0  | 0     | 0                                | 0     | 2                                 | 2000  | 274                         |
| <b>India</b>          | 13,2   | 2,0  | 17                                  | 3779  | 6  | 2976  | 23                               | 21500 | 15                                | 20000 | 961                         |
| <b>Indonesia</b>      | 0  | 0    | 0                                   | 0     | 0  | 0     | 2                                | 2000  | 4                                 | 4000  | 0                           |
| <b>Iran</b>           | 0  | 0    | 0                                   | 0     | 1  | 915   | 2                                | 1900  | 1                                 | 300   | 143                         |
| <b>Israel</b>         | 0  | 0    | 0                                   | 0     | 0  | 0     | 0                                | 0     | 1                                 | 1200  | 0                           |
| <b>Italy</b>          | 0  | 0    | 0                                   | 0     | 0  | 0     | 0                                | 0     | 0                                 | 17000 | 0                           |
| <b>Japan</b>          | 240,5  | 24,9 | 53                                  | 46236 | 2  | 2285  | 13                               | 17915 | 1                                 | 1300  | 8388                        |
| <b>Kazakhstan</b>     | 0  | 0    | 0                                   | 0     | 0  | 0     | 2                                | 600   | 2                                 | 600   | 0                           |
| <b>North Korea</b>    | 0  | 0    | 0                                   | 0     | 1  | 950   | 0                                | 0     | 0                                 | 0     | 0                           |
| <b>South Korea</b>    | 144,3  | 35,6 | 20                                  | 17716 | 6  | 6700  | 6                                | 8190  | 0                                 | 0     | 3444                        |

|              | NUCLEAR<br>ELECTRICITY<br>GENERATION<br>2008 |           | REACTORS<br>OPERABLE<br>1 Dec. 2009 |                | REACTORS<br>UNDER<br>CONSTRUCTION<br>1 Dec. 2009 |               | REACTORS<br>PLANNED<br>Dec. 2009 |                | REACTORS<br>PROPOSED<br>Dec. 2009 |                | URANIUM<br>REQUIRED<br>2009 |
|--------------|--|-----------|-------------------------------------|----------------|--|---------------|----------------------------------|----------------|-----------------------------------|----------------|-----------------------------|
|              | TWh  | %E        | N                                   | MWe            | N  | MWe           | N                                | MWe            | N                                 | MWe            | Tonnes U                    |
| Lithuania    | 9,1  | 72,9      | 1                                   | 1185           | 0  | 0             | 0                                | 0              | 2                                 | 3400           | 134                         |
| Mexico       | 9,4  | 4,0       | 2                                   | 1310           | 0  | 0             | 0                                | 0              | 2                                 | 2000           | 242                         |
| Netherlands  | 3,9  | 3,8       | 1                                   | 485            | 0  | 0             | 0                                | 0              | 1                                 | 1000           | 97                          |
| Pakistan     | 1,7  | 1,9       | 2                                   | 400            | 1  | 300           | 2                                | 600            | 2                                 | 2000           | 65                          |
| Poland       | 0  | 0         | 0                                   | 0              | 0  | 0             | 0                                | 0              | 6                                 | 6000           | 0                           |
| Romania      | 7,1  | 17,5      | 2                                   | 1310           | 0  | 0             | 2                                | 1310           | 1                                 | 655            | 174                         |
| Russia       | 152,1  | 16,9      | 31                                  | 21743          | 9  | 7310          | 7                                | 8000           | 37                                | 36680          | 3537                        |
| Slovakia     | 15,5   | 56,4      | 4                                   | 1760           | 2  | 840           | 0                                | 0              | 1                                 | 1200           | 251                         |
| Slovenia     | 6,0  | 41,7      | 1                                   | 696            | 0  | 0             | 0                                | 0              | 1                                 | 1000           | 137                         |
| South Africa | 12,7   | 5,3       | 2                                   | 1842           | 0  | 0             | 3                                | 3565           | 24                                | 4000           | 303                         |
| Spain        | 56,4   | 18,3      | 8                                   | 7448           | 0  | 0             | 0                                | 0              | 0                                 | 0              | 1383                        |
| Sweden       | 61,3   | 42,0      | 10                                  | 9399           | 0  | 0             | 0                                | 0              | 0                                 | 0              | 1395                        |
| Switzerland  | 26,3   | 39,2      | 5                                   | 3237           | 0  | 0             | 0                                | 0              | 3                                 | 4000           | 531                         |
| Thailand     | 0  | 0         | 0                                   | 0              | 0  | 0             | 4                                | 4000           | 2                                 | 2000           | 0                           |
| Turkey       | 0  | 0         | 0                                   | 0              | 0  | 0             | 2                                | 2400           | 1                                 | 1200           | 0                           |
| Ukraine      | 84,3   | 47,4      | 15                                  | 13168          | 0  | 0             | 2                                | 1900           | 20                                | 27000          | 1977                        |
| UAE          | 0  | 0         | 0                                   | 0              | 0  | 0             | 3                                | 4500           | 11                                | 15500          | 0                           |
| U. K.        | 52,5   | 19        | 11035                               | 0              | 0  | 4             | 6600                             | 6              | 9600                              | 0              | 2059                        |
| USA          | 809,0  | 19,7      | 104                                 | 101119         | 1  | 1180          | 11                               | 13800          | 19                                | 25000          | 18867                       |
| Vietnam      | 0  | 0         | 0                                   | 0              | 0  | 0             | 2                                | 2000           | 8                                 | 8000           | 0                           |
| <b>WORLD</b> | <b>2601</b>                                  | <b>15</b> | <b>435</b>                          | <b>372,707</b> | <b>53</b>  | <b>49,588</b> | <b>136</b>                       | <b>149,645</b> | <b>299</b>                        | <b>304,005</b> | <b>65,405</b>               |

Table 2: WORLD NUCLEAR POWER REACTORS & AND URANIUM REQUIREMENTS

Reactor data: WNA to 01/12/09

IAEA: for nuclear electricity production & percentage of electricity (%e) 5/09

WNA: Global Nuclear Fuel Market (Reference scenario) for U.

Operating = Connected to the grid

Building/Construction = first concrete for reactor poured or major refurbishment under way

Planned = Approvals and funding in place, or construction well advanced but suspended indefinitely

Proposed = clear intention but still without funding and/or approvals.

TWh = Terawatt/hours (billion kilowatt-hours),

MWe = megawatt net (electrical as distinct from thermal),

Kwa = kilowatt/hour

It is therefore important:

- maximizing the efficiency of nuclear power plants
- considering other fissionable isotopes beyond the most commercially exploited  $^{235}\text{U}$
- face with the waste production problem and proliferation risks

This last item would remain even shutting down all civil and military reactors, unless humanity is ready to renounce to produce radioisotopes for medical diagnosis and cancer therapy.

### 1.3 The need of nuclear data

Burn-up efficiency maximization, optimization of alternative fuel cycles and waste elimination are goals achievable only through an improved knowledge of nuclear data. The concept of "cross section" is explained in § 5. For the moment it is enough to know that a reaction cross section is a scalar numerical value, with its own dimension ( $b$ , named *barn* and equal to  $10^{-24}$  cm<sup>2</sup>), proportional to the probability <sup>2</sup> of that reaction to occur. This quantity, designated with the Greek letter  $\sigma$ , is a function of the energy of the particle producing the studied process and thus assumes different values for different incident energies.

With neutron induced fission cross section ( $\sigma_{(n,f)}(E)$ ), the fission probability caused by incident neutrons of energy  $E$  is meant.

#### 1.3.1 Burning efficiency

The main fissile isotopes <sup>3</sup> are  $^{233}\text{U}$ ,  $^{235}\text{U}$ ,  $^{239}\text{Pu}$  and  $^{241}\text{Pu}$ . Among these, only  $^{235}\text{U}$  is found in nature and is therefore the principal source of energy production exploited by actual reactors.

Thermal reactors are loaded with uranium dioxide pellets (3.6%  $^{235}\text{U}$  and 96.4%  $^{238}\text{U}$ ). In order to enrich the fuel, natural U is divided into two streams. Part of the  $^{235}\text{U}$  from one stream is "transferred" to the other one, resulting in enriched uranium on one side and depleted uranium (where the  $^{235}\text{U}$  content is  $< 0.25\%$ ) on the other. This "tail" is then employed in radiation shielding, its density being higher than that of lead. But its potential energetic content is lost forever.

The fissile isotope of uranium generates a chain reaction, while fast neutrons emitted in the fission process provoke just a small fraction of  $^{238}\text{U}$  to split. Some of the

---

<sup>2</sup>Cross sections can assume values ranging from 0 on, while a probability can not exceed 1. By the way, the higher the cross section value and the higher is the probability.

<sup>3</sup>A fissile material is one that is capable of sustaining a chain reaction of nuclear fission, a fissionable isotope is simply one isotope which can fission. Not all fissionable isotopes are therefore fissile.

$^{238}\text{U}$  in the reactor core is turned into plutonium and about half of this is also fissioned, providing about one third of the reactor's energy output. With a frequency of once per year or once every 18 months, about  $\frac{1}{3}$  of the spent fuel has to be replaced by fresh fuel.

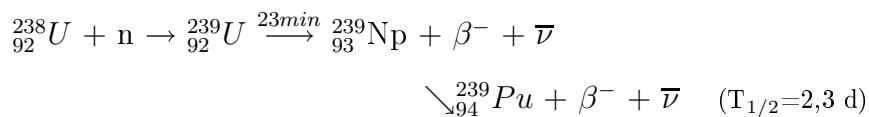
In such reactors just a small fraction of fuel is exploited, the rest resulting in nuclear waste and therefore potentially <sup>4</sup> lost.

Being capable of maximizing the burning rate, would result in a longer availability of uranium reserves. The reactor core is a mixture of all different isotopes created following fission, neutron capture,  $\alpha$  emission,... The time evolution of the core is really complicated and a precise knowledge of capture and reaction cross sections, including  $\sigma_{(n,f)}$  of several transuranic elements, would allow to tune the neutron flux on the point of maximum fuel burn-up and energy production.

### 1.3.2 Alternative fuel cycles

$^{238}\text{U}$  and  $^{232}\text{Th}$  are the two most abundant fertile <sup>5</sup> nuclei on earth. Following neutron capture they are transformed respectively into the fissile  $^{239}\text{Pu}$  and  $^{233}\text{U}$ , giving rise to two different fuel cycles.

The U/Pu fuel cycle, here schematically reported, has been widely exploited in fast reactors (i.e. reactors where fission is induced by fast - MeV - neutrons). Though  $^{239}\text{Pu}$  is an even-Z, odd-N isotope, the fission to absorption ratio favors its employment in the fast energy region of the neutron spectrum. For 0.025 eV incident neutrons  $^{239}\text{Pu}\sigma_{(n,f)} = 747 \text{ b}$ ,  $^{239}\text{Pu}\sigma_{(n,\gamma)} = 270 \text{ b}$ . Hence at thermal energies fission probability is about 2.76 times higher than capture probability. For 1 MeV incident neutrons instead  $^{239}\text{Pu}\sigma_{(n,f)} = 1.7 \text{ b}$ ,  $^{239}\text{Pu}\sigma_{(n,\gamma)} = 0.025 \text{ b}$ , and therefore fission probability is about 70 times higher than capture probability.



Fast reactors have the advantage of fissioning part of the produced actinides and therefore end up with a lower waste toxicity (see next paragraph). The reason why reactors based on the U/Pu cycle have been built, while the Th/U cycle has not been deeply investigated relies in the availability of the fissile material. Though neither  $^{233}\text{U}$  nor  $^{239}\text{Pu}$  exists in nature, this last isotope had been largely produced in thermal reactors.

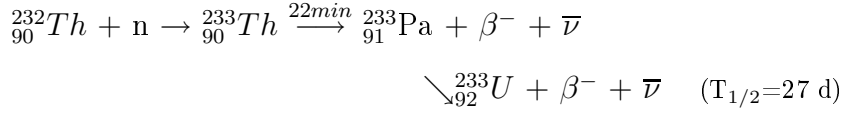
With the renaissance of nuclear interest, new attention is being paid to the Th/U

---

<sup>4</sup>Countries like USA, Switzerland and Sweden do not reprocess waste.

<sup>5</sup>A fertile material is a nuclide which is turned into fissile by neutron absorption.

fuel cycle [12]. As schematically shown here, the working principle of the two cycles is exactly the same:



In a comparison of advantages and disadvantages, the Th/U fuel cycle (reported in Fig. 3) results the winner. Its benefits are the following:

1. Thorium is 3 to 4 times more abundant than Uranium.
2. Thorium is isotopically pure, while natural Uranium is a mixture of  ${}^{234}\text{U}$ ,  ${}^{235}\text{U}$  and  ${}^{238}\text{U}$ .
3. Thorium is a better fertile material than  ${}^{238}\text{U}$  in thermal reactors. The absorption cross-section for thermal neutrons of  ${}^{232}\text{Th}$  (7.4 b) is almost 3 times that of  ${}^{238}\text{U}$  (2.7 b). A higher conversion to  ${}^{233}\text{U}$  is therefore possible with  ${}^{232}\text{Th}$ , than to  ${}^{239}\text{Pu}$  with  ${}^{238}\text{U}$ .
4. Contrary to what happens for  ${}^{235}\text{U}$  and  ${}^{239}\text{Pu}$ , the number of neutrons emitted per neutron absorbed ( $\eta$ ) by  ${}^{233}\text{U}$  is greater than 2.0 over a wide energy range of the thermal neutron spectrum. Hence, while in the U/Pu fuel cycle breeding is achievable only with fast neutrons, the Th/U fuel cycle can be operated with thermal, epithermal as well as with fast neutrons.
5. The Th/U fuel cycle ends up with a lower production of MA (minor actinides) with respect to the U/Pu one. This is because the cycle starts with a lighter nucleus: 6 units in mass and 2 in atomic number. Moreover the capture cross section of  ${}^{233}\text{U}$  is smaller (46 b) than that of  ${}^{235}\text{U}$  (101 b) and  ${}^{239}\text{Pu}$  (271 b) for thermal neutrons, while their fission cross sections are of same order of magnitude (525 b, 577 b and 742 b respectively for  ${}^{233}\text{U}$ ,  ${}^{235}\text{U}$  and  ${}^{239}\text{Pu}$ ). Therefore neutron absorption leading to higher isotopes ( ${}^{234}\text{U}$ ,  ${}^{236}\text{U}$  and  ${}^{240}\text{Pu}$ ) with higher absorption cross section is less probable.
6. Uranium ashes produced can be used as seeds for further utilization.
7. Thanks to generation of  ${}^{232}\text{U}$  via  ${}^{233}\text{U}(\text{n},2\text{n}){}^{232}\text{U}$  reactions, the Th/U fuel cycle is considered intrinsically proliferation resistant. This is because  ${}^{232}\text{U}$  has a half life  $\tau_{1/2} = 73.6 \text{ y}$  and decays to  ${}^{212}\text{Bi}$  and  ${}^{208}\text{Tl}$ , strong gamma emitters, making  ${}^{233}\text{U}$  handling more difficult.

Its disadvantages are the following:

1. There is not already available  $^{233}\text{U}$ .
2. The Th based fuel contains  $^{232}\text{U}$  which, if on one side makes the Th/U fuel cycle intrinsically proliferation resistant, on the other gives rise to build-up radiation and increases the cost of this fuel cycle.
3. The time taken by  $^{233}\text{Pa}$  to decay to  $^{233}\text{U}$  is much longer ( $\sim 27$  d) than the time taken by  $^{239}\text{Np}$  to decay to  $^{239}\text{Pu}$ . An on-line extraction of  $^{233}\text{Pa}$  followed by reinjection after it has decayed is one possible solution.
4. Lack of experience and of nuclear data.

Both cycles, when the high energy region of the neutron spectrum is exploited, end up with production of the fissile material at a rate higher than it is consumed. Such fast reactors are known as *breeders*. Making use of the more available  $^{238}\text{U}$  and  $^{232}\text{Th}$ , these systems, thought a little bit more tricky than the thermal ones because of some technological challenges, are foreseen to increase from 80 to 400 years our possibility of producing nuclear energy. Therefore the U/Pu fuel cycle is not going to be abandoned and 3 out of the 6 proposed projects for new Generation reactors are going to be fast reactors based on it.

Since benefits highly exceed disadvantages, one of the Generation IV reactors [13] under study is based on the Th/U fuel cycle. Reactor generations are discriminated on the basis of technological improvements with respect to previous systems and of their safety level, which is as to say according to the period of construction. Early prototypes reactors built in the 1950s and 1960s represented the 1<sup>st</sup> Generation. Current reactors in operation around the world are generally considered 2<sup>nd</sup> (large commercial power plants built from the 1970s to 1990s) or sometimes 3<sup>rd</sup> (built from the 1990s on) generation systems. Generation IV reactors are a set of 6 reactor designs which should be operative from 2030 or later.

Given the foreseen employment of the Th/U fuel cycle for one of the proposed reactor types, an extremely accurate knowledge of  $^{232}\text{Th}(n,\gamma)$  and  $^{233}\text{U}(n,f)$  cross sections is of primary importance. For this reason the European Union is financing feasibility studies. Among them the n\_TOF experiment.

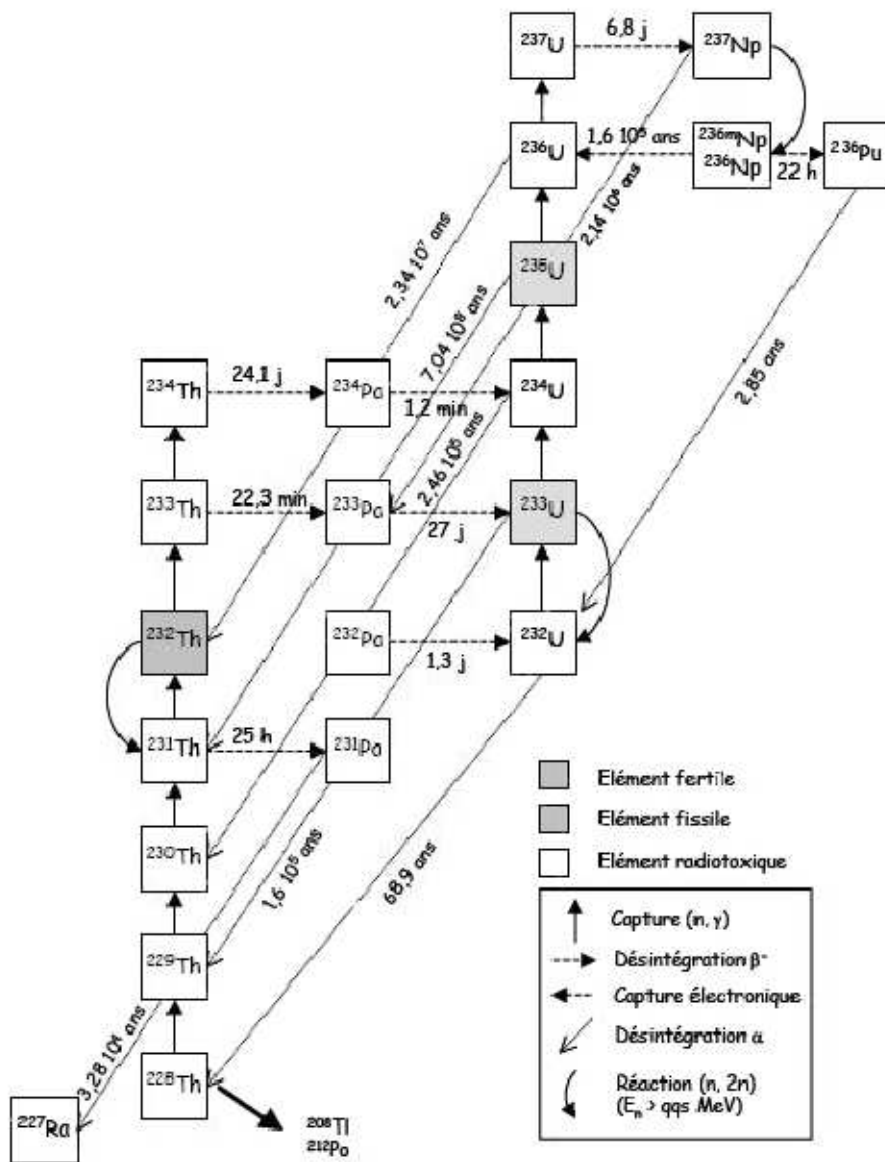


Figure 3: Th/U FUEL CYCLE. PICTURE TAKEN FROM [14].

### 1.3.3 Waste production and weapon proliferation

The production of nuclear energy and the use of radioactive materials in industrial applications as well as in research and medicine, creates radioactive waste. In 1994 International Atomic Energy Agency (IAEA) published a classification of radioactive waste which is nowadays internationally accepted [15]. These classes in which waste is grouped address activity content, radiotoxicity and thermal power. The principal waste classes include exempt waste (EW: the recommended activity concentrations are dependent on the individual radionuclide and range from about 0.1 Bq/g to about  $10^4$  Bq/g), low and intermediate level waste (LILW: requiring no or little shielding), which may be subdivided into short lived ( $\tau_{1/2} < 30$  y) and long lived ( $\tau_{1/2} \geq 30$  y), and high level waste (HLW).

High-level waste is material that remains at dangerously high levels of radioactivity for hundreds or even thousands of years and has therefore to be kept isolated from the biosphere for periods as long as the human history. This poses several constraints on the features of geological disposals.

There are two types of high level waste: fission products, transuranics and  $\alpha$ -,  $\beta$ - and  $\gamma$ -emitters separated from the spent fuel <sup>6</sup> during the reprocessing <sup>7</sup>, and the spent fuel elements themselves from the reactor core when they are not reprocessed. While representing only 3% of the volume of all radwaste, it holds 95% of the radioactivity.

According to IAEA, nuclear power generation facilities produce about 200000 m<sup>3</sup> of LILW and 10000 m<sup>3</sup> of HLW (including spent fuel designated as waste) each year worldwide. Keeping in mind that the Yucca Mountain capacity is 150000 m<sup>3</sup>, a 210000 m<sup>3</sup> discharge per year is - provocatively speaking - as filling 1 Yucca Mountain each 8 months and a half. As evident, a first problem is represented by physical space.

Another remarkable point is that the so called spent fuel is not *spent* in the sense that all its energy has been completely extracted. It is composed for 96% by uranium (comparable to natural uranium), 1% transuranic elements (principally plutonium, but also other actinides), the rest being radioactive and stable fission products and activation elements.

The residual energy content of the uranium and actinides could be extracted in power reactors. The actinides alone have an energy content equivalent to 30% of the

---

<sup>6</sup>Spent fuel is fuel removed from the reactors when its reactivity has decreased due to the buildup of fission and activation products and because the mechanical integrity of the fuel has been reduced. It has undergone at least one year's decay since being used as a source of energy in a power reactor, and has not been chemically separated into its constituent elements by reprocessing. Spent fuel includes special nuclear material, byproduct material, source material, and other radioactive materials associated with fuel assemblies.

<sup>7</sup>Reprocessing consists in separation of elements composing waste in order to recover part of them.

energy released by fission during generation of the spent fuel. The remaining uranium has a very large residual energy content - about two orders of magnitude higher than the energy released during fission.

A reutilization of the spent fuel would allow to recover the primary source necessary to operate nuclear reactors, increasing the time availability of present ore reserves.

A possible solution to space and energy problems was identified in partitioning (separation of different isotopes composing waste) and transmutation (conversion of one isotope into another isotope by inducing a change in the nucleus). When an isotope is subject to a neutron flux, among the possible processes which can take place, there are transmutation and induced fission. This last is still considered transmutation, but it is properly known as incineration. So a distinction must be made between actinides and fission products. Under a neutron flux, the former can either be transmuted, the result being another actinide, or fissioned, hence producing energy and fission products. Fission products can instead only be transmuted. The goals of transmutation are therefore the reduction of highly radioactive elements to stable (or shortly radioactive) ones, with a consequent decrease of the space allocated for geological disposal and a more efficient exploitation of the nuclear fuel.

Transmutation can be achieved using normal critical reactors, both fast and thermal. Nevertheless, transmutation in critical reactors has been practically abandoned because of its low efficiency and high hazardness (due to difficulty in maintaining criticality in delayed neutrons deficiency conditions). Accelerator Driven Systems (ADS) have been proposed.

ADS are subcritical reactors equipped with an external neutron source (coupling of an accelerator with a spallation target) and a partitioning facility. The incineration efficiency is basically determined by the neutron economy, which makes the external neutron source necessary, and the neutron energy spectrum of the critical or sub-critical reactor.

The actinide nuclei with an odd number of neutrons, like  $^{233}\text{U}$ ,  $^{235}\text{U}$  and  $^{239}\text{Pu}$ , have large thermal fission cross sections. Vice-versa, isotopes with even neutron numbers only fission by fast neutrons. Some of the latter transmute to thermally fissile nuclei by neutron capture, like  $^{232}\text{Th}$  and  $^{238}\text{U}$ , as already seen. Most of the fission products have large thermal capture cross sections and also large epithermal resonance capture cross sections in comparison with the cross sections for fast neutrons. This means that a thermal or a fast neutron transmutation system can only transmute a certain fraction of the nuclear waste in an optimal way. A reactor having a fast neutron spectrum is needed to incinerate the non-thermally fissile transuranic isotopes. Among them there are isotopes of the so called minor actinide elements (Np, Am and Cm), which constitute a primary goal to incinerate. The control of a self-sustained chain reaction, or criticality control, relies on the small fraction of delayed neutrons emitted from the fission products "long time" after the fission it-

self. This small fraction of delayed neutrons determines the criticality safety margins, which put some serious constraints on the fissile fuel composition, for example reactors can't operate purely on minor actinide fuel, because of the very low fraction of delayed neutrons.

Several ADS projects are under study and few are already in construction. A perfect knowledge of the neutron induced fission cross sections of minor actinides (i.e. Am, Np and Cm) is essential.

While representing a solution to two important problems, the partitioning necessary to transmutation seems to worsen the issue of nuclear weapon proliferation by making fissile materials (like  $^{239}\text{Pu}$ ) available. Separation of perfectly calculated harmless mixes of isotopes are foreseen.

#### 1.4 Nuclear libraries and experimental data

Summarizing  $^{233}\text{U}$   $\sigma_{(n,f)}$  are highly requested in view of the construction of Generation IV reactors based on the Th/U fuel cycle, while a precise knowledge of minor actinides (n,f) cross section is desirable in order to perform transmutation and tune the energy of the neutron spectrum looking for higher burn-up efficiency.

Thanks to the synergy between experiments and theoretical models, data libraries can be compiled. Unfortunately, due to our limited knowledge of the nuclear interactions and to experimental limits (reachable purity of fission deposits,  $\alpha$  activity of the sample, precise knowledge of the detection efficiency and of the neutron source intensity), results are not always in agreement. Experimental data often reports huge discrepancies and different evaluations are filled assigning them different weights, or even ignoring them in some energy ranges in order to match some benchmarks.

There are evaluation libraries dedicated to photonuclear reactions, fusion processes, ion beams,... As for nuclear data of interest in this thesis, reference evaluations are represented by JENDL (Japanese Evaluated Nuclear Data Libraries), ENDF/B (Evaluated Nuclear Data File version B, USA), JEF (Joint Evaluated File, Europe) and JEFF (Joint Evaluated Fission and Fusion file, NEA Data Bank, Europe), CENDL (Chinese Evaluated Nuclear Data Library), BROND (library of recommended neutron data, Russian Federation), RUSFOND (RUSSian File Of evaluated Neutron Data, Russian Federation) and Minsk Actinide Library (Maslov's Evaluations, Russian Federation). Libraries are being continuously updated thanks to experimental results. A number is associated to each version. The higher the number, the most recent the version.

Experimental data are collected in EXFOR files (Experimental Nuclear Reaction Data).

Nuclear libraries are of primary importance because they allow to project facilities. Knowing that the fission probability of one isotope for a certain incident particle in a

defined energy range is null, no one will spend money to build a facility fulfilling such conditions. Moreover safety margins are decided on the basis of the present evaluations. Finally, nuclear data libraries are loaded in Monte Carlo codes. By running simulations, a realistic idea of the results got in a certain experiment is obtained. This allows to tune experimental parameters in optimal way, avoiding to waste money by building different trial set-ups. Simulations act also as a test. If results obtained by running Monte Carlo codes and experiments are different, it means either the implemented code/model is wrong, or nuclear data are not precise.

As for the minor actinides, experimental data lack and evaluations are therefore affected by high uncertainties. This does not prevent reactors from working, but of course affects their performance. A working party on International Evaluation Cooperation has been established by the OECD/NEA Nuclear science committee [16]. Among its duties, a study to evaluate the impact of neutron cross section uncertainties on some integral parameters (like criticality) related to the core and fuel cycle of Generation IV reactors was performed. The most stringent requirements were indicated for Advanced Minor Actinides Burners [13]. Table 3 reports the required accuracies for neutron induced fission cross sections for the minor actinides analyzed in this work.

Table 3: TARGET ACCURACIES.

| Isotope           | Reactor Type | Energy Range [MeV] | Uncertainty [%] |               |                  |
|-------------------|--------------|--------------------|-----------------|---------------|------------------|
|                   |              |                    | Initial         | Required      |                  |
|                   |              |                    |                 | $\lambda = 1$ | $\lambda \neq 1$ |
| $^{241}\text{Am}$ | SFR          | 6.07 - 2.23        | 11.7            | 6.8           | 6.8              |
|                   |              | 2.23 - 1.35        | 9.8             | 6.4           | 6.5              |
|                   |              | 1.35 - 0.498       | 8.3             | 5.8           | 5.8              |
|                   | GFR          | 6.07 - 2.23        | 11.7            | 3.3           | 3.6              |
|                   |              | 2.23 - 1.35        | 9.8             | 3.3           | 3.6              |
|                   |              | 1.35 - 0.498       | 8.3             | 3.0           | 3.3              |
|                   | LFR          | 1.35 - 0.498       | 8.3             | 5.2           | 5.6              |
|                   | ADMAB        | 19.6 - 6.07        | 12.7            | 5.6           | 5.6              |
|                   |              | 6.07 - 2.23        | 11.7            | 1.7           | 1.7              |
|                   |              | 2.23 - 1.35        | 9.8             | 1.4           | 1.4              |
|                   |              | 0.498 - 0.183      | 8.3             | 3.9           | 3.9              |

| Isotope           | Reactor Type       | Energy Range [MeV] | Uncertainty [%] |               |                  |
|-------------------|--------------------|--------------------|-----------------|---------------|------------------|
|                   |                    |                    | Initial         | Required      |                  |
|                   |                    |                    |                 | $\lambda = 1$ | $\lambda \neq 1$ |
| $^{243}\text{Am}$ | SFR                | 6.07 - 2.23        | 11.0            | 8.2           | 8.1              |
|                   |                    | 2.23 - 1.35        | 9.2             | 7.2           | 7.2              |
|                   | ADMAB              | 6.07 - 2.23        | 11.0            | 2.3           | 2.3              |
|                   |                    | 2.23 - 1.35        | 6.0             | 1.9           | 1.9              |
|                   |                    | 0.498 - 0.183      | 9.2             | 1.6           | 1.6              |
|                   |                    | 2.23 - 1.35        | 44.2            | 14.3          | 15.2             |
| SFR               | 1.35 - 0.498       | 49.4               | 8.8             | 8.8           |                  |
|                   | 0.498 - 0.183      | 37.2               | 6.6             | 6.6           |                  |
|                   | 0.183 - 0.0674     | 47.5               | 6.7             | 6.8           |                  |
|                   | 0.0674 - 0.0248    | 26.5               | 8.8             | 8.8           |                  |
|                   | 0.0248 - 0.0912    | 13.5               | 9.1             | 9.1           |                  |
|                   | EFR                | 1.35 - 0.498       | 49.6            | 43.1          | 40.9             |
| 0.498 - 0.183     |                    | 37.2               | 37.3            | 35.8          |                  |
| 0.183 - 0.0674    |                    | 47.4               | 41.8            | 39.1          |                  |
| $^{245}\text{Cm}$ | GFR                | 1.35 - 0.498       | 49.4            | 16.3          | 16.7             |
|                   |                    | 0.498 - 0.183      | 37.2            | 13.3          | 13.9             |
|                   |                    | 0.183 - 0.0674     | 47.5            | 10.7          | 11.4             |
|                   | LFR                | 0.0674 - 0.0248    | 26.5            | 10.8          | 11.6             |
|                   |                    | 1.35 - 0.498       | 49.4            | 11.1          | 11.9             |
|                   |                    | 0.498 - 0.183      | 37.2            | 7.0           | 7.5              |
| ADMAB             | LFR                | 0.183 - 0.0674     | 47.5            | 7.2           | 7.8              |
|                   |                    | 0.0674 - 0.0248    | 26.5            | 8.9           | 9.4              |
|                   |                    | 6.07 - 2.23        | 31.0            | 7.1           | 7.1              |
|                   | ADMAB              | 2.23 - 1.35        | 44.2            | 5.8           | 5.8              |
|                   |                    | 1.35 - 0.498       | 49.4            | 3.3           | 3.3              |
|                   |                    | 0.498 - 0.183      | 37.2            | 2.9           | 2.9              |
|                   |                    | 0.183 - 0.0674     | 47.5            | 2.9           | 2.9              |
|                   |                    | 0.0674 - 0.0248    | 26.5            | 3.2           | 3.2              |
|                   |                    | 0.0248 - 0.00912   | 13.5            | 3.3           | 3.4              |
| ADMAB             | 0.00912 - 0.0203   | 13.2               | 3.6             | 3.6           |                  |
|                   | 0.00203 - 0.000454 | 13.0               | 4.7             | 4.7           |                  |

$\lambda$  is a cost parameter giving a relative figure of merit of the difficulty of improving accuracies.

ADMAB = Advanced Minor Actinides Burners;

SFR = Sodium-Cooled Fast Reactor;

LFR = Lead-Cooled Fast Reactor;

EFR = European Fast Reactor;

GFR = Gas-Cooled Fast Reactor.

## 2 The n\_TOF facility

*Salagadoola mechicka boola bibbidi-bobbidi-boo*  
(1950)

An extensive measurement campaign for reducing the  $\sigma_{n,f}$  uncertainties for both minor and major actinides was performed at the n\_TOF (Neutron Time of Flight) facility [17]. Thanks to its characteristics, summarized in § 2.4, the installation results the best station for studying not only the neutron induced fission cross sections of the isotopes discussed in this thesis, but also for a wider research project involving neutron induced reactions of elements relevant for nuclear technology and nuclear astrophysics.

The n\_TOF facility is a high fluence spallation neutron source located at CERN (Geneva, Switzerland), in the Meyrin site. The installation was proposed by Rubbia *et al.* [18] in 1998 and its construction was finished in 2001. The first commissioning took place in 2002 and data analyzed in this thesis were collected in 2004. After 4 years of stop, due to radioactive problems of the spallation target, in 2008 n\_TOF began a second life and it is now fully operative.

The facility was built in order to measure neutron induced cross section reactions. Neutrons are produced by collision of 20 GeV/c protons on a Pb spallation target, and driven to an experimental area through a vacuum pipe. The neutron kinetic energy is determined by time of flight.

The installation includes:

- proton extraction line
- spallation target with moderation and cooling system
- neutron beam optics
- experimental area (EAR-1)
- beam dump

Protons are created through hydrogen ionization by a duoplasmatron [19] and injected at 100 keV in a linear accelerator (linac-2). Here their kinetic energy is increased up to 50 MeV, before immission in a Booster (PSB). The PSB consists of 4 superimposed rings supplying the CERN Proton Synchrotron (CPS or simply PS) with 1.4 GeV kinetic energy protons. The PS is a circular accelerator delivering 20 GeV/c proton bunches to the n\_TOF experiment.

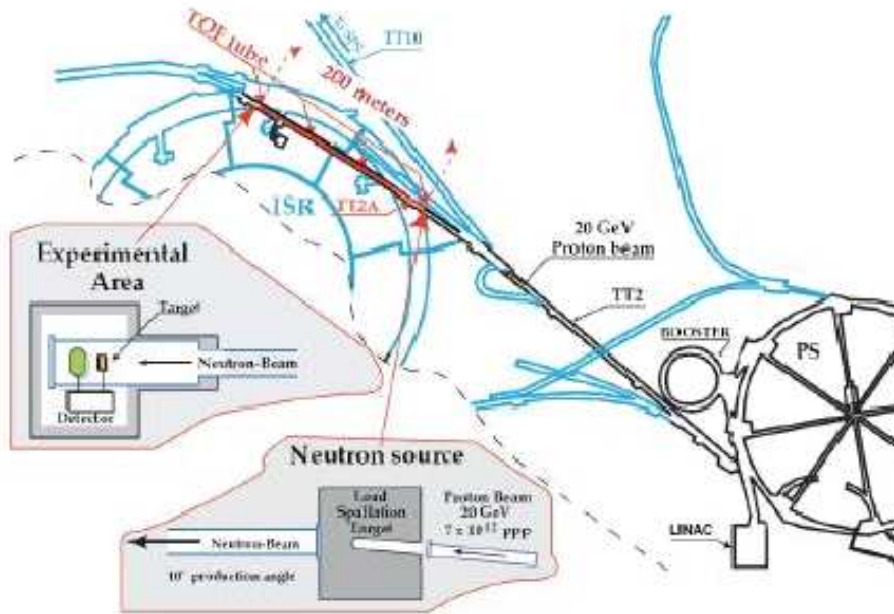


Figure 4: PS COMPLEX. PICTURE TAKEN FROM [20].

Two different PS beam configurations are exploited: dedicated and parasitic. In the first case, all protons are extracted and sent to the n\_TOF spallation target. The nominal bunch intensity is  $7 \times 10^{12}$  protons. In parasitic mode, the beam is split into two independent bunches, with a nominal intensity of  $4 \times 10^{12}$  and  $2 \times 10^{11}$  respectively. Both bunches are accelerated up to 20 GeV kinetic energy. Then, a bunch rotation<sup>8</sup> is applied to make bunches as short as possible and the larger one is extracted by a kicker<sup>9</sup> (fast extraction) in the TT2 line towards n\_TOF. The remaining bunch is accelerated to 24 GeV kinetic energy and slowly extracted to the East Area [21].

Proton bunches are delivered in super-cycles (SC). One SC is a time interval of about 14.4 s. Considering both the higher acceptable power dissipation on the lead target and the radiation level in the target area, a maximum of 4 bunches per SC (all parasitic, all dedicated or some parasitic and some others dedicated) is possible<sup>10</sup>. Though a lower beam intensity is delivered in the parasitic mode, this configuration allows an easier scheduling, as the beam is shared with other experiments.

A shorter bunch, means a smaller uncertainty on the proton position inside the bunch itself. Thus, bunch rotation enhances the TOF resolution and hence also the energy resolution (for more information about energy resolution see § 2.2.2).

<sup>8</sup>Bunch rotation = reduction of the energy spread.

<sup>9</sup>Kicker magnet = fast pulsed magnet used to deflect bunches without affecting the preceding or following ones. The transition times between no and full deflection can be of the order of tenths of ns.

<sup>10</sup>These data refer to the 2001-2004 measurements. Now one SC is about 48 s and a maximum of 10 bunches per super-cycle was tested [22].

All bunches delivered towards the n\_TOF facility have the following characteristics:

- 20 GeV kinetic energy
- 7 ns r.m.s.

The PS division takes care about everything related to the beam.

## 2.1 Description

### 2.1.1 Proton extraction line

The proton extraction line (FTN) is equipped with bending magnets to deflect the beam, quadrupoles to focus it and beam position as well as beam current monitors.

This last one (TRA 468 ) is a current transformer (two coupled coils). A signal proportional to the proton beam intensity (current) is detected and visible on a screen inside the n\_TOF control room.

The FTN intersects the neutron beam line at an angle of about  $10^\circ$ .

### 2.1.2 Spallation module

At the n\_TOF facility neutrons are generated by spallation reactions. This process was preferred to other neutron source mechanisms because it offers the best coupling of the energy range of operation and the provided flux (see Appendix A, pag. 133).

The term *spallation* was coined by W. H. Sullivan and G. T. Seaborg at Lawrence Radiation Laboratory (Berkeley, California) on 20<sup>th</sup> August 1947 [23] to address the process in which a heavy nucleus emits a large number of particles as a result of being hit by a light and high-energy projectile. Though this definition meets a wide variety of processes, for example fission, only some reactions can be classified as "spallation". The incident particle is a nucleon or a light projectile and its minimum kinetic energy must be  $100 \div 150$  MeV. Below this threshold other processes, and other nuclear models, take over [24] :

- elastic scattering  $\rightarrow$  optical model
- pre-equilibrium reactions  $\rightarrow$  exciton model
- equilibrium reactions  $\rightarrow$  Hauser-Feshbach model
- fission.

The spallation reaction can be described as a two-steps mechanism: an intranuclear cascade (INC) followed by pre-equilibrium and equilibrium evaporation. Fig. 5 shows the chain of events occurring when 1 GeV proton strikes a target.

At such high incident energies, the De-Broglie wavelength associated to the projectile is so small that more quasi free nucleon-nucleon collisions occur. This is the intranuclear cascade stage. In this direct process ( $t \approx 10^{-22}$  s), knock-out of nucleons is caused. Since the energy of the projectile exceeds the threshold for particle production in nucleon-nucleon collisions, intermediate-energy hadron generation and emission takes place as well.

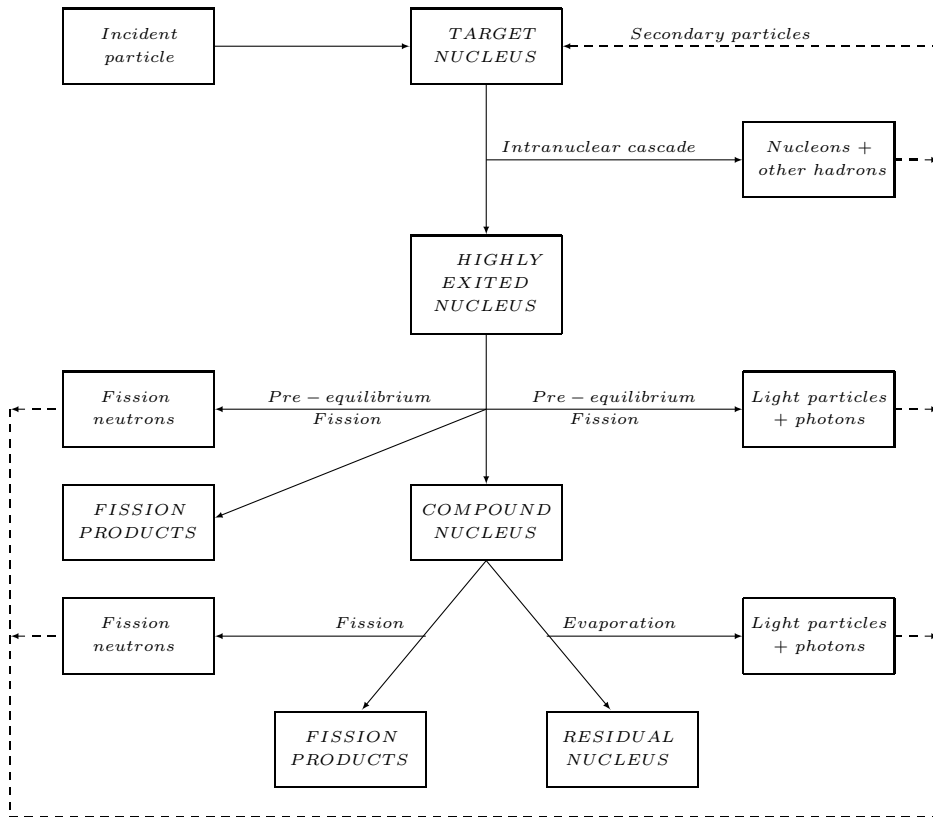


Figure 5: SCHEMATIC REPRESENTATION OF A SPALLATION PROCESS CAUSED BY 1 GeV INCIDENT PROTON. THE SOLID ARROWS REFER TO INTRANUCLEAR CASCADE, WHILE DOTTED ARROWS TO INTERNUCLEAR CASCADE [24].

The residual energy given to a nucleus through the collision is distributed among all its nucleons. Since there is no preferential way of sharing energy, it may happen that at a certain time, even before attainment of statistical equilibrium, all energy is given to only one nucleon and pre-compound emission takes place ( $t < 10^{-18}$  s). Another possible reaction in this stage is fission. When the thermalization process finishes ( $t < 10^{-15}$  s), a compound nucleus is left and evaporation of slow neutrons takes over. Again a competing reaction is fission. Once below the threshold for neutron emission, the nucleus de-excites by  $\gamma$  and  $\beta$  decay.

Secondary particles can now travel until they strike another nucleus. According to their momenta, they will proceed through different paths. The intermediate-energy secondary particles produced in knock-out, provoke the whole process to start by scratch (internuclear cascade), while the low-energy secondary particles promptly form a compound nucleus with the colliding body. Evaporation follows soon after, while the INC and pre-equilibrium stage are skipped.

The number of neutrons produced in spallation reactions strongly varies with the target material and incident energy of the projectile, but reaches a saturation above about  $2 \div 3$  GeV as shown in Fig. 6.

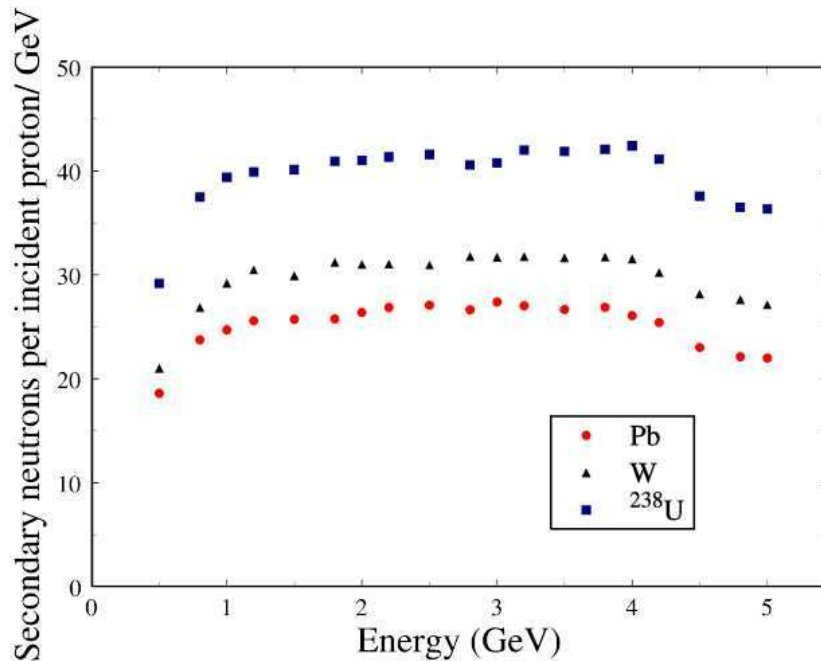


Figure 6: NUMBER OF NEUTRONS PER INCIDENT PROTON AS A FUNCTION OF THE PROTON ENERGY [25].

In order to achieve a proper p/n conversion in the spallation process, different high A materials are available. Neglecting uranium and transuranic elements because of their radioactivity, the choice was essentially between lead and tungsten. Owing to its better radiation damage resistance, prompt availability (from the TARC experiment [26]) and high transparency to low energy ( $\leq 1$  MeV) neutrons, the decision fell on lead.

The geometry of the spallation target was accurately studied [27]<sup>11</sup>. As a compromise among neutron flux intensity, neutron energy and the achievable precision in its knowledge, a high purity (99.99%)  $80 \times 80 \times 60$  cm<sup>3</sup> lead block (Fig. 7), in direct contact with demineralized water, acting both as a cooling and as a moderator, was installed. H<sub>2</sub>O thickness is 3 cm at the target entrance, to avoid unnecessary reactions, and 5 cm at the exit, for better moderation, and flows in a closed loop for safety reasons.

The window between the vacuum tube and the lead block is in aluminum alloy (AA 6082) because of well known material composition and good physical properties. Six thermocouples monitor the temperature of the lead target.

The spallation target is mounted into a stainless steel support, which makes its handling easier. The area is shielded by conventional concrete, with addition of marble blocks (marble suffers less activation under radiation than concrete). A picture of the target zone is shown in Fig. 8.

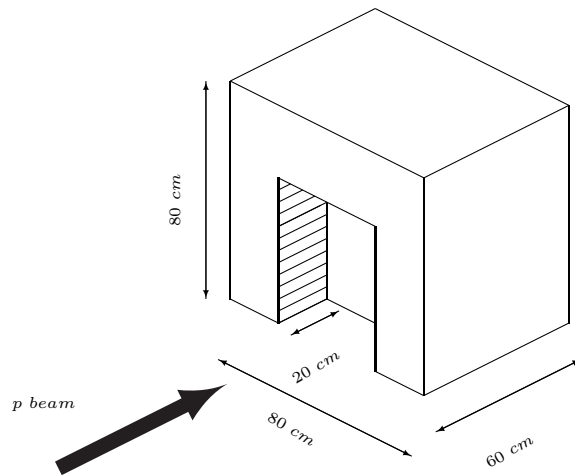


Figure 7: LEAD TARGET.

<sup>11</sup>Information here reported describes the spallation target layout dealing with the measurement campaign treated in this thesis. After 2004 a new spallation target was installed [28].

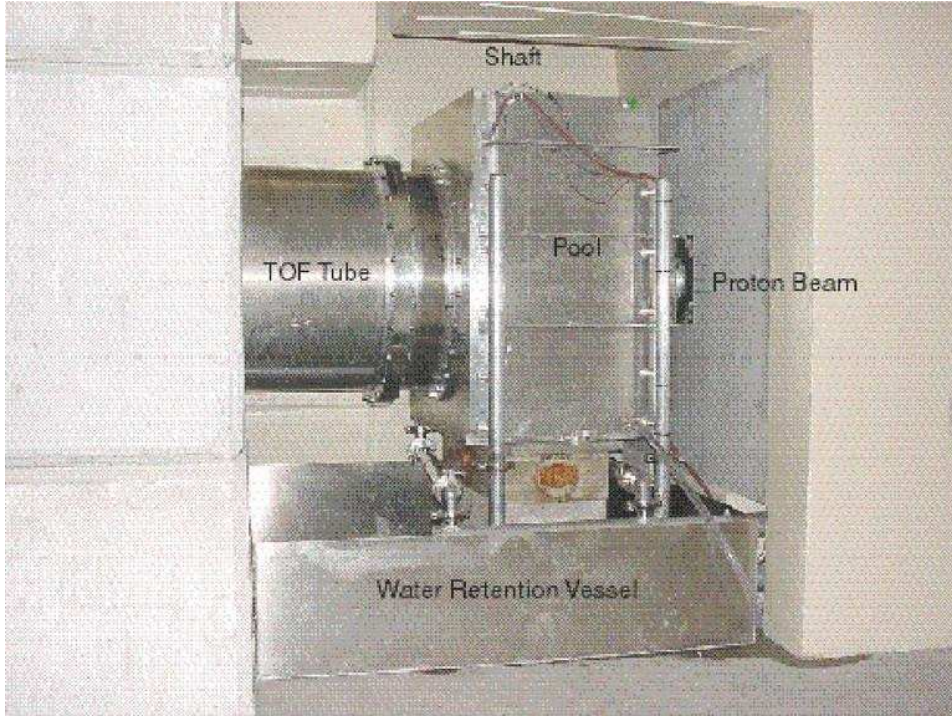


Figure 8: PICTURE OF THE TARGET ZONE.

### 2.1.3 Neutron beam optics

The time of flight tube is 199.607 m long and extends from the water tank, through the experimental area down to the beam dump, allowing extraordinary energy resolution. Background minimization is achieved thanks to the presence of shielding walls. In order to reduce beam contamination by fast relativistic particles and  $\gamma$  radiation, the neutron tube draws an angle of  $10^\circ$  with the proton line. A sweeping magnet removes the remaining charged particles.

The neutron tube is divided in different sectors of decreasing diameters for beam shaping purpose. A layout of the TOF line is reported in Fig. 9. A first aluminum alloy sector 3.9 m long and with  $\varnothing = 80$  cm is directly flanged onto the water tank. A  $\sim 70$  m long stainless steel tube, of the same diameter, follows. A second sector, with  $\varnothing = 60$  cm and in stainless steel, extends for another  $\sim 70$  m. The third sector, still in stainless steel and with  $\varnothing = 40$  cm, is equipped with a filter station and two collimators. It extends for  $\sim 40$  m and goes through the sweeping magnet (Fig. 10). The filter station allows background study thanks to 8 thick filters with strong neutron resonances. The first collimator, in iron and concrete, simply reduces the beam diameter, while the second one even shapes the neutron spectrum, thanks to the polyethylene hydrogen and  $^{10}\text{B}$  content, which respectively acts as a moderator and captures slow neutrons [29]. Since capture and fission measurements optimization

require different beam sizes <sup>12</sup>, the internal radius of the second collimator can be decreased or increased according to necessity. Just two values are possible: 4 cm and 9 cm (see Table 4). In both collimators the entrance radius is equal to the exit radius. The experimental area (EAR-1) is located between the third and fourth sector, called neutron escape line (NEL) and is delimited by shielding walls. The NEL extends for 12 m beyond the EAR-1, before beam dump.

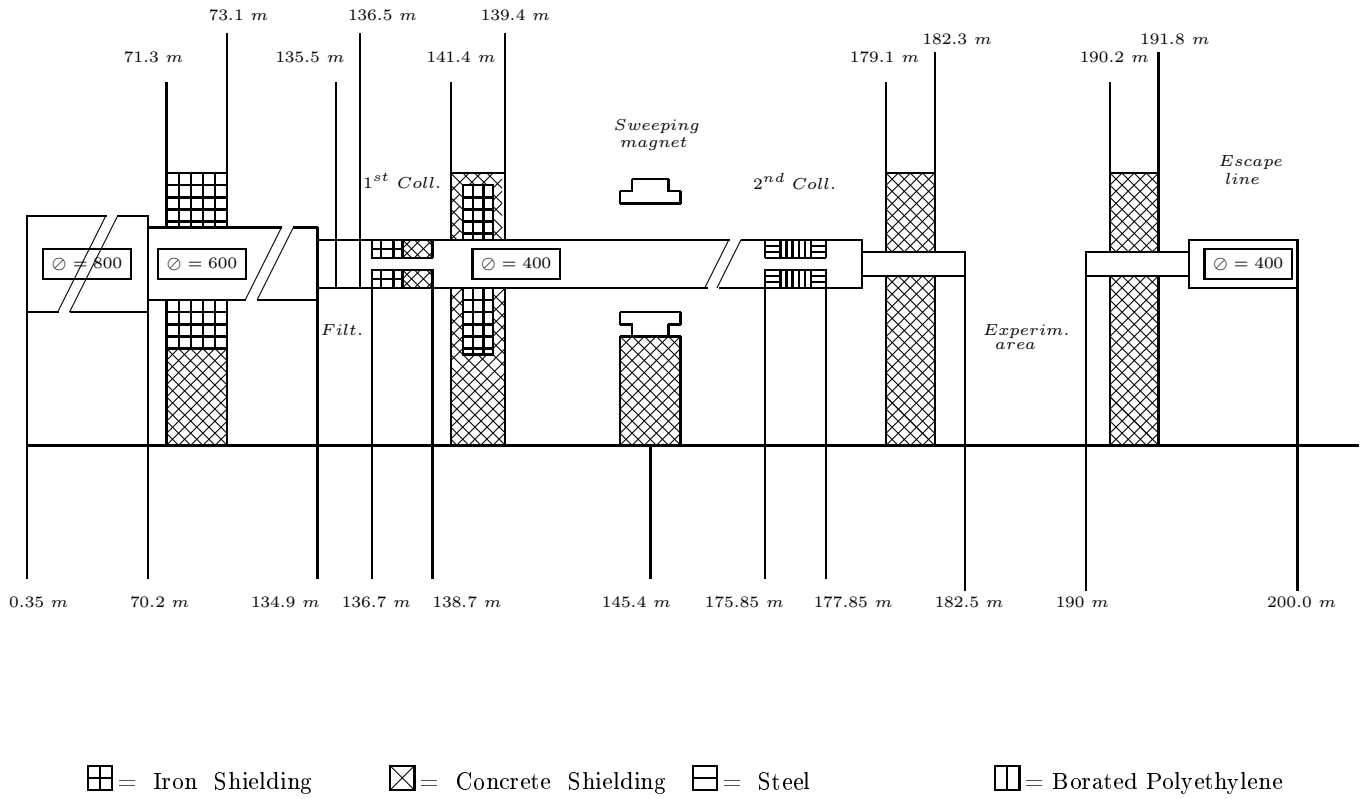


Figure 9: NEUTRON BEAM LINE

<sup>12</sup>Since sample thickness affects FFs detection efficiency, a large and thin sample is more desirable than a thick one for fission measurements.



Figure 10: SWEEPING MAGNET.

Table 4: COLLIMATOR PARAMETERS.

| Collimator                 | Segment Material        | Inner-Outer radius<br>[cm] | Length<br>[m] |
|----------------------------|-------------------------|----------------------------|---------------|
| $1^{st}$                   | 1-Iron                  | 5.5-25.0                   | 1             |
|                            | 2-Concrete              | 5.5-25.0                   | 1             |
| $2^{nd}$ C.M. <sup>a</sup> | 1-Borathed polyethylene | 0.9-20.0                   | 0.5           |
|                            | 2-Iron                  | 0.9-20.0                   | 1.25          |
|                            | 3-Borathed polyethylene | 0.9-20.0                   | 0.75          |
| $2^{nd}$ F.M. <sup>b</sup> | 1-Borathed polyethylene | 4.0-20.0                   | 0.5           |
|                            | 2-Iron                  | 4.0-20.0                   | 1.25          |
|                            | 3-Borathed polyethylene | 4.0-20.0                   | 0.75          |

<sup>a</sup> C.M. = Capture mode.

<sup>b</sup> F.M. = Fission mode.

#### 2.1.4 Experimental Area

The experimental area extends from 182.5 m downstream from the spallation target up to 190 m and can house several movable detectors and flux monitors at the same time<sup>13</sup>. A list of all available detectors follows:

- SIMON (Silicon MONitor) [30] : <sup>6</sup>Li based flux monitor
- MICROMEGAS [31] : <sup>10</sup>B and <sup>235</sup>U based flux monitor
- PTB (from Physikalisch-Technische Bundesanstalt Institute) [32] : parallel plate ionization chamber as <sup>235</sup>U and <sup>238</sup>U based flux monitor
- Medipix [33] : <sup>6</sup>Li and Polyethylene (H) based Silicon detector for beam profile determination
- TAC (Total Absorber Calorimeter) [34] : A 4  $\pi$  detector using 40 BaF<sub>2</sub> scintillators for capture measurements
- K6D6 (Karlsruhe C<sub>6</sub>D<sub>6</sub>) [35] : deuterated benzene liquid scintillators for capture measurements
- PPAC (Parallel Plate Avalanche Counter) [36] : for fission measurements
- FIC (Fission Ionization Chamber) [37; 38], § 3 : for fission measurements
- CR-39 [39] : solid state track edge detectors

#### 2.1.5 Beam dump

The beam dump is situated at the end of the NEL and consists in a 490 × 490 × 475 mm<sup>3</sup> polyethylene box composed by 19 490 × 490 × 25 mm<sup>3</sup> plates. Each side is covered by one cadmium foil and additional polyethylene, so that the total dimension of the beam-dump is 543 × 527 × 528 mm<sup>3</sup>.

A thick concrete wall separates the EAR-1 from this box, which is situated 12 m downstream from the shielding in order to further reduce backscattering.

The polyethylene box houses 3 BF<sub>3</sub> (boron trifluoride counters) for neutron position and flux monitoring.

---

<sup>13</sup>In order to avoid undesired scattering or flux attenuation, and because of the limited physical space, the EAR-1 never houses *all* detectors contemporally.

## 2.2 Beam characteristics

Two main quantities are relevant for beam characterization: the neutron flux and the energy resolution.

### 2.2.1 Neutron flux

The spallation of 20 GeV kinetic energy protons against a massive lead target gives rise to a white (i.e. energetically wide) neutron spectrum. The p/n conversion is estimated to be about 1:300. For this reason, though only one neutron out of  $10^7$  reaches the end of the TOF tube, the instantaneous beam intensity at the EAR-1 position is comparable and even higher than in other dedicated facilities with shorter flight-paths (see Fig. 11). This makes the n\_TOF station particularly suitable for measurements with a low signal to background ratio. As a result, neutron induced cross section reaction determination of extremely low masses of significantly radioactive isotopes is possible (for quantitative example see § 3). It is worthwhile underlying that, at instantaneous neutron flux parity, the advantage of a 200 m long beam line on energy resolution is overwhelming (see next paragraph).

In Fig. 11 n\_TOF is compared to other facilities available at Los Alamos laboratory (LANSCE) and at IRMM-Gel (GELINA).

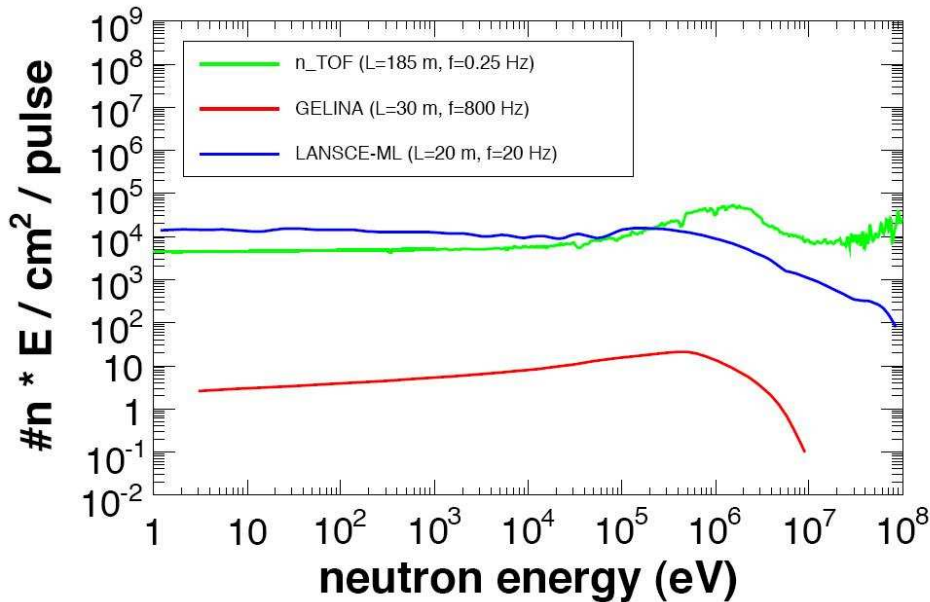


Figure 11: INSTANTENOUS NEUTRON FLUX AT DIFFERENT FACILITIES.

Thanks to the low repetition rate, no proton bunch overlap occurs at the n\_TOF facility. The averaged neutron flux is thus a little lower than at other facilities (Fig. 12), but the mentioned advantage of this situation strongly exceeds the lit-

the longer running time necessary to gain the same statistics as at LANSCE ([40]) or GELINA ([41]).

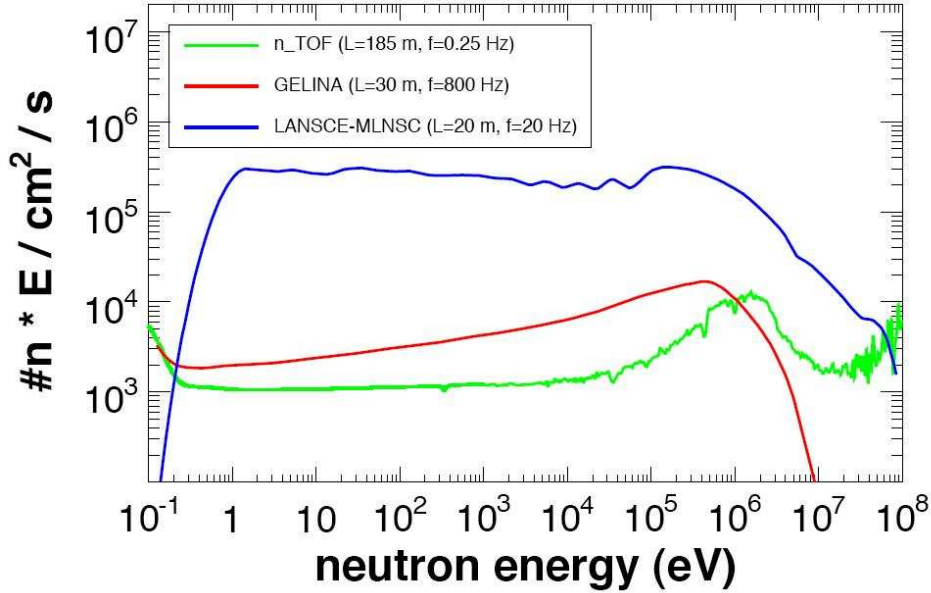


Figure 12: AVERAGED NEUTRON FLUX AT DIFFERENT FACILITIES.

An extensive study of the neutron flux at the EAR-1 position was performed with Monte Carlo Simulations. The FLUKA [42], MNCPIX [43] and EA-MC [44] codes were employed. The result of the simulations, compared to experimental measurement, is shown in Fig. 13, where the total number of neutrons entering the experimental area is plotted in isolethargic units:  $dn/d\ln E/cm^2/7 \times 10^{12}$  protons. The neutron flux determination was performed in capture measurements configuration (inner radius of the second collimator equal to 4 cm). Different features are visible:

- a flat shape from 1 eV to 10 keV, confirming the isolethargic character due to the presence of a moderator
- some local depletions because of neutron capture in structural material as aluminum.

The agreement between simulation and experimental data is excellent, the 20% discrepancy below 1 MeV being due to a simulated moderated thickness of 5 cm instead of 5.8 cm <sup>14</sup>.

<sup>14</sup>On projects the thickness of the moderation at the target exit was 5 cm. After the removal of the spallation block, it was found out that in reality it was 5.8 cm and not just 5 cm.

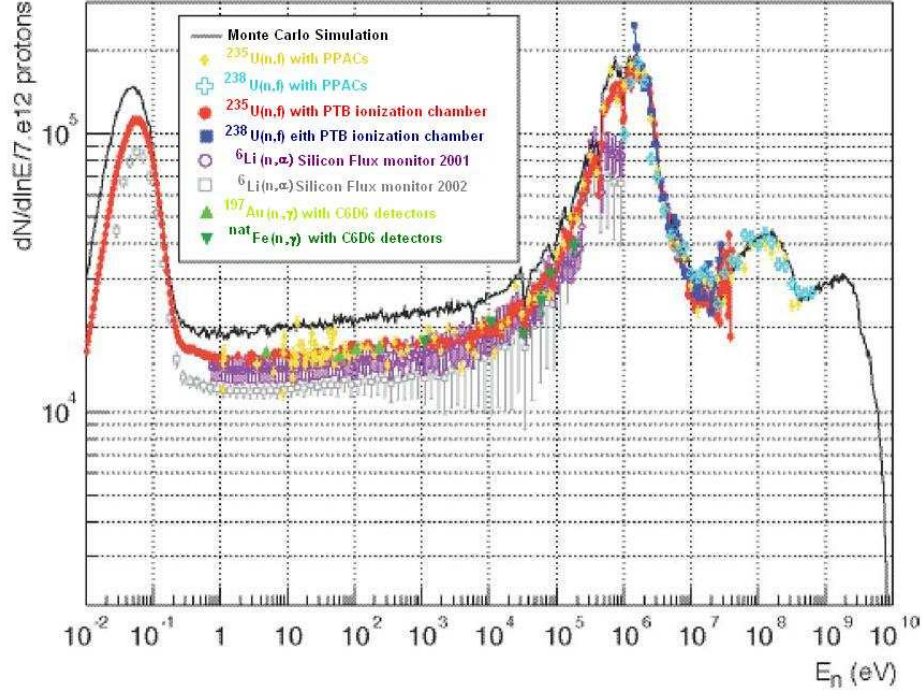


Figure 13: MEASURED AND MONTE CARLO SIMULATED NEUTRON FLUX IN THE EXPERIMENTAL AREA.

### 2.2.2 Energy resolution

When a neutron strikes a nucleus, it excites and many reaction channels open. The energy region where individual states are excited is known as *resonance region*. A resonance occurs where the cross section has a maximum. Each discrete state is unstable against decay and therefore has a certain width. When resonances are so closed together that their widths are larger than their spacings, a continuum results. This happens at higher momenta, where energy resolution is worst and resonances can not be isolated.

Neglecting the contribution of detectors, energy resolution is determined by:

- Doppler broadening
- incident beam-pulse width
- moderation time

Doppler broadening is important for the determination of the resolution function, i.e. where resonances can be resolved. The data analysis reported in this thesis deals with incident neutron energies  $E_n \geq 0.5$  MeV and Doppler broadening can be

neglected.

The TOF energy resolution  $\Delta E$  due to the beam time uncertainty  $\Delta t$  for a neutron of kinetic energy, is given by [18]:

$$\left. \frac{\Delta E}{E} \right|_{BEAM} = \frac{2\Delta t}{t} \approx \frac{2c}{L} \sqrt{2 \frac{E}{m_n}} \Delta t \quad (1)$$

Fig. 14 shows the trend of neutron energy relative uncertainty for  $L = 185$  m and  $\Delta t = 10$  ns.

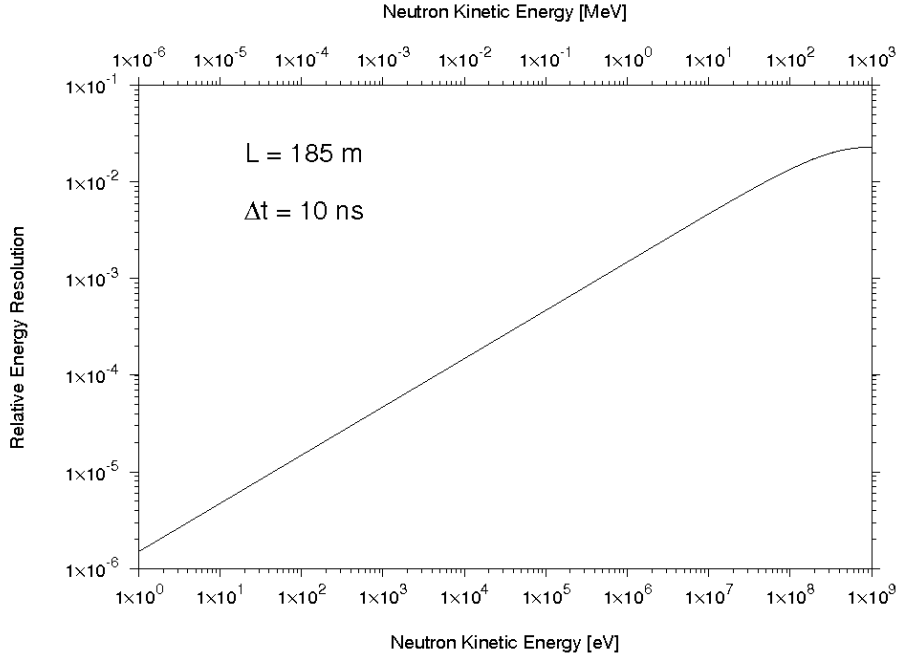


Figure 14: RELATIVE ENERGY UNCERTAINTY DUE TO THE PROTON BEAM TIME SPREAD.

The contribution due to moderation path  $\lambda$  inside the 5.8 cm water thickness is instead given by:

$$\frac{\Delta E}{E} = \frac{2\lambda}{\lambda + L} \quad (2)$$

$\lambda$  changes according to the neutron energy and, since moderation is a stochastic process, the variance  $\Delta\lambda$  can be estimated either as the r.m.s of the  $\lambda$  distribution or the standard deviation from a Gaussian fit of the peaks. Fig 15 shows the moderation time contribution calculated in these two different ways (black and red lines) for  $L = 185$  m, and the apport given by the incident beam-pulse to the energy resolution (green line) for the same flight-path. In the energy range of interest for the analysis reported in this thesis, this last term prevails.

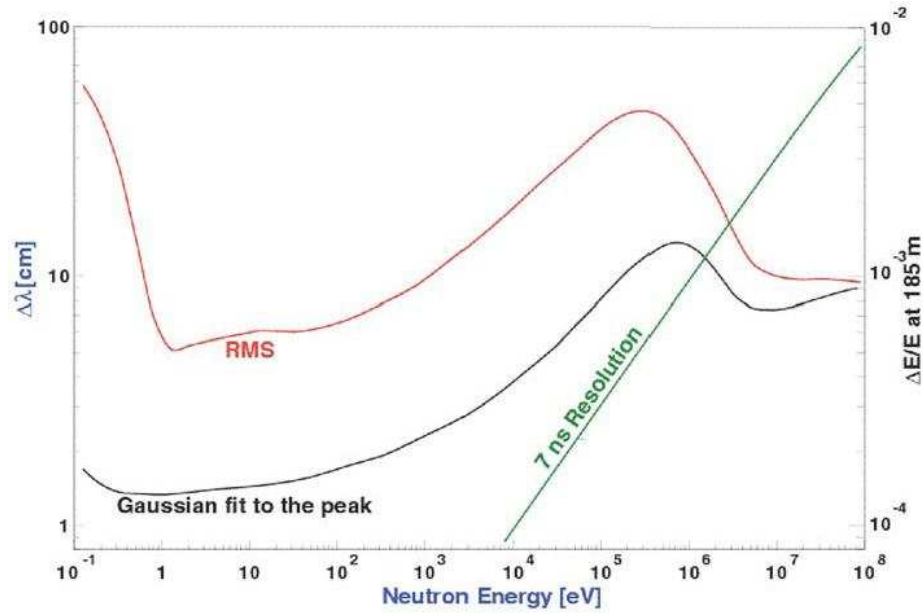


Figure 15: RELATIVE ENERGY UNCERTAINTY DUE TO MODERATION PATH AND BEAM TIME SPREAD.

## 2.3 Background

In neutron capture reactions it is not possible discriminating between  $\gamma$ 's from the investigated process or coming from other sources just as in fission measurements a distinction between (n,f) events due to spallation neutrons or to differently generated neutral nucleons is not feasible. For this reason the n\_TOF Collaboration devoted big efforts to background minimization. After deep investigation it was found that the most relevant background sources in a spallation facility are represented by:

- $\gamma$ -flash, i.e.  $\gamma$ 's and relativistic particles generated in the spallation process and travelling in the neutron beam line
- negative muons created in the spallation process: the fastest contributes to the  $\gamma$ -flash, while the  $\mu^-$  captures give rise to additional neutrons
- $\gamma$  rays from neutron capture in structural material
- neutrons scattered in the beam line or backscattered in the beam dump

These are known as in-beam components. Sample-related background has to be considered as well.

Though a sweeping magnet removed charged particles from the beam line, additional concrete walls were built. A suppression of a factor of 1000 in the number of  $\mu^-$  reaching the experimental area was achieved [45].

The third and fourth components were studied by measurements in absence of any sample [27]. Moreover, as already mentioned, the beam-dump was positioned 12 m downstream the end of the experimental area and equipped with polyethylene layers.

The sample related background was strongly suppressed using low neutron sensitivity detectors. A series of measurements (in absence of any sample and with C, Pb and Fe targets) showed that a further reduction of the  $\gamma$  contamination of the beam could be obtained by simple geometrical considerations [27].

A separate speech is needed for the  $\gamma$ -flash (see § 5). This background component is somehow desirable, since it gives the real trigger used in data analysis. But when it is too strong it represents a problem, because its intensity makes detectors blind.

## 2.4 Performance summary

The n\_TOF facility is unique in terms of the possibilities it offers. Neutron induced fission cross sections in data libraries are obtained matching data from various experiments, each one performed in a specific and limited energy range. Thanks to spallation of high momenta protons, at present **n\_TOF is the only one facility allowing to sweep on 10 orders of magnitude in energy**, from thermal up to 250 MeV <sup>15</sup>.

The 200 m long neutron beam line assures excellent energy resolution, while the high instantaneous (i.e. per proton bunch) neutron flux and low repetition rate open the way to measurements of strongly radioactive samples.

Table 5: CHARACTERISTICS OF THE N\_TOF FACILITY.

|   |   |
|---|---|
| <b>Proton beam momentum</b>                     | 20 GeV/c  |
| <b>Intensity</b>                                | 7×10 <sup>12</sup> dedicated beam<br>4×10 <sup>12</sup> parasitic beam  |
| <b>Repetition frequency</b>                     | 1 pulse/2.4s  |
| <b>Pulse width</b>                              | 6 ns  |
| <b>n/p</b>                                      | 300   |
| <b>Target material</b>                          | Pb (99.99%)   |
| <b>Target dimension</b>                         | 80 × 80 × 60 × cm <sup>3</sup>  |
| <b>Cooling and moderation material</b>          | Ordinary water  |
| <b>Energy resolution @ 187.5 m <sup>a</sup></b> | $\Delta E/E = 3.0E-4$ ( $\sim 1$ eV)<br>$\Delta E/E = 5.5E-4$ ( $\sim 1$ keV)<br>$\Delta E/E = 4.2E-3$ ( $\sim 1$ MeV)<br>$\Delta E/E = 2.1E-2$ ( $\sim 100$ MeV) |

<sup>a</sup> = Collimator for capture mode

<sup>15</sup>As visible from the neutron spectrum reported in Fig. 13, and considering total energy conservation, the maximum neutron energy is of the order of GeV. Thought potentially much more powerful, the facility suffers signal fluctuations at relativistic time limits, which makes measurements in this region still too imprecise.

## 3 The detector

*"Welcome, Ion."*  
(Plato Dialogue)

Measurements of neutron induced fission cross-sections at the n\_TOF facility have been carried out using three Fast Ionization Chambers (FIC) [37; 38] and a Parallel Plate Avalanche Counter [36]. The FICs were built in the frame of a collaboration between the Joint Institute of Nuclear Research (JINR, Dubna, Russian Federation), the Institute of Physics and Power Engineering (IPPE, Obninsk, Russian Federation), INFN, and CERN. Two identical chambers were designed for samples with high (FIC 1 and FIC 0)  $\alpha$ -activities, and a third (FIC 2) was intended for  $^{235}\text{U}$  and  $^{238}\text{U}$  samples to be used as a flux monitor. Data analyzed in the frame of this PhD were collected with FIC 1.

The FICs were designed in order to meet the following requests, discussed in detailed in 3.3:

1. maximum safety
2. fast charge collection time
3. maximization of the energy range of operation
4. minimization of neutron interaction with the material of the chamber

### 3.1 Working principle

An ionization chamber is a gas-filled detector sensing direct ionization caused by radiation. When a charge passes through the active volume, electron-ion pairs are created. Their drifting under the application of an electric field gives rise to a current signal revealing the process.

The FICs are optimized for fission fragment recognition. They work in ionization regime, which means that all pairs generated by direct ionization are collected, but no charge multiplication takes place. The higher the charge and kinetic energy of the passing-by particle, the more pairs it produces and the higher the amplitude of the detected current. The isotopes housed in the FIC 1 naturally decay emitting  $^4\text{He}$  nuclei and, when hit by incident neutrons, undergo fission. These represent the two detectable ionization sources for the considered samples. The energy released in fission as kinetic energy of FFs is about 180 MeV and is distributed inversely proportional to their masses. Helium nuclei are instead emitted with a kinetic energy around 5 MeV. The neutron induced reactions are thus expected to produce much

larger signals, which allows the use of a simple amplitude discrimination to recognize FFs.

### 3.2 Design of FIC 1

A simplified layout of the FIC 1 is shown in Fig. 16. The basic cell is composed of three aluminum electrodes 12 cm in diameter. The central electrode is 100  $\mu\text{m}$  in thickness and is plated on both sides with the fissile isotope under study. This central electrode is connected to the bias voltage for defining the electric field of 800V/cm in the 5 mm wide gas-filled gaps. The two outer electrodes 15  $\mu\text{m}$  in thickness are kept at ground potential. The sample layers are 8 cm in diameter. The whole detector is 50 cm long and houses 16 basic cells perpendicular to the neutron beam. Given the  $2\pi$  geometry of the chamber, the detection efficiency for fission events is close to 100% for each cell.

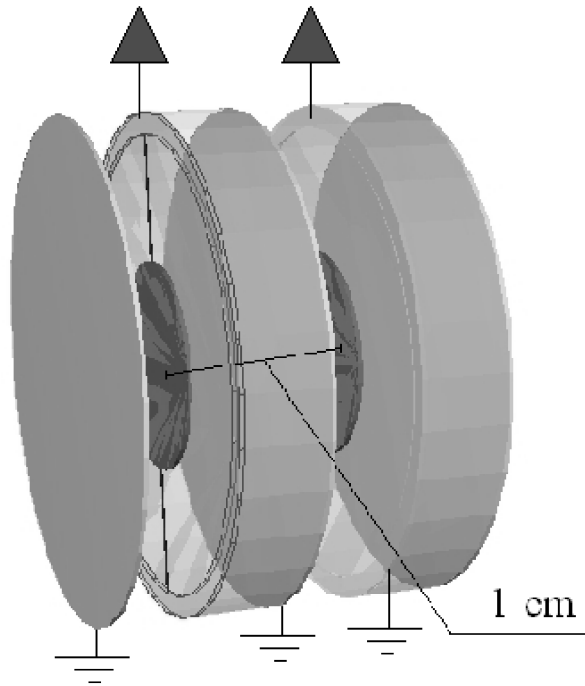


Figure 16: SCHEMATIC LAYOUT OF 4 FIC 1 CELLS.

An additional cell is added at the downstream extremity of the detector and is positioned perpendicular to the previous sixteen. It houses a  $^{235}\text{U}$  sample for neutron background monitoring.

Table 6 reports the samples accommodated in FIC 1, while in Table 7 the working parameters of the detector are shown.

Table 6: FIC 1 SAMPLES.

| Position<br>in the<br>beam | Position<br>from<br>$^{235}\text{U}$ | Isotope           | Label   | Mass<br>[mg] | DAQ<br>channel |
|----------------------------|--------------------------------------|-------------------|---------|--------------|----------------|
| 1                          | 0.052                                | Dummy             |         |              | 9              |
| 2                          | 0.042                                | $^{245}\text{Cm}$ | 48-49   | 0.806        | 15             |
| 3                          | 0.031                                | $^{245}\text{Cm}$ | 46-47   | 0.905        | 14             |
| 4                          | 0.021                                | $^{233}\text{U}$  | 7-8     | 15.35        | 16             |
| 5                          | 0.01                                 | $^{233}\text{U}$  | 5-6     | 15.49        | 13             |
| 6                          | 0.0                                  | $^{235}\text{U}$  | 11-12   | 31.8         | 12             |
| 7                          | 0.01                                 | $^{238}\text{U}$  | 26-27   | 25.2         | 11             |
| 8                          | 0.021                                | $^{238}\text{U}$  | 24-25   | 27.1         | 10             |
| 9                          | 0.046                                | $^{243}\text{Am}$ | 38-39   | 1.141        | 7              |
| 10                         | 0.057                                | $^{243}\text{Am}$ | 40-41   | 1.244        | 5              |
| 11                         | 0.067                                | $^{243}\text{Am}$ | 42-43   | 1.095        | 4              |
| 12                         | 0.078                                | $^{243}\text{Am}$ | 44-45   | 1.306        | 8              |
| 13                         | 0.088                                | $^{241}\text{Am}$ | 30-31   | 0.464        | 6              |
| 14                         | 0.099                                | $^{241}\text{Am}$ | 32-33   | 0.559        | 3              |
| 15                         | 0.109                                | $^{241}\text{Am}$ | 34-35   | 0.640        | 1              |
| 16                         | 0.12                                 | $^{241}\text{Am}$ | 36-37   | 0.598        | 2              |
| BG                         |                                      | $^{235}\text{U}$  | 5-4,5-1 | ?            | -              |

Table 7: FIC 1 WORKING PARAMETERS.

|                     |                            |
|---------------------|----------------------------|
| Gas composition     | 90% Ar + 10% $\text{CF}_4$ |
| Gas pressure        | 720 mb                     |
| Applied Voltage     | -400 V                     |
| Inter-electrode gap | 5 mm                       |
| Electrode diameter  | 12 cm                      |
| Sample diameter     | 8 cm                       |
| Backing thickness   | 100 $\mu\text{m}$ (Al)     |
| Electrode thickness | 15 $\mu\text{m}$ (Al)      |
| Windows diameter    | 12 cm                      |

### 3.3 Detector characteristics

As already mentioned, the detectors had to fulfill some stringent requests.

#### 3.3.1 Maximum safety

In order to fulfill CERN safety regulations, the FICs had to be certified as ISO/04/43323, i.e. "sealed sources for a general neutron source application", of the standard ISO 2919 (sealed radioactive sources). Their design and operation parameters were decided keeping in mind this constraint.

Being operated in ionization regime, no gas flow circulation is needed. Dealing with highly radioactive isotopes, this is of great advantage. The gas pressure (720 mbar) was chosen to be lower than atmospheric pressure, in order to avoid spills in case of damage of its structure, while the applied voltage was kept far away from electric discharge risk.

Since CERN has neither the permission for construction of radioactive sealed sources, nor the infrastructure for required tests, the FICs were assembled in a Class A Laboratory at Paul Scherer Institut (PSI) and the certification for their use was obtained in a second moment.

#### 3.3.2 Fast charge collection time

The time occupancy of the detector depends on the time taken by electrons to drift between electrodes. For FIC 1, at the chosen working parameters of electric field and gas pressure (see Table 7), only  $\text{CH}_4$ ,  $\text{CF}_4$ , and  $\text{ArCF}_4$  show a good mobility (see Table 8). Isobutane is flammable and was thus discarded. Freon is highly problematic from an environmental point of view. Moreover inhalation of high quantities of  $\text{CF}_4$  causes arrhythmia and leads to death people with heart-problems, while argon is less dangerous. Ar, if inhaled in excessive dose, provokes loss of consciousness and could just indirectly lead to death, because of confusion or errors in judgement. For these reasons, the final choice fell on  $\text{ArCF}_4$ , corresponding to a maximum time occupancy of the detector equal to  $\frac{5 \text{ mm}}{88 (\text{mm}/\mu\text{s})} = 56.8 \text{ ns}$ .

#### 3.3.3 Maximization of the energy range of operation

Though only FIC 2 was intended for flux monitoring, all ionization chambers house at least one  $^{235}\text{U}$  sample. This isotope is a standard for (n,f) reactions in a wide energy range, namely from thermal up to 200 MeV and its presence makes it possible extracting neutron induced fission cross sections with reference to it.

Table 8: ELECTRON DRIFT VELOCITY IN DIFFERENT GAS MIXTURES IN MM/ $\mu$ S [46].

| Field strength per unit pressure [V·m/N <sup>-1</sup> ] |       |      |      |      |      |      |      |     |     |     |      |     |
|---|-------|------|------|------|------|------|------|-----|-----|-----|------|-----|
| Gas   | 0.075 | 0.15 | 0.3  | 0.45 | 0.6  | 0.75 | 1.5  | 3   | 4.5 | 6   | 7.5  | 15  |
| H <sub>2</sub>  | 3.1   | 5    | 6.8  | 8.0  | 9.2  | 10   | 15   | 23  | 30  | 36  | 42   | 70  |
| He  | 2.7   | 4    | 6    | 7    | 8.5  | 9.6  | 15   | 36  |     |     |      |     |
| N <sub>2</sub>  | 3.1   | 3.9  | 5    | 6    | 7    | 8    | 14   | 22  | 30  | 36  | 43   | 80  |
| Ne  | 4     | 5    | 7    | 10   | 12   | 16   | 26   | 52  |     |     |      |     |
| Ar  | 2.3   | 2.7  | 3.2  | 3.5  | 3.9  | 4.1  | 6.2  | 13  | 30  |     |      |     |
| Kr  | 1.5   | 1.8  | 2.1  | 2.4  | 2.5  | 3.1  |      |     |     |     |      |     |
| Xe  | 1.0   | 1.2  | 1.4  | 1.6  | 1.7  | 1.8  |      |     |     |     |      |     |
| CO <sub>2</sub>   | 0.56  | 1.1  | 2.3  | 3.4  | 4.6  | 5.7  | 11   | 33  | 66  | 94  | 109  | 137 |
| CO  | 4.8   | 6.5  | 9.4  | 11   | 13   | 14   | 17   | 20  | 25  | 28  | 29   |     |
| BF <sub>3</sub>   | 0.13  | 0.25 | 0.5  | 0.75 | 1.0  | 1.3  | 2.5  | 5.0 | 7.5 | 10  | 12.5 | 25  |
| Air   | 3.5   | 5    | 8    | 9.3  | 11   | 12   | 17   | 26  | 34  | 43  | 51   | 88  |
| CH <sub>4</sub>   | 8     | 24   | 60   | 80   | 95   | 100  | 100  |     |     |     |      |     |
| CF <sub>4</sub>   | 30    | 51   | 74   | 87   | 96   | 101  | 117  | 140 | 141 | 129 | 116  | 95  |
| Ar/CH <sub>4</sub>                                      | 49    | 55   | 45   | 36   | 32   | 30   | 26   | 24  |     |     |      |     |
| Ar/N <sub>2</sub>                                       | 4     | 6    | 9    | 13   | 16.8 | 19.3 | 27.3 |     |     |     |      |     |
| Ar/C <sub>2</sub> H <sub>2</sub>                        | 14.3  | 27.3 | 44.3 | 49.3 | 48.3 | 45.3 | 45.2 |     |     |     |      |     |
| Ar/CF <sub>4</sub>                                      | 34    | 63   | 100  | 120  | 120  | 111  | 66   |     |     |     |      |     |
| He/CF <sub>4</sub>                                      | 6     | 10.8 | 19.2 | 25.8 | 31.4 | 36   |      |     |     |     |      |     |
| <sup>3</sup> He/CO <sub>2</sub>                         | 0.30  | 0.56 | 0.99 | 1.4  | 1.7  | 2.0  | 2.5  |     |     |     |      |     |
| Ar/CO <sub>2</sub>                                      | 5     | 10.6 | 26.5 | 37.5 | 43   | 42   |      |     |     |     |      |     |

All binary mixtures are 90% - 10% by volume

### 3.3.4 Minimization of neutron interaction with the material of the chamber

Care was taken to minimize the quantity of material interposed on the way of the incident neutron flux in order to limit its attenuation. Along the about 16 cm where aluminum electrodes, aluminum windows and various samples follow one other, the flux reduction depends on  $\sigma(n,\text{tot})$  of the material. Attenuation is mainly due to  $(n,\gamma)$  reactions in aluminum<sup>16</sup>.

Fig. 17 shows the result of a FLUKA [42] simulation<sup>17</sup>. It reports the number of neutrons per incident neutral nucleon calculated at different positions inside the FIC 1. Four monochromatic neutron beams with  $r = 4$  cm were considered. The first point corresponds to the backward surface of the dummy electrode, the last is after the fourth <sup>241</sup>Am sample, while all others are referred to the backward face of Al windows following the sample mentioned on the graph.

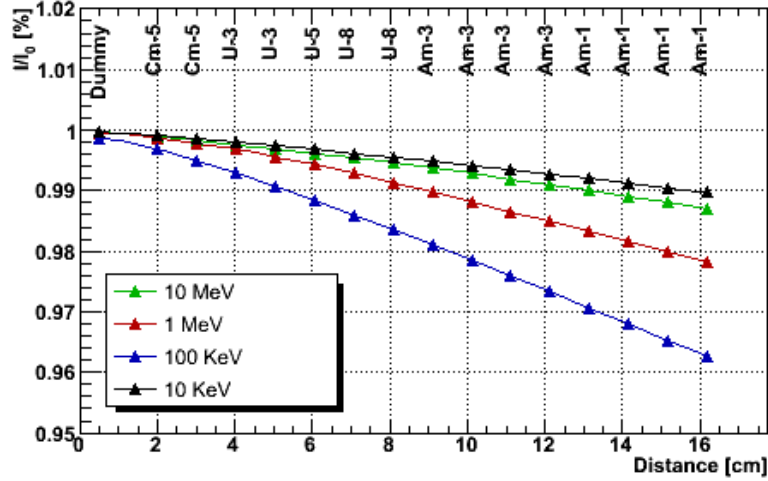


Figure 17: NEUTRON FLUX ATTENUATION AT DIFFERENT POSITIONS INSIDE FIC (FLUKA SIMULATION).

Since low energy neutron libraries for <sup>245</sup>Cm are not available in FLUKA, this isotope was replaced by <sup>233</sup>U<sup>18</sup>. The maximum flux attenuation (less than 4%) is found for 100 keV incident neutrons, representing only a small fraction of all neutrons (see Fig. 13). Results should be integrated over the whole neutron spectrum and flux attenuation can thus be discarded because negligible.

<sup>16</sup>Neutron absorption takes place also inside samples, but their thickness is negligible if compared with Al layers.

<sup>17</sup>FLUKA is a Monte Carlo multipurpose multiparticle code treating particle transport and interactions with matter.

<sup>18</sup>The choice was performed after considering various  $(n,f)$  cross sections for even Z and odd N isotopes.

## 4 FIC Front-end electronics and DAQ

*How much wood could a woodchuck chuck,  
if a woodchuck could chuck wood?  
He'd chuck all the wood that a woodchuck could chuck,  
if a woodchuck could chuck wood!*

About the n\_TOF Data acQuisition a detailed paper has been written [47]. For this reason only a schematic view of the FIC 1 front-end electronics and few words about DAQ are here summarized.

### 4.1 Front-end electronics

As already seen in § 3.2, the fission ionization chamber #1 houses 16 samples and is fed by -HV. In Fig. 18 a cable for HV (in red) is connected to a metallic box positioned above the FIC 1. Inside the box is a circuit delivering the -HV to the electrodes facing samples. The 16 black cables pick up the 16 output signals.



Figure 18: FIC 1 SIGNAL PICK-UP.

Fig. 19 shows the steps through which signals are shaped and processed.

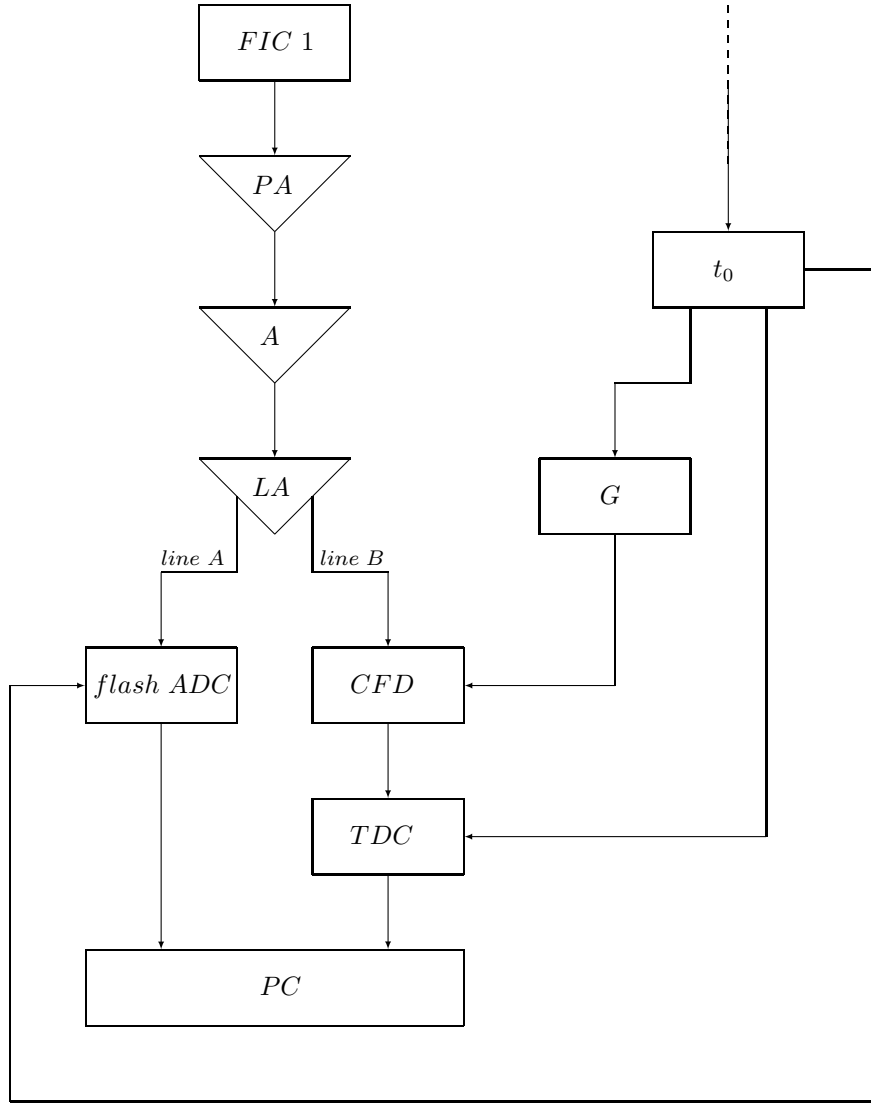


Figure 19: FIC 1 Front-end electronics. Layout copied from the n\_TOF web-site

Each black cable of Fig. 18 is connected to the FIC at one end, and to a preamplifier (PA) at the other extremity. The PA integrates the electric signal, assuring proportionality between its amplitude and the quantity of charge produced in the ionization process inside the FIC sensitive volume. In order to cut its long tail, the signal is then differentiated in an amplifier (A). In a parallel chain, at the moment  $t_0$  (time-start) trigger arrives (from PS) and a 80 ms gate G for signal acquisition opens. The signal on the left part of the diagram continues its travel. A Linear Amplifier splits it into two parts: one - line A - is sent to a Constant Fraction Discriminator (CFD) and the other one - line B - to a flash-ADC (digitizer). The CFD is a device taking an analogic signal as input and delivering a digital constant value as output. First it checks if the gate for acquisition is opened. If it is closed, it delivers a 0 to the following component of the front-end electronics. In contrary case, it checks if the signal is

higher than a set threshold and its output assumes value 0 before the zero crossing point <sup>19</sup>, and 1 after that. A Time to Digital Converter (TDC) calculates the time  $t$  as the difference between the moment when it receives a "true" ( $= 1$ ) from the CFD and  $t_0$ . In case of "false" value (acquisition gate already closed, i.e.  $t-t_0 > 80$  ms, or signal lower than threshold), a predefined output (for example -10.0) is sent to the connected PC, otherwise the digitized calculated time is communicated. On line A, the signal passes through the flash-ADC and, if trigger arrived, is translated into an integer number, otherwise a constant null output is delivered. The range of possible values depends on the resolution of the digitizer. The flash-ADC modules used for FIC have a resolution of 8 bit and were exploited at 100 MHz sampling rate. This means that  $100 \cdot 10^6$  times per second (or equally once every  $\frac{1 \text{ s}}{100 \cdot 10^6} = 10$  ns) the signal is sampled. The analogic value (sampled amplitude of the signal) is translated into an integer, said "channel", spanning on  $2^8$  possible numbers from 0 to 255. A PC, located in the experimental area, receives both the digital amplitude of the signal from the flash-ADC, and the digital time from the TDC. If this number is different from -10.0, data are processed, otherwise they are discarded.

The flash-ADC modules employed for FIC 1 have 4 channels for data input and one for trigger. Every signal is read separately, i.e. each black cable of Fig. 18 is connected to a different entrance of the 4 possible ones offered by a single flash-ADC. This means that the 16 electrodes of FIC 1 are read by 4 flash-ADC.

## 4.2 DAQ

The memory allocated to store information collected thanks to the previously described electronic chain would be really huge. For this reason PCs operate an on-line data reduction. Only true event signals with amplitude higher than a value set by flash-ADCs, along with a pre-selected number of samplings before and after threshold crossing, are kept for storage [47]. Data from each electrode are organized in buffers, i.e. a certain quantity of memory allocated. A buffer can be for example 800MByte. Buffers from 8 different electrodes are grouped in streams and thus identified by a same "stream number". Additional information from the PS (bunch intensity,type,..) is integrated in a separate stream.

The chain of events that follows is sketched in Fig. 20. In a first moment data are stored in a local disk pool, readable through a computer interface. When no place is left for additional data, they are moved to the Cern Advance STORAge manager CASTOR [48], making the local disk pool able to house new data. From CASTOR data are migrated to tapes. CASTOR comprises both the physical tapes where data are stored and the program interface to access them.

---

<sup>19</sup>Zero crossing point = time at which the signal crosses the set threshold, or better, becomes higher than a fixed fraction of its maximum amplitude.

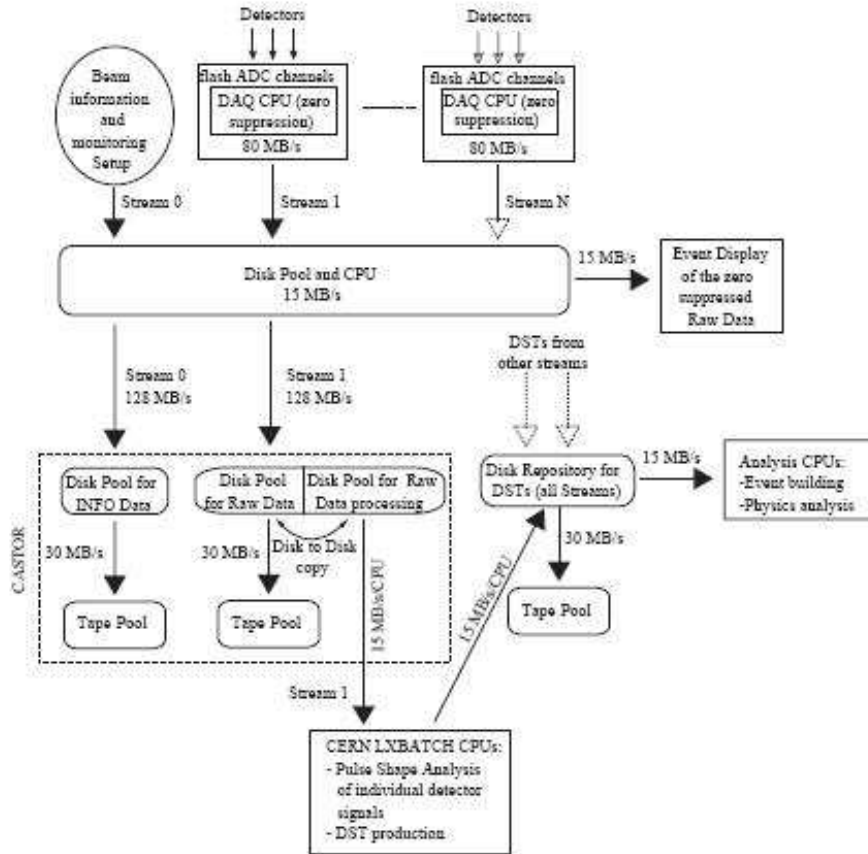


Figure 20: DATA FLOW FROM DETECTORS TO TAPES. PICTURE TAKEN FROM [47].

### 4.3 The n\_TOF singularity

Due to the required high speed of data read-out, the n\_TOF Collaboration decided to fully base its acquisition system on flash-ADCs. Other experiments had previously employed this kind of digitizers, but never at the sampling rate exploited at n\_TOF, nor so extensively.

## 5 Analysis

*"Curiosity begins as an act of tearing to pieces or analysis."*  
(Samuel Alexander)

A wave function  $\Psi_i(\vec{x},t)$  can be associated to each particle and a nucleus can be described in terms of an appropriate  $\sum_i \Psi_i$  [Kra87; Erb97]. Without entering into details, when two particles approach, their wave functions approach as well, and when a collision occurs, the wave functions superimpose. This happens only if the kinetic energy  $K$  of the projectile is high enough, while the impact parameter must be low. Neglecting this last term by considering a large beam impinging on the center of an extensive sample, different degrees of overlap of wave functions result as a function of  $K$ .

A current of particles is mathematically given by:

$$j = \frac{\hbar}{2mi}(\Psi^* \frac{\partial \Psi}{\partial r} - \frac{\partial \Psi^*}{\partial r} \Psi) \quad (3)$$

The cross section of a process is the probability for that process to occur and is linked both to the entering and exiting current of particles, i.e. depends on how wave functions match.

If the kinetic energy of the projectile is low, its De Broglie wavelength is quite long. The incident particle sees the average nuclear field and is scattered by that (potential scattering or shape elastic scattering). At increasing  $K$ , the projectile can penetrate the nuclear field and interacts with it giving life to a compound nucleus (CN). The energy brought by the incident particle is shared among all nucleons and the nucleus results in an excited state.

Since the CN levels are discrete, the overlap between the wave function of the incident particle and of the target nucleus is really good just for some precise incident kinetic energies. A good superposition means high probability for the reaction to occur, or equivalently, a high cross section. Excitation of different individual states is thus reflected in maxima in the cross section, that is in a series of resonances.

A qualitative explanation of their formation is obtained by representing the nuclear potential as a square well. The oscillatory inside and outside wave functions (see Fig. 21) must match smoothly at the boundary. Varying the energy of the incident particle, the relative phase of the inner and outer wave functions, as well as their relative amplitudes, change. Going from case (a) to situation (c) the probability for the incident particle to penetrate the nucleus increases. Only for certain incident energies condition (c) results. These are the energies of the capture resonances in the cross sections.

Each discrete excited state is unstable against decay and therefore has a certain width. The lower the energy of the projectile and the fewer combinations of sharing it among nucleons are possible. This results in fewer available decay modes, thus in a longer life of the excited states of the compound nucleus and therefore a smaller width. As the energy of the projectile increases, more reaction channels open, the life time of the excited state gets smaller and its width larger. Resonances begin to overlap because their distance decreases, while their FWHM enhances. The reaction cross section consequently becomes smooth.

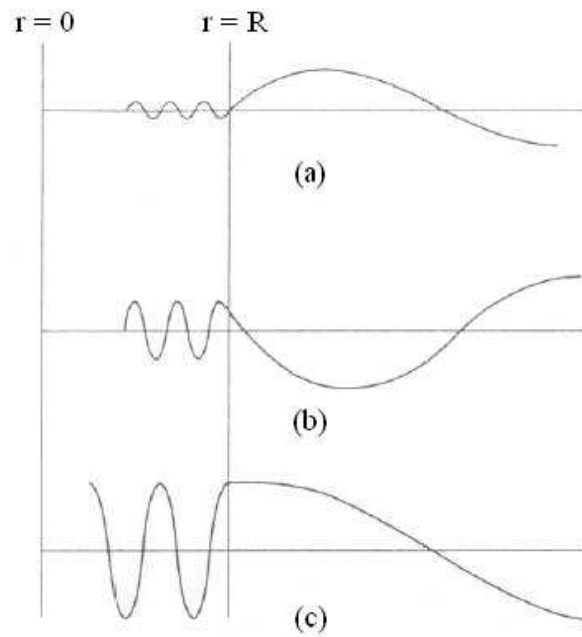


Figure 21: MATCHING OF WAVE FUNCTIONS AT THE BOUNDARY OF A SQUARE POTENTIAL WELL. (A) FAR FROM RESONANCE THE EXTERIOR AND INTERIOR WAVE FUNCTIONS MATCH BADLY, AND LITTLE PENETRATION OF THE NUCLEUS OCCURS. (B) AS THE MATCHING IMPROVES, THE PENETRATION GETS HIGHER. (C) THE INCIDENT PARTICLE HAS A HIGH PENETRATION PROBABILITY AND THE CROSS SECTION SHOWS A MAXIMUM. THIS IS THE RESONANT CONDITION. (PICTURE TAKEN FROM [KRA87].)

As the kinetic energy of the projectile further increases, the wavelength associated to the incident wave function gets smaller and smaller. The incoming nucleon does not see anymore the average nuclear potential, but can distinguish single nucleons and directly interacts with them. No compound nucleus is formed. Reaction mechanisms are really fast. Elastic scattering as well as non elastic reactions can take place. In the last case the residual target nucleus is left in an excited state, from which it can decay in different ways. Resonances occur, but due to the large incident kinetic

energy, they overlap and the reaction cross section is smooth.

Conventionally the passage from the energy regime where resonances are due to excitation of the compound nucleus to the region where they correspond to excitation of the residual target nucleus is assumed to occur at a reduced De Broglie wavelength of the incident neutron more or less equivalent to the dimension of a nucleon. Considering  $\lambda \sim 1$  fm, and thus  $p_r = \frac{h}{\lambda}$ , from

$$K + m_0c^2 = \sqrt{(m_0 c^2)^2 + (p_r c)^2} \quad (4)$$

with  $m_0c^2 = 938.9$  MeV (nucleonic rest mass),  $K = 20$  MeV is obtained. This is just an agreed value and in reality a neutron energy around 10 - 20 MeV corresponds to transition from compound nucleus to direct reactions, so that both processes can occur. The analysis reported in this thesis deals with neutral projectiles with energy higher than 500 keV. The extracted neutron induced fission cross section is therefore smooth and due sometimes to decay of a CN and other times to scission of the residual excited target nucleus.

## 5.1 Experimental cross-section determination

### 5.1.1 Reading raw data

The number of a specific type of reactions occurring in a target is proportional to the ratio between the incoming and outgoing current of particles:

$$Reaction\ Rate \propto \frac{j_{out}}{j_{in}} \quad (5)$$

Experimentally this is determined by counting the amount of signatures the studied process leaves, in our specific case (gas detector), each fission event is characterized by the emission of two fragments in opposite directions<sup>20</sup>. Given the  $2\pi$  geometry of detector cells, the amount of fission fragments seen by one electrode is equal to the number of fission events.

What is revealed by the FIC is an output signal (translated into channels by flash-ADCs) as a function of time (see Fig. 22). In a certain moment a signal of start for time counting arrives ( $t = 0$ ) and the acquisition system is thus "alerted". After  $x$  ns a pre-trigger arrives and the acquisition opens ( $t = 5200$  ns) before beam start. When protons run in the PS ring, the trigger is given by their passage inside the coil TRA648 (2.1.1) and a time window of 80 ms opens. If during this period

---

<sup>20</sup>The fission reactions analysed in this work are induced by neutrons of 20 MeV maximum kinetic energy.

the detected signal falls for long under the threshold set on the flash-ADC, it is not registered (data reduction). After the 80 ms time window, the acquisition is closed and a new alert message is waited for.

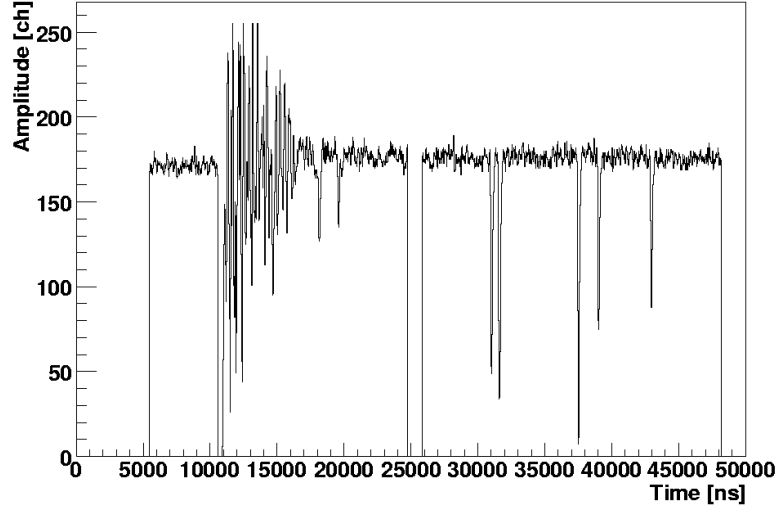


Figure 22: RAW DATA.

Neglecting for the moment the region around 10500 ns, signals due to charge collection after gas ionization in the FIC are visible as depressions in Fig. 22. The deeper is the hole and the higher is the speed and/or charge of the ionizing particle. This makes possible discriminating between  $\alpha$ 's and fission fragments.

### 5.1.2 Time Of Flight (TOF)

Each signal with amplitude greater than a certain threshold is caused by a neutron reaction inside the target. From the TOF of the neutral projectile, its kinetic energy can be calculated, and thus each fission event can be associated to the K value of the nucleon which caused it.

With reference to Fig. 23, at the time  $t_\gamma$  light and relativistic particles produced in the spallation target reaches the experimental area and a  $\gamma$ -flash is detected. This informs that the beam is on. At  $t^*$  a signal reveals the occurrence of a fission event (amplitude higher than a certain threshold). The time between spallation and fission fragment detection in the FIC is the neutron time of flight (TOF).

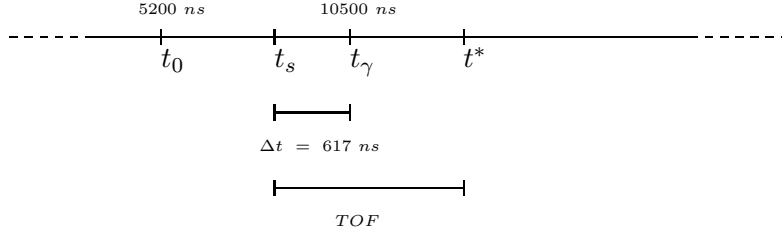


Figure 23: TIME SCHEME OF THE RECORDED SIGNAL.

Electromagnetic radiation generated in the spallation process is recorded by detectors after travelling the vacuum tube length. Since the beam pipe extends for  $L = 186.95$  m before reaching the FIC and light travels at speed  $c$ , the  $\gamma$ -flash is detected after  $t = L/c = 617$  ns from proton collision with the Pb target. Thus:

$$TOF = t^* - t_s = t^* - t_\gamma + 617 \text{ ns} \quad (6)$$

In order to consider the time spent by neutrons inside the moderator [49] and the stochastic behavior of their flight-path in water, eq. 6 was slightly modified:

$$TOF = t^* - t_\gamma + 617 \text{ ns} - 64 \text{ ns} + (1.0 - 2.0 * r) * 5 \text{ ns} \quad (7)$$

with  $r \in [0,1]$  a random variable. From the relativistic formula:

$$\gamma m_0 c^2 = \frac{1}{\sqrt{1 - \frac{L^2}{(tc)^2}}} = K + m_0 c^2 \quad (8)$$

given the TOF  $t$ , for each fission event the kinetic energy of the neutron inducing it is known.

### 5.1.3 Data treatment

Looking again at Fig. 23, indeed from about 10500 ns to 16000 ns the situation is quite confused. The  $\gamma$ -flash produced by prompt  $\gamma$ -rays and relativistic particles originating from spallation reactions in the Pb target is so intense that even after 3000 ns the electronic chain is still affected by its fading away and signal recognition is impossible.

The problem of strong fluctuations in the time evolution of the signal amplitude can be solved, up to a given energy, by observing that two adjacent electrodes react to the same  $\gamma$ -flash radiation in identical ways (see Fig. 24). Therefore, a software

compensation technique [50] can be applied in order to extract the signals of fission fragments. The technique consists in subtracting the output of two adjacent electrodes. The results of this procedure is illustrated in Fig. 25.

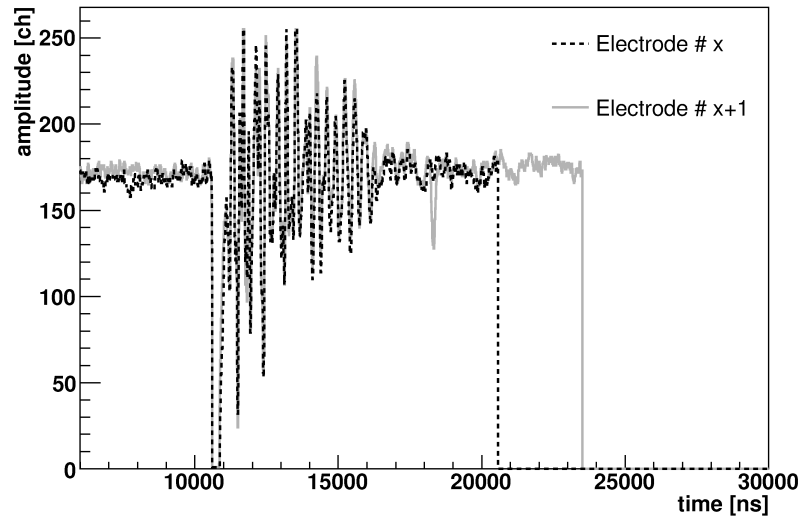


Figure 24: RECORDED RAW SIGNALS FROM NEIGHBORING ELECTRODES.

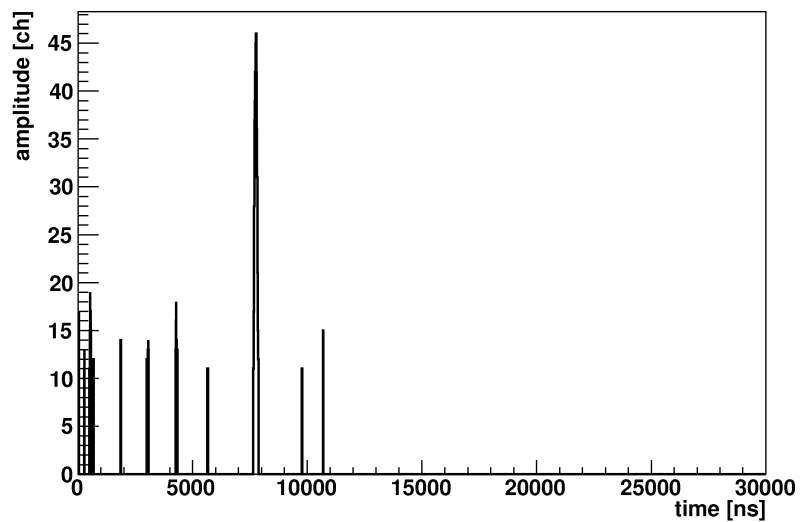


Figure 25: SIGNALS AFTER SUBTRACTION OF  $\gamma$ -FLASH.

Since the more intense the beam and the stronger the  $\gamma$ -flash, with all problems it causes, the high energy analysis presented in this thesis was performed considering only parasitic pulses.

The obtained signals are then subjected to a pulse shape and amplitude analysis [50] discriminating between fission fragments and  $\alpha$  particles (see Fig. 26). Each true event is characterized by a  $\frac{\text{charge}}{\text{amplitude}}$  value Gaussian distributed around a mean. Virtual signals can show the same amplitude as the real ones, but their integral (i.e. charge) is really low. Residual electronic noise is thus reduced by considering the charge-to-amplitude ratio of the signals.

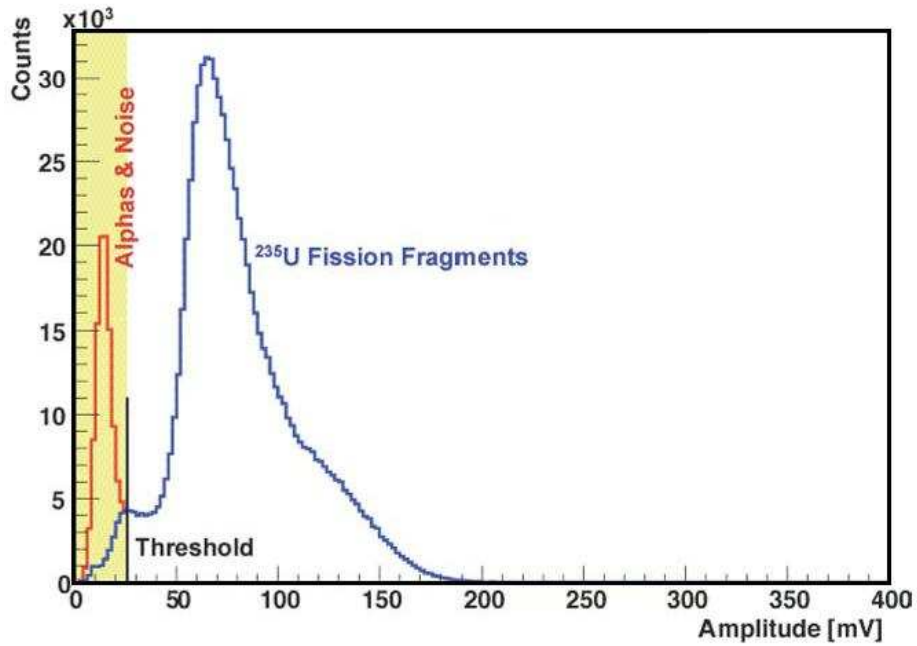


Figure 26: PULSE HEIGHT DISTRIBUTION OF  $^{235}\text{U}$  FISSION EVENTS. THE DISCRIMINATION THRESHOLD SET ON THE CDF IS ALSO VISIBLE. PICTURE TAKEN FROM [27].

#### 5.1.4 Cross section extraction

The emission rate of particles  $b$  ( $R_b$ ), is linked to the current of projectiles  $a$  per unit time ( $I_a$ ) and the number of target nuclei per unit area  $N$  through  $\sigma$ , which for simplicity can be thought as a term of proportionality meaning their halos, according to the relation:

$$R_b = \sigma I_a N \quad (9)$$

$\sigma$  has thus the dimension of an area. Netherless it can be much larger or far smaller than the target nucleus seen by the incident beam and must be considered a quantity saying how probable a process is.

Given the  $2\pi$  geometry of the detector, no solid angle has to be considered and the neutron induced fission cross section in a generic target X can be simply extracted by eq. 9 with reference to a  $^{235}\text{U}$  sample, as:

$$\frac{\sigma_X}{\sigma_{235}} = \frac{R_{b-X}}{I_a N_X} \cdot \frac{I_a N_{235}}{R_{b-235}} \quad (10)$$

with  $R_{b-X} = \frac{Y_X}{t}$  number of fission fragments emitted by the isotope X in the unit time t and  $I_a$  constant because, as seen in section § 3.3.4, doesn't change appreciably on the detector length.  $^{235}\text{U}$  was chosen as reference isotope because it is a standard for (n,f) reactions between 0.15 MeV and 200 MeV. Among all possible available libraries, the IAEA evaluation of ENDF (Evaluated Nuclear Data File) was preferred.

Since the number  $n$  of nuclei in a sample of mass  $m$  for an isotope of mass number A is  $n = \frac{mN_A}{A}$ , for an area S it results  $N = \frac{n}{S} = \frac{m N_A}{A S}$  and eq. 10 can be written:

$$\sigma_{xxx} = \sigma_{235} \cdot \frac{Y_X}{Y_{235}} \cdot \frac{m_{235}}{m_X} \cdot \frac{A_X}{A_{235}} \quad (11)$$

## 5.2 Corrections to the the cross-section determination

Formula 11 is complete, but theoretical. In the reality of fact we do not have Y, i.e. the number of fission fragments *emitted*. We only have the amount of *detected* FFs, which we designate as  $y$ . Therefore the experimental incomplete formula is:

$$\sigma_{xxx} = \sigma_{235} \cdot \frac{y_X}{y_{235}} \cdot \frac{m_{235}}{m_X} \cdot \frac{A_X}{A_{235}} \quad (12)$$

Care must be taken that different isotopes are normalized to the same number of protons. Once this is done, in order to pass from the number of FFs detected  $y$  to the amount of fission fragments emitted  $Y$ , dead-time and thickness corrections have to be considered.

### 5.2.1 Dead time correction

Each time a signal is seen, the electronic chain is busy. In case of high count rates, this represents a problem. Thanks to the use of flash-ADCs the dead time due to electronics is practically zero. But the signal reconstruction routine introduces a 270 ns dead time, which has to be considered.

The dead time of a counting system can be treated by assuming a paralysable or

a non-paralysable response [Kno79]. In the non-paralysable mode a fixed dead time is assumed for each recorded event. Signals falling in this time window are lost, so that a correction has to be applied in the extracted cross-section. A non-paralysable model has been used in the present analysis.

In order to pass from the detected count rate ( $C_d$ ) to the true interaction rate ( $C_r$ ) the following formula was employed [Kno79]:

$$C_r = \frac{C_d}{1 - C_d \Delta t} \quad (13)$$

with  $\Delta t = 270$  ns. Since in formula 12  $Y$  stands for the number of detected fission events, each  $y_X$  has to be multiplied times a correction factor  $W_X = \frac{C_r}{C_d}$  and the referred equation becomes:

$$\sigma_{xxx} = \sigma_{235} \cdot \frac{y_X}{y_{235}} \cdot \frac{W_X}{W_{235}} \cdot \frac{m_{235}}{m_X} \cdot \frac{A_X}{A_{235}} \quad (14)$$

For most of the measured isotopes, the dead-time correction goes from a few percent at low energy, to 20% at higher energy. However, since the count-rate in the various isotopes is similar, the corrections mostly cancel out in the ratio, with a residual effect of the order of a few percent, with a corresponding uncertainty less than 1%.

### 5.2.2 Thickness correction

Another correction that needs to be applied in extracting the cross-section is related to the detection efficiency. The number of particles leaving the sample as well as the spectrum of energy loss in the gas volume, is determined by the sample thickness, so that differences in the detection efficiency may exist for the different measured isotopes. The effect of fragment absorption in the sample thickness was estimated by simulating the energy loss of fission fragments in the gas with the FLUKA code [42]. The considered geometry was minimal. In each simulation only half of the target and the gas in front of that were drawn (see Fig. 27).

For each isotope, FFs are generated according to the Adeev's [51] mass and charge distribution (see Appendix B and C, pag. 136 and pag. 147 for details). Fig 28 shows the mass distribution of fragments generated in neutron induced fission of  $^{235}\text{U}$ . The FFs are emitted isotropically in angle on  $4\pi$  and their emission point is homogeneously sampled inside the target. Targets are cylinders of radius equal to 4 cm and are in the form of an oxide ( $\text{U}_3\text{O}_8$ ,  $\text{AmO}_2$  and  $\text{CmO}_2$ ). The fission fragments are sampled only in the forward direction, since a backing (not simulated) would stop those emitted backwards. In order to take into account energy conservation, the total available ki-

netic energy  $K$  of FFs is given as the sum of two contribution: the Coulomb repulsion and the incident neutron kinetic energy, sampled from the experimental spectrum. The total  $K$  is then distributed between the 2 fragments inversely proportional to their mass (Fig. 29):

$$\frac{E_L}{E_H} = \frac{M_H}{M_L} \quad (15)$$

with  $E_L$  = kinetic energy of the light fragment,  $E_H$  = kinetic energy of the heavy fragment,  $M_L$  = atomic mass of the light fragment and  $M_H$  = atomic mass of the heavy fragment.

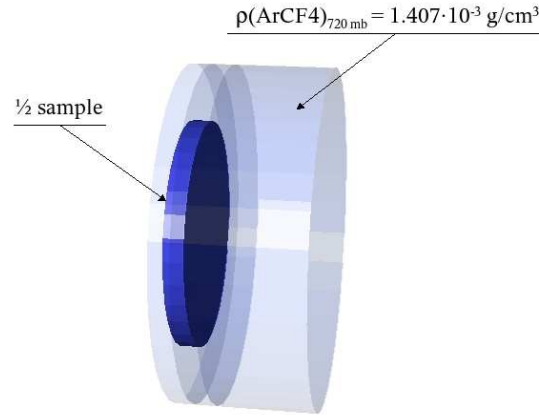


Figure 27: GEOMETRY CONSIDERED IN EACH FLUKA [42] SIMULATION.

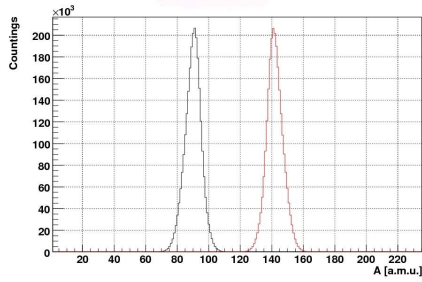


Figure 28: MASS DISTRIBUTION OF FFs GENERATED IN NEUTRON INDUCED FISSION OF  $^{235}\text{U}$ .

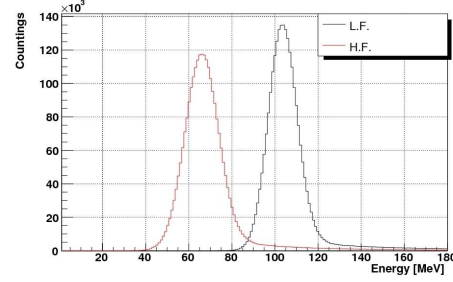


Figure 29: KINETIC ENERGY DISTRIBUTION OF FFs GENERATED IN NEUTRON INDUCED FISSION OF  $^{235}\text{U}$ .

The gas thickness and pressure strongly determines the shape of the distribution of the energy deposited by FFs. Since the cell width is 0.5 cm, most fragments loose just part (80%) of their energy (see Fig. 30 and Fig. 31). Increasing the gas thickness up to 7 cm, the characteristic double humped distribution is visible (see Fig. 32).

The simulated distributions of the energy deposited by the fission fragments in the gas volume of the chamber were folded with an energy resolution calculated for each isotope (see next chapter) to match the measured pulse height spectrum as shown in Fig. 33.

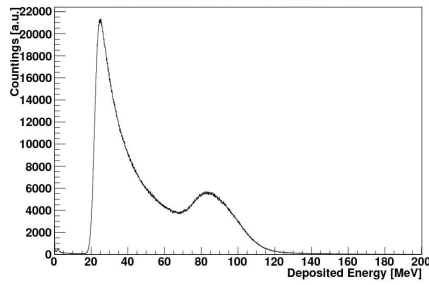


Figure 30: ENERGY DEPOSITED IN 0.5 CM OF  $\text{ArCF}_4$  BY *light* FFs GENERATED IN NEUTRON INDUCED FISSION OF  $^{235}\text{U}$ .

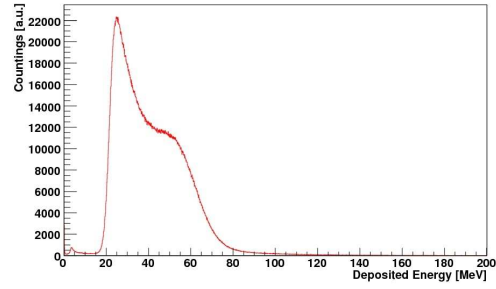


Figure 31: ENERGY DEPOSITED IN 0.5 CM OF  $\text{ArCF}_4$  BY *heavy* FFs GENERATED IN NEUTRON INDUCED FISSION OF  $^{235}\text{U}$ .

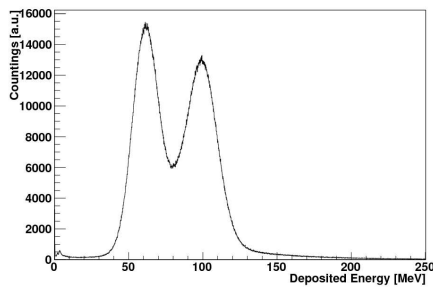


Figure 32: ENERGY DEPOSITED IN 7 CM OF  $\text{ArCF}_4$  BY THE FFs GENERATED IN NEUTRON INDUCED FISSION OF  $^{235}\text{U}$ .

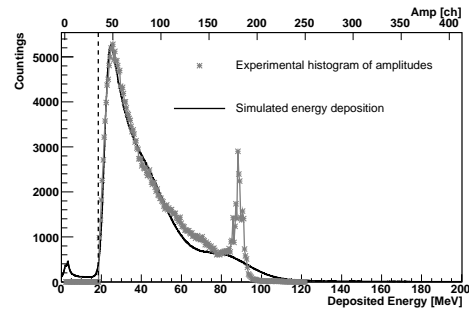


Figure 33: SIMULATION OF THE ENERGY DEPOSITED BY FISSION FRAGMENTS IN THE FIC FOLDED WITH AN ENERGY RESOLUTION OF 15% AND NORMALIZED TO THE MEASURED PULSE HEIGHT SPECTRUM. THE THRESHOLD AT CHANNEL 35 CORRESPONDS TO A DEPOSITED ENERGY OF ABOUT 18 MEV.

Thanks to the channel to energy calibration, the detection efficiency can be calculated for each isotope, taking into account the threshold applied in the pulse shape analysis. Since the neutron induced fission cross sections are extracted with respect to  $^{235}\text{U}$ , the total correction factor to be applied to formula 14 has to consider both the investigated isotope and the reference one. The detection efficiency relative to a sample X results as the percentage of FFs losing an energy higher than a certain value in the gas. That is:

$$D_X = \frac{\# \text{ of FFs depositing in the gas an energy higher than threshold}}{\# \text{ of FFs losing energy in the gas}} \quad (16)$$

and thus eq. 14 becomes:

$$\sigma_{xxx} = \sigma_{235} \cdot \frac{y_X}{y_{235}} \cdot \frac{W_X}{W_{235}} \cdot \frac{m_{235}}{m_X} \cdot \frac{A_X}{A_{235}} \cdot \frac{D_{235}}{D_X} \quad (17)$$

where  $\frac{y_X}{D_X} \cdot W_X = Y_X$ , with  $Y_X$  from eq. 11.

For almost all samples here the simulated efficiency is very high, ranging between 95% and 98%. Therefore, when extracting the cross-section for the various isotopes relative to  $^{235}\text{U}$ , a correction of only a few percent has to be applied. Consequently, the uncertainty related to the detection efficiency is below 1%.

### 5.3 Uncertainties analysis

#### 5.3.1 Uncertainty on neutron energy

Although the samples are separated by 10 mm, a common flight-path (186.95 m) was used in the analysis. From the non-relativistic formula of the kinetic energy, a rough estimation of the introduced uncertainty can be obtained:

$$K = \frac{m L^2}{2 t^2} \quad (18)$$

Deriving K with respect to L:

$$\frac{\partial K}{\partial L} = \frac{m L}{t^2} \quad (19)$$

and:

$$\frac{\partial K}{K} = \frac{\partial L}{2 L} \quad (20)$$

with  $\partial L$  equal to the sensitive FIC length (18 cm) and  $L = 186.95$  m. The corresponding uncertainty of about 0.04% in neutron energy introduced in this way is

negligible in view of the smooth cross section trend in the MeV region.

The contribution of the 7 ns incident beam-pulse width to the energy uncertainty is visible in Fig. 14. It increases with the neutron energy and ranges from a minimum of 0.1% around 1 MeV to a maximum of about 1.3 % for 1 GeV.

### 5.3.2 Cross section uncertainty

Different factors contribute to the cross section uncertainty. First, the mass of targets was derived from  $\alpha$  spectrometry and is thus provided with a percentage error (see Table 9), which never exceeds 1.4%.

Even the mass numbers are given with their uncertainty, equal to one half of the last significative digit. This contribution is completely negligible, affecting results for less than 0.002%.

As for the detection efficiency, it mostly cancels out in the ratio between the correction to be applied to the investigated isotope and to the reference one, remaining below 1%. The same argument applies for dead time.

For normalization to  $^{235}\text{U}$ , the ENDF [52] (Evaluated Nuclear Data File) library, version B-VII.0 was used. It is assumed error-free, thought being the result of the matching between theoretical models and experimental data, an uncertainty analysis has been performed by compilers. By the way, up to 20 MeV incident neutron kinetic energy, error bars associated to  $^{235}\text{U}(\text{n},\text{f})$  cross sections are smaller than 1% of its value [53].

The neutron flux attenuation along the FIC length was simulated and found to be negligible (see § 3.3.4).

The change in the beam profile from 186.95 m backwards with respect to the spallation target to 187.11 cm was calculated using a FLUKA [42] tool available on the n\_TOF web site [54]. The variation in its shape resulted completely negligible [55]. Fig. 34 shows the beam profile for neutron energies between between 100 keV and 100 MeV for  $L = 186.95$  m and  $L = 187.11$  m. The neutron flux attenuation due only to the geometrical divergence of the beam was found to be less than 0.17% considering the whole energy range.

As for the statistical uncertainty, let us define  $N$  as the number of nuclei composing a sample and  $n$  the amount of nuclei of this sample which experience fission ( $n \leq N$ ). For simplicity let us think about a target made of 3 heavy nuclei: one red, one yellow and one green. If the probability, under neutron irradiation, of one nucleus to fission is, for absurd,  $p = 1/3$  (its complementary being  $q = 1 - 1/3 = 2/3$ ), then all possible scenarios should be considered. It may be that only the yellow nucleus splits ( $p^1 \cdot q^2$ ), or only the red one, or the green one, or two nuclei fission ( $p^2 \cdot q^1$ ), or all three or no one. Since, under neutron irradiation, it is not know which ones of the  $n$  nuclei out the  $N$ 's composing the target will experience fission, (n,f) probability must be

treated as a binomial distribution.

$$\binom{N}{n} p^n \cdot q^{N-n}$$

This reduces to the Poisson law because the number of fission events occurring is far smaller than  $N$ . Following the Poissonian distribution the statistical uncertainty on the number of fission events  $n$  is thus calculated as its root square, i.e.  $\sigma = \sqrt{N}$ . In our specific case  $Y$  is the amount of (n,f) reactions detected and induced by neutrons in a precise energy range (histogram bin). Both  $\sqrt{Y_X}$  and  $\sqrt{Y_{235}}$  are considered because (n,f) cross sections are obtained from the detected  $Y_X$  and  $Y_{235}$  (see eq. 17). The statistical component represents the most important contribution to the total uncertainty on the extracted cross sections and can not be neglected.

Considering all effects and corrections introduced in extracting the cross-sections, the overall systematic uncertainty on the extracted cross-section for the two isotopes here investigated is slightly higher than 4%, mostly determined by the uncertainty on the mass of the various deposits (including the  $^{235}\text{U}$  sample used as reference).

In order to avoid confusion about the meaning of  $\sigma$ , in the following mathematical derivation  $S$  stands for cross section, while  $\sigma$  is the error associated to the derived term. From eq. 17:

$$\frac{\partial S}{S} = \sqrt{\left(\frac{\partial S}{\partial m_{235}}\right)^2 \sigma_{m_{235}}^2 + \left(\frac{\partial S}{\partial m_X}\right)^2 \sigma_{m_X}^2 + \left(\frac{\partial S}{\partial A_{235}}\right)^2 \sigma_{A_{235}}^2 + \left(\frac{\partial S}{\partial A_X}\right)^2 \sigma_{A_X}^2 + \left(\frac{\partial S}{\partial Y_{235}}\right)^2 \sigma_{Y_{235}}^2 + \left(\frac{\partial S}{\partial Y_X}\right)^2 \sigma_{Y_X}^2} \quad (21)$$

In the light of the present discussion, results reported in this PhD thesis are provided only with the statistical uncertainty, thus eq. 21 reduces to:

$$\frac{\partial S}{S} = \sqrt{\left(\frac{\partial S}{\partial Y_{235}}\right)^2 \sigma_{Y_{235}}^2 + \left(\frac{\partial S}{\partial Y_X}\right)^2 \sigma_{Y_X}^2} \quad (22)$$

with  $\sigma_{Y_{235}} = \sqrt{Y_{235}}$  and  $\sigma_{Y_X} = \sqrt{Y_X}$

Table 9: FIC 1 MASS UNCERTAINTIES. MASS VALUES REFER TO THE RADIOACTIVE ISOTOPE CONTAINED IN THE SAMPLE.

| Nuclide           | Sample                 | Mass*<br>[mg] | Uncertainty<br>% | DAQ<br>channel |
|-------------------|------------------------|---------------|------------------|----------------|
| $^{233}\text{U}$  | $\text{U}_3\text{O}_8$ | 8.04          | 1.2              | 13             |
|                   |                        | 7.45          | 1.2              |                |
|                   |                        | 7.49          | 1.3              | 16             |
|                   |                        | 7.86          | 1.1              |                |
| $^{235}\text{U}$  | $\text{U}_3\text{O}_8$ | 15.2          | 1.4              | 12             |
|                   |                        | 16.4          | 1.3              |                |
| $^{238}\text{U}$  | $\text{U}_3\text{O}_8$ | 12.8          | 1.4              | 11             |
|                   |                        | 12.4          | 1.4              |                |
|                   |                        | 13.4          | 1.2              | 10             |
|                   |                        | 13.7          | 1.4              |                |
| $^{241}\text{Am}$ | $\text{AmO}_2$         | 0.234         | 1.1              | 6              |
|                   |                        | 0.230         | 1.2              |                |
|                   |                        | 0.280         | 1.2              | 3              |
|                   |                        | 0.279         | 1.2              |                |
|                   |                        | 0.304         | 1.2              | 1              |
|                   |                        | 0.336         | 1.2              |                |
|                   |                        | 0.321         | 1.2              | 2              |
| 0.277             | 1.2                    |               |                  |                |
| $^{243}\text{Am}$ | $\text{AmO}_2$         | 0.556         | 1.2              | 7              |
|                   |                        | 0.585         | 1.3              |                |
|                   |                        | 0.613         | 1.3              | 5              |
|                   |                        | 0.631         | 1.3              |                |
|                   |                        | 0.537         | 1.2              | 4              |
|                   |                        | 0.558         | 1.2              |                |
|                   |                        | 0.595         | 1.3              | 8              |
| 0.710             | 1.2                    |               |                  |                |
| $^{245}\text{Cm}$ | $\text{CmO}_2$         | 0.367         | 1.3              | 14             |
|                   |                        | 0.538         | 1.2              |                |
|                   |                        | 0.407         | 1.3              | 15             |
|                   |                        | 0.399         | 1.3              |                |

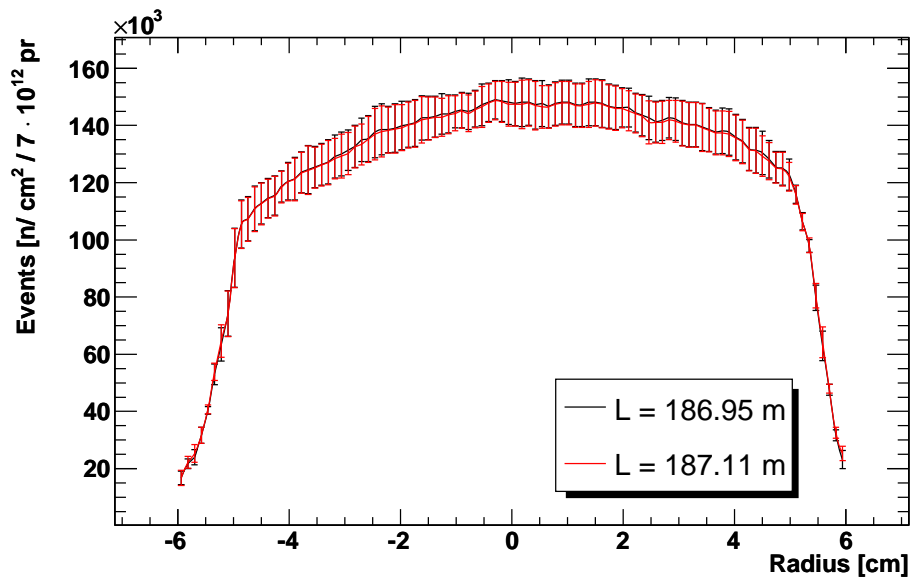


Figure 34: SIMULATED BEAM PROFILE FOR NEUTRON ENERGY BETWEEN 100 KEV AND 100 MEV FOR TWO TARGETS SPACED BY 16 CM.

## 6 Experimental results

*I want to believe*  
(The X-Files)

Cross-sections obtained during this PhD are extracted with reference to the  $\sigma_{n,f}$  U-5 ENDF standard, therefore a detailed analysis of the  $^{235}\text{U}$  sample is mandatory.

### 6.1 $^{235}_{92}\text{U}$

Inside the fast ionization chamber (FIC) there is only one  $^{235}\text{U}$  sample. This means that there are two deposits of this isotope separated by a backing and read by the same electrode. In Table 10 the "identity card" of this sample is reported.

Table 10:  $^{235}\text{U}$  SAMPLE CHARACTERISTICS.

| Nuclide          | $\tau_{\frac{1}{2}}$<br>[years] | Mass<br>[mg] | $\alpha$ -activity<br>[Bq] | DAQ<br>channel | Sample                 | Sample<br>mass<br>[mg] |
|------------------|---------------------------------|--------------|----------------------------|----------------|------------------------|------------------------|
| $^{235}\text{U}$ | $7.1 \times 10^8$               | 31.8         | 2.5 K                      | 12             | $\text{U}_3\text{O}_8$ | 37.57                  |

#### 6.1.1 Pulse shape analysis

Fig. 35 shows that there are a lot of small amplitude pulses in the high neutron energy region. They are due to fragmentation (not fission), i.e. more than two nuclei are present in the exit channel. A 10 channels threshold set in the routine to download data from CASTOR [48] is visible.

Because of its long half-life, the  $^{235}\text{U}$  sample is not supposed to show  $\alpha$  pile-up and the channel discriminating between  $^4\text{He}$  nuclei and fission fragments in the pulse-shape analysis is expected to be quite low. The amplitudes distribution obtained for  $^{235}\text{U}$  shows that  $\alpha$  particles extend up to channel number 35 (see Fig. 36. Again a 10 channels threshold set in the routine to download data from CASTOR [48] is visible.). Only peaks with amplitude higher than this 35-channels threshold are considered in the analysis.

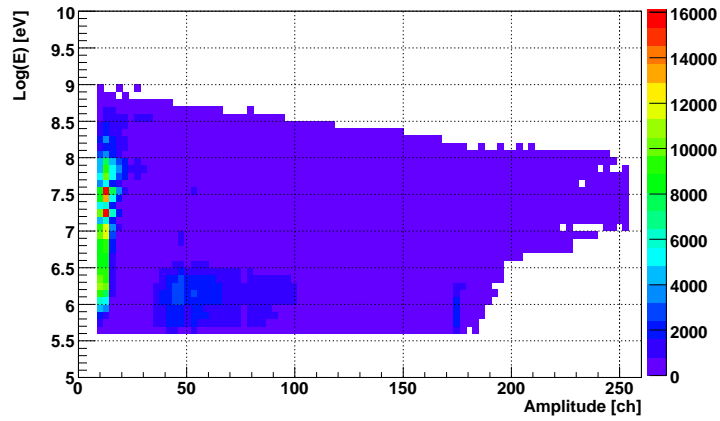


Figure 35: EXPERIMENTAL CORRELATION BETWEEN AMPLITUDE OF DETECTED DIGNSLS AND ENERGY OF THE INCIDENT NEUTRONS FOR  $^{235}\text{U}$  CASE. SMALL AMPLITUDE PULSES IN THE HIGH NEUTRON ENERGY REGION ARE DUE TO FRAGMENTATION.

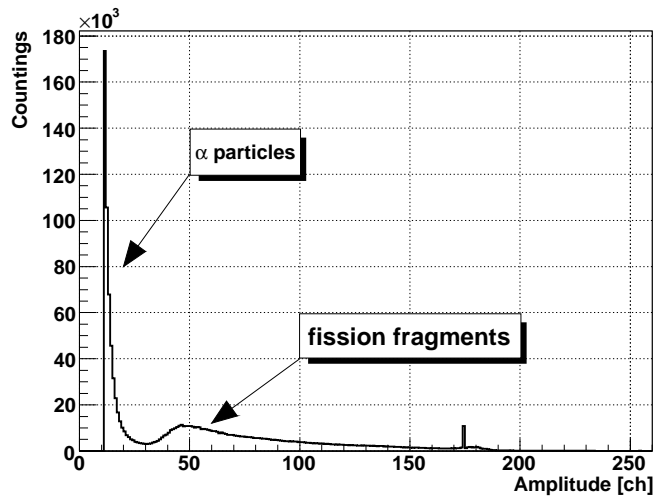


Figure 36: EXPERIMENTAL AMPLITUDE DISTRIBUTION FOR  $^{235}\text{U}$ . SIGNALS WITH AN AMPLITUDE HIGHER THAN 35 CHANNELS ARE DUE TO IONIZATION OF THE FIC GAS BY FISSION FRAGMENTS.

In order to get rid of virtual signals the ratio of collected charge <sup>21</sup> to amplitude of detected events is plotted towards their amplitude. In Fig. 37 the coloured area is bent towards low amplitudes. This is due to the 10 channel offset previously seen and an additional variable offset gained in charge calculation once only signals with an amplitude higher than 35 channels are considered. By the way this offset can be neglected here. The vertical line at channel 175 is due to a saturation effect. Looking at Fig. 37 two regions are visible: one with a higher density of points and another with a lower density of points. Since most of countings are situated in the zone above a charge to amplitude ratio equal to 8 channels, it is assumed that virtual signals are situated under this threshold. These events are discarded.

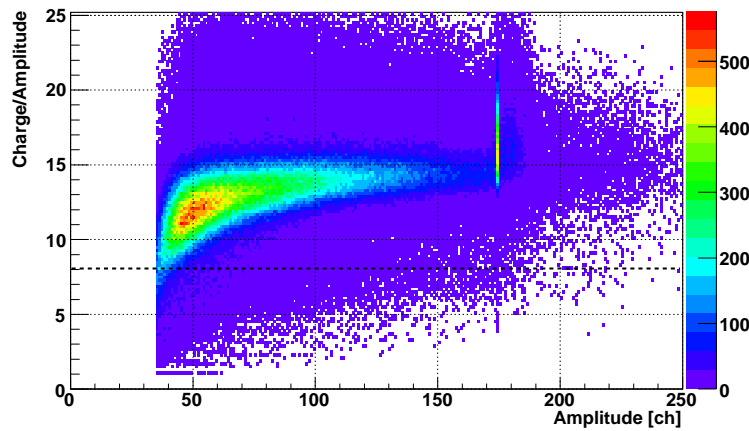


Figure 37: EXPERIMENTAL DISTRIBUTION OF THE CHARGE TO AMPLITUDE RATIO VERSUS AMPLITUDE FOR <sup>235</sup>U. EVENTS BELOW THE DOT LINE CORRESPOND TO VIRTUAL SIGNALS. A THRESHOLD OF 35 CHANNELS ON AMPLITUDE IS APPLIED.

From pulse shape analysis it is derived that, in order to isolate FFs, the following conditions apply to <sup>235</sup>U:

$$\begin{cases} \text{amplitude} \geq 35 & \text{ch} \\ \frac{\text{charge}}{\text{amplitude}} > 8.0 \end{cases}$$

### 6.1.2 FFs histogram

Fig. 38 shows the number of detected fission events (the  $y_{235}$  value in eq. 17) induced by neutrons with energy between  $E_n$  and  $E_n + dE_n$  (that is, neutron energy in a defined energy bin).

<sup>21</sup>Charge of a signal: in this PhD thesis, for charge of a signal the integral on amplitudes of a peak  $i$  is meant, i.e.  $q_i = \sum_i \text{amp}_i$ .

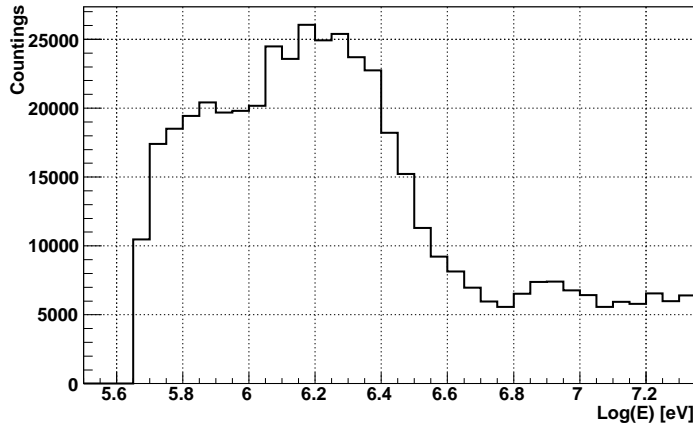


Figure 38: EXPERIMENTAL DISTRIBUTION OF THE NUMBER OF DETECTED FISSION EVENTS AS A FUNCTION OF THE ENERGY OF THE NEUTRON INDUCING IT. A THRESHOLD OF 35 CHANNELS ON AMPLITUDE IS APPLIED AND EVENTS WITH A CHARGE TO AMPLITUDE RATIO SMALLER THAN 8 ARE DISCARDED.

### 6.1.3 Dead Time Correction

The peak reconstruction routine introduces a dead time of 270 ns each time it sees a signal with amplitude greater than 35 channels. For this reason the dead time correction is obtained from an histogram similar to the one shown in Fig. 38, with the difference that no charge to amplitude threshold is applied.

The width of each energy bin is translated into a  $\Delta t$  and the detection rate  $C_d$  of eq. 13 is simply given by  $\frac{Y_{235}}{\Delta t}$ . The correction factor  $W_{235}$ , that is the ratio of the real count rate to the detected one, is shown in Fig. 39.

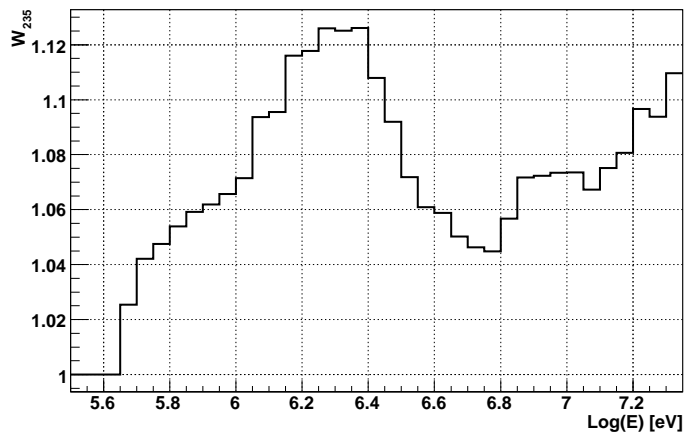


Figure 39: DEAD TIME CORRECTION FACTOR.

The correction factor is always quite low and shows a maximum ( $\sim 12\%$ ) for neutron energy around 2 MeV, where the neutron flux is higher (see for instance Fig 13).

#### 6.1.4 Thickness Correction

In order to evaluate the correction for the chosen amplitude threshold and the sample thickness, the histogram of the energy deposited inside the sensitive volume of the FIC obtained through a FLUKA [42] simulation (see § 5.2.2), has to be calibrated on the experimental amplitude, or equivalently charge, distribution (see § 6.5.2). At the beginning for simplicity the first option was chosen, while later on the second one was preferred because of the better resolution: while amplitudes extend on 256 channels, charges run up to more than 6000 ch. By the way results are almost the same of course, and since the relation between charges and amplitude will be introduced in the section about 241Am, for now we report the "standard analysis" performed.

Fig. 40 and Fig. 41 show the experimental amplitude distribution and the simulated energy deposition for  $^{235}\text{U}$ . The peak at channel 175 in Fig. 40 is not physical, but due to a saturation effect and therefore has not to be considered. Indeed shapes are similar and the two histograms can be superimposed.

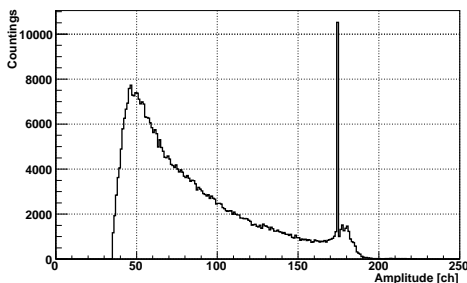


Figure 40: EXPERIMENTAL CHARGE DISTRIBUTION FOR  $^{235}\text{U}$  ISOTOPE.

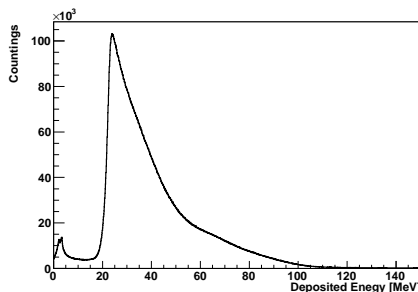


Figure 41: SIMULATED ENERGY DEPOSITION FOR  $^{235}\text{U}$  ISOTOPE.

The distribution of the energy deposited by fission fragments obtained with FLUKA is completely "reality-free". But the experimental setup has its own energy resolution which spreads the theoretical distribution. In other words, a nominal 1 eV will never be detected as 1 eV, but as an energy with a value in the range  $1 \text{ eV} \pm x\%$ . The energy resolution of the electronic chain of  $^{235}\text{U}$  was determined to be 10%<sup>22</sup>.

Calibration was performed through a root routine looking for the energy and charge

<sup>22</sup>For details about the energy resolution determination see 241Am section.

channel corresponding to the maximum in both distributions, and then considering as reference points predefined percentages of the peak height (90%, 80%, 70%,...). See Table 11 for details. Fig. 43 shows the calibration curve.

From calibration it is found that discarding signals whose amplitude is lower than 35 ch means that only fission fragments depositing more than 19.8 MeV inside FIC are being considered. These represent 95.1382% of all fragments emitted.

**The FIC efficiency for  $^{235}\text{U}$  is thus 95.14%.**

Table 11: CORRESPONDENCE BETWEEN THE AMPLITUDE OF SIGNALS DETECTED IN FISSION OF  $^{235}\text{U}$  AND THE SIMILUTED ENERGY DEPOSITED IN THE GAS CELL BY FFs COMING FROM  $^{235}\text{U}$  SAMPLE.

| % Peak<br>[MeV] | Position w.r.t<br>the peak | Amplitude<br>[ch] | Energy<br>[MeV] |
|-----------------|----------------------------|-------------------|-----------------|
| 30              |                            | 37                | 20.5            |
| 40              |                            | 38                | 21              |
| 50              |                            | 39                | 21.5            |
| 60              | left                       | 40                | 21.9            |
| 70              |                            | 41                | 22.3            |
| 80              |                            | 42                | 22.7            |
| 90              |                            | 45                | 23.2            |
| 100             | peak                       | 47                | 25.1            |
| 90              |                            | 53                | 27.5            |
| 80              |                            | 59                | 30              |
| 70              |                            | 64                | 33.2            |
| 60              | right                      | 68                | 36.4            |
| 50              |                            | 79                | 39.9            |
| 40              |                            | 88                | 43.5            |
| 30              |                            | 104               | 48.6            |

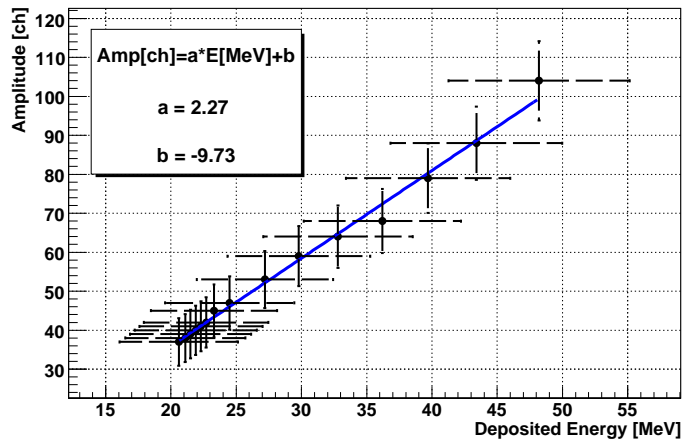


Figure 42: CALIBRATION CURVE. A LINEAR RELATION IS VISIBLE.

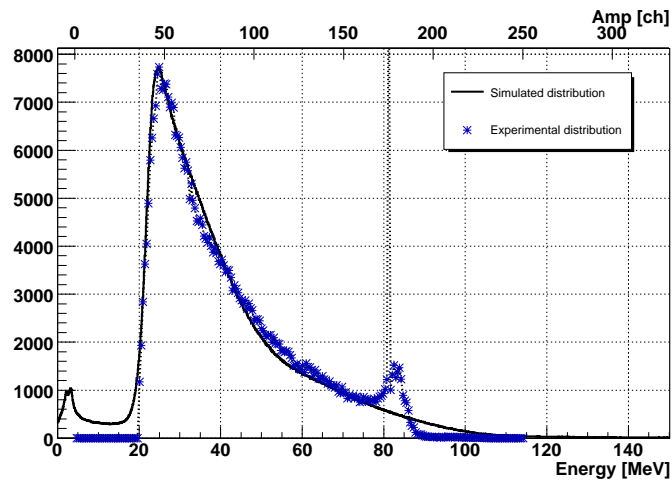


Figure 43: SIMULATED ENERGY DEPOSITION (10% ENERGY RESOLUTION IS APPLIED) CALIBRATED ON THE EXPERIMENTAL HISTOGRAM OF AMPLITUDES.

## 6.2 $^{238}_{92}\text{U}$

$^{238}\text{U}$  is a standard for (n,f) reactions from 2 MeV up to 200 MeV [56]. It is fissionable, but not fissile. Being an even Z - even N isotope, it presents a threshold to neutron induced fission [Kra87]. In this section  $\sigma_{n,f}$  for this isotope is derived.

Inside FIC 2  $^{238}\text{U}$  samples were lodged. This means there are four deposits of this isotope, grouped 2 by 2 and thus read by two electrodes. One electrode presented instability problems and was therefore neglected. In Table 12 is the "identity card" of the sample used.

Table 12:  $^{238}\text{U}$  SAMPLE CHARACTERISTICS.

| Nuclide          | $\tau_{\frac{1}{2}}$ | Mass<br>[mg] | $\alpha$ -activity<br>[Bq] | DAQ<br>channel | Sample                 | Sample<br>mass<br>[mg] |
|------------------|----------------------|--------------|----------------------------|----------------|------------------------|------------------------|
| $^{238}\text{U}$ | $4.47 \times 10^9$   | 25.2         | 313                        | 11             | $\text{U}_3\text{O}_8$ | 29.7                   |

### 6.2.1 Pulse shape analysis

Since the activity of the  $^{238}\text{U}$  sample is 8 times lower than the activity of the  $^{235}\text{U}$  one, the  $\alpha$  background is expected to be completely negligible. On the other hand, a calculation of the neutron induced fission rate on the basis of the  $^{235}\text{U}(n,f)$  and  $^{238}\text{U}(n,f)$  ENDF/B-VII.0 (IAEA) cross sections reveals that for this isotope the (n,f) reaction rate is far smaller as well, and - in proportion - it is diminished by a factor greater than the ones  $\alpha$  decays is reduced by. Therefore we expect a smaller  $\alpha$  to FFs rate ratio. Fig. 44 confirms this forecast.

The threshold on amplitudes to discriminate between fission fragments and He nuclei is set again at 35 ch and the ratio charge to amplitude at 8 (see Fig. 45).

Summarizing, from pulse shape analysis the following conditions to isolate FFs are obtained :

$$\begin{cases} \text{amplitude} \geq 35 \text{ ch} \\ \frac{\text{charge}}{\text{amplitude}} > 8.0 \end{cases}$$

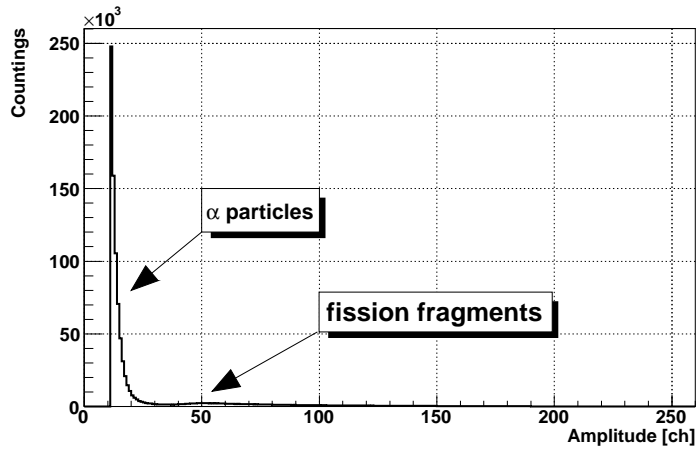


Figure 44: EXPERIMENTAL AMPLITUDE DISTRIBUTION FOR  $^{238}\text{U}$ . SIGNALS WITH AN AMPLITUDE HIGHER THAN 35 CHANNELS ARE DUE TO IONIZATION OF THE FIC GAS BY FISSION FRAGMENTS.

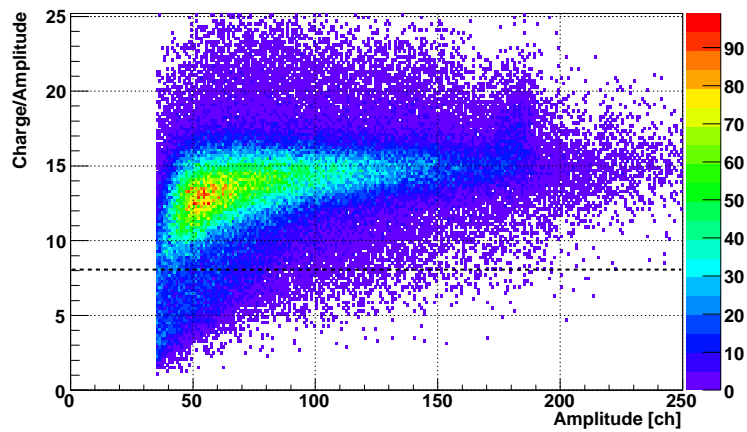


Figure 45: EXPERIMENTAL DISTRIBUTION OF THE CHARGE TO AMPLITUDE RATIO VERSUS AMPLITUDE FOR  $^{238}\text{U}$ . EVENTS BELOW THE DOT LINE CORRESPOND TO VIRTUAL SIGNALS. A THRESHOLD OF 35 CHANNELS ON AMPLITUDE IS APPLIED.

### 6.2.2 FFs histogram

Fig. 46 shows the number of detected fission events (the  $Y_{238}$  value in eq. 17) induced by neutrons with energy between  $E_n$  and  $E_n + dE_n$  (that is, neutron energy in a defined energy bin). Because of the fission threshold of even-even nuclei, FFs before 1 MeV -as expected - are not numerous at all.

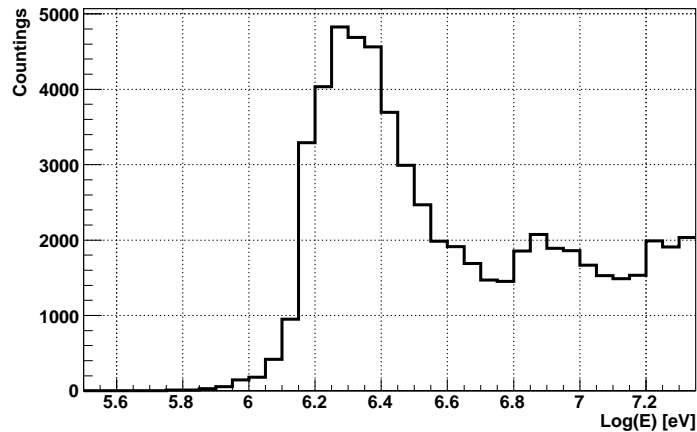


Figure 46: EXPERIMENTAL DISTRIBUTION OF THE NUMBER OF DETECTED FISSION EVENTS AS A FUNCTION OF THE ENERGY OF THE NEUTRON INDUCING IT. A THRESHOLD OF 35 CHANNELS ON AMPLITUDE IS APPLIED AND EVENTS WITH A CHARGE TO AMPLITUDE RATIO SMALLER THAN 8 ARE DISCARDED.

### 6.2.3 Dead Time Correction

Being both the  $\alpha$  activity and fission rate of  $^{238}\text{U}$  smaller than that of  $^{235}\text{U}$ , the dead time for the even-even investigated sample is lower than that for the previously examined isotope. Fig. 47 shows the trend of the correction factor to be applied. Around 2 MeV it doesn't exceed 4%, against the 12% of  $^{235}\text{U}$ .

### 6.2.4 Thickness Correction

The calibration of  $^{238}\text{U}$  was performed taking into account an energy resolution equal to 11.95%<sup>23</sup>. The obtained results are shown in Fig. 48 and Fig. 49.

---

<sup>23</sup>For details about the energy resolution determination see <sup>241</sup>Am section.

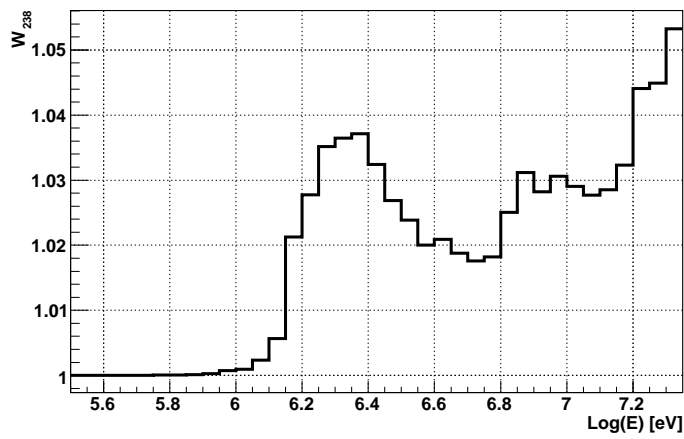


Figure 47: DEAD TIME CORRECTION FACTOR.

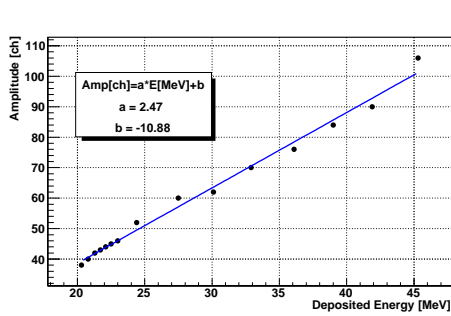


Figure 48: CALIBRATION CURVE. A LINEAR RELATION IS VISIBLE.

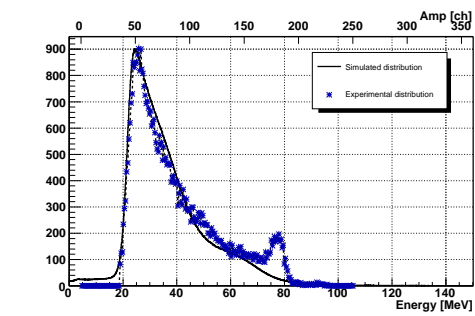


Figure 49: SIMULATED ENERGY DEPOSITION (11.95% ENERGY RESOLUTION IS APPLIED) CALIBRATED ON THE EXPERIMENTAL HISTOGRAM OF AMPLITUDES.

Discarding signals whose amplitude is lower than 35 ch means therefore that only fission fragments depositing more than 18.5 MeV inside FIC are being considered. These represent 97.4% of all fragments emitted.

The FIC efficiency for  $^{238}\text{U}$  is thus 97.4%.

## 6.2.5 Results

The upper panel of Fig. 50 shows a comparison between  $^{238}\text{U}$  (n,f) cross sections obtained at the n\_TOF facility and the ENDF/B-VII.0 evaluations, released in December 2006. The agreement doesn't look really good.

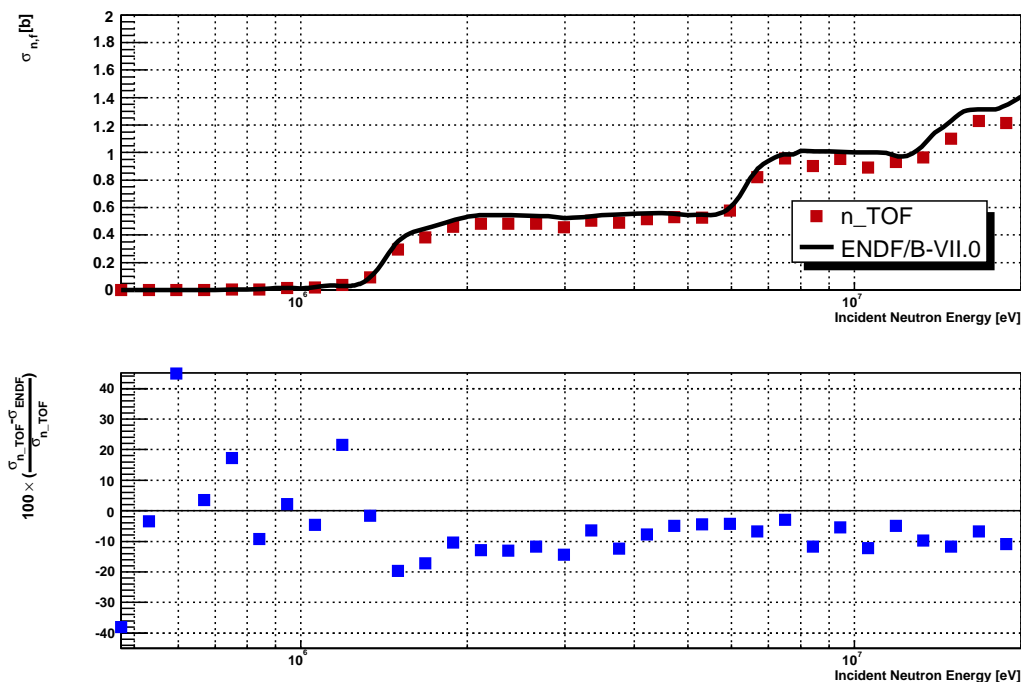


Figure 50: CALIBRAZIONE.

In order to quantify previous considerations, in the lower panel of Fig. 50 the percentage difference between n\_TOF results and the ENDF/B-VII.0 library is plotted. n\_TOF cross sections, for energies higher than 2 MeV, are always lower than the ENDF/B-VII.0, and the discrepancy varies between 2% and 10%.

In the low energy region instead the difference between n\_TOF and ENDF/B-VII.0  $^{238}\text{U}$   $\sigma_{(n,f)}$  strongly oscillates from -38% to +45%.

The reason of such high discrepancies in this standard isotope is discussed in the conclusions.

For a better cross-check, a comparison between n\_TOF experimental results and other evaluations was considered (Fig. 51).

As already seen our results are below the ENDF/B-VII.0 evaluation from 2 MeV on. This library differs from its previous version (ENDF/B-VI.8) only at high energies. Around 18 MeV in fact ENDF/B-VII.8 matches n\_TOF results. The discrepancy between the two evaluations in the high energy region is due to availability of new data in 2006, when the more recent version was compiled. JEFF-3.1  $^{238}\text{U}$   $\sigma_{(n,f)}$  grows faster than the two ENDF libraries between 1 MeV and 2 MeV and therefore matches our results. Nevertheless between 2 MeV and 3 MeV it is almost 16% higher than n\_TOF. In the energy region 3 MeV - 10 MeV it follows the two ENDF libraries and soon after grows faster than ENDF/B-VII.0, reaching again a 15% discrepancy with our results.

Fig. 52 shows a comparison between the n\_TOF (n,f) cross sections for  $^{238}\text{U}$  and other evaluations. Again our results are complexively lower than the referred libraries.

Since evaluations are based both on theoretical nuclear models and experimental data, a comparison between our and previous results is plotted. Given the high discrepancies met up to now, a detailed discussion makes little sense and only general considerations follow. Fig. 53 and Fig. 54 directly reports  $^{238}\text{U}$   $\sigma_{(n,f)}$  /  $^{235}\text{U}$   $\sigma_{(n,f)}$ . When such data are available, they're preferred, in order to avoid to introduce discrepancies between  $^{238}\text{U}$   $\sigma_{(n,f)}$  due to a normalization based on different  $^{235}\text{U}$  (n,f) cross section.

In Fig. 53 some experimental data are plotted. Kanda *et al.* [57], Goverdovskij *et al.* [58], Behrens *et al.* [59] and Fursov *et al.* [60] all agree with each other, but from 1.3 MeV neutron incident kinetic energy on they are always higher than n\_TOF, reaching 16% discrepancy with our data. Nevertheless, n\_TOF  $^{238}\text{U}$   $\sigma_{(n,f)}$  reproduce the shape of all other experimental data.

As shown in Fig. 54, first data by Lisowski's *et al.* [61] oscillates around n\_TOF results, leading to a fairly good agreement (at some energies data superimpose). But this trend is not confirmed neither by the more recent data from Lisowski's *et al.* [62], nor by Shcherbakov's *et al.* [63], which show cross sections complexively higher than ours.

In order to quantify the agreement/disagreement between the extracted  $^{238}\text{U}$   $\sigma_{(n,f)}$  and reported libraries or experimental data, cross sections were integrated over the energy region of overlap of the different data sets. Table 13 shows the results. In the first column is reported the name of the referred library/author, the minimum and maximum extremes of integration follow. The percentage difference is calculated as:

$$\frac{[\int \sigma_{(n,f)}(E) dE]_{n\_TOF} - [\int \sigma_{(n,f)}(E) dE]_{ref.}}{[\int \sigma_{(n,f)}(E) dE]_{n\_TOF}}$$

therefore a plus sign signifies that n\_TOF results are higher than the referred ones, while a minus has the opposite meaning.

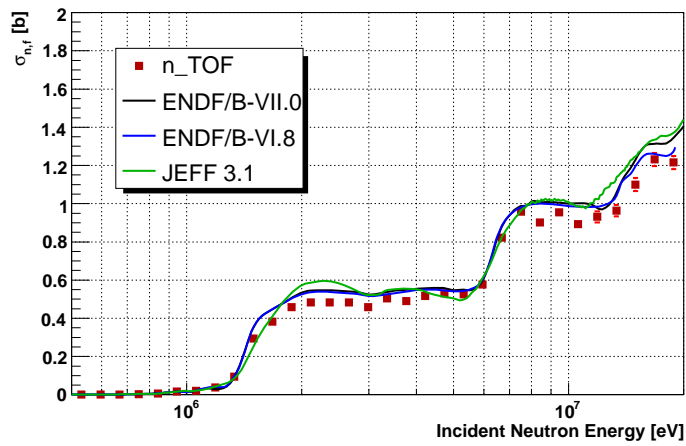


Figure 51: COMPARISON BETWEEN n\_TOF (20 BINS/DECADE)  $^{238}\text{U}$  (N,F) EXPERIMENTAL CROSS SECTIONS AND DIFFERENT EVALUATIONS.

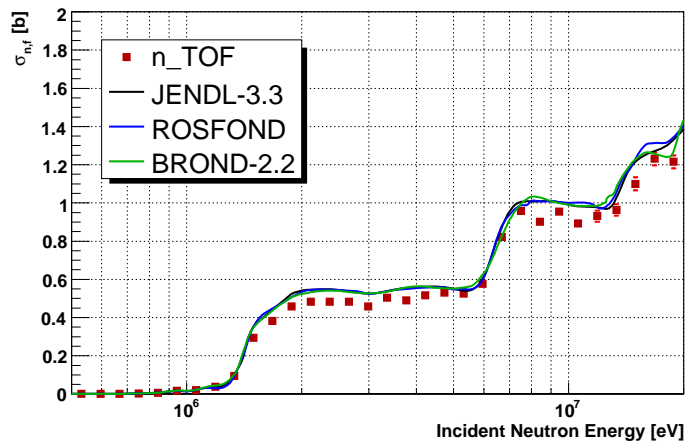


Figure 52: COMPARISON BETWEEN n\_TOF (20 BINS/DECADE)  $^{238}\text{U}$  (N,F) EXPERIMENTAL CROSS SECTIONS AND DIFFERENT EVALUATIONS.

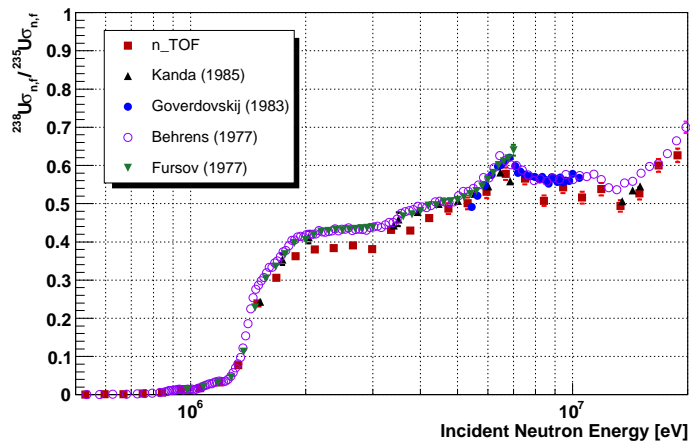


Figure 53: COMPARISON BETWEEN n\_TOF (20 BINS/DECADE)  $^{238}\text{U}$  (N,F) EXPERIMENTAL CROSS SECTIONS AND PREVIOUS EXPERIMENTAL DATA.

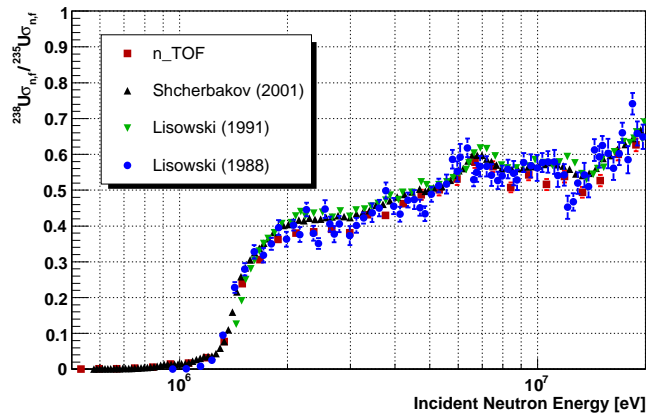


Figure 54: COMPARISON BETWEEN n\_TOF (20 BINS/DECADE)  $^{238}\text{U}$  (N,F) EXPERIMENTAL CROSS SECTIONS AND PREVIOUS EXPERIMENTAL DATA.

Table 13:  $^{238}\text{U}$  SUMMARY.

| Referred data set | $E_{min}$<br>[MeV] | $E_{max}$<br>[MeV] | Difference<br>[%] |
|-------------------|--------------------|--------------------|-------------------|
| ENDF/B-VII.0      | 0.5                | 20.0               | -8.7              |
| ENDF/B-VI.8       | 0.5                | 20.0               | -6.2              |
| JEFF-3.1          | 0.5                | 20.0               | -10.0             |
| JENDL-3.3         | 0.5                | 20.0               | -7.5              |
| ROSFOND           | 0.5                | 20.0               | -8.7              |
| BROND-2.2         | 0.5                | 20.0               | -7.6              |
| Kanda             | 1.52               | 15                 | -2.5              |
| Goverdovskij      | 5.44               | 10.4               | -5.6              |
| Behrens           | 0.5                | 20.0               | -7.0              |
| Fursov            | 0.981              | 7.0                | -7.2              |

As evident, our results for the  $^{238}\text{U}$  (n,f) cross sections are not correct. The reason is probably due to instability of the electronic chain. For more details see §7.

### 6.3 $^{233}\text{U}$

$^{233}\text{U}$  is an even Z - odd N isotope and therefore presents no threshold to neutron induced fission reactions [Kra87]. Inside FIC two  $^{233}\text{U}$  samples were lodged. In Table 14 their "identity card" is presented.

Table 14:  $^{233}\text{U}$  SAMPLE CHARACTERISTICS.

| Nuclide          | $\tau_{\frac{1}{2}}$<br>[years] | Mass<br>[mg] | $\alpha$ -activity<br>[Bq] | DAQ<br>channel | Sample                 | Sample<br>mass<br>[mg] |
|------------------|---------------------------------|--------------|----------------------------|----------------|------------------------|------------------------|
| $^{233}\text{U}$ | $1.59 \times 10^5$              | 15.49        | 5.48 M                     | 13             | $\text{U}_3\text{O}_8$ | 18.32                  |
|                  |                                 | 15.35        | 5.53 M                     | 16             |                        | 18.16                  |

#### 6.3.1 Pulse shape analysis

Though the  $\alpha$  background is higher than in previous discussed cases, from pulse shape analysis  $\alpha$  pile-up is seen not to play a significant role. The amplitude channel discriminating between  $^4\text{He}$  nuclei and FFs is placed at channel 35, as for  $^{238}\text{U}$  and  $^{235}\text{U}$ , as shown in Fig. 55.

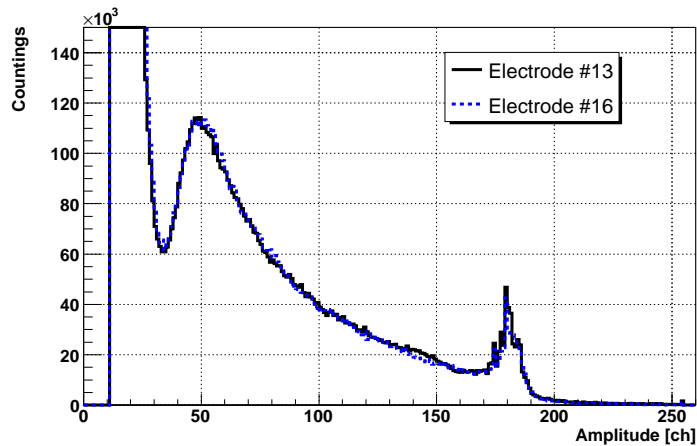


Figure 55: EXPERIMENTAL AMPLITUDE DISTRIBUTION READ BY THE TWO ELECTRODES OF  $^{233}\text{U}$  SEPARATELY, NORMALIZED FOR THE VALUE OF THE SAMPLE MASS.

In order to discriminate between  $^4\text{He}$  nuclei and FFs, a threshold on the  $q/A$  value is set. In Fig. 56 all detected fission signals for  $^{233}\text{U}$  were considered, adding data coming from all available  $^{233}\text{U}$  samples. Events below the dot line correspond to virtual signals. The threshold value for  $q/A$  is 8.0.

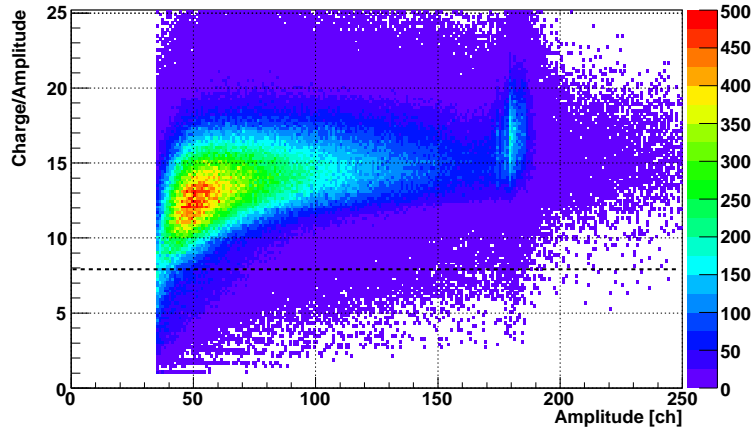


Figure 56: EXPERIMENTAL DISTRIBUTION OF THE CHARGE TO AMPLITUDE RATIO VERSUS AMPLITUDE FOR  $^{233}\text{U}$ . EVENTS BELOW THE DOT LINE CORRESPOND TO VIRTUAL SIGNALS. A THRESHOLD OF 35 CHANNELS ON AMPLITUDE IS APPLIED.

Once again, from pulse shape analysis, the following conditions to discriminate between  $\alpha$  particles and fission fragments are derived:

$$\begin{cases} \text{amplitude} \geq 35 \text{ ch} \\ \frac{\text{charge}}{\text{amplitude}} > 8.0 \end{cases}$$

### 6.3.2 FFs histogram

The total fission yield normalized for the mass of the sample corresponds to the fission yield per unitary mass. Therefore, when more targets are available for a same isotope, the distribution of the amount of detected fission fragments as a function of the energy of the neutron inducing that can be used as a cross check on their masses. Two samples of same isotopic composition, comparable mass<sup>24</sup> and subjected to a common neutron flux are indeed expected to experience an equal number of (n,f) reactions.

The FIC houses 2 samples of  $^{233}\text{U}$  and Fig. 57 shows a very good compatibility of the two distributions.

<sup>24</sup>If masses are totally different, the thickness correction plays a dominant role.

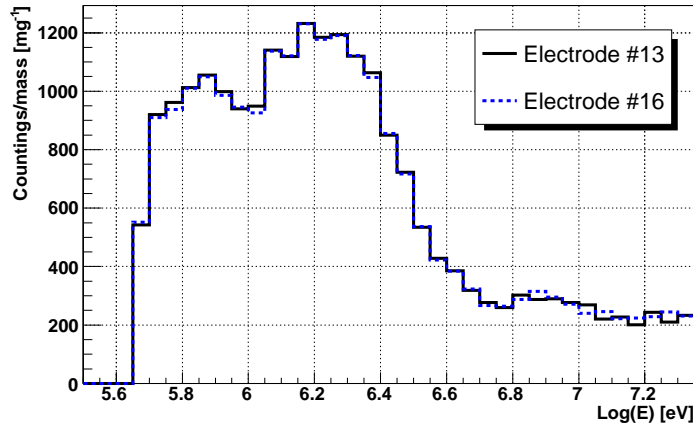


Figure 57: EXPERIMENTAL DISTRIBUTION OF DETECTED FISSION EVENTS FOR UNIT MASS AS A FUNCTION OF THE NEUTRON ENERGY. THE COMPATIBILITY BETWEEN THE TWO HISTOGRAMS IS USED AS A CROSS CHECK ON THE VALUES OF THE SAMPLE MASSES.

### 6.3.3 Dead Time Correction

Fig. 58 directly reports the total dead time correction factor obtained as a ratio between the ones to be applied to  $^{233}\text{U}$  and  $^{235}\text{U}$ . This correction factor is mostly smaller than 1 because the considered  $^{235}\text{U}$  sample is more massive than the  $^{233}\text{U}$  one. Its maximum discrepancy from 1 is reached around 2 MeV incident-neutron kinetic energy, where the neutron flux is higher, and around 10 MeV, where the difference in (n,f) cross section between the two isotopes diminishes and therefore masses play a significant role.

### 6.3.4 Thickness Correction

The calibration of  $^{233}\text{U}$  was performed considering an energy resolution equal to 14.6% for electrode number 13 and 17.6% for electrode number 16 respectively <sup>25</sup>. The obtained results are weighted on the isotope masses, i.e.:

$$\epsilon_{tot}(\%) = \epsilon_{El13}(\%) \cdot \frac{mass_{El13}}{mass_{tot}} + \epsilon_{El16}(\%) \cdot \frac{mass_{El16}}{mass_{tot}}$$

From calibration it is found that **the FIC efficiency for  $^{233}\text{U}$  is 97.7%**. As already seen, the efficiency for  $^{235}\text{U}$  is instead 95.1%. The result is compatible with expectations, since the U-5 sample is thicker than the U-3 one and therefore more FFs are blocked inside  $^{235}\text{U}$  than inside  $^{233}\text{U}$ . As a consequence, the difference in

<sup>25</sup>For details about the energy resolution determination see <sup>241</sup>Am section.

efficiency is equal to  $1 - 0.951/0.977 = 2.65\%$ .

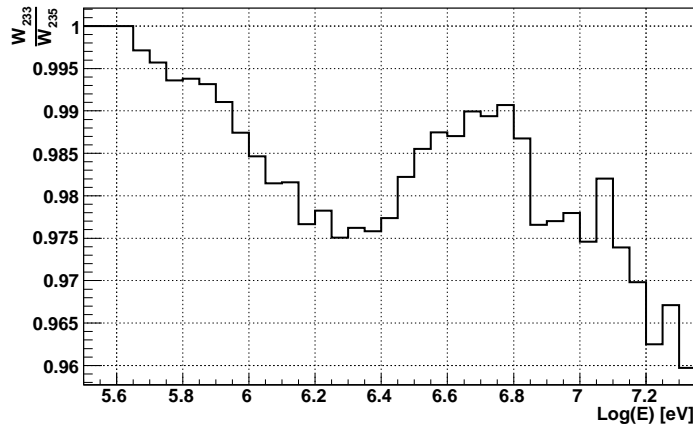


Figure 58: TOTAL DEAD TIME CORRECTION FACTOR TO BE APPLIED TO THE ANALYSIS OF THE  $^{233}\text{U}$  ISOTOPE.

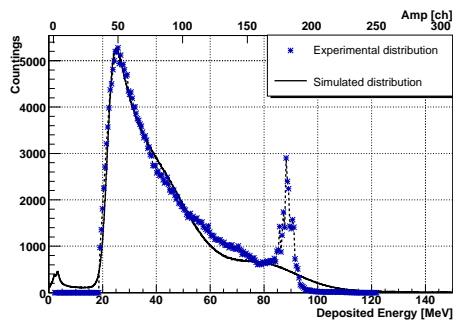


Figure 59: SIMULATED ENERGY DEPOSITION (14.5% ENERGY RESOLUTION IS APPLIED) CALIBRATED ON THE EXPERIMENTAL HISTOGRAM OF AMPLITUDES FOR ELECTRODE # 13.

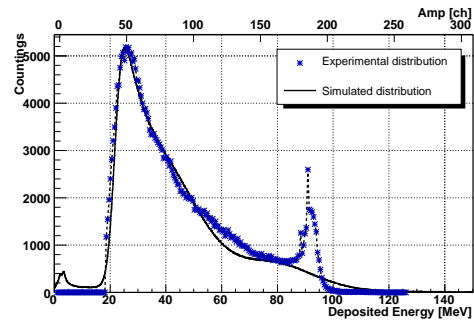


Figure 60: SIMULATED ENERGY DEPOSITION (17.6% ENERGY RESOLUTION IS APPLIED) CALIBRATED ON THE EXPERIMENTAL HISTOGRAM OF AMPLITUDES FOR ELECTRODE # 16.

### 6.3.5 Results

The upper panel of Fig. 61 shows a comparison between experimental  $^{233}\text{U}$  (n,f) cross sections obtained at the n\_TOF facility and the ENDF/B-VII.0 evaluations, released in December 2006. A good agreement is visible on the whole energy range considered, though around 13 MeV a discrepancy shows up.

In order to quantify previous considerations, in the lower panel of Fig. 61 the percentage difference between n\_TOF results and the ENDF/B-VII.0 library is plotted. n\_TOF cross sections are complexively higher than the ENDF/B-VII.0, but the discrepancy is generally below 5% and reaches 10% only in the high energy region.

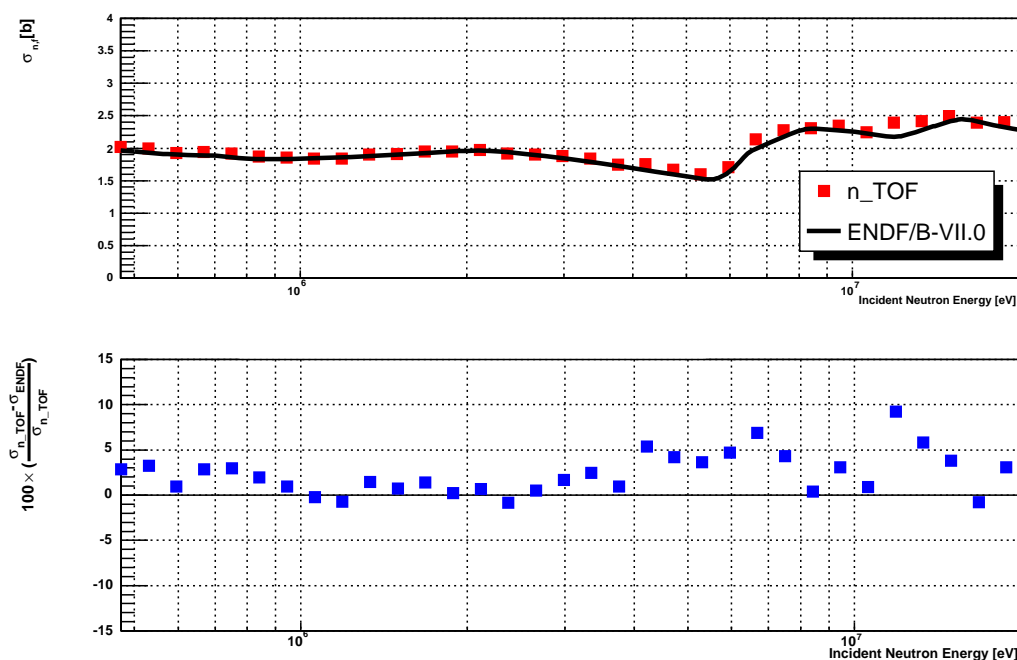


Figure 61: COMPARISON BETWEEN n\_TOF (20 BINS/DECADE) AND ENDFB-VII.0  $\sigma_{(n,f)}$ .

For a better cross check, a comparison between n\_TOF experimental results and other evaluations was considered (Fig. 62). The JEFF-3.1 library was not reported, since it is based on the JENDL-3.3 original data. At low energies (below 1 MeV) the agreement with ENDF/B-VI.8 is very good, between 1 MeV and 8 MeV n\_TOF cross sections are compatible with both the two versions of the Evaluated Nuclear Data Files, while above 8 MeV our data better approach ENDF/B-VII.0.

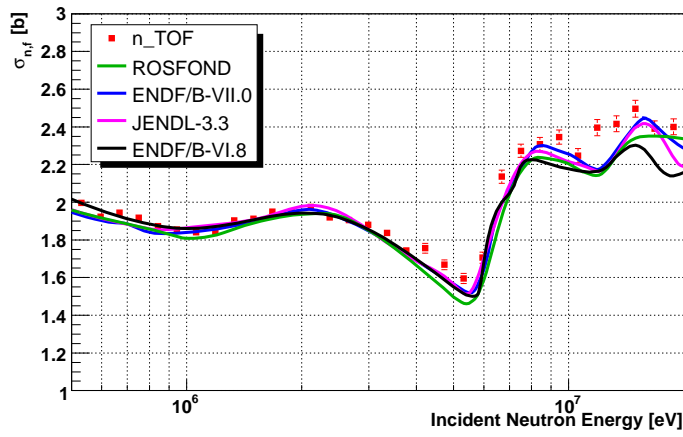


Figure 62: COMPARISON BETWEEN n\_TOF (20 BINS/DECADE)  $^{233}\text{U}$  (N,F) EXPERIMENTAL CROSS SECTIONS AND DIFFERENT EVALUATIONS.

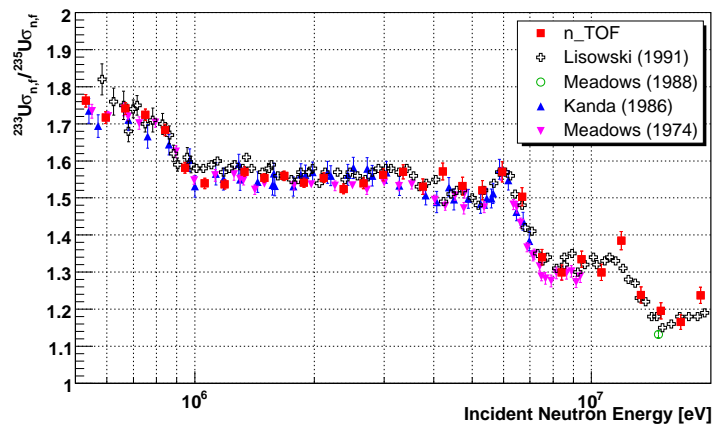


Figure 63: COMPARISON BETWEEN n\_TOF (20 BINS/DECADE)  $^{233}\text{U}$  (N,F) CROSS SECTIONS AND PREVIOUS EXPERIMENTAL DATA.

Since the ENDF/B-VII.0 evaluation of  $^{233}\text{U}(n,f)$  is mainly based on Kanda *et. al* [64], Meadows *et. al* [65; 66] and Lisowski's *et. al* [67] data [68], Fig. 63 reports the comparison between n\_TOF and the referred experimental cross sections<sup>26</sup>. The agreement with Lisowski *et. al* [67] is very good, apart for one point at low energy ( $\approx 0.6$  MeV) and one at high energy ( $\approx 13$  MeV). As for the low energy region ( $E_n \leq 0.7$  MeV), the referred datum is  $\approx 5.5\%$  higher than the n\_TOF one and therefore, if normalized, would approach more ENDF/B-VI than ENDF/B-VII.0. At about 11 MeV, the discrepancy between Lisowski *et. al* [67] and ENDF/B-VI or ENDF/B-VII.0 is the same because the overlap of the two evaluations is complete. The only conclusion we can thus trace is that our cross section looks  $\approx 8\%$  higher in this point. Kanda *et. al* [64] and Meadows *et. al* [65; 66] data very good agree with n\_TOF results, confirming - if converted to  $^{233}\text{U} \sigma_{(n,f)}$  using the  $^{235}\text{U} \sigma_{(n,f)}$  IAEA evaluation exploited for our data- ENDF/B-VI at low energies ( $E_n \leq 0.7$  MeV) and ENDF/B-VII.0 in the high energy region ( $E_n \geq 0.7$  MeV). The reason why ENDF/B-VII.0  $^{233}\text{U} \sigma_{(n,f)}$  library provides higher values than the ones used to create that, is that "a somewhat higher  $^{235}\text{U}$  fission cross section was used to convert experimental data, since it produces better agreement with fast critical benchmark" [68]. On the other hand ENDF/B-VII.0 at low energies ( $E_n \leq 0.9$  MeV) results less compatible than ENDF/B-VI.0, as proved in the following pages by considering more experimental data.

Fig. 64 shows that n\_TOF data, at low energies ( $E_n \leq 0.7$  MeV), are in agreement with Fursov *et. al*[69] and Carlson *et. al* [70], confirming once again the ENDF/B-VI library. Above 1 MeV instead our results are always  $\approx 3\%$  higher than the referred ones. For Shcherbakov *et. al* [71] the same considerations previously made for Lisowski *et. al* [67] apply.

Fig. 65 directly reports cross sections because Tovesson *et. al* [72] data were extracted with reference to  $^{237}\text{Np}$ , while CENBG [73] (Centre d'Etudes Nucleaires de Bordeaux Gradignan)  $^{233}\text{U} \sigma_{(n,f)}$  were provided us in this form. n\_TOF experimental cross sections agrees both with Tovesson *et. al* [72] and CENBG [73], but result complexively  $\approx 1\% \div 2\%$  lower.

A check of self-consistency of n\_TOF data was performed by comparing the neutron induced fission cross sections extracted in the high energy regime ( $E_n \geq 0.5$  MeV) with those obtained at low energies [50] ( $E_n \leq 2$  MeV) with the same detector. The two analysis were divided because different data treatment apply. This check is important because n\_TOF is the only one facility giving the possibility to extract neutron induced cross sections ranging on so many orders of magnitude. Moreover

---

<sup>26</sup>For some experiments, the EXFOR web site provides both  $^{233}\text{U} \sigma_{(n,f)}$  relative to  $^{235}\text{U} \sigma_{(n,f)}$  and already normalized  $^{233}\text{U} \sigma_{(n,f)}$ , while for some other experiments only  $^{233}\text{U} \sigma_{(n,f)}$  relative to  $^{235}\text{U} \sigma_{(n,f)}$  are available. Moreover different authors used different  $^{235}\text{U} \sigma_{(n,f)}$  libraries (ENDF/B-V, JENDL3.2,...) for normalization purposes. For sake of easy comparison, only  $^{233}\text{U} \sigma_{(n,f)}$  relative to  $^{235}\text{U} \sigma_{(n,f)}$  were plotted. This line is followed for experimental results along the whole PhD work.

low energy data extend from 0.027 eV up to about 2 MeV, giving the chance to test the possible necessity of normalization factors by comparison with resonances. No normalization was applied to the n\_TOF extracted  $^{233}\text{U}$   $\sigma_{(n,f)}$  neither in the high energy region, nor in the low, and results are reported in Fig. 66. The agreement is very good.

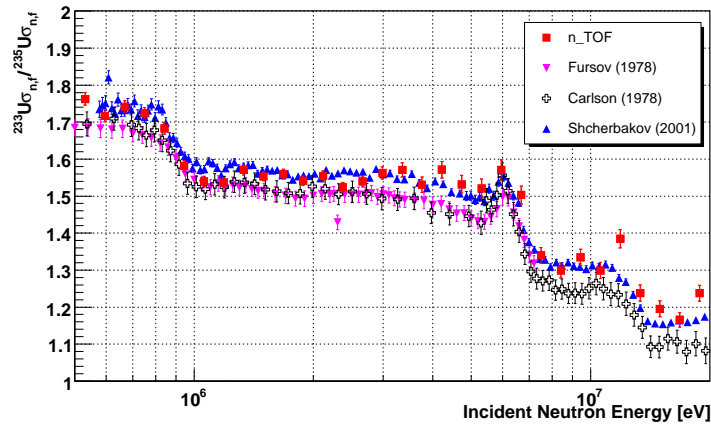


Figure 64: COMPARISON BETWEEN n\_TOF (20 BINS/DECADE)  $^{233}\text{U}$  (N,F) CROSS SECTIONS AND DIFFERENT EXPERIMENTAL DATA.

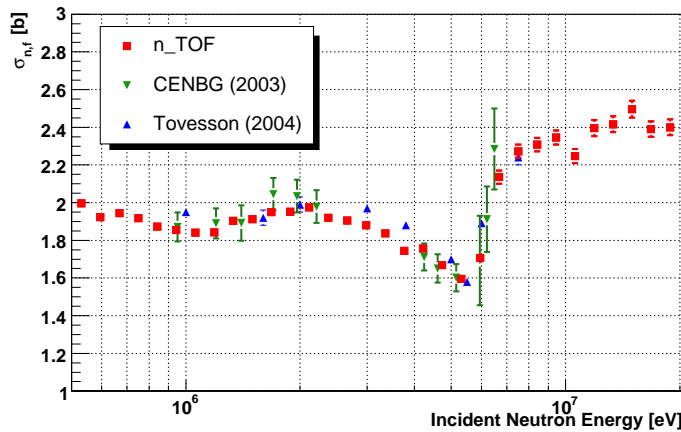


Figure 65: COMPARISON BETWEEN n\_TOF (20 BINS/DECADE)  $^{233}\text{U}$  (N,F) EXPERIMENTAL CROSS SECTIONS AND DIFFERENT EXPERIMENTAL DATA.

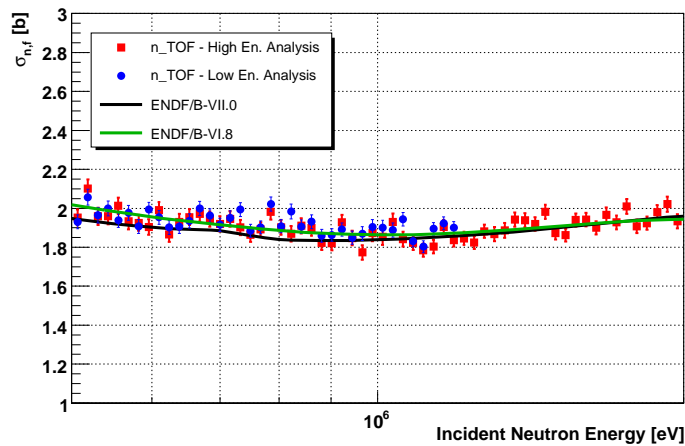


Figure 66: COMPARISON BETWEEN n\_TOF (100 BINS/DECADE)  $^{233}\text{U}$  (N,F) EXPERIMENTAL CROSS SECTIONS OBTAINED IN THE HIGH AND LOW ENERGY ANALYSIS. ENDF/B-VII.0 AND ENDF/B-VI.8 ARE REPORTED AS REFERENCE.

As an additional check, cross sections extracted analyzing data collected with the FIC were compared to  $^{233}\text{U}$   $\sigma_{(n,f)}$  obtained by the PPAC [36] detector [74], always at the n\_TOF facility. Results are reported in Fig. 67

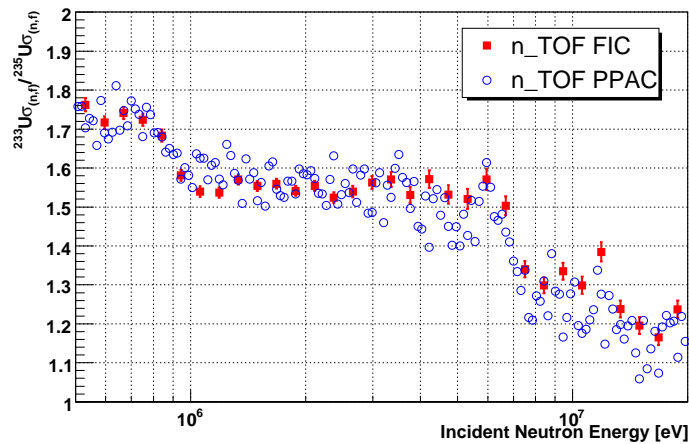


Figure 67: COMPARISON BETWEEN n\_TOF (20 BINS/DECADE)  $^{233}\text{U}$  (N,F) EXPERIMENTAL CROSS SECTIONS OBTAINED IN THE HIGH ENERGY ANALYSIS OF FIC DATA WITH  $\sigma_{(n,f)}$  EXTRACTED BY PPAC ANALYSIS.

As before, in order to quantify the agreement/disagreement between the extracted  $^{233}\text{U}$   $\sigma_{(n,f)}$  and reported libraries or experimental data, cross sections were integrated over the energy region of overlap of the different data sets. Table 15 shows the results.

Table 15:  $^{233}\text{U}$  SUMMARY.

| Referred data set      | $E_{min}$<br>[MeV] | $E_{max}$<br>[MeV] | Difference<br>[%] |
|------------------------|--------------------|--------------------|-------------------|
| ENDF/B-VII.0           | 0.5                | 20.0               | +3.2              |
|                        | 0.5                | 1.0                | +2.2              |
| ENDF/B-VI.8            | 0.5                | 20.0               | +6.1              |
|                        | 0.5                | 1.0                | -0.02             |
| ROSFOND                | 0.5                | 20.0               | +4.8              |
| JENDL-3.3              | 0.5                | 20.0               | +3.9              |
| Lisowski               | 0.583              | 20.0               | +0.8              |
| Meadows                | 0.5                | 9.367              | +2.1              |
| Kanda                  | 0.5                | 6.97               | +1.3              |
| Fursov                 | 0.5                | 7.4                | +4.3              |
| Carlson                | 0.5                | 20.0               | +6.3              |
| Shcherbakov            | 0.577              | 20.0               | +1.9              |
| CENBG                  | 0.950              | 6.49               | -1.0              |
| Tovesson               | 1.0                | 7.5                | -2.4              |
| n_TOF FIC - Low Energy | 0.5                | 1.2                | -1.3              |
| n_TOF PPAC             | 0.5                | 20.0               | +3.5              |

## 6.4 $^{243}_{95}\text{Am}$

$^{243}\text{Am}$  is an odd Z - even N isotope and therefore presents a threshold to neutron induced fission [Kra87]. Inside FIC 4  $^{243}\text{Am}$  samples were lodged. In Table 16 is their "identity card".

Table 16:  $^{243}\text{Am}$  SAMPLE CHARACTERISTICS.

| Nuclide           | $\tau_{\frac{1}{2}}$<br>[years] | Mass<br>[mg] | $\alpha$ -activity<br>[Bq] | DAQ<br>channel | Sample         | Sample<br>mass<br>[mg] |
|-------------------|---------------------------------|--------------|----------------------------|----------------|----------------|------------------------|
| $^{243}\text{Am}$ | $7.37 \times 10^3$              | 1.095        | 8.092 M                    | 4              | $\text{AmO}_2$ | 1.239                  |
|                   |                                 | 1.244        | 9.139 M                    | 5              |                | 1.408                  |
|                   |                                 | 1.141        | 8.432 M                    | 7              |                | 1.291                  |
|                   |                                 | 1.305        | 9.644 M                    | 8              |                | 1.477                  |

### 6.4.1 Pulse shape analysis

Since the  $\alpha$  activity of the considered samples of  $^{243}\text{Am}$  is higher than for previous isotopes, in order to visually discriminate between FFs and  $^4\text{He}$  nuclei only signals with amplitude higher than 35 channels (considered the minimum in the light of what seen up to now) are plotted in Fig. 68. Otherwise the  $\alpha$  background would be so huge that the tail of the  $\alpha$  particles strongly affects the FFs one.

Only three electrodes out of four were considered, since the number 7 showed some instability problems. In Fig. 68 the signal seen by electrode # 8 is shifted of about 10 channels. A different gain of the electronic chain was supposed for this electrode and amplitudes of raw data were lowered by 20% before being passed to the peak recognition routine. This caused the "spikes" visible in Fig. 69.

In Fig. 69 the minimum between the peaks of  $\alpha$  and FFs distributions falls at different channels for different electronic chains (see Table 17) :

Table 17: CHANNEL DISCRIMINATING BETWEEN FFs AND  $\alpha$  PARTICLES.

| Electrode | Amp. | Electrode | Amp. | Electrode | Amp. |
|-----------|------|-----------|------|-----------|------|
| 4         | 38   | 5         | 41   | 8         | 39   |

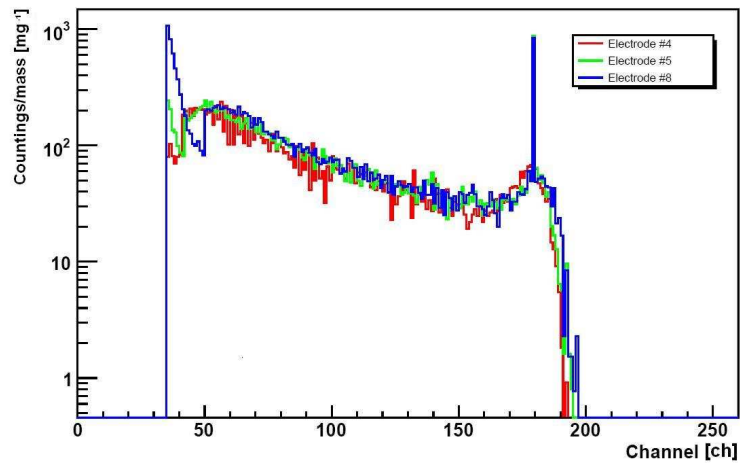


Figure 68: EXPERIMENTAL AMPLITUDE DISTRIBUTION READ BY THE THREE ELECTRODES OF  $^{243}\text{Am}$  SEPARATED, NORMALIZED FOR THE VALUE OF THE MASS SAMPLE. AN OFFSET OF 10 CHANNELS IS VISIBLE FOR ELECTRODE # 8.

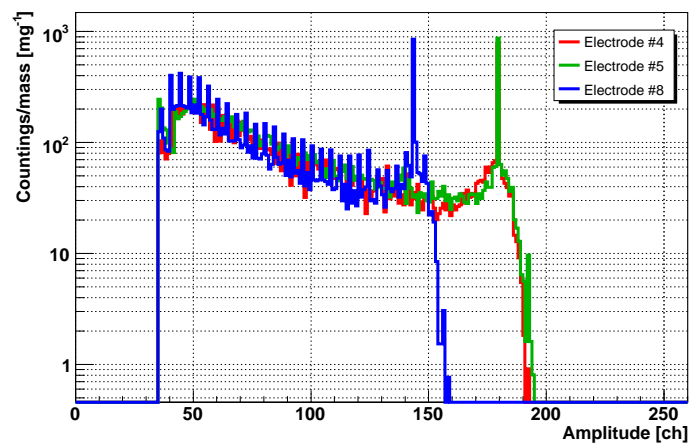


Figure 69: EXPERIMENTAL AMPLITUDE DISTRIBUTION READ BY THE THREE ELECTRODES OF  $^{243}\text{Am}$  SEPARATED, NORMALIZED FOR THE VALUE OF THE MASS SAMPLE. THE AMPLITUDES OF SIGNALS SEEN BY ELECTRODE # 8 ARE CORRECTED FOR THE OFFSET.

As for all other isotopes, a threshold on the value  $q/a$  in order to discriminate between virtual and real signals was looked for. Since the obtained ratio was found to be the same for the three electrodes separately, Fig. 70 reports data for all of them without distinction.

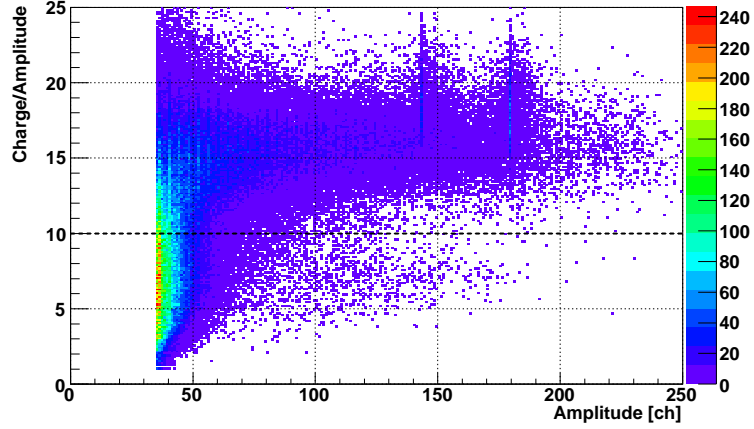


Figure 70: EXPERIMENTAL DISTRIBUTION OF THE CHARGE TO AMPLITUDE RATIO VERSUS AMPLITUDE FOR ALL  $^{243}\text{Am}$  SAMPLES. EVENTS BELOW THE DOT LINE CORRESPOND TO VIRTUAL SIGNALS.

Summarizing, from pulse shape analysis, the following conditions are derived:

$$Electrode \#4 = \begin{cases} amplitude \geq 38 & ch \\ \frac{charge}{amplitude} > 10.0 \end{cases}$$

$$Electrode \#5 = \begin{cases} amplitude \geq 41 & ch \\ \frac{charge}{amplitude} > 10.0 \end{cases}$$

$$Electrode \#8 = \begin{cases} amplitude \geq 39 & ch \\ \frac{charge}{amplitude} > 10.0 \end{cases}$$

#### 6.4.2 FFs histogram

Applying the previously listed conditions, the distribution of the amount of detected fission fragments as a function of the energy of the neutron inducing that is plotted. Since more  $^{243}\text{Am}$  samples are available, the distribution normalized for the value of sample masses is used as a cross check on the mass values. Fig. 71 shows quite good compatibility of the three distributions, though discrepancies up to 15% show up between electrode #4 and electrode #5 at about 1.7 - 1.8 MeV. This would lead to a 15% difference in the cross sections extracted for the different electrodes at

that incident neutron energy, but considering all the available statistics and the total mass of  $^{243}\text{Am}$  contained inside the FIC detector, fluctuations are averaged.

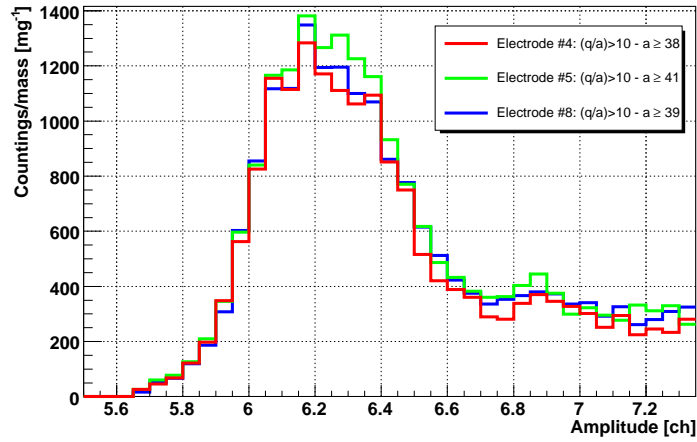


Figure 71: EXPERIMENTAL DISTRIBUTION OF DETECTED FISSION EVENTS FOR UNIT MASS AS A FUNCTION OF THE NEUTRON ENERGY. THE COMPATIBILITY AMONG THE THREE HISTOGRAMS IS USED AS A CROSS CHECK ON THE VALUES OF THE SAMPLE MASSES.

#### 6.4.3 Dead Time Correction

Fig. 72 directly reports the total dead time correction factor obtained as the ratio of the ones to be applied to  $^{243}\text{Am}$  and  $^{235}\text{U}$ . As for  $^{233}\text{U}$ , this correction factor is mostly smaller than one because the considered  $^{243}\text{Am}$  samples are less massive than the  $^{235}\text{U}$  one. Discrepancy from 1 reaches a maximum of 10% around 2 MeV, much more than the about 2.5% used for  $^{233}\text{U}$ . Once again, the difference lies in the mass of the samples. At about 10 MeV the total correction factor for  $^{243}\text{Am}$  is much higher than for  $^{233}\text{U}$  (compare Fig. 72 and Fig. 58) because the former isotope fissions at high energies, while the latter at low.

#### 6.4.4 Thickness Correction

The calibration of the amplitude distribution on the distribution of the energy deposited by FFs inside the FIC detector was performed for the three electronic chains involved in the  $^{243}\text{Am}$  analysis separately. The considered energy resolutions were respectively 12.9% for electrode number 4, 14.0% for electrode number 5 and 11.7% for electrode number 8 <sup>27</sup>. Since the obtained efficiencies were similar, they were averaged on the sample masses as for the case of  $^{233}\text{U}$  and the three deposits of  $^{243}\text{Am}$  were treated as one target.

<sup>27</sup>For details about the energy resolution determination see  $^{241}\text{Am}$  section.

The FIC efficiency for  $^{243}\text{Am}$  is 99.7%. Therefore, being the efficiency of the  $^{235}\text{U}$  sample equal to 95.14%, in agreement with its larger thickness, the correction factor to apply to  $^{243}\text{Am}$  is  $1 - 0.95514/0.997 = 95.7\%$ .

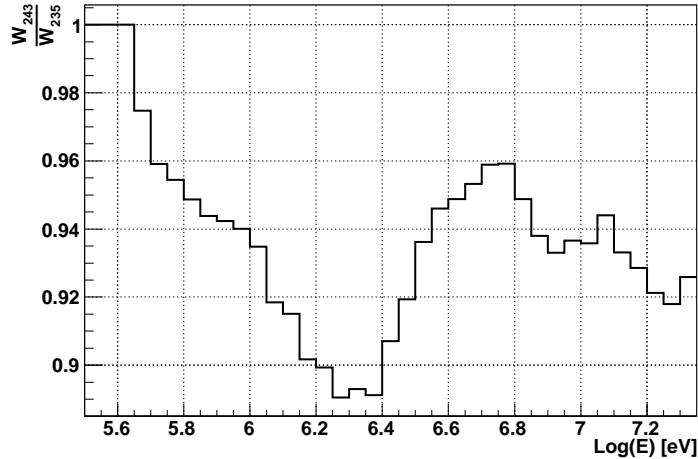


Figure 72: TOTAL DEAD TIME CORRECTON FACTOR TO BE APPLIED TO THE ANALYSIS OF THE  $^{243}\text{Am}$  ISOTOPE.

#### 6.4.5 Results

The upper panel of Fig. 73 shows a comparison between experimental  $^{243}\text{Am}$  (n,f) cross sections obtained at the n\_TOF facility and the ENDF/B-VII.0 evaluations, released in December 2006. A good agreement is visible on the whole energy range considered, though again, as for  $^{233}\text{U}$ , around 13 MeV a discrepancy shows up.

In order to quantify previous considerations, in the lower panel of Fig. 73 the percentage difference between n\_TOF results and the ENDF/B-VII.0 library is plotted. The n\_TOF cross section agrees really well (discrepancies around 5%) with the evaluation between 1 MeV and 10 MeV. A problem shows up around 13 MeV. Below 1 MeV, the discrepancy with ENDF/B-VII.0 reaches almost 40%. Before drawing fast conclusions, it must be remembered that  $^{243}\text{Am}$  fissions at high energy and therefore (n,f) cross section - both n\_TOF and evaluated - is about 0 at low energies. By performing the ratio of one almost null value to another almost null value, it is really easy obtaining a huge number as a result. In fact, errors associated to the cross section are very similar to cross section itself.

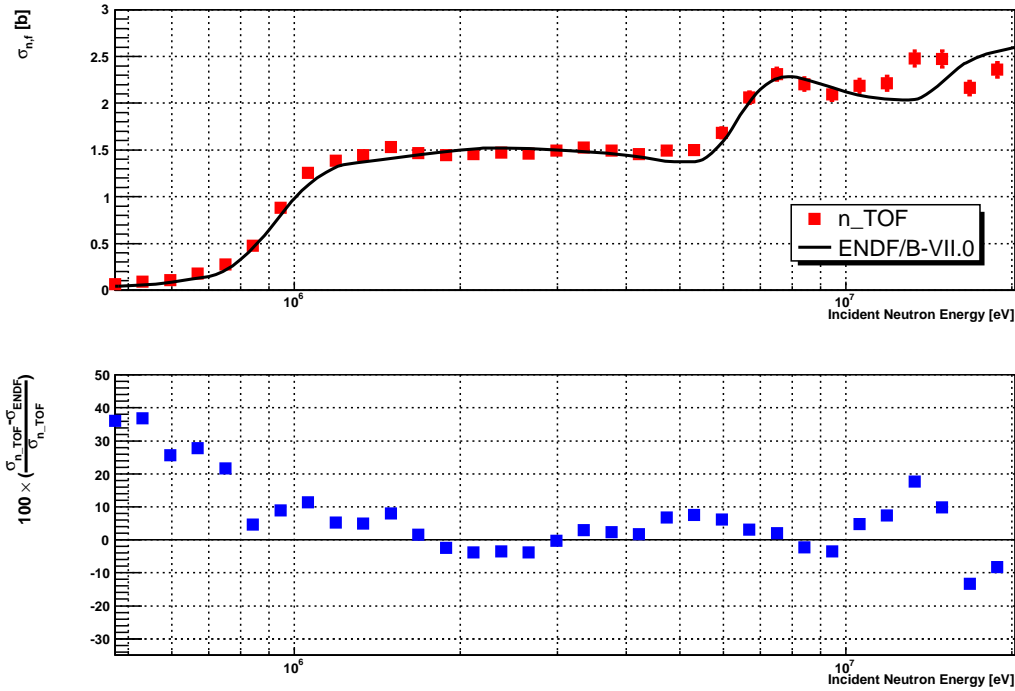


Figure 73: COMPARISON BETWEEN n\_TOF (20 BINS/DECADE) AND ENDFB-VII.0  $\sigma_{(n,f)}$ .

For a better cross check, a comparison between n\_TOF experimental results and other evaluations was considered. In Fig. 74 the only ENDF data visible are from version B-VI.8. ENDF/B-VII.0 data are covered by  $\sigma_{(n,f)}$  the previous version, because no changes were made in the passage from ENDF/B-VI.8 and ENDF/B-VII.0 for this nuclear reaction (see pag. 92). The agreement between n\_TOF and ENDF  $\sigma_{(n,f)}$  looks good ( $\approx 2\% \div 3\%$ ) in the whole energy range, but between 13 MeV and 20 MeV. Nentherless, considering the shape, JENDL-AC2008 better suits to our data in the double humped region around 2 MeV. The agreement with this evaluation (JENDL-AC2008) is by the way worst (around 4% discrepancy) than with ENDF/B-VII.0 and with JENDL-3.3 for 8 MeV incident neutrons.

Fig. 75 shows a comparison between the extracted n\_TOF neutron induced fission cross section of  $^{243}\text{Am}$  and other evaluated libraries. Again the agreement looks really good ( $\approx 2\% \div 3\%$ ) up to 13 MeV.

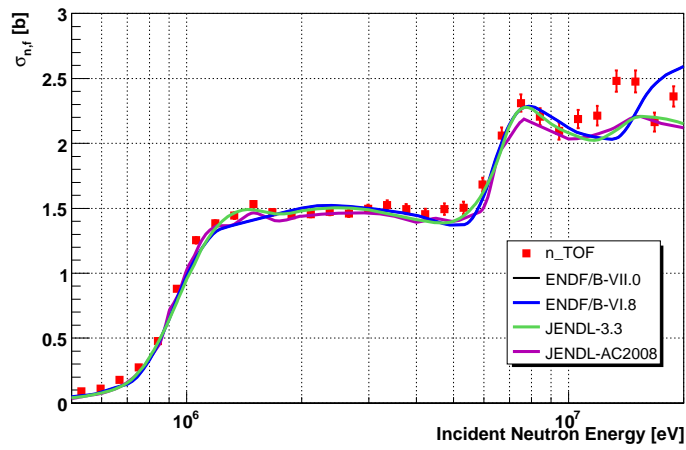


Figure 74: COMPARISON BETWEEN n\_TOF (20 BINS/DECADE)  $^{243}\text{Am}$  (N,F) EXPERIMENTAL CROSS SECTIONS AND DIFFERENT EVALUATIONS.

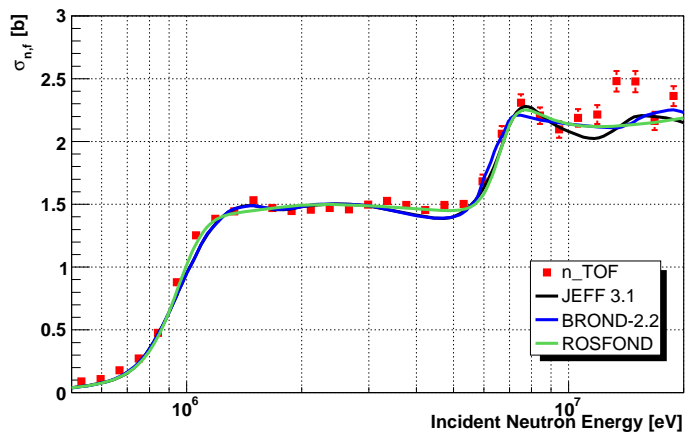


Figure 75: COMPARISON BETWEEN n\_TOF (20 BINS/DECADE)  $^{243}\text{Am}$  (N,F) EXPERIMENTAL CROSS SECTIONS AND DIFFERENT EVALUATIONS.

Fig. 76 reports the comparison between n\_TOF and some experimental results. Cross sections were directly plotted for Aiche *et al.* [75] because data were not extracted with reference to any isotope. For Seeger *et al.* [76] the plotted values are the only available data and Fursov *et al.* [77] employed  $^{237}\text{Np}$  as a monitor. Cross sections are instead provided by the EXFOR data base both as absolute and with reference to the  $^{235}\text{U}$  standard, and the choice to superimpose Laptev's *et al.* [78]  $\sigma_{(n,f)}$  on Fig. 76 was performed in order to visually underline the big discrepancies among existing experimental determinations. Up to 1 MeV n\_TOF cross sections agree with all available data, but the height at which the first chance fission channel opens, and thus also  $\sigma_{(n,f)}$  in the plateau region, strongly varies ( $\approx 20\%$ ) from Fursov *et al.* [77] to Laptev *et al.* [78]. Here (n,f) cross sections extracted during this PhD are about 2% higher than Fursov *et al.* [77] and up to 5% lower than Aiche *et al.* [75]. Seeger *et al.* [76] stays more or less midway between n\_TOF and Laptev *et al.* [78].

Fig. 77 shows the only available experimental data extending up to higher energies. Again a huge discrepancy shows up in the region of the first chance fission plateau, where Behrens *et al.* [79] confirms Laptev *et al.* [78], while Fomichev *et al.* [80] agrees with n\_TOF  $\sigma_{(n,f)}$ . At high energies, taking into account that may be the  $^{235}\text{U}$  fission yield use to extract our data is lower than it should be, n\_TOF is in agreement with Fomichev *et al.* [80], while Behrens *et al.* [79] oscillates between Laptev *et al.* [78] and Fomichev *et al.* [80].

Summarizing, as noted by the ENDF/B-VII evaluators, fission cross sections experimental data tend to cluster in two distinct groups, in the 1-6 MeV range, separated by about 20% from each other. The most recent experimental data set available at the time of the ENDF/B-VII.0 release was by Laptev *et al.* [78], and those values lie in the higher-energy group, about 20% higher than the ENDF/B-VI evaluation. Nentherless such higher values are in disagreement with the averaged cross sections obtained in the ZEBRA reactor spectrum [82]. This explains why ENDF/B-VII.0 evaluators decided to keep the ENDF/B-VI evaluated values unchanged. n\_TOF data, as well as Fomichev, therefore agree with the ZEBRA data (reactor benchmark [83]).

The same check of self consistency performed for  $^{233}\text{U}$ , was repeated for  $^{243}\text{Am}$  neutron induced fission cross sections. Fig. 78 reports the comparison between  $^{243}\text{Am}$   $\sigma_{(n,f)}$  extracted in the high energy regime and those obtained at low energies [50] with the same detector. No normalization was applied, neither in the high nor in the low energy region and the agreement is very good.

Once again, in order to quantify the agreement/disagreement between the extracted  $^{243}\text{Am}$   $\sigma_{(n,f)}$  and reported libraries or experimental data, cross sections were integrated over the energy region of overlap of the different data sets. Table 18 shows the results.

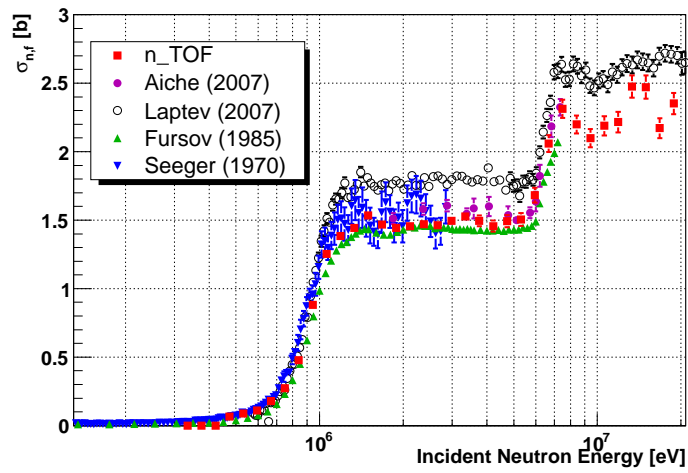


Figure 76: COMPARISON BETWEEN n\_TOF (20 BINS/DECADE)  $^{243}\text{Am}$  (N,F) CROSS SECTIONS AND PREVIOUS EXPERIMENTAL DATA.

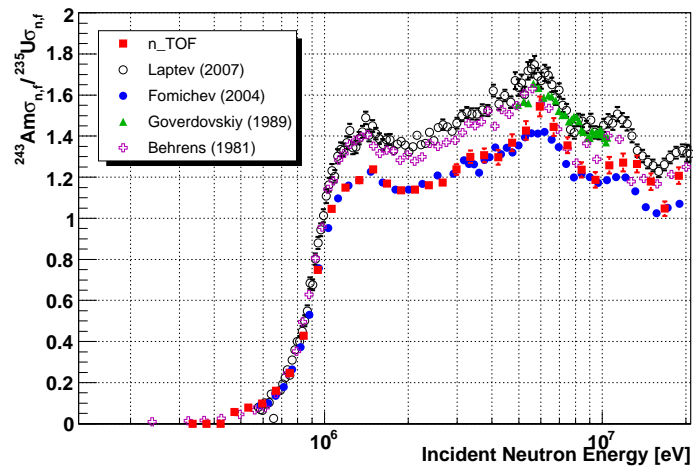


Figure 77: COMPARISON BETWEEN n\_TOF (20 BINS/DECADE)  $^{243}\text{Am}$  (N,F) CROSS SECTIONS AND PREVIOUS EXPERIMENTAL DATA.

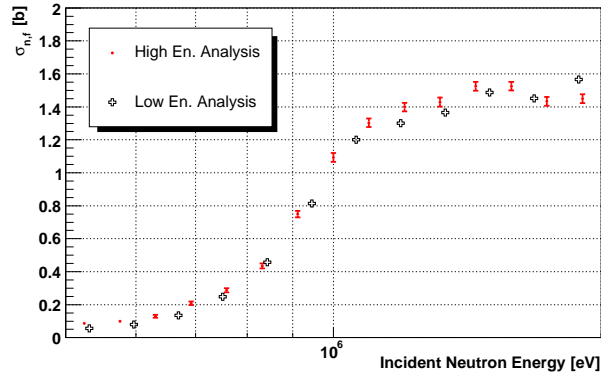


Figure 78: COMPARISON BETWEEN n\_TOF (80 BINS/DECADE)  $^{243}\text{Am}$  (N,F) CROSS SECTIONS OBTAINED IN THE HIGH AND LOW ENERGY ANALYSIS.

Table 18:  $^{243}\text{U}$  SUMMARY.

| Referred data set           | $E_{min}$<br>[MeV] | $E_{max}$<br>[MeV] | Difference<br>[%] |
|-----------------------------|--------------------|--------------------|-------------------|
| ENDF/B-VII.0 (=ENDF/B-VI.8) | 0.5                | 20.0               | +1.6              |
| JENDL-3.3                   | 0.5                | 20.0               | +5.4              |
| JENDL-AC2008                | 0.5                | 20.0               | +6.6              |
| JEFF-3.1                    | 0.5                | 20.0               | +5.4              |
| BROND-2.2                   | 0.5                | 20.0               | +4.3              |
| ROSFOND                     | 0.5                | 20.0               | +5.0              |
| Fursoy                      | 0.5                | 7.4                | +5.7              |
| Laptev                      | 0.577              | 20.0               | -15.3             |
| Aiche                       | 1.841              | 7.350              | -3.4              |
| Seeger                      | 0.5                | 2.973              | -6.5              |
| Fomichev                    | 0.588              | 20.0               | +5.2              |
| Goverdovskiy                | 4.97               | 10.41              | -11.8             |
| Behrens                     | 0.5                | 20.0               | -6.4              |
| n_TOF FIC - Low Energy      | 0.5                | 2.0                | +2.15             |

## 6.5 $^{241}_{95}\text{Am}$

$^{241}\text{Am}$  is an odd  $Z$  - even  $N$  isotope and therefore presents a threshold to neutron induced fission [Kra87]. Inside FIC 4  $^{241}\text{Am}$  samples were lodged. In Table 19 is their "identity card".

Table 19:  $^{241}\text{Am}$  SAMPLE CHARACTERISTICS.

| Nuclide           | $\tau_{\frac{1}{2}}$<br>[years] | Mass<br>[mg] | $\alpha$ -activity<br>[Bq] | DAQ<br>channel | Sample         | Sample<br>mass<br>[mg] |
|-------------------|---------------------------------|--------------|----------------------------|----------------|----------------|------------------------|
| $^{241}\text{Am}$ | 432.7                           | 0.640        | 81.3 M                     | 1              | $\text{AmO}_2$ | 0.73                   |
|                   |                                 | 0.598        | 75.9 M                     | 2              |                | 0.68                   |
|                   |                                 | 0.559        | 70.9 M                     | 3              |                | 0.64                   |
|                   |                                 | 0.464        | 58.9 M                     | 6              |                | 0.53                   |

Because of the huge  $\alpha$  activity, a different approach was necessary in order to extract (n,f) cross section of  $^{241}\text{Am}$ . In the following paragraphs the attempt to lead the usual analysis is described, bringing to light the impossibility of obtaining reliable results without an unwanted normalization. The new approach is therefore described soon after.

### 6.5.1 Pulse shape analysis

Since the  $\alpha$  activity of the considered samples of  $^{241}\text{Am}$  is higher than for previous isotopes, in order to visually discriminate between FFs and  $^4\text{He}$  nuclei, as for  $^{243}\text{Am}$ , only signals with amplitude higher than 35 channels are plotted. Otherwise the  $\alpha$  background would be so huge that the tail of the  $\alpha$  particles strongly affects the FFs one.

Three electrodes were considered, the fourth presenting instability problems. In Fig. 79 the minimum between the peaks of  $\alpha$  and FF distributions falls at different channels for different electronic chains (see Table 20) :

Table 20: CHANNEL DISCRIMINATING BETWEEN FFs AND  $\alpha$  PARTICLES.

| Electrode | 1  | 2  | 3  |
|-----------|----|----|----|
| Amplitude | 58 | 54 | 57 |

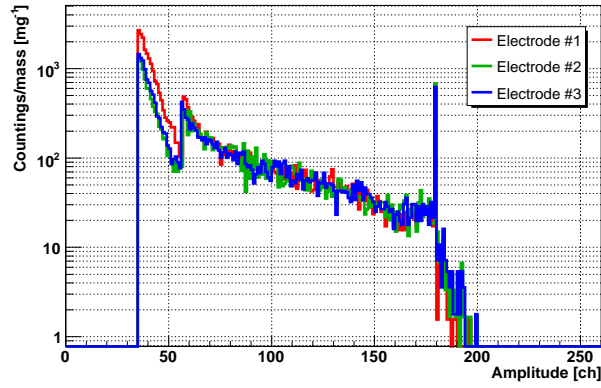


Figure 79: EXPERIMENTAL AMPLITUDE DISTRIBUTION READ BY THE THREE ELECTRODES OF  $^{241}\text{Am}$  SEPARATED AND NORMALIZED FOR THE VALUE OF THE MASS SAMPLE.

As a matter of fact, in reality, the thresholds discriminating between  $^4\text{He}$  nuclei and FFs are higher than those reported in Table 20. Differently from what happened for  $^{243}\text{Am}$ , the activity of each  $^{241}\text{Am}$  sample is so high, that a long tail prolong far behind the minimum between the peaks of  $\alpha$  and fission fragments distributions. As for now this fact is neglected, but will be considered while extracting  $\sigma_{n,f}$  for  $^{241}\text{Am}$  samples.

As for all other isotopes, a threshold on the value  $q/a$  in order to discriminate between virtual and real signals was looked for. Fig. 80, Fig. 81 and Fig. 82 report data for the three electrodes separately. In Fig. 81, points seem to cluster around two different lines ( $q/a = 16$  and  $q/a = 13$ ). For the moment this observation was not considered.

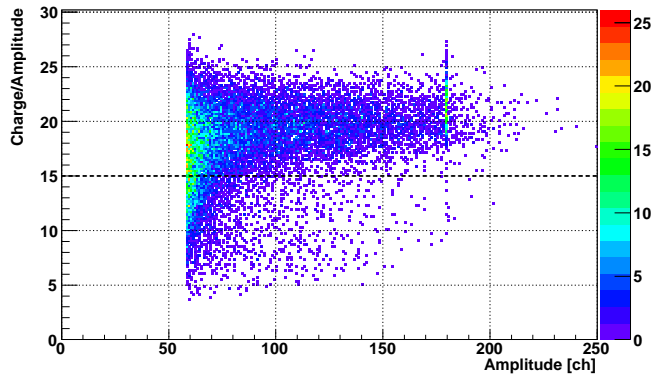


Figure 80: EXPERIMENTAL DISTRIBUTION OF THE CHARGE TO AMPLITUDE RATIO VERSUS AMPLITUDE FOR ELECTRODE # 1 OF THE ISOTOPE  $^{241}\text{Am}$ . ONLY AMP  $\geq 58$  WERE CONSIDERED. EVENTS BELOW THE DOTTED LINE CORRESPONDS TO VIRTUAL SIGNALS.

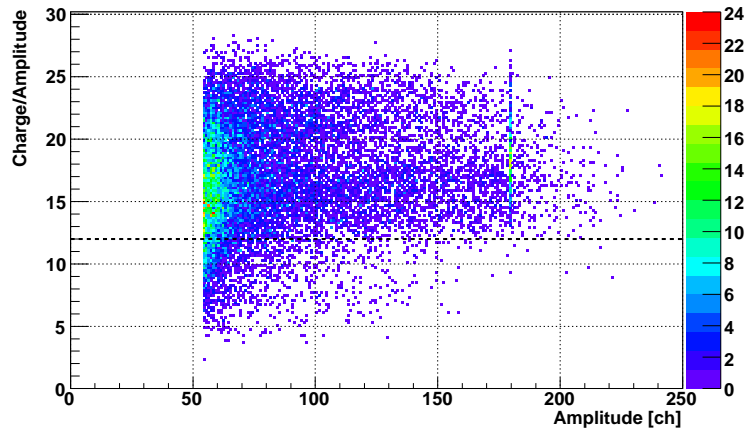


Figure 81: EXPERIMENTAL DISTRIBUTION OF THE CHARGE TO AMPLITUDE RATIO VERSUS AMPLITUDE FOR ELECTRODE # 2 OF THE ISOTOPE  $^{241}\text{Am}$ . ONLY AMP  $\geq 58$  WERE CONSIDERED. EVENTS BELOW THE DOTTED LINE CORRESPONDS TO VIRTUAL SIGNALS.

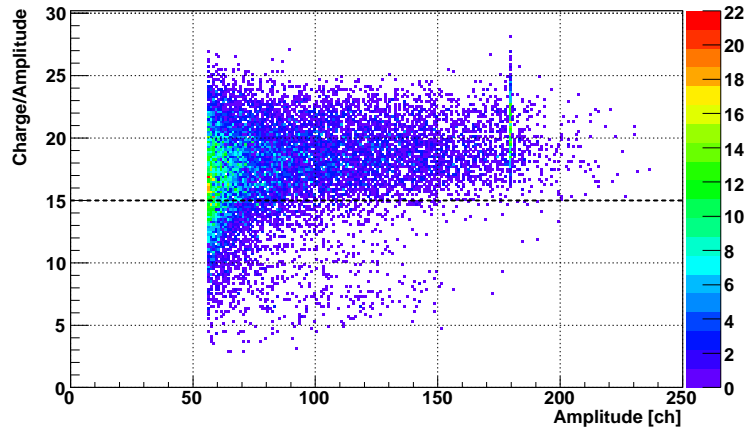


Figure 82: EXPERIMENTAL DISTRIBUTION OF THE CHARGE TO AMPLITUDE RATIO VERSUS AMPLITUDE FOR ELECTRODE # 3 OF THE ISOTOPE  $^{241}\text{Am}$ . ONLY AMP  $\geq 58$  WERE CONSIDERED. EVENTS BELOW THE DOTTED LINE CORRESPONDS TO VIRTUAL SIGNALS.

Summarizing, from pulse shape analysis, the following conditions are derived:

$$Electrode \#1 = \begin{cases} amplitude \geq 58 & ch \\ \frac{charge}{amplitude} > 15.0 \end{cases}$$

$$Electrode \#2 = \begin{cases} amplitude \geq 54 & ch \\ \frac{charge}{amplitude} > 12.0 \end{cases}$$

$$Electrode \#3 = \begin{cases} amplitude \geq 57 & ch \\ \frac{charge}{amplitude} > 15.0 \end{cases}$$

These conditions lead to the impossibility of determining the thickness correction factor, since they make unfeasible performing a calibration of the amplitude distributions based on the distribution of the energy deposited inside the  $ArCF_4$  by FFs. Cutting amplitudes lower than more than 50 channels means cutting the main reference point (i.e. the peak) necessary for calibration. Fig. 83 shows the amplitude distribution of signals read by electrode # 1. As visible the left side of the histogram is missing. As far as know, the rising of the amplitude distribution could culminate at a channel different from the one where the peak seems to be placed, because the peak is cut.

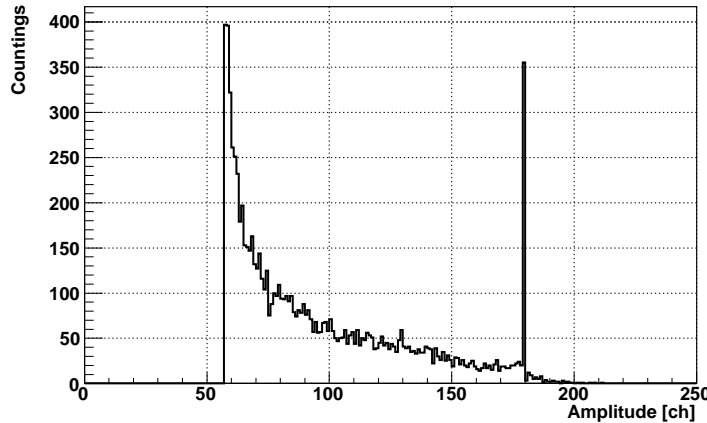


Figure 83: EXPERIMENTAL AMPLITUDE DISTRIBUTION OF SIGNALS READ BY ELECTRODE # 1. CONDITIONS DERIVED FROM PULSE SHAPE ANALYSIS HAVE BEEN APPLIED.

The usual analysis can be performed with respect to a reference point at low energy (in the RRR - resolved resonance region - regime). However the correction for efficiency due to the sample thickness can not be considered with high accuracy. In order to avoid, when possible, normalization, a new approach was chosen.

## 6.5.2 Preliminary considerations

In order to proceed to (n,f) cross section extraction, some preliminary observations and considerations have to be mentioned [85].

### 6.5.2.1 Basic assumption

The basic assumption is that extracting neutron induced fission cross sections by using all available "cleaned" data or by using only a portion of them, opportunely chosen, both for  $^{235}\text{U}$  and for the investigated isotope, should play no difference in results.

### 6.5.2.2 Observations

1. The distribution of the ratio  $\frac{\text{charge}}{\text{amplitude}}$  as a function of the amplitude of a signal, is bent at low amplitudes. This happens for all isotopes. In Fig. 84 and Fig. 85, as in all plots from here on, the amplitude runs up to a maximum of 160 - 170 channels, because at channel 180 the saturation peak is present.

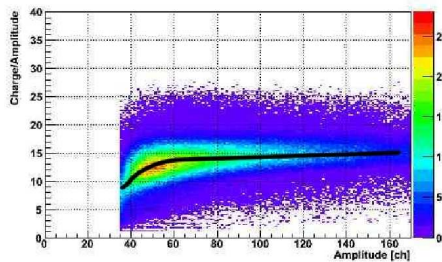


Figure 84: EXPERIMENTAL DISTRIBUTION OF THE CHARGE TO AMPLITUDE RATIO VERSUS AMPLITUDE FOR  $^{233}\text{U}$  SIGNALS COLLECTED BY ELECTRODE NUMBER 13.

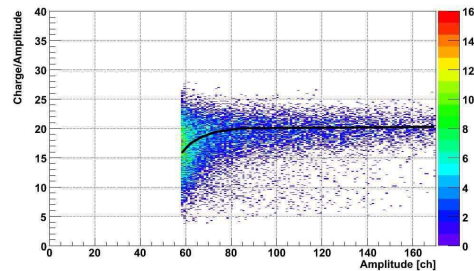


Figure 85: EXPERIMENTAL DISTRIBUTION OF THE CHARGE TO AMPLITUDE RATIO VERSUS AMPLITUDE FOR  $^{241}\text{Am}$  SIGNALS COLLECTED BY ELECTRODE NUMBER 1.

These diagrams include all the available statistics (but  $\alpha$ 's) for the considered isotopes, with no distinction between real and virtual signals. By the way, looking at Fig. 84 and Fig. 85, it seems that virtual signals appear mainly at low

amplitudes. Since there's no reason why they should occur preferentially in a region of the diagrams instead than all along the whole plots, we may infer that the behaviour is not physical, but artificial.

2. A linear relation is visible between amplitude and charge of signal for all isotopes (see Fig. 86 and Fig. 87 )

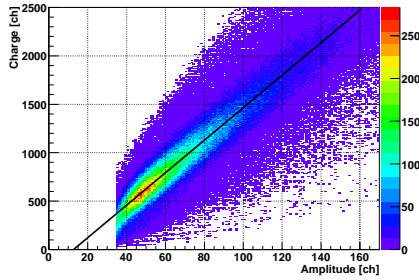


Figure 86: EXPERIMENTAL DISTRIBUTION OF THE CHARGE TO AMPLITUDE RATIO VERSUS AMPLITUDE FOR  $^{233}\text{U}$  SIGNALS COLLECTED BY ELECTRODE NUMBER 13.

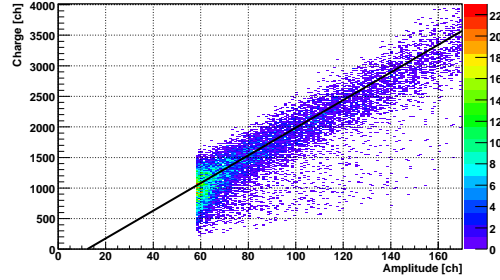


Figure 87: EXPERIMENTAL DISTRIBUTION OF THE CHARGE TO AMPLITUDE RATIO VERSUS AMPLITUDE FOR  $^{241}\text{Am}$  SIGNALS COLLECTED BY ELECTRODE NUMBER 1.

In both plots, the "interpolation line" is not in the form  $y = mx$ , but  $y = mx + q$ . An offset is therefore present. It is introduced in the analysis routines and its value is always about 12 - 13 ch. Of course, if both the charge and the amplitude are high enough, the influence of a tenth of channels offset results negligible and this explains why the bending put in evidence in Fig. 84 and Fig. 85 is visible only in the low amplitude signals <sup>28</sup>.

From the observation of a linear relation between the amplitude and charge of real signals, it follows that, in order to derive the thickness correction to apply to different isotopes, the calibration of the histogram reporting the energy deposited in the gas by FFs can be indifferently performed on the charge or amplitude distributions. Results are indeed the same, but the former option gives the advantage of better resolution: while amplitudes extend on 256 channels, charges run up to more than 6000 ch.

From the observed equivalence between charge and amplitude of real signals, it moreover follows that for each threshold condition or cut imposed in ampli-

<sup>28</sup>In Fig. 84 the average  $q/a$  value is about 15. For signals with an amplitude equal to 35, this corresponds to  $q = a \cdot 15 = 35 \cdot 15 = 525$ . In this case an offset of 12 channels leads to  $q / (a - \text{offset}) = 525 / (35 - 12) = 22.8$ . The discrepancy with the average value is therefore  $(22.8 - 15)/15 = 52\%$ .

For signals with an amplitude equal to 150 instead an average  $q/a$  value equal to 15 corresponds to  $q = a \cdot 15 = 100 \cdot 15 = 2250$ . In this case an offset of 12 channels leads to  $q / (a - \text{offset}) = 2250 / (150 - 12) = 16.3$ . The discrepancy with the average value is therefore  $(16.3 - 15)/15 = 8.6\%$ .

tude, a corresponding threshold condition or cut to set in charge must exist. Fig. 88 shows, as an example, the equivalence between charge and amplitude cut conditions.

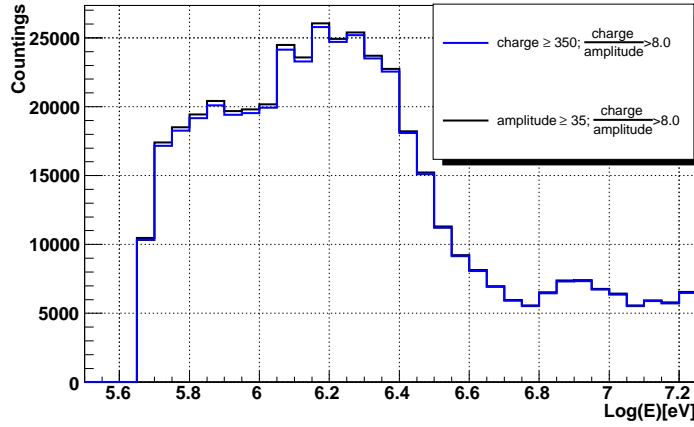


Figure 88: EXPERIMENTAL DISTRIBUTION OF DETECTED FISSION EVENTS AS A FUNCTION OF THE NEUTRON ENERGY. AS SHOWN PULSE SHAPE ANALYSIS CAN BE PERFORMED ON CHARGE OR AMPLITUDE DISTRIBUTION EQUIVALENTLY.

The conditions derived from pulse shape analysis of  $^{235}\text{U}$ , that is:

$$\begin{cases} \text{amplitude} \geq 35 & ch \\ \frac{\text{charge}}{\text{amplitude}} > 8.0 \end{cases}$$

are equivalent to:

$$\begin{cases} \text{charge} \geq 351 & ch \\ \frac{\text{charge}}{\text{amplitude}} > 8.0 \end{cases}$$

3. The distribution of the ratio  $\frac{\text{charge}}{\text{amplitude}-\text{offset}}$  (i.e. the distribution of the ratio  $\frac{\text{charge}}{\text{amplitude}}$  corrected for the the offset) as a function of the amplitude of a signal, shows a Gaussian shape, visible in Fig. 89 and Fig. 90.

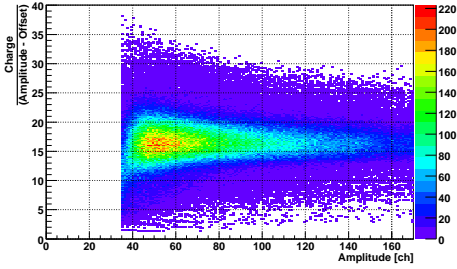


Figure 89: EXPERIMENTAL DISTRIBUTION OF THE CHARGE TO AMPLITUDE RATIO CORRECTED FOR THE OFFSET VALUE VERSUS AMPLITUDE FOR  $^{233}\text{U}$  SIGNALS COLLECTED BY ELECTRODE NUMBER 13.

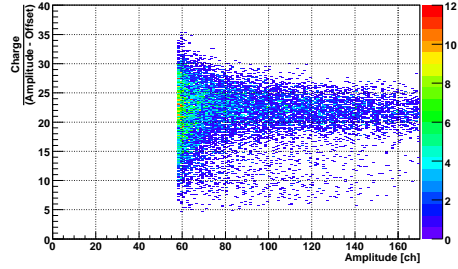


Figure 90: EXPERIMENTAL DISTRIBUTION OF THE CHARGE TO AMPLITUDE RATIO CORRECTED FOR THE OFFSET VALUE VERSUS AMPLITUDE FOR  $^{241}\text{Am}$  SIGNALS COLLECTED BY ELECTRODE NUMBER 1.

Virtual signals at low value of the ratio  $\text{Charge}/(\text{Amplitude} - \text{Offset})$  are still visible, but they're distributed along all amplitude range proportionally to the density of detected signals in each subrange region.

At the light of what just found out, the basic assumption can be translated in other words: extracting neutron induced fission cross sections by using all "cleaned" data or by using only  $x$  sigmas of the Gaussian distributions obtained, both for  $^{235}\text{U}$  and for the investigated isotope, should play no difference.

4. All Gaussians have different centroids (i.e.  $\frac{\text{Charge}}{(\text{Amplitude}-\text{Offset})}$ ) and width (therefore  $\sigma$  or r.m.s.).

Looking at the distributions of the energy deposited by fission fragments in the cell gas for different samples, it is evident that, at least up to 40 MeV (which is almost the limit used in calibration), they can be superimposed by stretching, i.e. by a relation  $E_{dist1} = m E_{dist2}$ , where  $E_{dist1}$  is the energy distribution of one isotope, and  $E_{dist2}$  the energy distribution of the second one. This is possible because shapes are similar.

The expression describing the specific energy loss, known as Bethe formula, is written [84] [Kno79]:

$$-\frac{dE}{dx} = \frac{4\pi e^4 z^2}{m_0 v^2} \cdot N \cdot Z \cdot B \quad (23)$$

where:

$$B = \left[ \ln \frac{2 m_0 v^2}{I} - \ln \left( 1 - \frac{v^2}{c^2} \right) - \frac{v^2}{c^2} \right]$$

with  $v$  and  $ze$  velocity and charge of the primary particle (i.e. fission fragment),  $N$  and  $Z$  number density and atomic number of the absorber,  $m_0$  electron rest mass,  $e$  electronic charge and  $I$  average excitation and ionization potential.

For non relativistic charged particles, only the first term in B is significative <sup>29</sup>. Therefore eq. 23 can be written:

$$-\frac{dE}{dx} = \frac{4 \pi e^4 z^2}{m_0 v^2} \cdot N \cdot Z \cdot \left[ \ln \frac{2 m_0 v^2}{I} \right] \quad (24)$$

Both the atomic mass and charge distribution of FFs are peaked around 2 values. Since all isotopes housed inside the FIC detector have similar atomic masses (ranging from 233 amu to 245 amu) and charge numbers (spanning from 92 to 96), in the same conditions the distribution should superimpose within 5% confidence level.

But of course conditions are not the same and, what plays a key role on the shape of the energy deposited by FFs inside the gas, is the thickness ( $\Delta x$ ) of the deposit. When  $\Delta x$  is thin ( $\sim 10^{-7}$  cm), FFs leave the target after losing a little portion of their energy and a second hump is visible. On the contrary, when the thickness of the sample is  $\sim 10^{-5}$  cm, fragments can deposit little or huge amounts of energy inside the actinide before reaching the gas, and the shape of the energy released inside  $\text{ArCF}_4$  results smooth. Since the second hump, if present, appears around 40 MeV, up to this energy distributions are really similar and can be superimposed.

The charge distribution of the detected signals due to (n,f) events resembles the distribution of the energy deposited inside the gas cell by FFs, therefore what just said holds for the experimental histograms as well. Unfortunately, because the electronic chains of the 16 FIC electrodes behave differently (different offsets and energy resolutions), it is not possible deriving the multiplication factor from the simulated distribution of the energy deposition and applying that to the histograms of signal amplitudes. And it is not feasible neither extracting the stretching factor by superimposing the amplitude distributions, since for  $^{241}\text{Am}$  the reference peak is not accessible.

What is instead possible is superimposing the Gaussians. The resulting multiplication factor is then applied to derive  $^{241}\text{Am}$  thickness correction as a function of the calibration obtained for another isotope, i.e. the reference  $^{235}\text{U}$  (see § 6.5.5).

This method was first applied to  $^{233}\text{U}$  to check its validity and then employed to extract neutron induced fission cross sections of  $^{241}\text{Am}$ . Since  $\sigma_{(n,f)}$  are obtained with reference to  $^{235}\text{U}$ , this isotope and the investigated one ( $^{241}\text{Am}$ ) are treated in parallel in the following pages.

---

<sup>29</sup> As a practical matter a particle is considered relativistic when its kinetic energy is greater than 2% of its rest-mass energy [Bar01]. The lighter FFs have atomic mass around 90 a.m.u (Fig. 28), i.e. 83.8 GeV. In order to be considered relativistic, FFs should have a kinetic energy  $K \geq 0.02 \cdot 83.8$  GeV, which means  $K \geq 1.6$  GeV. But from it results that the lightest (and fastest) FFs are emitted with kinetic energies around 110 MeV (Fig. 29).

### 6.5.3 Offset selection

#### 6.5.3.1 $^{235}\text{U}$

Fig. 91 shows the linear relation between the charge and amplitude of signals for the  $^{235}\text{U}$  sample. All the available statistics for FFs (amplitude  $\geq 35$  ch) is reported. No other condition is imposed. **The offset was found to be 13 channels.**

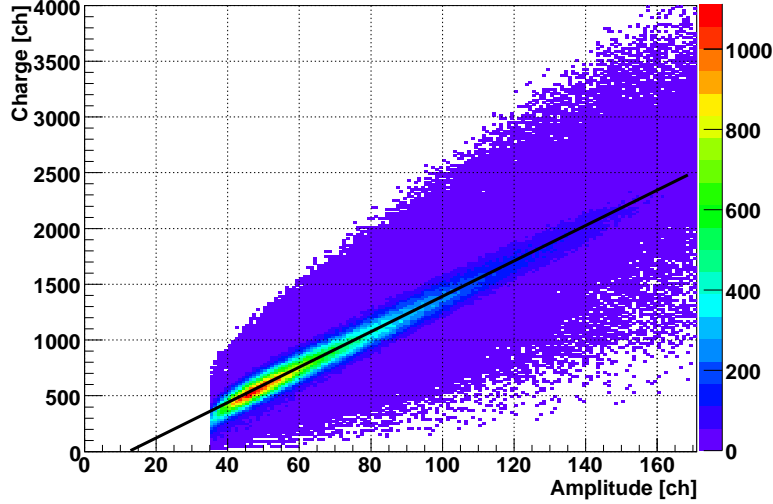


Figure 91: EXPERIMENTAL CHARGE DISTRIBUTION OF SIGNALS VERSUS THEIR AMPLITUDES FOR  $^{235}\text{U}$  SAMPLE. A LINEAR RELATION IS VISIBLE.

Fig. 92 and Fig. 93 report the distribution of the charge to amplitude versus amplitude ratio before and after applying the offset correction.

#### 6.5.3.2 $^{241}\text{Am}$

As previously noted (§ 6.5.1), the  $\alpha$  activity of  $^{241}\text{Am}$  samples is so high to cause considerable  $\alpha$  pile-up. Thresholds reported in Table 20 therefore still allow appreciable background. A linear fit of the peak due both to  $\alpha$  particles and fission fragments for electrode number 1 is shown in Fig 94.

As a compromise between background reduction and statistics, it was decided to put amplitude thresholds discriminating between  $^4\text{He}$  nuclei and FFs at channel # 70, where the linear fit takes a value  $\leq 1\%$  with respect to the corresponding height of the amplitude spectrum. Table 21 reports the new considered thresholds:

Table 21: AMPLITUDES CHOSEN AS THRESHOLD DISCRIMINATING BETWEEN FFs AND  $^4\text{He}$  NUCLEI AFTER  $\alpha$  PILE-UP CONSIDERATION.

| Electrode | 1  | 2  | 3  |
|-----------|----|----|----|
| Amp.      | 70 | 70 | 69 |

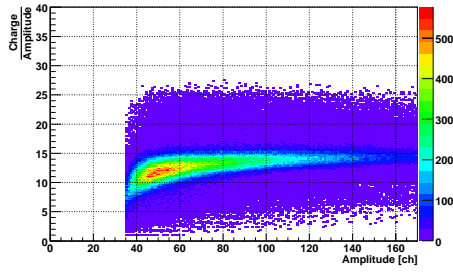


Figure 92: EXPERIMENTAL DISTRIBUTION OF THE CHARGE TO AMPLITUDE RATIO VERSUS AMPLITUDE FOR  $^{235}\text{U}$ . A DISTORSION AT LOW AMPLITUDES IS VISIBLE.

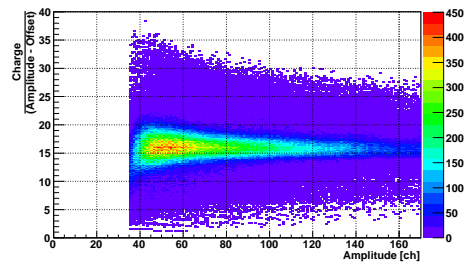


Figure 93: EXPERIMENTAL DISTRIBUTION OF THE CHARGE TO AMPLITUDE RATIO CORRECTED FOR THE OFFSET VALUE VERSUS AMPLITUDE FOR  $^{235}\text{U}$ .

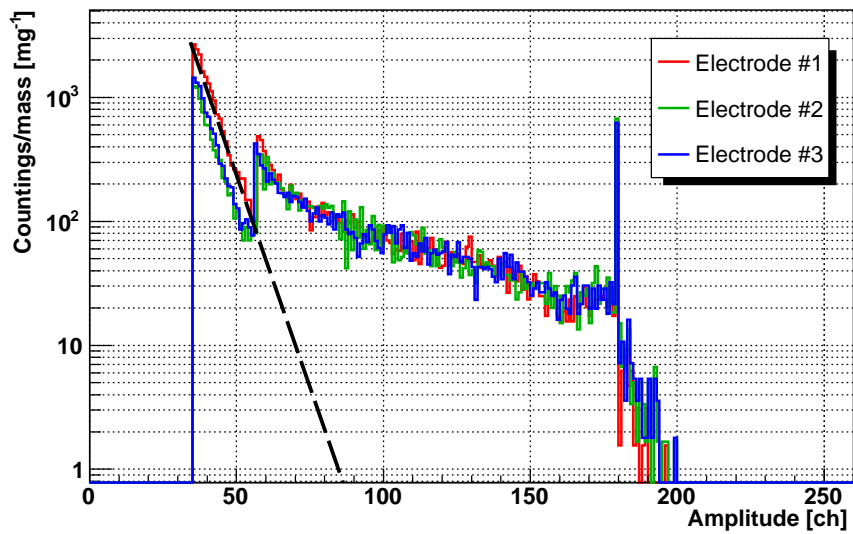


Figure 94: LINEAR FIT OF THE PEAK OF THE AMPLITUDE DISTRIBUTION DUE TO FFs AND  $\alpha$  PARTICLES.

### 6.5.3.2.1 Electrode #1

Fig. 95 shows the linear relation between the charge and amplitude of signals collected by electrode #1 for the  $^{241}\text{U}$  sample. All the available statistics for FFs (amplitude  $\geq 70$  ch) is reported. No other condition is imposed. **The offset was found to be 12 channels.**

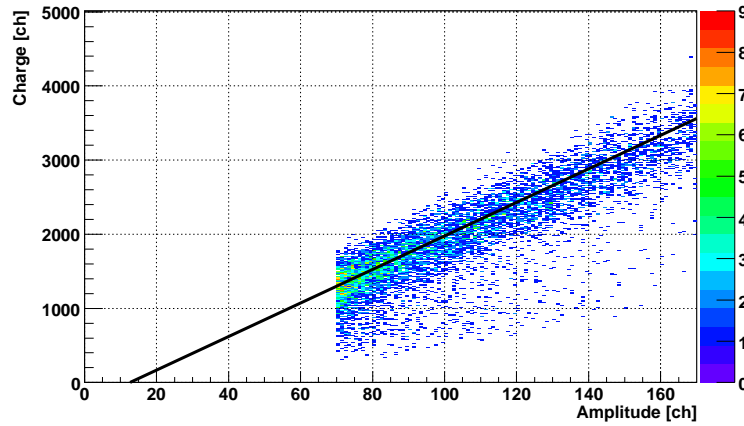


Figure 95: EXPERIMENTAL CHARGE DISTRIBUTION OF SIGNALS VERSUS THEIR AMPLITUDES. A LINEAR RELATION IS VISIBLE.

Fig. 96 and Fig. 97 report the distribution of the charge to amplitude versus amplitude ratio before and after applying the offset correction.

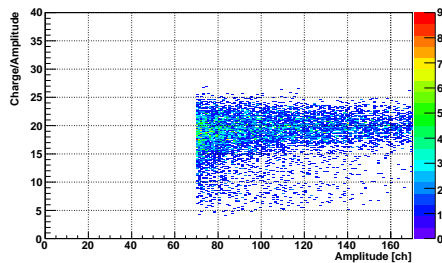


Figure 96: EXPERIMENTAL DISTRIBUTION OF THE CHARGE TO AMPLITUDE RATIO VERSUS AMPLITUDE FOR ELECTRODE #1.

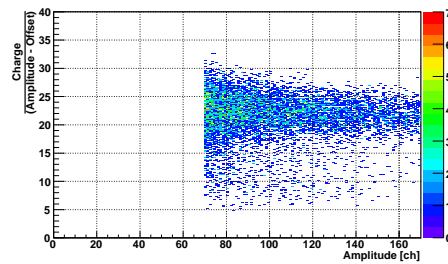


Figure 97: EXPERIMENTAL DISTRIBUTION OF THE CHARGE TO AMPLITUDE RATIO CORRECTED FOR THE OFFSET VALUE VERSUS AMPLITUDE FOR ELECTRODE #1 OF  $^{241}\text{Am}$ .

### 6.5.3.2.2 Electrode #2

Fig. 98 shows the linear relation between the charge and amplitude of signals collected by electrode #2 for the  $^{241}\text{U}$  sample. All the available statistics for FFs (amplitude  $\geq 70$  ch) is reported. No other condition is imposed.

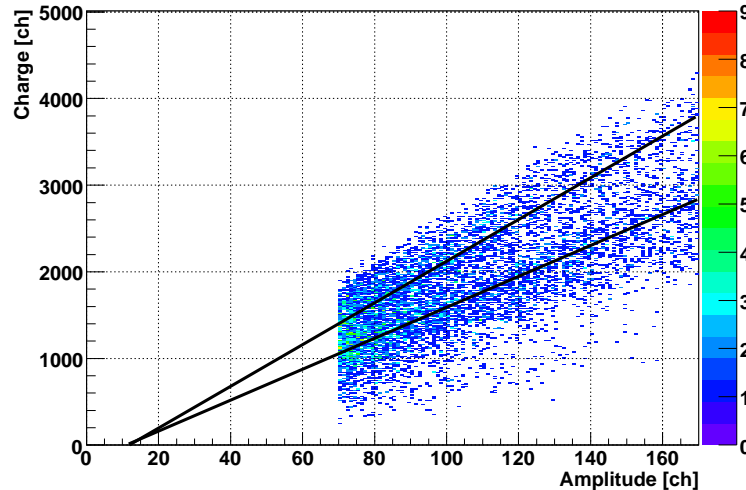


Figure 98: EXPERIMENTAL CHARGE DISTRIBUTION OF SIGNALS VERSUS THEIR AMPLITUDES. A LINEAR RELATION IS VISIBLE.

The offset was found to be 13 channels, but 2 lines are visible. Single runs were checked, in order to see if during the time the gain had changed. This was not the case, since data cluster around two different lines even in a same data acquisition (i.e. in correspondence of a single proton bunch). For this reason the electrode was considered unstable.

This problem makes present analysis not possible and data obtained through this electronic chain were discarded.

### 6.5.3.2.3 Electrode #3

Fig. 99 shows the linear relation between the charge and amplitude of signals collected by electrode #3 for the  $^{241}\text{Am}$  sample. All the available statistics for FFs (amplitude  $\geq 68$  ch) is reported. No other condition is imposed. **The offset was found to be 13 channels.**

Fig. 100 and Fig. 101 report the distribution of the charge to amplitude versus amplitude ratio before and after applying the offset correction.

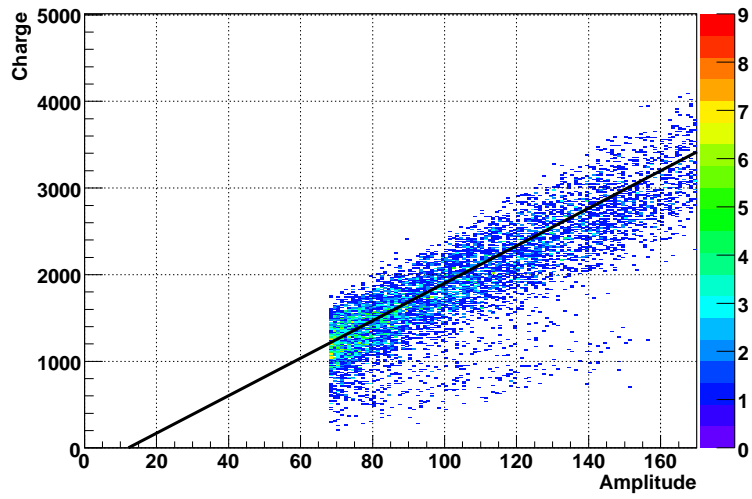


Figure 99: EXPERIMENTAL CHARGE DISTRIBUTION OF SIGNALS VERSUS THEIR AMPLITUDES. A LINEAR RELATION IS VISIBLE.

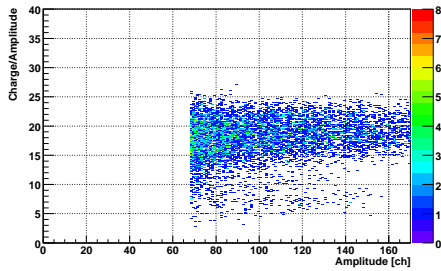


Figure 100: EXPERIMENTAL DISTRIBUTION OF THE CHARGE TO AMPLITUDE RATIO VERSUS AMPLITUDE FOR ELECTRODE # 3 OF  $^{241}\text{Am}$ .

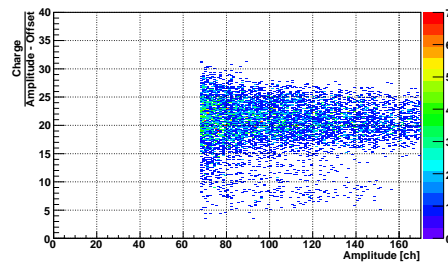


Figure 101: EXPERIMENTAL DISTRIBUTION OF THE CHARGE TO AMPLITUDE RATIO CORRECTED FOR THE OFFSET VALUE VERSUS AMPLITUDE FOR ELECTRODE # 3 OF  $^{241}\text{Am}$ .

### 6.5.4 Analysis of the charge to amplitude ratio distribution

In all plots reporting the charge to amplitude distribution of signals versus their amplitude, a Gaussian shape is visible. This is an obvious consequence of how detector and electronic chain form the output signal. The density of points reported has a maximum in correspondence of the centroid of the Gaussian. It is moreover visible that the density of plotted points is distributed as a Gaussian and therefore fitting the bidimensional histograms is equivalent to fit monodimensional histograms reporting the occurrence of a certain value of the Charge/(Amplitude - Offset) ratio.

#### 6.5.4.1 $^{235}\text{U}$

In Fig. 102 the monodimensional histogram reporting the occurrence of a certain value of the Charge/(Amplitude - Offset) ratio is shown.

From the Gaussian fit, the following values are extracted:

$$\begin{cases} \sigma = 1.65 \\ \bar{x} = 15.8 \end{cases}$$

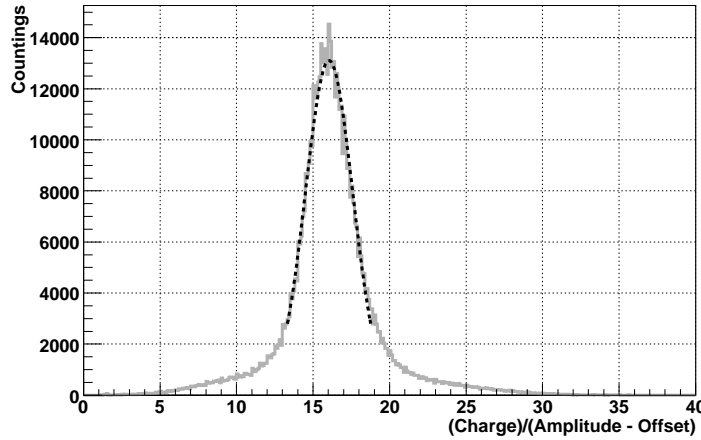


Figure 102: EXPERIMENTAL DISTRIBUTION OF CHARGE TO AMPLITUDE RATIO CORRECTED FOR THE OFFSET.

Fig. 102 was obtained by considering all the available statistics, i. e. imposing as only condition that the amplitude of signals must be higher than 35 channels. A trial performed considering only amplitudes higher than 68 ch (i.e. putting a threshold effective to cut  $\alpha$ 's contamination in the  $^{241}\text{Am}$ ) gave a similar result ( $\bar{x} = 16$ ,  $\sigma = 1.65$ ).

The ratio  $\frac{\sigma}{\bar{x}}$  gives the resolution employed to fold the simulated distribution of the energy deposited by fission fragments inside the cell gas.

### 6.5.4.2 $^{241}\text{Am}$

#### 6.5.4.2.1 Electrode # 1

From the Gaussian fit of the plot reported in Fig. 103, the following values are extracted:

$$\begin{cases} \sigma = 2.6 \\ \bar{x} = 22.2 \end{cases}$$

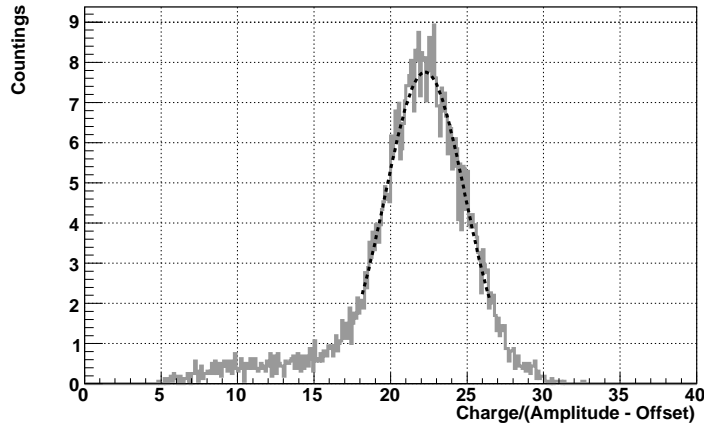


Figure 103: EXPERIMENTAL DISTRIBUTION OF CHARGE TO AMPLITUDE RATIO CORRECTED FOR THE OFFSET FOR ELECTRODE # 1 OF  $^{241}\text{Am}$ .

Fig. 103 was obtained by considering as only condition that the amplitude of signals must be higher than 70 channels. The tail at low amplitudes at the left side of the Gaussian should correspond to electronic noise (virtual signals)

#### 6.5.4.2.2 Electrode # 2

A monodimensional histograms reporting the occurrence of a certain value of the Charge/(Amplitude - Offset) ratio was built for electrode # 2, considering only signals whose amplitude is higher than 70 channels. As visible in Fig. 104, a broad distribution is visible, which makes analysis not possible.

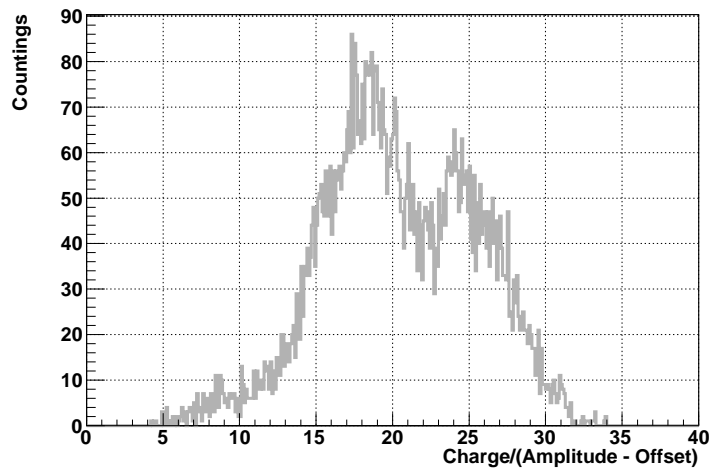


Figure 104: EXPERIMENTAL DISTRIBUTION OF CHARGE TO AMPLITUDE RATIO CORRECTED FOR THE OFFSET FOR ELECTRODE # 2 OF  $^{241}\text{Am}$ .

#### 6.5.4.2.3 Electrode # 3

From the Gaussian fit of the plot reported in Fig. 105, the following values are extracted:

$$\begin{cases} \sigma = 3.1 \\ \bar{x} = 20.99 \end{cases}$$

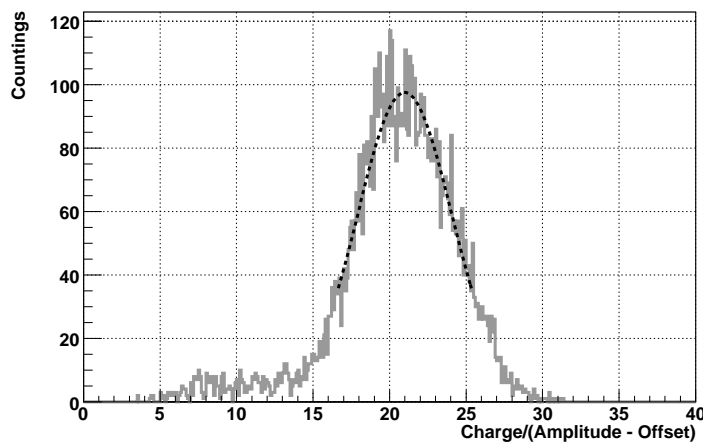


Figure 105: EXPERIMENTAL DISTRIBUTION OF CHARGE TO AMPLITUDE RATIO CORRECTED FOR THE OFFSET FOR ELECTRODE # 3 OF  $^{241}\text{Am}$ .

### 6.5.5 Overlap of Charge ditributions

It was noted [85] that by using a correct multiplicative factor, the tails of the charge distributions can be superimposed (see Fig. 106). It was inferred that calibrations of different isotopes are in the same relation as centroids. This is because, as seen in § 6.5.2.2, the Charge/(Amplitude - Offset) ratio is Gaussian distributed around a "medium" value (centroid), which changes with the considered electronic chain. In other words:

$$Q_X = centroid_X \cdot (A_X - Off_X) \quad (25)$$

with Q = Charge, A = Amplitude, Off = offset and X = electrode collecting the ionization charges generated by neutron induced fission of the isotope X. By considering eq. 25 both for  $^{235}\text{U}$  and  $^{241}\text{Am}$ , the following reltio is obtained:

$$Q_{241} = Q_{235} \cdot \frac{centroid_{241}}{centroid_{235}} \cdot \frac{(A_{241} - Off_{241})}{(A_{235} - Off_{235})} \quad (26)$$

The experimental Charge distribution for the  $^{235}\text{U}$  isotope ( $Q_{235}$ ) is known, since for this sample there are no  $\alpha$  background problems. From the previous analysis  $centroid_{241}$  and  $centroid_{235}$  were extracted. What is still unknown, looking at the right side of eq. 26, is  $A_{241}$ . By the way, because of the poor resolution of the Amplitude distributions, the ratio  $\frac{(A_{241} - Off_{241})}{(A_{235} - Off_{235})}$  should not differ from 1 for more than a small percentage <sup>30</sup>. Therefore this factor can be negleted in a first approximation.

This is the relation we were looking for, since it allows to perform calibration.

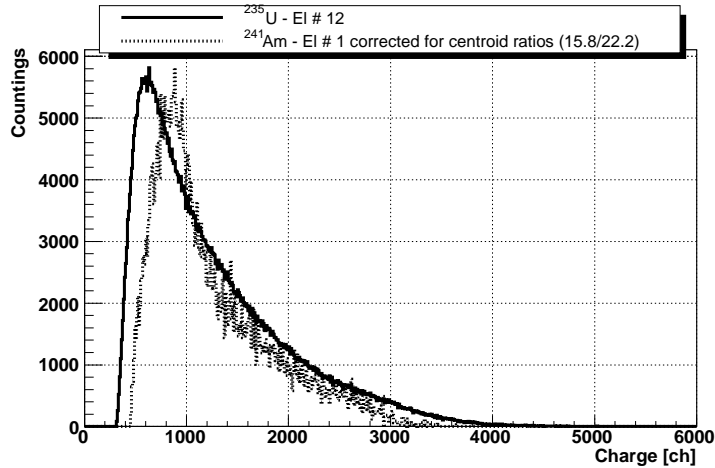


Figure 106: EXPERIMENTAL DISTRIBUTION OF CHARGE FOR  $^{235}\text{U}$  AND FOR ELECTRODE # 1 OF  $^{241}\text{Am}$ . THIS LAST WAS CORRECTED FOR THE RATIO OF THE GAUSSIAN CENTROIDS. TAILS OVERLAP.

<sup>30</sup>estimated in the discussion of results.

## 6.5.6 Signal selection

### 6.5.6.1 $^{241}\text{Am}$

#### 6.5.6.1.1 Electrode # 1

As previously seen, in order to discriminate FFs by  $^4\text{He}$  nuclei and  $\alpha$  pile-up a threshold of 1400 ch on the signal-charge (i.e. amplitude  $\geq 70$  ch) was set. Virtual signals were discarded through a  $\frac{q}{a}$  ratio higher than 11.

#### 6.5.6.1.2 Electrode # 3

In order to discriminate FFs by  $^4\text{He}$  nuclei and  $\alpha$  pile-up a threshold of 1270 ch on the signal-charge (i.e. amplitude  $\geq 69$  ch) was set. Virtual signals were discarded through a  $\frac{q}{a}$  ratio higher than 11.

### 6.5.6.2 $^{235}\text{U}$

In principle data selection of this isotope could have been chosen equal to the one considered for previous analysis in order to increase the statistics. By the way, while performing various checks, it was realized that at an amplitude of 35 ch  $^{235}\text{U}$  in reality still presents little  $\alpha$  background. This does not affect  $^{233}\text{U}$  results, since the employed thresholds were the same and effects partially cancel (actually  $^{233}\text{U}$   $\sigma_{(n,f)}$  could be 0.5% lower), nor the extracted  $^{243}\text{Am}$  (n,f) cross sections (where the little higher threshold imposed on the investigated isotope and the different behaviour of N-odd and N-even samples compensate for the  $^{235}\text{U}$  background).

By the way, the difference in amplitude threshold between  $^{241}\text{Am}$  (70 ch) and  $^{241}\text{Am}$  (35 ch) would be so high (200%) to affect results. Therefore it was decided to consider equivalent lower limits of the amplitude (or better charge) distributions. Averaging on the 996 ch and 1270 ch derived from calculations shown in the following paragraph, a threshold of 1133 ch on the  $^{235}\text{U}$  distribution was imposed.

## 6.5.7 Calibration

The thickness correction was extracted again for  $^{235}\text{U}$  by calibrating the histogram of the energy deposited by FFs inside the cell gas on the charge distribution. Results are the same as before, but the resolution is better (see Fig. 107).

For the correspondence set before, a cut at  $q = 1400$  ch for electrode # 1 of  $^{241}\text{Am}$  is equal to a cut at  $q \approx 1400 * (\text{centroid}_{235})/(\text{centroid}_{241}) = 1400 * 15.8/22.2 = 996$  ch. According to  $^{235}\text{U}$  calibration, this is 33.5 MeV, which is translated into  $33.5 \text{ MeV} * (\text{centroid}_{241})/(\text{centroid}_{235}) = 47.1 \text{ MeV}$  for  $^{241}\text{Am}$  and therefore an

efficiency equal to 45.5%.

Through the same "mathematics", a cut in charge of 1270 ch is translated into 50.7 % efficiency for electrode #3.

As mentioned before,  $^{235}\text{U}$  was cut at a threshold equivalent to the one used for  $^{241}\text{Am}$ . A cut at charge  $q = 1133$  ch for  $^{235}\text{U}$  is equivalent to a cut at energy 36.6. FFs depositing in the gas an energy higher than this value are 45.3% of the total

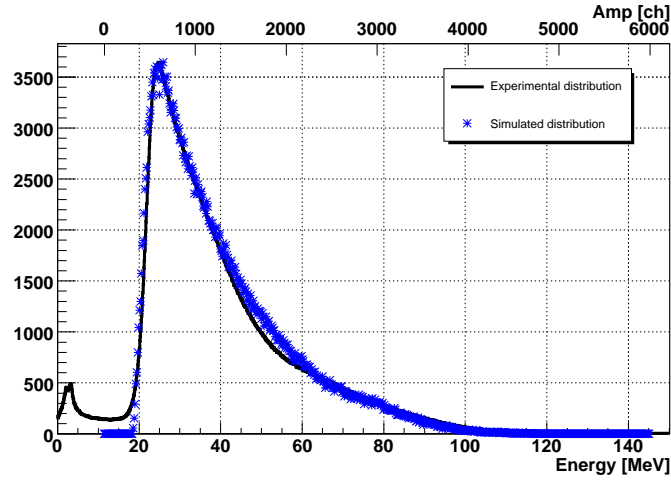


Figure 107: SIMULATED ENERGY DEPOSITION (10% ENERGY RESOLUTION IS APPLIED) CALIBRATED ON THE EXPERIMENTAL HISTOGRAM OF AMPLITUDES FOR  $^{235}\text{U}$ .

### 6.5.8 Cross section extraction

Fig. 108 reports the comparison among results obtained imposing the previously listed conditions (§ 6.5.6), and considering all signals satisfying them:

1. only data within  $(\text{centroid} - 1 \text{ sigma}) \leq \frac{q}{a\text{-offset}} \leq (\text{centroid} + 1 \text{ sigma})$
2.  $(\text{centroid} - 2 \text{ sigma}) \leq \frac{q}{a\text{-offset}} \leq (\text{centroid} + 2 \text{ sigma})$
3. no additional condition applied

The small discrepancies in Fig. 108 are due to the difficulty of exactly defined the centroid and r.m.s. of Gaussians. By the way, **results are in agreement, validating the hypothesis that selecting opportunely chosen portions of the recorded fission events or all of them, makes no difference.**

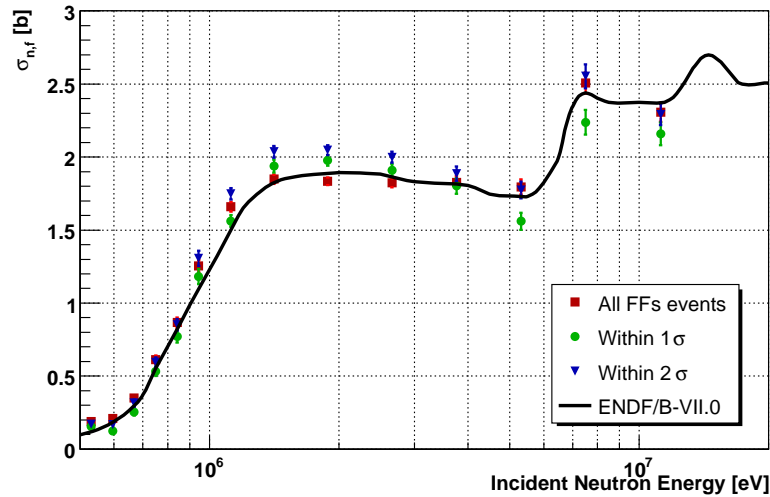


Figure 108: COMPARISON AMONG  $^{241}\text{Am}$   $\sigma_{(n,f)}$  EXTRACTED BY SELECTING DIFFERENT PORTIONS OF ALL AVAILABLE DATA.

### 6.5.9 Results

$^{241}\text{Am}$   $\sigma_{(n,f)}$  were extracted considering 20 bins/decade as always. Because of the low statistics available it was decided to show here results obtained with variable binning.

Moreover, the developed method is based on normalization of one distribution with respect to another. Since the shapes of the energy distributions are slightly different, the calibration extracted is affected by an uncertainty which is different for different charge-thresholds imposed. The maximum uncertainty for the conditions imposed in this analysis was estimated to be 13%.

The upper panel of Fig. 109 shows a comparison between experimental  $^{241}\text{Am}$  (n,f) cross sections obtained at the n\_TOF facility and the ENDF/B-VII.0 evaluations, released in December 2006. A good agreement is visible on the whole considered energy range.

In order to quantify the discrepancy between our experimental data and the referred library, in the lower panel of Fig. 109 the percentage difference between n\_TOF results and the ENDF/B-VII.0 cross sections is plotted. For energies higher than 1.2 MeV discrepancies never exceed 5%, and between 0.6 MeV and 1.2 MeV they remain below 13%, which is the estimated uncertainty linked to the employed method. Below 0.6 MeV, the discrepancy with ENDF/B-VII.0 reaches even 43%. Before drawing fast conclusions, it must be remembered that  $^{241}\text{Am}$ , as  $^{243}\text{Am}$ , fissions at high energy and therefore (n,f) cross section - both n\_TOF and evaluated - is about 0 at low energies. By performing the ratio of one almost null value to another almost null value, it is really easy obtaining a huge number as a result.

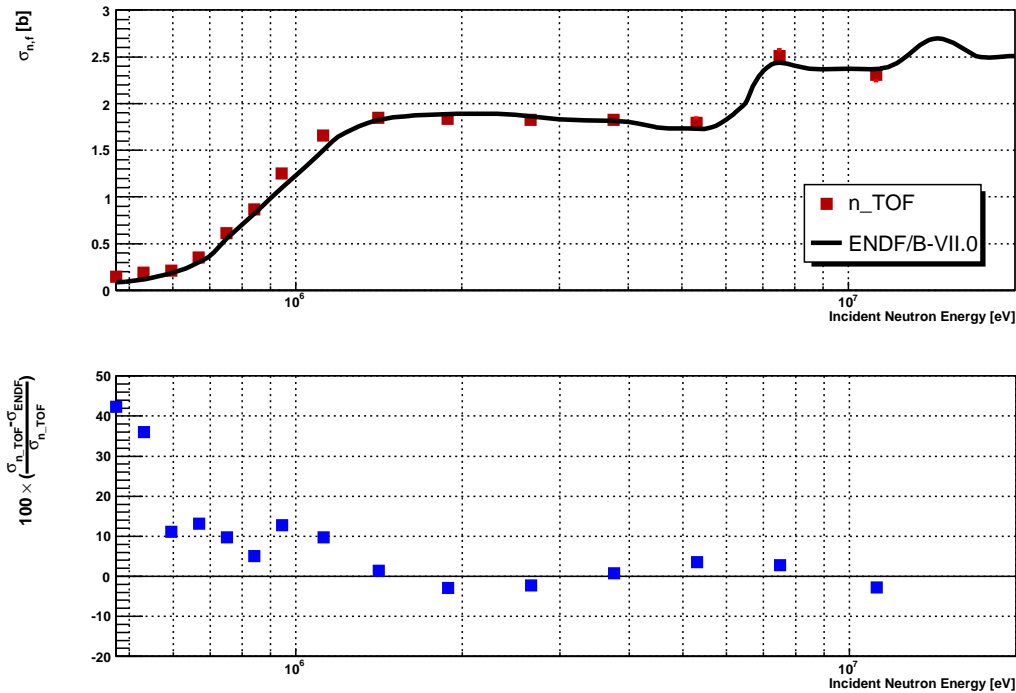


Figure 109: COMPARISON BETWEEN n\_TOF (VARIABLE BINNING) AND ENDFB-VII.0  $\sigma_{(n,f)}$ .

For a better cross check, a comparison between n\_TOF experimental results and other evaluations was considered. In Fig. 110, as already underlined, the agreement between n\_TOF and ENDF/B-VII.0  $\sigma_{(n,f)}$  looks good (i.e. within the estimated 13% uncertainty) in the whole energy range (but around 0.5 MeV). Above 8 MeV ENDF/B-VI.8 shows cross sections about 8% higher than ENDF/B-VII.0, and therefore the discrepancy with our results is worst. Nevertheless, since the rising of the ENDF/B-VI.8  $^{241}\text{Am}$   $\sigma_{(n,f)}$  between 6 and 8 MeV has a greater slope than the rising of ENDF/B-VII.0, our datum at about 7 MeV agrees within 4% with both evaluations. The difference between the two ENDF evaluations for energies higher than 8 MeV lays in the employed codes [86]. JEFF-3.1 follows ENDF/B-VII.0, but again its rising between 6 and 8 MeV has a greater slope than the rising of ENDF/B-VII.0. Our datum at about 7 MeV agrees with both. n\_TOF experimental  $^{241}\text{Am}$  (n,f) cross sections follow CENDL-2 up to 1.5 MeV. For higher energies the evaluation is sometimes about 6-8% higher than ENDF/B-VII.0 and sometimes superimpose with our results. Discrepancy with n\_TOF data varies from about 0% around 3 MeV to 12% around 10 MeV.

In Fig. 111 a comparison of the extracted  $^{241}\text{Am}$   $\sigma_{(n,f)}$  with other evaluations is reported. The agreement with ROSFOND is really good ( $< 1\%$ ) up to 1 MeV and

in the energy region 2 MeV - 12 MeV, while from 1 MeV to 2 MeV the discrepancy is always around 6% ÷ 7%. From 0.5 MeV up to 2 MeV JENDL-3.3, JENDL/AC-2008 and BROND-2.2 are about 1%-2% higher than ROSFOND, and therefore the agreement with our data is really good. For energies higher than 10 MeV the 3 evaluations show different shapes, but because of the low statistics the number of reported n\_TOF data is too little to confirm or deny one of the 3 trends.

Fig. 112 shows the comparison between n\_TOF and some experimental results. Cross section ratios are reported. Our results follow the same trend as Behren's *et al.* [87], but the absolute value is quite different, reaching more than 11% discrepancy around 5 MeV and more than 16% discrepancy around 10 MeV. Knitter *et al.* [88] is compatible with n\_TOF cross sections up to 2 MeV, but the last reported 2.5 MeV datum is about 12% higher than ours. Before 1 MeV Fomushkin *et al.* [89] a little lower (3%) than data extracted in the present work, but above 1 MeV the discrepancy with n\_TOF data reaches about 15%.

In Fig. 113 cross sections, and not cross section ratios, are reported. The only  $^{241}\text{Am}\sigma_{(n,f)}$  available extending to more than 8 MeV are Dabbs *et al.* [90]. The agreement of the extracted n\_TOF cross sections with Dabbs *et al.* [90] is very good ( $\leq 3\%$ ) on the whole energy range where data exist (0.5 MeV ÷ 11 MeV). The agreement with Shpak *et al.* [91] is a little worst ( $\leq 4\%$ ). For Cance *et al.* [92] only 2 data are available: the low energy one (between 0.9 and 1 MeV) confirms Nobles *et al.* [93], which is about 30% lower than our data, while the high energy one (about 1.5 MeV) overlaps to n\_TOF cross sections. As visible from Fig. 113, Nobles *et al.* [93]  $^{241}\text{Am}\sigma_{(n,f)}$  are always far lower than other experimental data and therefore not reliable.

Once again, in order to quantify the agreement/disagreement between the extracted  $^{241}\text{Am}\sigma_{(n,f)}$  and reported libraries or experimental data, cross sections were integrated over the energy region of overlap of the different data sets. Table 22 shows the results. Looking at the table, uncertainties of up to 13% have to be considered.

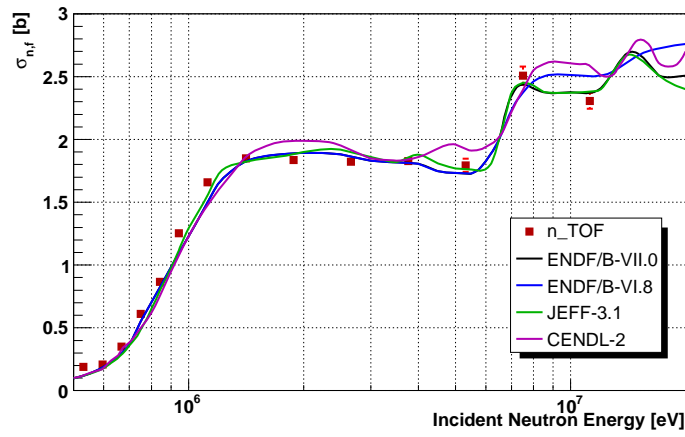


Figure 110: COMPARISON BETWEEN n\_TOF (VARIABLE BINNING)  $^{241}\text{Am}$  (N,F) EXPERIMENTAL CROSS SECTIONS AND DIFFERENT EVALUATIONS.

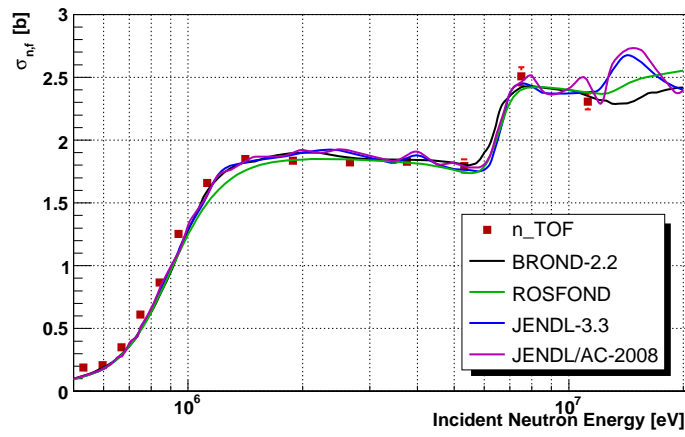


Figure 111: COMPARISON BETWEEN n\_TOF (VARIABLE BINNING)  $^{241}\text{Am}$  (N,F) EXPERIMENTAL CROSS SECTIONS AND DIFFERENT EVALUATIONS.

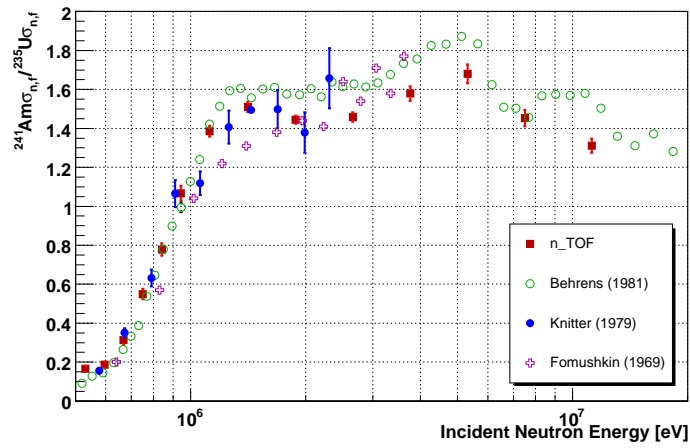


Figure 112: COMPARISON BETWEEN n\_TOF (VARIABLE BINNING)  $^{241}\text{Am}$  (N,F) CROSS SECTIONS AND PREVIOUS EXPERIMENTAL DATA.

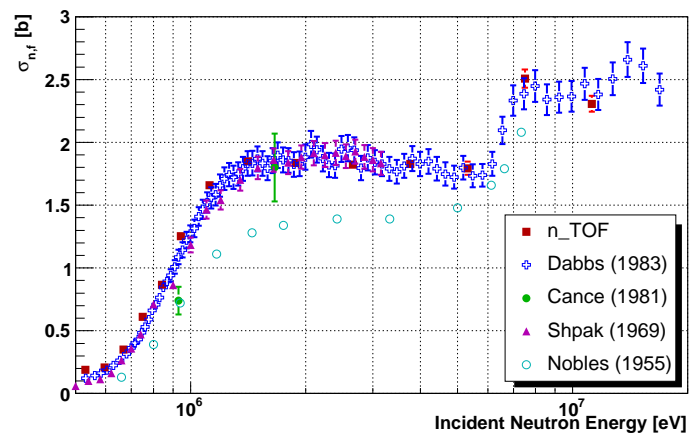


Figure 113: COMPARISON BETWEEN n\_TOF (VARIABLE BINNING)  $^{241}\text{Am}$  (N,F) CROSS SECTIONS AND PREVIOUS EXPERIMENTAL DATA.

Table 22:  $^{241}\text{Am}$  SUMMARY.

| Referred data set | $E_{min}$<br>[MeV] | $E_{max}$<br>[MeV] | Difference<br>[%] |
|-------------------|--------------------|--------------------|-------------------|
| ENDF/B-VII.0      | 0.5                | 20.0               | -3.2              |
| ENDF/B-VI.8       | 0.5                | 20.0               | -6.3              |
| JEFF-3.1          | 0.5                | 20.0               | -2.9              |
| CENDL-2.2         | 0.5                | 20.0               | -7.7              |
| BROND-2.2         | 0.5                | 20.0               | +0.008            |
| ROSFOND           | 0.5                | 20.0               | -1.6              |
| JENDL-3.3         | 0.5                | 20.0               | -2.9              |
| JENDL/AC-2008     | 0.5                | 20.0               | -4.2              |
| Dabbs             | 0.5                | 18.7               | -1.8              |
| Cance             | 0.930              | 2.66               | -12.3             |
| Shpak             | 0.5                | 3.3                | +1.1              |
| Nobles            | 0.5                | 7.34               | +22.4             |
| Behrens           | 0.588              | 20.0               | -9.7              |
| Knitter           | 4.97               | 2.65               | -3.9              |
| Fomushkin         | 0.5                | 3.62               | 0.91              |

## 6.6 $^{245}_{96}\text{Cm}$

$^{245}\text{Am}$  is an even  $Z$  - odd  $N$  isotope and therefore does not present any threshold to neutron induced fission [Kra87]. Inside FIC 2  $^{245}\text{Cm}$  samples were lodged. In Table 23 is their "identity card".

Table 23:  $^{245}\text{Cm}$  SAMPLE CHARACTERISTICS.

| Nuclide           | $\tau_{\frac{1}{2}}$<br>[years] | Mass<br>[mg] | $\alpha$ -activity<br>[Bq] | DAQ<br>channel | Sample         | Sample<br>mass<br>[mg] |
|-------------------|---------------------------------|--------------|----------------------------|----------------|----------------|------------------------|
| $^{245}\text{Cm}$ | $8.5 \times 10^3$               | 0.806        | 81.3 M                     | 15             | $\text{AmO}_2$ | 0.73                   |
|                   |                                 | 0.905        | 75.9 M                     | 14             |                | 0.68                   |

By looking at Table 23, a situation similar to that of  $^{233}\text{U}$ , i.e. a low  $\alpha$  background, is expected. On the contrary, this is not the case. The sample was contaminated by  $^{244}\text{Cm}$ , with an half life  $\tau_{\frac{1}{2}} = 18.1$  years. The impurity represents 6.6% of the total mass of samples (see Fig. 114) and therefore the  $\alpha$  background detected by electrodes # 14 and #15 is about 100 MBq. Such a high rate of  $^4\text{He}$  nuclei emission causes not only a huge  $\alpha$  pile-up, but also space-charge accumulation, preventing the FIC from working fine [37]. This does not allow us to perform any calibration and both the analysis method seen up to now can be indifferently employed. Results here extracted are therefore normalized with respect to ENDF/B-VII.0 1 MeV datum.

### 6.6.1 Pulse shape analysis

As already mentioned, the  $\alpha$  background due to  $^{244}\text{Cm}$  contamination is higher than in all previous cases. Again, in order to visually discriminate between FFs and  $^4\text{He}$  nuclei, signals with amplitude higher than 35 channels are plotted. Both  $^{245}\text{Cm}$  samples were considered.

Because of the pile-up, the thresholds discriminating between  $^4\text{He}$  nuclei and FFs are higher than those corresponding to the minimum between the two peaks. As a first guess it was decided to put the amplitude threshold where the linear fit assumes a value  $\leq 1\%$  with respect to the corresponding height of the amplitude spectrum (see Fig. 115 ), as for  $^{241}\text{Am}$ . Table 24 reports the inferred thresholds. As will be shown later (see § 6.6.2), values shown in Table 24, are still too low.

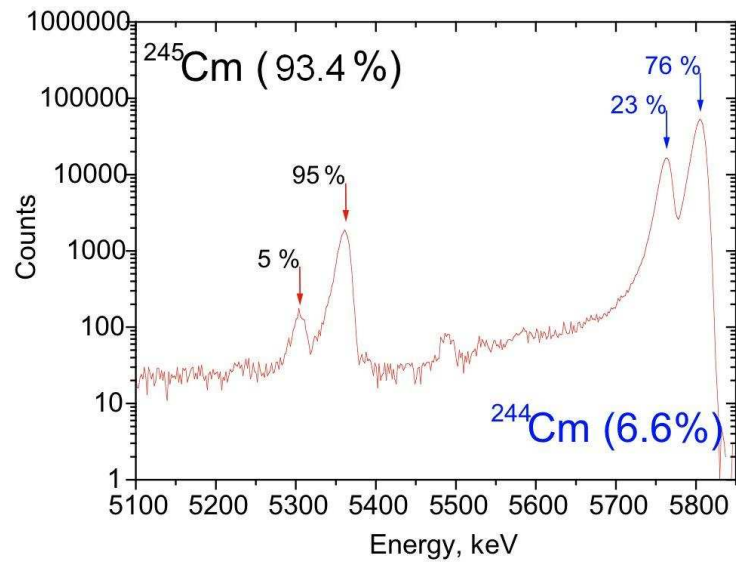


Figure 114: ISOTOPIC COMPOSITION OF THE CM SAMPLES HOUSED IN FIC. THE SPECTROSCOPIC ANALYSIS WAS PERFORMED IN DUBNA (JINR, RUSSIAN FEDERATION).

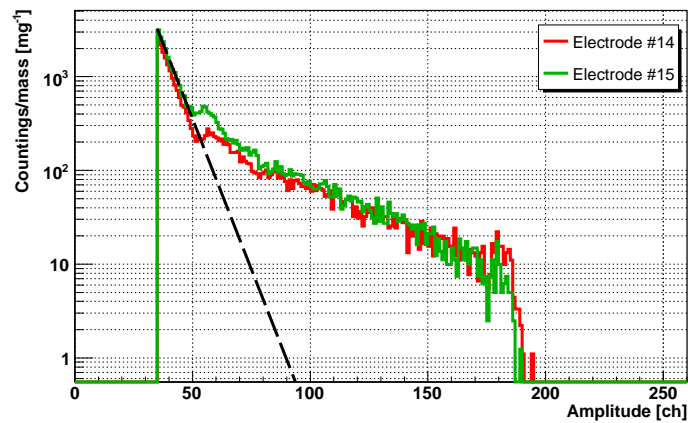


Figure 115: LINEAR FIT OF THE PEAK OF THE AMPLITUDE DISTRIBUTION DUE TO FF'S AND  $\alpha$  PARTICLES.)

Table 24: CHANNEL DISCRIMINATING BETWEEN FFs AND  $\alpha$  PARTICLES.

| Electrode | 14 | 15 |
|-----------|----|----|
| Amplitude | 75 | 75 |

## 6.6.2 Offset selection

### 6.6.2.1 $^{245}\text{Cm}$

#### 6.6.2.1.1 Electrode #14

Fig. 116 shows the linear relation between the charge and amplitude of signals collected by electrode #14 for the  $^{245}\text{Cm}$  sample. All the available statistics (amplitude  $\geq 35$  ch) is reported. No other condition is imposed. **The offset was found to be 12 channels.**

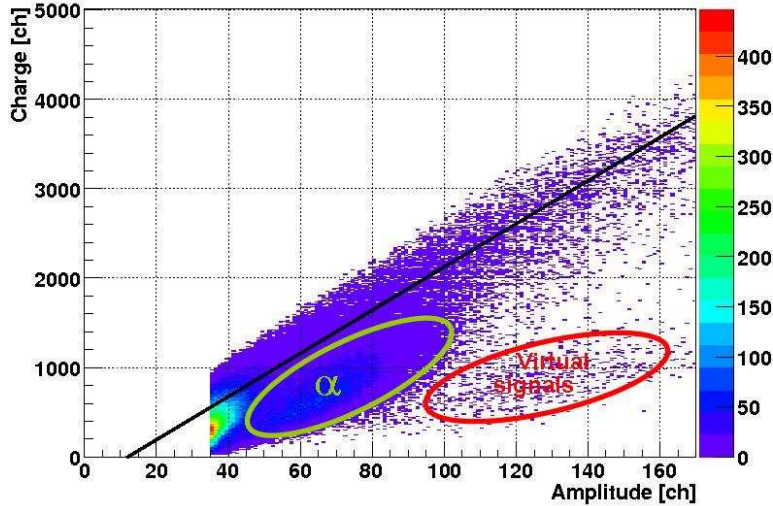


Figure 116: EXPERIMENTAL CHARGE DISTRIBUTION OF SIGNALS VERSUS THEIR AMPLITUDES. A LINEAR RELATION IS VISIBLE.

In Fig. 116 two clusters are visible: one with a higher density of points and one with a lower density. The first is due to pile up of  $\alpha$ 's among themselves and with FFs, while the second corresponds to virtual signals.

Fig. 117 reports the distribution of the charge to amplitude versus amplitude ratio after applying the offset correction. Though it was inferred that, for electrode #14, the  $\alpha$  background is hindered by considering amplitudes higher than 75 channels (see Table 24), Fig. 117 shows that in order to get rid of the problem a threshold of 105 ch in amplitude is needed. As a result of pulse shape and offset analysis, only data in the upper-right square of Fig. 117 are selected for this electrodes.

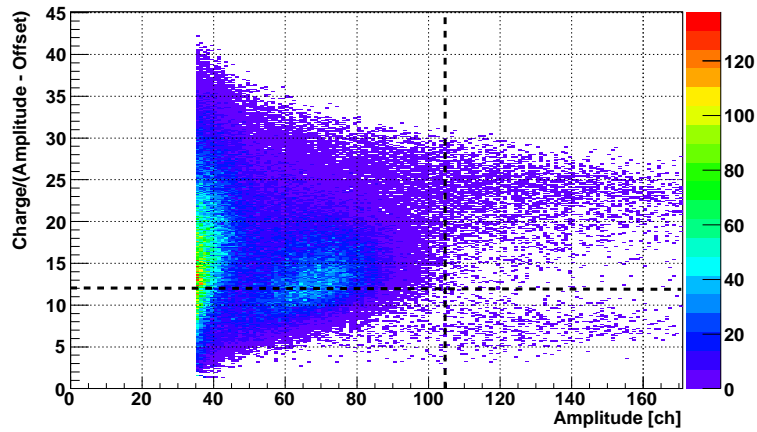


Figure 117: EXPERIMENTAL CHARGE DISTRIBUTION OF SIGNALS VERSUS THEIR AMPLITUDES.

#### 6.6.2.1.2 Electrode #15

Fig. 118 shows the linear relation between the charge and amplitude of signals collected by electrode #15 for the  $^{245}\text{Cm}$  sample. All the available statistics (amplitude  $\geq 35$  ch) is reported. No other condition is imposed. **The offset was found to be 12 channels.**

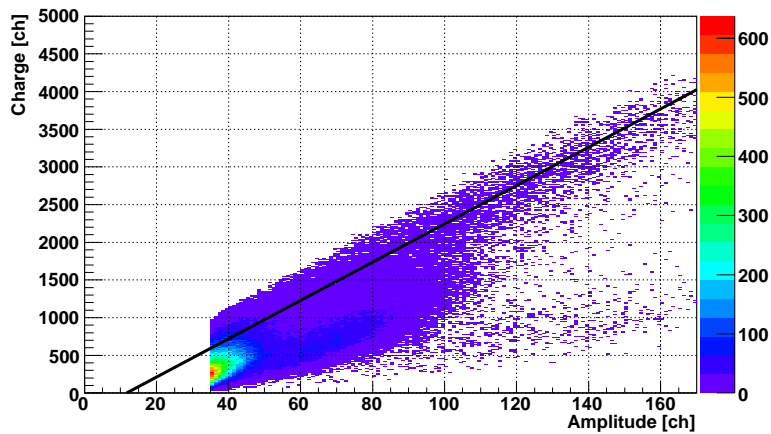


Figure 118: EXPERIMENTAL CHARGE DISTRIBUTION OF SIGNALS VERSUS THEIR AMPLITUDES.

The same considerations made for Fig. 116, apply to Fig. 118.

Fig. 119 reports the distribution of the charge to amplitude versus amplitude ratio after applying the offset correction. Again the threshold to impose in order to get rid of the background is far higher than the one reported in Table 24.

As a result of pulse shape and offset analysis, only data in the upper-right square

of Fig. 119 are selected for this electrode.

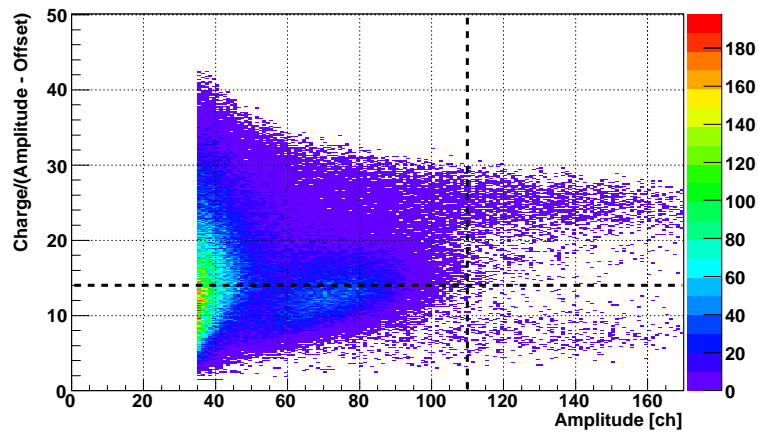


Figure 119: EXPERIMENTAL CHARGE DISTRIBUTION OF SIGNALS VERSUS THEIR AMPLITUDES.

### 6.6.2.2 $^{235}\text{U}$

For  $^{235}\text{U}$  practically no background is present. Nevertheless, as already seen for  $^{241}\text{Am}$ , any threshold on the charge (or amplitude) of signals, affects the shape of the correspondent distributions. In order to limit the effects of a distortion of the yield distribution, we are therefore pushed to perform our analysis by considering equivalent amplitude thresholds on the signals detected both for the investigated and the reference isotopes.

## 6.6.3 Space-charge equivalence

### 6.6.3.1 $^{245}\text{Cm}$

#### 6.6.3.1.1 Electrode # 14

By considering the yield distribution of fission fragments as a function of the incident neutron energy, it was (see Fig. 120) found that an amplitude threshold of 105 ch is equivalent to set a minimum charge equal to 2240 ch.

#### 6.6.3.1.2 Electrode # 15

By considering the yield distribution of fission fragments as a function of the incident neutron energy, it was found that an amplitude threshold of 110 ch is equivalent to set a minimum charge equal to 2440 ch (Fig. 121).

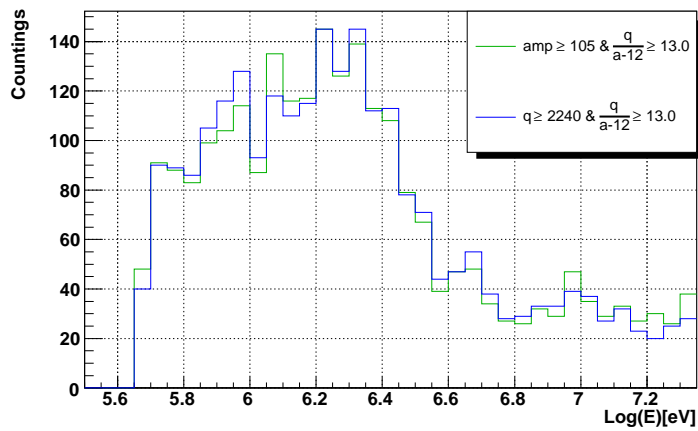


Figure 120: EXPERIMENTAL DISTRIBUTION OF DETECTED FISSION EVENTS AS A FUNCTION OF THE NEUTRON ENERGY. THE EQUIVALENCE BETWEEN PERFORMING AN ANALYSIS ON THE CHARGE OF SIGNALS OR ON THEIR AMPLITUDE IS EVIDENT.

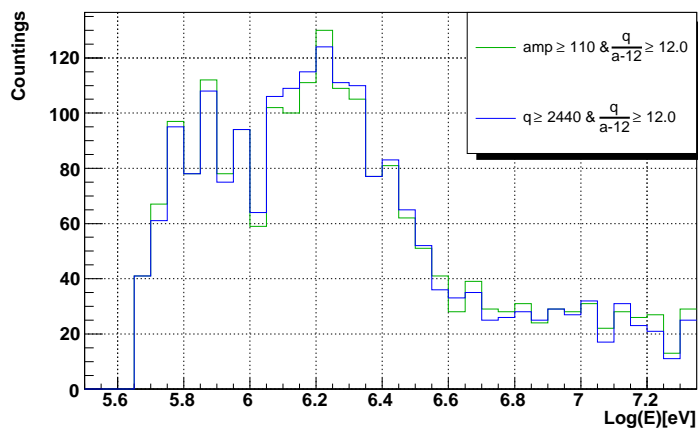


Figure 121: EXPERIMENTAL DISTRIBUTION OF DETECTED FISSION EVENTS AS A FUNCTION OF THE NEUTRON ENERGY. THE EQUIVALENCE BETWEEN PERFORMING AN ANALYSIS ON THE CHARGE OF SIGNALS OR ON THEIR AMPLITUDE IS EVIDENT.

### 6.6.3.2 $^{235}\text{U}$

The threshold to impose on the charge distribution for this isotope can be stated only after the determination of the centroids of the usual Gaussian distributions for the two electrodes of  $^{245}\text{Cm}$ .

## 6.6.4 Analysis of the charge to amplitude ratio distribution

### 6.6.4.1 $^{245}\text{Cm}$

Without reporting all pictures, by the same Gaussian fits performed in § 6.5.4, results summarized in Table 25 were obtained.

Table 25: PARAMETERS OBTAINED BY THE GAUSSIAN FITS OF THE CHARGE TO AMPLITUDE DISTRIBUTIONS (OFFSET CORRECTION APPLIED).

| $^{245}\text{Cm}$ | Centroid | $\sigma$ |
|-------------------|----------|----------|
| E114              | 24.4     | 2.75     |
| E115              | 25.3     | 2.08     |
| E112*             | 15,8     | 1.65     |

\* Values taken from § 6.5.4

From the supposed <sup>31</sup> relationship among the centroids of the Gaussian distributions and the charge histograms, the threshold to impose on the  $^{235}\text{U}$  can be calculated.

A threshold equal to 1240 ch on the charge of El # 14, is equivalent to the condition  $q \geq 1240 \cdot \frac{\text{centroid}_{235\text{U}}}{\text{centroid}_{241\text{Am}-\text{E114}}} \approx 1451$ .

A threshold equal to 1440 ch on the charge of El # 15, is equivalent to the condition  $q \geq 1440 \cdot \frac{\text{centroid}_{235\text{U}}}{\text{centroid}_{241\text{Am}-\text{E115}}} \approx 1524$ .

The average value of 1487 channels was used in the analysis.

## 6.6.5 Cross section extraction

Up to now all the statistics detected for the  $^{245}\text{Cm}$  samples has been considered in order to isolate, among all data, those corresponding to fission events. But the selected signals can be due to (n,f) reactions occurred in  $^{245}\text{Cm}$  as well as in the  $^{244}\text{Cm}$  contaminant.

$^{244}\text{Cm}$  is an even N isotope and therefore presents a threshold to neutron induced fission [Kra87]. Its (n,f) cross section, as far as is known, in the MeV region assumes

<sup>31</sup>Because of space charge accumulation, the centroids of the Gaussian fits relative to the  $^{245}\text{Cm}$  samples can be slightly different from the real value the would assume for a lower  $\alpha$  background.

values similar to the  $^{245}\text{Cm}$   $\sigma_{(n,f)}$ . Neglecting the contribution of the contaminant would therefore lead to a 6.6% uncertainty on the obtained results. For this reason, after cross section extraction, the 6.6% contribution due to  $^{244}\text{Cm}$   $\sigma_{(n,f)}$  was subtracted. The evaluation considered for this operation is ENDF/B-VII.0  $^{244}\text{Cm}$  (n,f) and results presented include this correction. No correction efficiency was instead considered.

### 6.6.6 Results

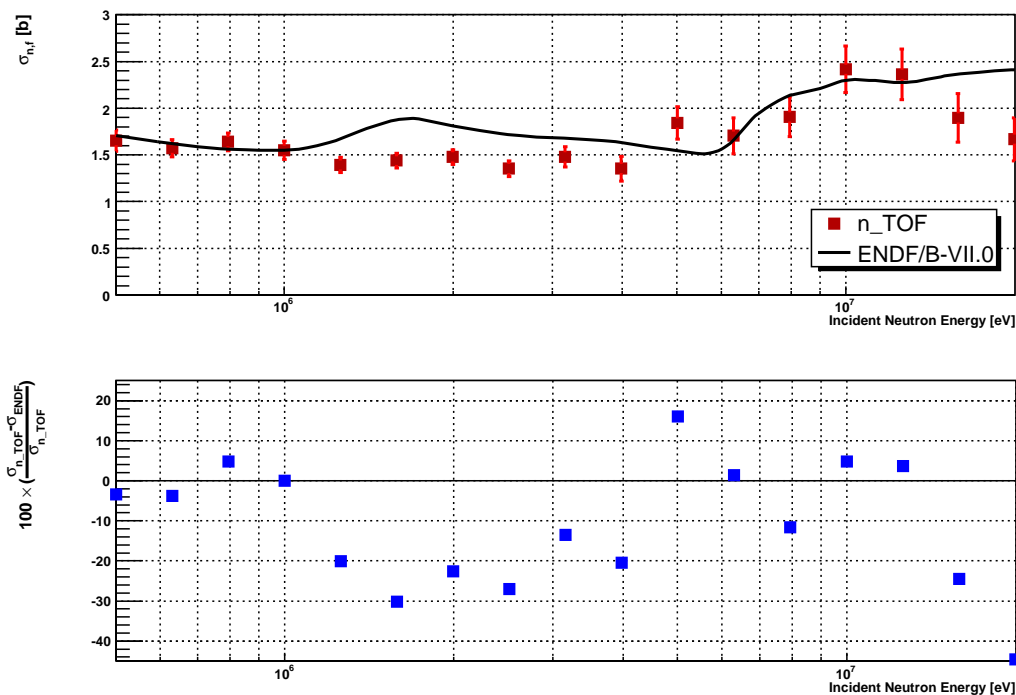


Figure 122: COMPARISON BETWEEN n\_TOF (VARIABLE BINNING) AND ENDFB-VII.0  $\sigma_{(n,f)}$ .

The upper panel of Fig. 122 shows a comparison between experimental  $^{245}\text{Cm}$  (n,f) cross sections obtained at the n\_TOF facility and the ENDF/B-VII.0 evaluations, released in December 2006.

The normalization factor was extracted by performing the ratio between the ENDF/B-VII.0 cross section at 1 MeV and our not-yet-normalized results.

In order to quantify discrepancies, in the lower panel of Fig 122 the percentage difference between n\_TOF results and the ENDF/B-VII.0 library is plotted. The n\_TOF cross sections oscillates around the considered evaluation, but remains complexively lower than that. Discrepancies ranges up to 45%. This was foreseen, since the statistics is low and the threshold imposed on the reference isotope is affected by sure uncertainty due to space-charge effects.

For a better cross check, a comparison between n\_TOF experimental results and other evaluations was considered.

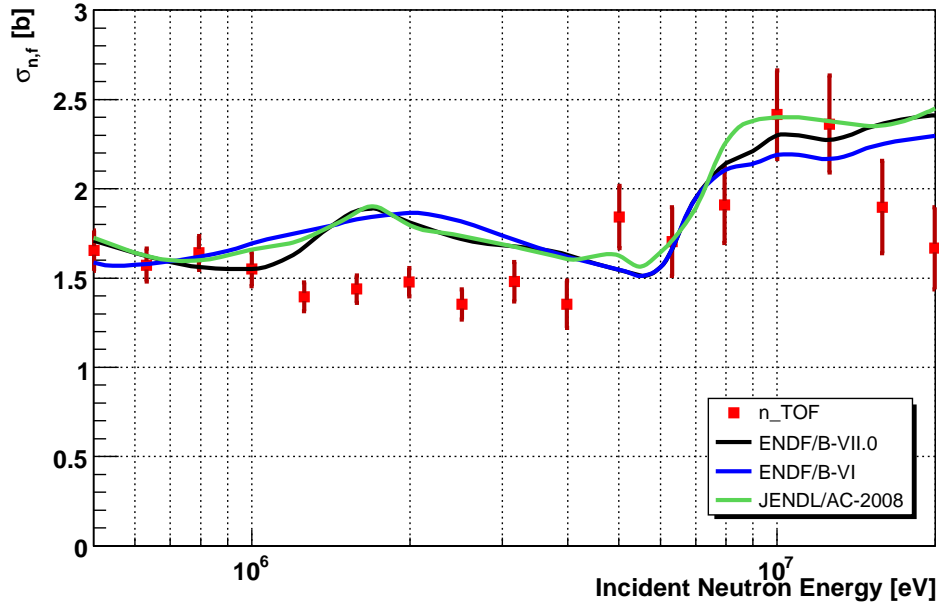


Figure 123: Comparison between n\_TOF (variable binning) and different evaluations

ENFB/B-VII.0 and JEFF-3.1 took data from JENDL-3.3, but for sake of continuity ENFB/B-VII.0, and not JENDL-3.3, is considered in Fig. 123.

The Russian ROSFOND and ENDF/B-VI.0 evaluations coincide, therefore only the last one was reported. CENDL-2.2 and BROND-2.2 doesn't provide any evaluation for neutron induced fission cross sections of  $^{245}\text{Cm}$ .

For energies higher than 7 MeV (but lower than 15 MeV), n\_TOF data seems to better agree with JENDL/AC-2008. Above 7 MeV, for this library, an eye-guided cross-section curve was drawn [94] adopting the data of Fursov *et al.* [95] and Moore *et al.* [96]. Around 19 MeV it is quite improbable that the first chance fission cross section falls so quickly, therefore our  $^{245}\text{Cm}$  data are reliable up to 15 MeV. By the way, all evaluation at that energy are based on the only 14.9 MeV available data by Fursov *et al.*.

Discrepancies in the 1 MeV - 7 MeV region are quite high, but below 20%, with respect to all evaluations.

In Fig 124 are all the available experimental data. Cross sections are directly reported because only one author used  $^{235}\text{U}$  as a reference.

Below 1 MeV our data are in agreement, within 5% discrepancy, with Fursov *et al.* [95], Ivanin *et al.* [97], White *et al.* [98] and Gokhberg *et al.* [99], while differences with Fomushkin *et al.* [100] and Moore *et al.* [96] are already consistent ( $> 5\%$ ).

Between 1 MeV and 2 MeV discrepancies with other experimental data increase up to 15% with respect to Gokhberg *et al.* [99], and even reaching 15% with respect to Moore *et al.* [96].

In the region 3 MeV - 7 MeV n\_TOF oscillates around Fursov *et al.* [95], Fomushkin *et al.* [100] and White *et al.* [98], while discrepancies with Ivanin *et al.* [97] results about 30%.

The 10 MeV datum overlap with White *et al.* [98], and the 13 MeV datum is compatible with Fursov *et al.* [95], but not with Fomushkin *et al.* [101].

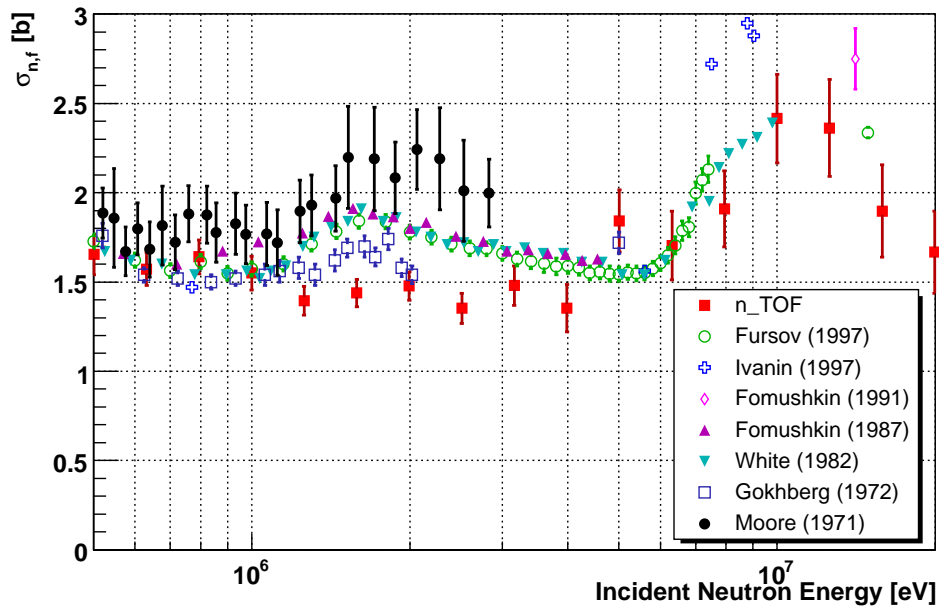


Figure 124: COMPARISON BETWEEN n\_TOF (VARIABLE BINNING) AND PREVIOUS EXPERIMENTAL DATA.

## 7 Conclusions

*Why do all good things come to an end?*

Nelly Furtado

Neutron induced fission cross section of actinides are relevant both in view of the growing energy demand and consumption and of the subsequent necessity of getting rid of the produced wastes. While waiting to perfectionate studies and develop technology allowing to reach higher efficiencies in the exploitation of alternative energetic sources, several countries are showing a renewed interest towards nuclear power plants. Sweden is the latest European country to change its mind about nuclear power. UK policy has gone from neglect to support since 2005, Italy announced a pro-nuclear change in 2008 and the Netherlands is likely to adopt a pro-nuclear position next year [102]. Belgium, Germany and Spain remain the only countries in the world that use nuclear power but wish to shut it down, thought, as for Germany, Members of Chancellor Merkel's new center-right alliance in September 2009 reaffirmed their commitment to delay Germany's nuclear phase-out [103].

More accurate fission cross-sections are required - among other physical parameters - to reach higher fuel burn-up on one side and increase the safety of future systems, which aim at a higher actinide fraction in the fuel mix, on the other. In fact, information inserted in databases present accuracies very far (up to 40%) with respect to those needed (<3% - 4%) to start with projects and prototypes of reactors of new generation.

The innovative features of the neutron beam of the n\_TOF facility at CERN (Genève) allows to collect new and more precise nuclear data to answer to the present request of the international community.

Neutron induced fission cross sections have been extracted for  $^{233}\text{U}$ ,  $^{238}\text{U}$ ,  $^{241}\text{Am}$ ,  $^{243}\text{Am}$ ,  $^{245}\text{Cm}$  in the energy range between 0.5 and 20 MeV with reference to  $^{235}\text{U}$ , which is a standard for (n,f) reactions from thermal energies up to 200 MeV. Data were collected in 2004 with a Fission Ionization Chamber and analyzed off-line.

$^{233}\text{U}$   $\sigma_{(n,f)}$  extracted data are accurate within 3% and the discrepancy with the latest ENDF/B evaluation on the whole energy region is 3.2%. At low energies (0.5 MeV  $\div$  1 MeV), by the way, we confirm the ENDF/B-VI.8 library.

The extracted  $^{238}\text{U}$   $\sigma_{(n,f)}$  are lower than expected. In order to understand if the problem was in the electronics or in the method, a check was performed. Since  $^{233}\text{U}$   $\sigma_{(n,f)}$  derived with respect to  $^{235}\text{U}$   $\sigma_{(n,f)}$  agree with previous data and with different evaluations, it was decided to try to extract  $^{233}\text{U}$   $\sigma_{(n,f)}$  with respect to  $^{238}\text{U}$   $\sigma_{(n,f)}$ . This would have revealed if maybe both  $^{233}\text{U}$  and  $^{235}\text{U}$  FFs signals are affected by some distortions in the same way, so that in the ratio the effect cancels. The obtained

neutron induced  $^{233}\text{U}$  cross sections (extracted with reference to  $^{238}\text{U}$ ) was found to be higher than expected, confirming a problem in the electronic chain of the  $^{238}\text{U}$  sample.

$^{243}\text{Am}$  (n,f) cross sections are provided with an accuracy of 3%, thus meeting the requests by the Working Party on International Evaluation Co-operation for SFR (Sodium cooled Fast Reactors). Previous fission cross section experimental data tended to cluster in two distinct groups in the  $1 \div 6$  Mev range, separated by about 20% from each other. The most recent experimental data set available at the time of the ENDF/B-VII.0 release was by Laptev *et al.* [78] (2007), and those values lie in the higher-energy group, about 20% higher than the ENDF/B-VI evaluation. n\_TOF data instead confirm the ENDF/B-VI evaluation, matching the ZEBRA [82] reactor benchmark.

The extracted  $^{241}\text{Am}$   $\sigma_{(n,f)}$  practically overlap with the BROND-2.2 evaluation. n\_TOF data for this isotope are again accurate within 3%, meeting the requests by the Working Party on International Evaluation Co-operation for SFR (Sodium cooled Fast Reactors), GFR (Gas cooled Fast Reactors), LFR (Lead cooled Fast Reactors) and even ADMAB (Accelerator Driven Minor Actinides Burners), where the stringest conditions apply (thought request here are met averaging on the whole energy range, but not for all single subranges). The agreement of our cross-sections with previous experimental data moreover validate the different analysis performed.

$^{245}\text{Cm}$  (n,f) cross sections is highly requested, due to the lackness of experimental data. This is confirmed also by the large uncertainties allowed by the Working Party on International Evaluation Co-operation. Unfortunately, because of a contamination by the much more  $\alpha$ -radioactive  $^{244}\text{Cm}$ , it was not possible to obtain reliable nor highly accurate results for  $^{245}\text{Cm}$   $\sigma_{(n,f)}$ .

New data are being collected in the measurement campaign programmed for May 2010. Thanks to the extremely high accuracy of the cross sections obtained at n\_TOF, the facility is playing a valuable role in the continuous changes and updates of nuclear evaluation libraries.

# APPENDIX A: Other neutron sources

Spallation reactions are not the only possibility for neutron production. Other white (i.e. wide energy range) neutron sources are:

1. Nuclear reactors.

Fig. 125 shows the neutron spectrum from a thermal and fast reactor [104]

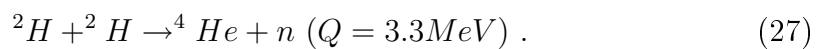
The energy distribution of neutrons from fission is always essentially the same, thus the difference between the two curves is due to the presence/absence of a moderator. As visible, the maximum neutron energy is not higher than  $\sim 10$  MeV.

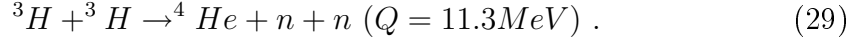
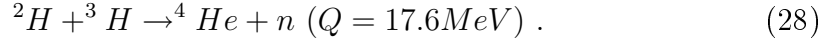
2. Electron-neutron converters.

An electron beam impinges on a thick target and gives rise to  $\gamma$  radiation through Bremsstrahlung process. Photoelectron emission is maximum in the region of the Giant Dipole Resonance (GDR). A GDR is a coherent motion of all protons against neutrons, which is described by a collective particle-hole vibrational mode in the nucleus. This state turns out, in experiments, in a large dipole moment. In other words, when the energy of the incident photons is close to the binding energy of the nucleons ( $> 5-15$  MeV), photoabsorption causes a relative displacement of tightly bound neutrons and protons inside the nucleus. This results in a giant resonance condition. Absorption of the incident photons excites the nucleus to a higher discrete energy state and the extra energy causes fission or is emitted in the form of neutrons in  $(\gamma, n)$  or  $(\gamma, 2n)$  reactions. Proton emission is instead strongly suppressed in heavy nuclei by the presence of the Coulomb barrier. The resonance energy and the resonance width depend little on the mass number but are insensitive to individual nuclear structures. This means that the GR can be excited with medium energy photons practically in every kind of nucleus. At incident photon energies higher than 30 MeV the cross section for giant resonance neutron production decreases very rapidly and above 50 MeV other processes dominate.

3. Fusion based systems [105] .

In deuterium-tritium (D-T), deuterium-deuterium (D-D) and tritium-tritium (T-T) reactions neutrons are created. If the colliding particles have negligibly small energies, the Q value of the reaction is shared between the emerging products.





The reactions reported in Eq. (27) and eq. (28) give rise to monochromatic 2.64 MeV and 14.08 MeV neutron beams respectively, while neutrons emerging from Eq. (29) share roughly  $\frac{6}{8}$  of the Q value and show a continuum spectrum (see Fig. 126).

Table 26 reports the neutron yield per incident particle for the considered reactions. The higher neutron flux is obtained employing nuclear reactors. These devices have strict building and working regulations and produce radioactive waste beyond "simple" structural material activation. Moreover, as already mentioned, the neutron energy spectrum is constrained below about 10 MeV.

Fusion based systems are quite expensive, provide neutrons with 14 MeV maximum kinetic energy and tritium is radioactive.

For these reason proton and electron accelerators are the preferred choice for neutron generation. Spallation has the advantage of a high neutron flux, while Bremsstrahlung coupled to photoneutrons reactions, though providing fewer neutrons, presents lower target activation

Table 26: COMPARISON OF NEUTRON YIELDS OBTAINED WITH DIFFERENT REACTIONS [106].

| <b>Nuclear Reaction</b> | <b>Projectile &amp; energy [MeV]</b> | <b>Beam Current [part/s]</b> | <b>Neutron yield [neut/part]</b> | <b>Emitted neutrons [neut/s]</b> |
|-------------------------|--------------------------------------|------------------------------|----------------------------------|----------------------------------|
| (e,γ) + (γ,n)           | 60 MeV e <sup>-</sup>                | 5 × 10 <sup>15</sup>         | 0.05                             | 2 × 10 <sup>14</sup>             |
| (D-T)                   | 0.3 MeV <sup>3</sup> H               | 6 × 10 <sup>19</sup>         | 10 <sup>-4 ÷ -5</sup>            | 10 <sup>15</sup>                 |
| Fission                 |                                      |                              | 1                                | 2 × 10 <sup>18</sup>             |
| Spallation              | 1 GeV p                              | 10 <sup>15</sup>             | 30                               | 3 × 10 <sup>16</sup>             |

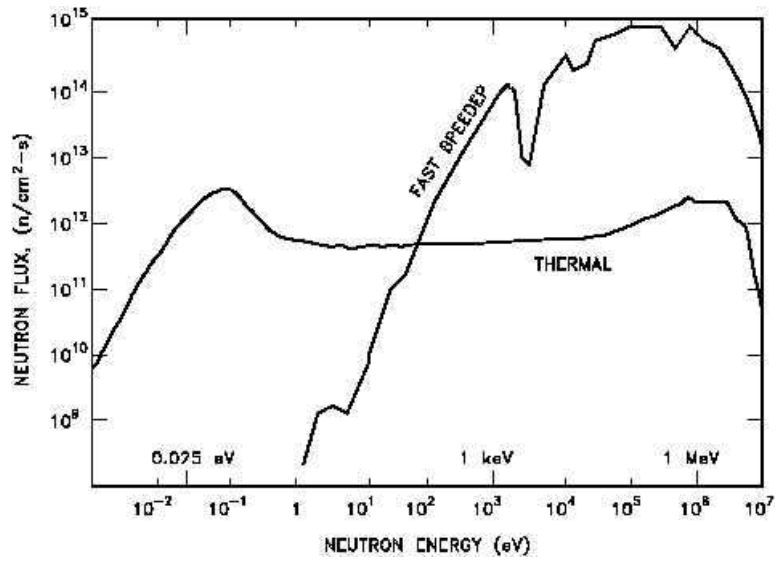


Figure 125: COMPARISON OF NEUTRON SPECTRA FROM THERMAL AND FAST BREEDER REACTORS [104].

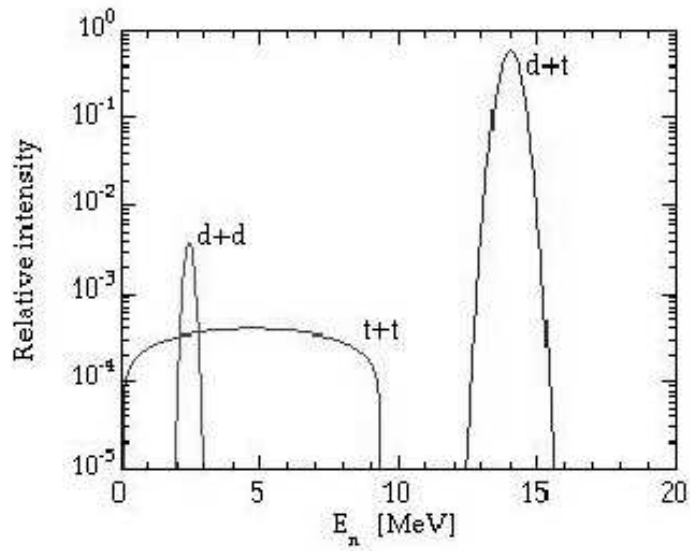


Figure 126: FUSION NEUTRON ENERGY SPECTRA [105].

# APPENDIX B: Preprint ИЯИ 816/93 <sup>32</sup>

“Method for calculation of the mass-energy distribution of medium-energy particle-induced fission fragments”

G. D. Adeev *et al.*

June 1993

## Abstract

A method to calculate the mass-energy distribution of medium-energy particle-induced fission fragments was created on the basis of a cascade-evaporation model. In such an approach, the composite nuclei were described with the help of the intra-nuclear cascade model, while excited nuclei by the evaporation model. The mass-energy distributions of the fission fragments from composite nuclei with high excitation energy ( $E^* \geq 50\text{MeV}$ ) were calculated on the basis of the diffusion model, while the distribution of the same nuclei, but with low excitation energy ( $E^* < 50\text{MeV}$ ), were calculated by empirical approximations.

The developed calculation method well describes the experimental data for mass-energy distribution of nuclear fission fragments generated by proton-induced and antiproton-induced fission.

## 1. Introduction

It is known [1,2] that in the deep-inelastic interaction of medium energy particles with a nucleus, two stages different for their nature arise:

- fast stage ( $\tau \sim \tau_0$ ) of the intranuclear cascade, during which the particles of the continuum spectrum (products of subsequent NN and  $\pi$  N collisions) leave the target, and after which a highly thermalized residual nucleus is created;
- low stage ( $\tau \gg \tau_0$ ) of disintegration of the residual nucleus through subsequent particle emissions or through fission (here  $\tau_0 \sim 10^{-22}$  s. - time of flight of fast particles through the nucleus).

The fission process gives unique opportunities for studying energy dissipation in deep-inelastic interactions. The point is that fission provokes a global nucleonic reconstruction of the nuclear structure in the slow process (even the shortest fission time of a nucleus with no fission barrier or fall time from the saddle point to the scission point, exceeds the value  $\tau_f^{min} \sim 10^{-20}$  s) [3,4]. Therefore fission can take place only during the evaporation stage of the deep-inelastic interaction and its study

---

<sup>32</sup>Only those sections relevant for simulating mass, charge and energy distribution of fission fragment in neutron induced fission of the analyzed isotopes have been here reported.

allows to obtain the knowledge of the complex of the residual nuclei.

The specificity of nuclear reactions with medium-energy particles is that all residual nuclei are characterized by a broad distribution in excitation energy  $E^*$  and neutron and proton numbers  $N$  and  $Z$ . In nuclear reactions initiated by particles with energy of a few GeV or by slow antiprotons, a large part of the residual nuclei has a high excitation energy  $E^* \geq 100$  MeV [1,5]. With this, as a whole a certain fraction of nuclei with low excitation energy is always present. Moreover, next to particle release from the residual nucleus, in the rings of the evaporative chain, intermediate nuclei with excitation energies ranging from the initial value up to  $E^* < B_n$  are created ( $B_n$  is the neutron binding energy). Therefore, in order to analyze data through medium energy particle induced fission, an evaporative model, capable of describing disintegration in a wide energy excitation range from some MeV up to some hundreds of MeV is necessary. Certainly, in the unexplored regions of very high excitations, new phenomena particularly interesting from for studying the properties of "hot" nuclei and the disintegration mechanism [6] may arise. Nevertheless at the present stage of development of this topic it seems reasonable, for the improvement of evaporative model, basing ourselves on the knowledge of the properties of nuclei and their fragmentation with  $E^* \leq 100$  MeV, accumulated in reactions with particles and heavy ions of low energy.

In our previous work [7] the evaporative model had been developed correctly taking into account the influence of the shell effects in nuclei. The parameters of this model had been fixed on the basis of the analysis of a huge amount of data dealing with the level density, decay widths and life time of nuclei with  $E^* \leq 100$  MeV. This allowed to increase not only the accuracy of this model, but also the extrapolation reliability in the region of high excitations.

Nevertheless with the help of this evaporative model [7] only the fission probability of nuclei in each ring of the evaporative chain and the total fission probability could be calculated. As a result, in the frame of a joint model of cascade-evaporation only a simple integral description of the medium energy particles induced fission could be analyzed, i.e. the probability  $P_f = \sigma_f/\sigma_{in}$  ( $\sigma_f$  is the fission cross section,  $\sigma_{in}$  is the inelastic interaction cross section) [8,9]. In this work the following step in the development of the evaporative model was made [7] and as a result also the mass-energy distribution of fission fragments could be calculated. The parameters of the model were determined through the analysis of data dealing with the mass-energy distribution of FFs on nuclei with  $E^* \leq 100$  MeV, obtained in nuclear reactions with particles and heavy ions of low energy. This enhanced also the extrapolation accuracy of the model in the energy region  $E^* > 100$  MeV. As a result, with the help of the cascade - evaporative model, the possibility of analyzing a wider range of data dealing with medium energy particle induced fission and the possibility of obtaining more and deeper information on the set of thermalized residual nuclei created arose.

In the second chapter of this article is given the description of the statistical non-equilibrium approach based on the Fokker-Plank equation (named diffusion model) [10], which is used in calculations of fission in highly excited nuclei  $E^* > 50$  MeV when shell effects disappear [7] and fission becomes symmetric. In the third chapter are derived the empirical approximations to calculate the mass-energy distribution of FFs on nuclei with relatively low excitation energy  $E^* < 30 - 50$  MeV, when shell effects strongly affect the fission process, the transmission process and the coexistence of symmetric and asymmetric fission. In the fourth chapter the calculation method of medium energy particle induced fission is described. In the end, in the fifth chapter, the obtained cascade-evaporative model is used for describing some data dealing with medium energy particle induce fission.

### 3. Low energy fission

Let us look now to the case of fission of a nucleus with  $A_0$  nucleons,  $Z_0$  protons and excitation energy relatively low  $E_0^* < 30 - 50$  MeV (temperature <sup>33</sup> $T < 1.0 - 1.5$  MeV). In this energy region  $E_0^*$ , as a result of the strong action of shell effects, fission has a complex nature. In particular, as a result of the action of these shell effects from the surface potential energy of the nucleus, appear 2 (or even more) fission valleys, which leads to the coexistence of symmetric fission with one or more modes of asymmetric fission (see note [26]) Advanced models forecast and qualitatively explain the nature of multimodal fission, but was also able to quantitatively describe the mass-energy distribution of fragments of spontaneous and induced fission of nuclei with  $E_0^* < B_n$ . Nowadays theoretical models are not yet able to take into account the manifestation of shell effects for high excitation energies and their thermal attenuation in the mass-energy distribution of fission fragments. Therefore here we obtained an empirical approximation for this distribution, based on experimental data analysis for  $E_0^* \leq 50$  MeV ( $T_0 \leq 1.5$  MeV).

#### 3.1 Mass distribution of fission fragments

As experimentally demonstrated (see for example [29]), the mass distribution  $Y(A)$  is made of a symmetric and an antisymmetric component:

$$Y(A) = Y_{asym}(A) + F \cdot Y_{sym}(A) \quad (15)$$

with  $F(E_0^*, A_0, Z_0)$  - fraction of these fission modes. As it follows from the work [30], experimental data can be good approximated, if for symmetric fission only one

---

<sup>33</sup>The temperature  $T$  of a nucleus is linked to its excitation energy by the simple relation  $E^* = a T^2$ , where  $a \approx A/10$  MeV is the parameter of the nuclear level density.

fission mode is considered:

$$Y_{sym}(A) \sim \exp\left[-\frac{(A - A_s)^2}{2\sigma_{A_s}^2}\right] \quad (16)$$

while in the asymmetric fission, 2 fission modes are taken into account:

$$Y_{asym}(A) \sim \exp\left[-\frac{(A - A_2)^2}{2\sigma_{A_2}^2}\right] + \exp\left[-\frac{[(A - (A_0 - A_2))]^2}{2\sigma_{A_2}^2}\right] + c_{as} \cdot \left\{ \exp\left[-\frac{(A - A_1)^2}{2\sigma_{A_1}^2}\right] + \exp\left[-\frac{[(A - (A_0 - A_1))]^2}{2\sigma_{A_1}^2}\right] \right\} \quad (17)$$

Here  $A_s = A_0/2$ ,  $A_1$  e  $A_2$  average value of appropriate Gaussian;  $\sigma_{A_s}$ ,  $\sigma_{A_1}^2$  and  $\sigma_{A_2}^2$  their dispersions;  $c_{as}$  gives the ratio between the 2 asymmetric fission modes.

All nuclei, asymmetrically fissioning, have the same values  $A_1 = 134$  and  $A_2 \approx 141$ [31-36], which shows the universal character of the asymmetric fission. It is worthwhile underlying that the deduction about the existence of these universal modes is confirmed by the theory [37,38]. Moreover the analysis of the experiments [34,35] shows that  $c_{as}$  has a value  $c_{as} \approx 1/2$ , which remains more or less the same for both nuclei.

From the analysis [33-35] the following values for the dispersion of asymmetric fission are obtained:

$$2\sigma_{A_1} = \sigma A_2 = \begin{cases} 5.6 & A_0 \leq 235 \\ 5.6 + 0.096(A_0 - 235) & A_0 > 235 \end{cases} \quad (18)$$

from data [33-35] it does not result possible getting information on the energy dependency of  $\sigma_{A_1}$  and  $\sigma_{A_2}$ , since the channels of asymmetric fission are clearly seen in the experiments only at low energies  $E_0^*$ .

Concerning the symmetric fission method, experimental data does not show any dependence of the dispersion  $\sigma_{A_s}^2$  from the mass of the fissioning nucleus. The energy dependence  $\sigma_{A_s}^2(E_0^*)$  is shown in picture 7, where the values  $\sigma_{A_s}^2$  got from the fission experiments [23, 26, 31, 32,39-41] of various nuclei with different excitation energies  $E_0^*$  are represented. It is thus supposed that after the fusion of the incoming nucleon or light nucleus with the target one, a compound nucleus which soon vaporizes particles (n, p, d, t,  $^3\text{He}$ ,  $\alpha$ ,  $\gamma$ ) of fissions is formed. Particles emitted before fission bring with them part of the excitation energy  $E_0^*$ . In order to evaluate the influence of this effect on the calculation of the dependence  $\sigma_{A_s}^2(E_0^*)$  for the reactions shown in picture 7, with the help of the evaporative model [1,7] which accounts for the competition between particle emission and fission, the average excitation energy of the compound nucleus before fission has been determined for each level of the evaporative cascade. Considering this effects leads to moving towards left the points in picture 7. An

overwhelming majority of experimental points falls, after such changes/progresses, in the shaded area in picture 7. Since experimental data deal with weakly fissionable nuclei, experiencing fission, as a rule, in the first part of the evaporative chain a fair modification of the excitation energy is seen at the expenses of evaporation of particles before fission. The energy dependence of the dispersion of the symmetric fission, corresponding to the shaded area in picture 7, is definitely approximated by the expression:

$$\sigma_{A_S} = \exp(5.53 \cdot 10^{-3}) \cdot E_0^* + 2.1386 \quad (19)$$

(here and further the energy  $E_0^*$  is given in MeV).

In order to extract the terms of the function F in expression (15), let us examine the ratio experimentally measured of the height of the peaks of symmetric and asymmetric fission. (In case of actinides this approximatively corresponds to the ratio valley/peak for asymmetric fission at low energy). In this case all data are distributed in 3 groups according to the charge of the fissioning nucleus: I)  $90 \leq Z_0 \leq 96$ ;  $Z_0 = 89$ ;  $Z_0 \leq 88$ ; so that in each one the energy dependence of this ratio  $F_{sa}$  results strongly evident. Thus in the first group (Th and heavier nuclei), at lower energies  $E_0^*$  asymmetric fission dominates, while at increasing  $E_0^*$ , the probability of symmetric modes fastly increases. In the case of fission of Ac (second group) at low  $E_0^*$  both can occur, but for lighter nuclei (third group) for each value of  $E_0^*$  symmetric fission dominates.

The energy dependence  $F_{sa}E_0^*$  for nuclei of the first and second group is presented in picture 8. On picture 7 the shaded area is shown, where are displaced experimental points obtained in reactions with different impinging particles, if evaporation of particles before fission is considered. In these regions the following empirichal approximations hold:

$$F_{sa} = \begin{cases} \exp(0.5385 \cdot E_0^* - 9.9564) & E_0^* \leq 16.25 \text{ MeV} \\ & Z_0 \geq 89 \\ \exp(0.09197 \cdot E_0^* - 2.7003) & E_0^* > 16.25 \text{ MeV} \end{cases} \quad (20.a)$$

$$F_{sa} = \exp(0.09197 \cdot E_0^* - 1.0808) \quad Z_0 = 89 \quad (20.b)$$

Nuclei with  $Z_0=86-88$  attract particular interest, since in this transition region it is possible studying how the character of the asymmetric fission mode interchanges into the symmetric one for a decreasing mass of nucleus. Yet experimental information about these nuclei is really poor. Nowadays we have only one experiment [26, 31, 32] allowing to trace conclusions about the ratio of these modes, in case of energies  $E_0^*$

$\sim B_f + 10$  MeV, slightly exceeding the fission barrier. Starting from these data, in the assumption that the energy dependence  $F_{sa}$  appears the same as in Ac nucleus, we obtain:

$$F_{sa} = \exp[(0.3 \cdot (227 - A_0)] \cdot e[0.09197(E_0^* - (B_f - 7.5)) - 1.08808] \quad Z_0 \leq 88 \quad (20.c)$$

For  $A_0 > 227$  and  $E_0^* < B_f - 7.5$  the factors in the exponent indexes are put equal to null. In order to express function  $F$  through  $F_{sa}$  it is enough considering the possible influence/impact of the tails of the distribution of one of the modes of fission on the value of the maximum outcomes of the other mode.

$$F \cong \frac{F_{sa} - I_{asy}}{1 - F_{sa} \cdot I_{sym}} \quad (21)$$

where  $I_{asy} = Y_{asy}(A_s)$  and  $I_{sym} = (\frac{A_1 + A_2}{2})$

Final correlation (= ratio) assumes that the maximum outcome of the asymmetric mode takes place for mass number  $\sim (A_1 + A_2)/2$

## Charge distribution of fission fragments

The issue of the charge distribution of fragments of mass number  $A$  was studied sufficiently in details both in theory and in practice (see the previous section and works [29,45,46]). The total charge is distributed among fission fragments proportionally to their mass, with slight corrections. Experimental data are well approximated by a Gaussian with charge dispersion  $\sigma_{\frac{Z}{Z}} \approx 0.36$  [29,45], not depending of the fragments mass and with a most probable charge  $\bar{Z}_p$  described by formula (11) with values:

$$\delta Z = \begin{cases} -0.45 & A \geq 134 \\ -0.45(A - A_0/2)(134 - A_0/2) & A_0 - 134 < A < 134 \\ +0.45 & A \leq A_0 - 134 \end{cases} \quad (22)$$

## Kinetic energy of the fission fragments

In order to determine the dependence of the average kinetic energy of fission fragments  $\bar{E}_k$  from the mass and charge of the fissioning atom, the empirical systematics [24] is used (see picture 3):

$$\bar{E}_k = 0.1178 \cdot \frac{Z_0^2}{A^{1/3}} + 5.8 \text{ MeV} \quad (23)$$

This energy, generally speaking, should be substantially distributed among fission fragments in various ways [23, 26, 29, 31, 32, 34, 36, 37, 40, 43]. Here we study the difference in this distribution only for the 2 main fission modes: symmetric and asymmetric fission. This implies that sufficient experimental information for the construction of a reliable approximation is available only for these modes.

In symmetric fission the fragments with  $A = A_S$  have the maximum kinetic energy  $E_k^{max}$  [23, 26, 29, 40]. The experimental data for the evaluation of the average kinetic energy of fission fragments versus this maximum kinetic energy as a function of the heaviest fragment mass are shown in picture 9. They well approximate the expression:

$$\epsilon(A) = \frac{\overline{E}_k(A)}{E_k^{max}} = \begin{cases} 1 - b\left(\frac{A-A_m}{A_0}\right)^2 \\ 1 - b\left(\frac{10}{A_0}\right) - 2\left(\frac{10}{A_0}\right)b\frac{(A-A_m-10)}{A_0} \end{cases} \quad (24)$$

with  $A_m=A_S$  and  $b= 5.32$

The mean square deviation of the kinetic energy from its averaged value in the symmetric mode of the low energy fission is though to be independent from  $A$  and to assume the value  $\sqrt{\sigma_E^2} \cong 8$  MeV [29, 40].

In asymmetric fission the maximum kinetic energy is possessed by fragments from the fission mode where the heaviest fragment has mass  $A = A_1 = 134$ . Experimental data for evaluation of the averaged kinetic energy versus this maximum kinetic energy as a function of the mass of the heaviest fragment are reported in picture 9. They can be represented by expression (24) as well with parameters  $A_m=A_1$  e  $b = 23.5$ . The standard square deviation of the kinetic energy in the asymmetric mode assumes the value  $\sqrt{\sigma_E^2} \cong 10$  MeV [26, 29, 31, 32, 36].

In such a construction, in order to determine the fission fragment energy, it is necessary knowing the maximum kinetic energy  $(\overline{E}_k^{max})_i$  separately for the symmetric fission mode ( $i= \text{sym}$ ) and the asymmetric one ( $i=\text{asy}$ ). This is obtained from the average kinetic energy of fragments according to the formula:

$$(\overline{E}_k^{max})_i = (\overline{E}_k)_i \cdot \left( \frac{\int \epsilon(A)Y_i(A)dA}{\int Y_i(A)dA} \right)^{-1} \quad (25)$$

From the data analysis [26, 31, 32, 36] it follows that in the symmetric mode of fission, the averaged kinetic energy of the fragments is about 12.5 MeV smaller than in the symmetric case. Thus:

$$\begin{cases} (\bar{E}_k)_{sym} = \bar{E}_k - 12.5 \cdot X_{asy} \text{ MeV} & (26.a) \\ (\bar{E}_k)_{asy} = \bar{E}_k + 12.5 \cdot X_{asy} \text{ MeV} & (26.b) \end{cases}$$

where  $X_{asy}$  and  $X_{sym}$  are the fraction of fission fragments generated in the symmetric and asymmetric modes of fission.

As a consequence they can be found from the mass distributions  $Y_{asy}(A)$  and  $Y_{sym}(A)$  with the help of the relation:

$$\begin{cases} X_{sym} = \int Y_{sym}(A)dA / \int Y(A)dA \\ X_{asy} = \int Y_{asy}(A)dA / \int Y(A)dA \end{cases}$$

For the symmetric and asymmetric mode of fission, the distribution according to the kinetic energy of A mass fragments is described by a Gaussian with average value  $\bar{E}_k(A)$  and dispersion  $\sqrt{\sigma_E^2}$ , which can be obtained through the method above mentioned.

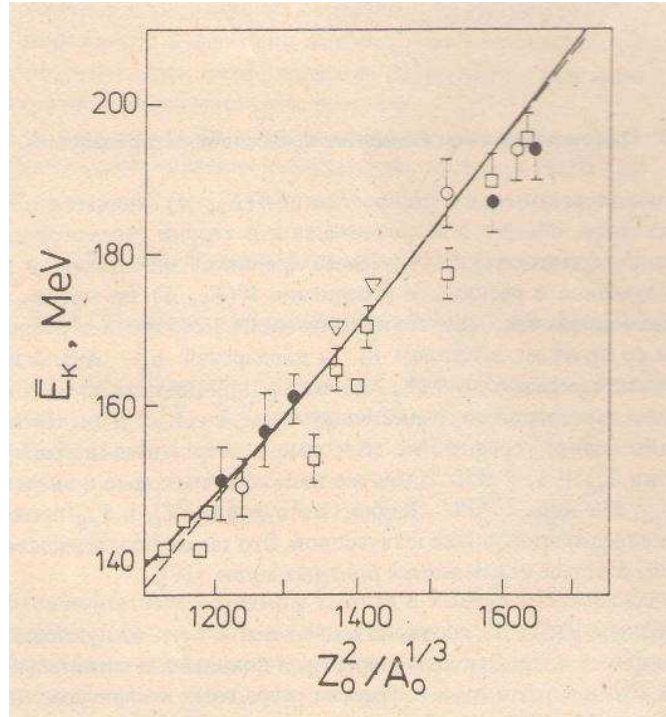


Figure 3: DEPENDENCE OF THE AVERAGE KINETIC ENERGY  $\bar{E}$  FROM  $Z_0^2/A_0^{1/3}$ : THE SOLID LINE IS THE CALCULATION ACCORDING THE DIFFUSION MODEL, POINTS ACCORDING TO THE SYSTEMATICS [24]. REFERENCES OF EXPERIMENTAL WORKS ARE GIVEN IN [10].

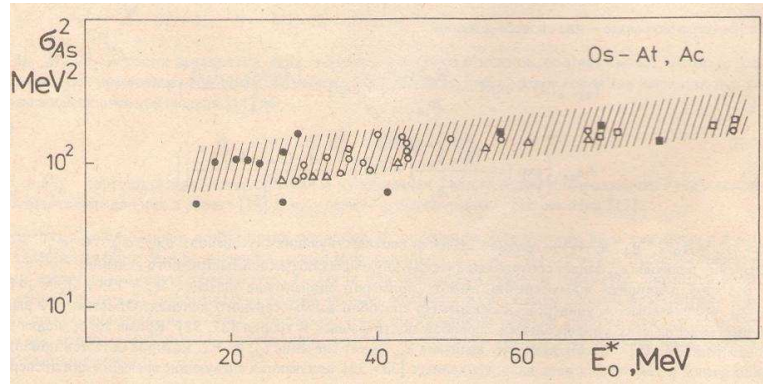


Figure 7: DISPERSION  $\sigma_{A_s}^2$  OF THE MASS DISTRIBUTION OF FRAGMENTS OF SYMMETRIC FISSION AS A FUNCTION OF THE EXCITATION ENERGY  $E_0^*$ . EXPERIMENTAL DATA [23, 26, 31, 32, 39 - 41] ARE SHOWN WITH DIFFERENT SYMBOLS FOR REACTIONS INDUCED BY DIFFERENT PARTICLES:  $\bullet$  = p, d;  $\Delta$  =  ${}^3\text{He}$ ;  $\circ$  =  $\alpha$ ;  $\blacksquare$  =  ${}^{12}\text{C}$ ;  $\square$  =  ${}^{16}\text{O}$ .

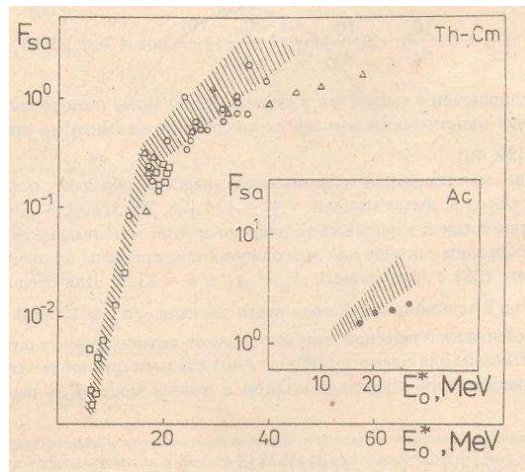


Figure 8: RATIO  $F_{sa}$  OF THE SYMMETRIC PEAK TO THE ASYMMETRIC IN THE MASS DISTRIBUTION OF FRAGMENTS AS A FUNCTION OF THE EXCITATION ENERGY  $E_0^*$  OF THE FISSIONING NUCLEUS. EXPERIMENTAL DATA [29, 33 - 35, 41 - 44] ARE SHOWN WITH DIFFERENT SYMBOLS FOR REACTIONS INDUCED BY DIFFERENT PARTICLES:  $\square$  = n,  $\Delta$  = p;  $\circ$  =  $\alpha$ ;  $\bullet$  = p, d.

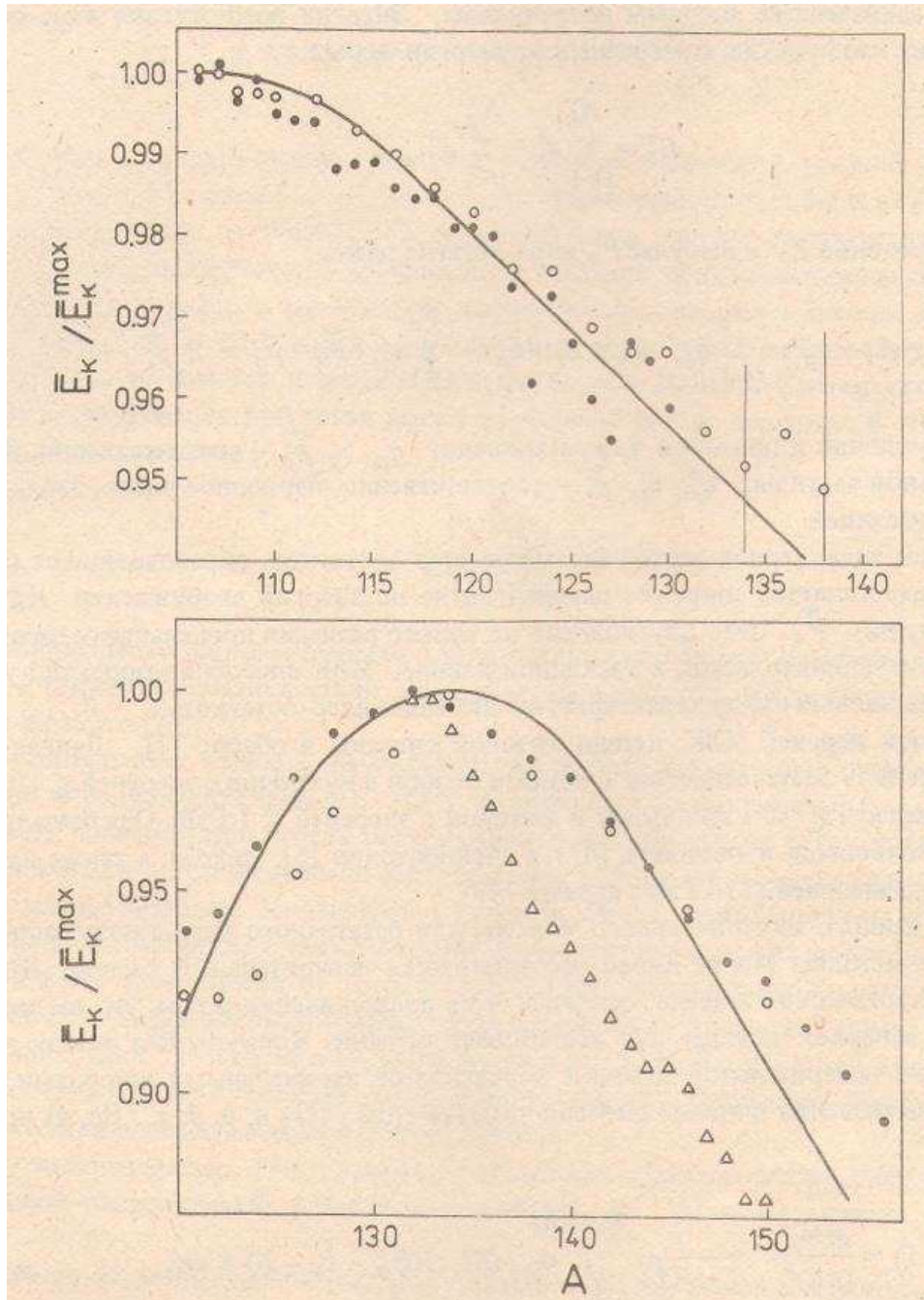


Figure 9: RATIO OF THE AVERAGE KINETIC ENERGY OF FRAGMENTS TO THE MAXIMUM KINETIC ENERGY AS A FUNCTION OF THE MASS NUMBER  $A$  OF THE HEAVIEST FRAGMENT  $\bar{E}_k / \bar{E}_k^{max}$  FOR SYMMETRIC (UPPER PANEL) AND ASYMMETRIC (LOWER PANEL) FISSION. LINES ARE CALCULATED ACCORDING TO THE APPROXIMATION (2). Upper panel: black circles are data from [40] for 53 MeV  $\alpha + \text{Bi}$ ; empty circles are data from [26, 31, 32] for 45 MeV  $\alpha + \text{Bi}$ . Lower panel: black circles are data from [26, 31, 32] for 10 MeV  $p + {}^{241}\text{Am}$ ; empty circles are data from [37] for 13 MeV  $\alpha + {}^{226}\text{Ra}$ ; triangles are from [34] for thermal  $n + {}^{235}\text{U}$ .

- [1] V. S. Barashenkov, A. S. Iljionov, V. D. Toneev, N. M. Sobolevsky, *Physics-Uspekhi*, **109** (1973) 91.
- [2] V. E. Bunakov, G. V. Matvejev, *Z. Phys.*, **A332** (1985) 511.
- [3] C. Ngo *et al.*, *Nucl. Phys.*, **A400** (1983) 295c.  
W. Q. Shen *et al.*, *Europhys.* **1** (1986) 113.
- [4] W. J. Swiatecki, *Three Lectures on Macroscopic Aspect of Nuclear Dynamics*, In: *Progr. in Part. and Nucl. Phys.*  
Ed. D. Wilkinson. - Oxford etc. : Pergamonn Press, 1980, Vol. 4, p. 383 - 450.
- [5] A. S. Iljionov, V. I. Nazaruk, S. E. Chigrinov. *Nucl. Phys.*, **A382** (1982) 378.
- [6] A. S. Botvina, A. S. Iljionov, I. N. Mishustin, *Nucl. Phys.*, **A507** (1990) 649.
- [7] A. S. Iljionov, M. V. Mebel, N. Bianchi *et al.*, *Nucl. Phys.*, **A543** (1992) 517.
- [8] A. S. Iljionov, M. V. Mebel, C. Guaraldo *et al.*, *Phys. Rev.*, **C39** (1989) 1420.
- [9] A. S. Iljionov, D. I. Ivanov, M. V. Mebel *et al.*, *Nucl. Phys.*, **A539** (1992) 263.
- [10] G. D. Adeev, I. I. Gonchar, V. V. Pashkevich *et al.*, *Phys. of Elementary Part. and Atomic Nucl. (EchaYa)* **19** (1988) 1229.
- [23] F. Plasil, D. S. Burnett, H. C. Britt, S. G. Thompson, *Phys. Rev.*, **142** (1966) 696.
- [24] V. E. Viola, K. K. Wiatkowski, M. Walker, *Phys. Rev.* **C31** (1985) 1550.
- [26] M. G. Itkis, V. N. Okolovich, A. Ya. Rusanov, G. N. Smirenkin, *Phys. of Elementary Part. and Atomic Nucl. (EchaYa)* **19** (1988) 701.
- [29] J. R. Huizenga, R. V. Andenbosch, *Nuclear Fission*, Academic Press, N. Y. & London, 1973.
- [31] S. D. Beyzin *et al.*, *Yadernaya fizika*, **53** (1991) 656.
- [32] M. G. Itkis *et al.*, *Yadernaya fizika*, **53** (1991) 1238.
- [33] H. H. Kintter *et al.*, *Z. Naturforsch.*, **A42** (1987) 786.
- [34] C. H. Straedl *et al.*, *Nucl. Phys.*, **A462** (1987) 85.
- [35] T. O. Hsuki *et al.*, *Phys. Rev.*, **C40** (1989) 2144.
- [36] A. Matthies *et al.*, *Z. Phys.*, **A337** (1990) 439.
- [37] B. D. Wilkins *et al.*, *Phys. Rev.*, **C14** (1976) 1832.
- [38] U. Brosa *et al.*, *Z. Phys.*, **A325** (1986) 241.  
U. Brosa *et al.*, *Z. Naturforsch.*, **A41** (1986) 1341.
- [39] E. F. Neuzil, A. W. Fairhall, *Phys. Rev.*, **129** (1963) 2705.
- [40] F. Plasil *et al.*, In: *Proc. of the 2-nd. IAEA Symp. on the Phys. and Chem. of Fission*. Vienna, 1969, p. 505.
- [41] D. G. Perry, A. W. Fairhall, *Phys. Rev.* **C4** (1971) 977.
- [43] I. F. Croall, J. G. Chiningname, *Nucl. Phys.* **A125** (1969) 401.
- [45] G. S. Iegert *et al.*, *Phys. Rev.* **C14** (1976) 1864.
- [46] A. C. Wahl *et al.*, In: *Proc. of the 2-nd. IAEA Symp. on the Phys. and Chem. of Fission*. Vienna, 1969, p. 813.

# APPENDIX C: FLUKA files

## FLUKA input file

TITLE

235U dioxide transparency to FFs. Cylinder: r=4 cm, h=1.6E-5 cm (m235=15.2mg)

DEFAULTS ICARUS

\*...+....1....+....2....+....3....+....4....+....5....+....6....+....7....+....8

\*

\* Simulate FFs coming out from the 235U target

SOURCE

BEAM -100.0 HEAVYION

\* FFs are uniformly emitted from the U3O8 target

GEOBEGIN COMBINAT

Large

\*...+....1....+....2....+....3....+....4....+....5....+....6....+....7....+....8

RPP 1 -90000.0 +90000.0 -90000.0 +90000.0 -90000.0 +90000.0

RPP 2 -20000.0 +20000.0 -20000.0 +20000.0 -20000.0 +20000.0

\* Cylinder defining the external vacuum world

ZCC 3 0.0 0.0 4.0

ZCC 4 0.0 0.0 6.0

\* Planes

XYP 5 0.0

XYP 6 4.2633E-5

XYP 7 0.5

XYP 8 1.0

\*...+....1....+....2....+....3....+....4....+....5....+....6....+....7....+....8

END

\*

\*

\* Region definition

\*

\*

\* Blackhole

001 10 +1 -2

\* Void

002 10OR +2 +5OR +2 -8OR +2 -4 -5 +8

\* Target

003 10 +3 -5 +6

\* Argon around the target

004 10OR +4 -3 -5 +6OR +4 -6 +7

```

* Argon again
005 10 +4 -7 +8
*...+...1....+...2....+...3....+...4....+...5....+...6....+...7....+...8
END
GEOEND +5.0 +5.0 +20.0 0.0 0.0 -20.0 DEBUG
GEOEND 10.0 10.0 40.0 &
*...+...1....+...2....+...3....+...4....+...5....+...6....+...7....+...8
* Material definition
MATERIAL 6.0 12.0107 2.0 6.0 CARBON
MATERIAL 8.0 15.994 0.00133 8.0 OXYGEN
MATERIAL 18.0 39.948 0.00166 20.0 ARGON
MATERIAL 92.0 235.044 18.9 26.0 235.0 235-U
MATERIAL 9.0 18.99840 0.001696 27.0 FLUORINE
MATERIAL 0.0 0.0 8.38 28.0 U3O8
MATERIAL 0.0 0.0 3.656E-3 29.0 CF4
MATERIAL 0.0 0.0 1.407E-3 30.0 ArCF4
*...+...1....+...2....+...3....+...4....+...5....+...6....+...7....+...8
*
* U3O8
* Composition
COMPOUND 8.0 8.0 3.0 26.0 U3O8
*
*
*
* CF4
*
COMPOUND 1.0 6.0 4.0 27.0 CF4
*
*
* ArCF4
*
COMPOUND -0.9 20.0 -0.1 29.0 ArCF4
*...+...1....+...2....+...3....+...4....+...5....+...6....+...7....+...8
* Material assignment
ASSIGNMA 1.0 1.0
ASSIGNMA 2.0 2.0
ASSIGNMA 28.0 3.0
ASSIGNMA 30.0 4.0
ASSIGNMA 30.0 5.0
*...+...1....+...2....+...3....+...4....+...5....+...6....+...7....+...8

```

```
EVENTYPE 2.0 EVAP
PHYSICS 3.0 EVAPORAT
*PHOTONUCL 1.0 6.0 30.0
*
*
*
*
* Score the energy deposition event per event
*
*
*
EVENTBIN 2.0 208.0 -36.0 4.0 0.0 0.0 UNF
EVENTBIN 4.0 0.0 0.0 1.0 &
*...+...1....+...2....+...3....+...4....+...5....+...6....+...7....+...8
RANDOMIZ 1.0
START 5000000.0
STOP
```

**FLUKA source file**

\*\$ CREATE SOURCE.FOR

\*COPY SOURCE

\*

\*==== source =====\*

\*

SUBROUTINE SOURCE ( NOMORE )

INCLUDE '(DBLPRC)'

INCLUDE '(DIMPAR)'

INCLUDE '(IOUNIT)'

\*

\*\_\_\_\_\_\*

**\* Version modified for FFs generation \***

**DIMENSION ASYM(0:235)**

**DIMENSION ANSYM(0:235)**

**DIMENSION ADIST(0:235)**

**DIMENSION CUMUL(0:235)**

**DIMENSION ENEDGE (0:1099)**

**DIMENSION FLUX (0:1099)**

**DIMENSION TEGR(0:1099)**

\* \*

\*\_\_\_\_\_\*

\*

INCLUDE '(BEAMCM)'

INCLUDE '(FHEAVY)'

INCLUDE '(FLKSTK)'

INCLUDE '(IOIOCM)'

INCLUDE '(LTCLCM)'

INCLUDE '(PAPROP)'

INCLUDE '(SOURCM)'

INCLUDE '(SUMCOU)'

\*

LOGICAL LFIRST

\*

SAVE LFIRST

DATA LFIRST / .TRUE. /

**\* Neutron energy group boundaries in MeV**

**\* The n\_TOF neutron flux is used**

**DATA ENEDGE /**

```

& 9.885531e-09,
& 1.011579e-08,
& [...]
& 9.660509e+02 /
* Flux
*-----*
DATA FLUX/
& 0.000000e+00,
& 0.000000e+00,
& [...],
& 5.442496e+03 /
*=====*
* *
* BASIC VERSION *
* *
*=====*
NOMORE = 0
* +-----*
* | First call initializations:
IF ( LFIRST ) THEN
* | *** The following 3 cards are mandatory ***
TKESUM = ZERZER
LFIRST = .FALSE.
LUSSRC = .TRUE.
* Calculate the cumulative function
TEGR(0)=FLUX(0)
DO I = 1, 1099
TEGR(I) = TEGR(I-1) + FLUX(I)
c If you want to use a simple trapezium integration, decomment the
c following two lines
c TEGR(I) = TEGR(I-1) + HLFHLF*(FLUX(I)+FLUX(I-1)) *
c & (I-(I-1))
END DO
* Normalize the cumulative function to 1
SOMMA = TEGR(1099)
DO I =0, 1099
TEGR(I)=TEGR(I)/SOMMA
END DO
* | *** User initialization ***
END IF

```

```

* |
* +-----*
* Push one source particle to the stack. Note that you could as well
* push many but this way we reserve a maximum amount of space in the
* stack for the secondaries to be generated
* Npflka is the stack counter: of course any time source is called it
* must be =0
NPFLKA = NPFLKA + 1
* Wt is the weight of the particle
WTFLK (NPFLKA) = ONEONE
WEIPRI = WEIPRI + WTFLK (NPFLKA)
* Particle type (1=proton.....). Ijbeam is the type set by the BEAM
* card
* +-----*
* Insert here the excitation energy of the compound nucleus
* The excitation energy  $U=E(235U)+E(n)+T(n)-E(236)$ 
* with  $E(235U)$  = mass _energy of 235U
*  $E(n)$  = mass _energy of neutron
*  $T(n)$  = kinetic energy of the incident spallation neutron
*  $E(236U)$  = mass _energy of 236U
* Keep in mind that  $E(235U)+E(n)-E(236U) = 6.5\text{MeV}$ 
*
*
*
* The kinetic energy of the spallation neutron si sampled from the
* neutron flux spectrum at the n_TOF facility
*
*
*
XYZ= FLRNDM(XYZW)
DO 10 I=0, 1098
IF (TEGR(I) .GE. XYZ) THEN
TNEUTENE = ENEDGE(I) + (ENEDGE(I+1) -ENEDGE(I))*
& (XYZ-TEGR(I))/(TEGR(I+1) - TEGR(I))
GO TO 20 END IF
10 CONTINUE
20 CONTINUE
EMIN = 6.5
U = EMIN + TNEUTENE
IF (U .LE. 16.25) THEN

```

```

WA = EXP(0.538*U-9.9564)
END IF
IF (U .GT. 16.25) THEN
WA = EXP(0.09197*U-2.7003)
END IF
*
*
*
*
*
*
*
*
*
*
* +-----*
* | (Radioactive) isotope:
IF ( IJBEAM .EQ. -2 .AND. LRDBEA ) THEN
IARES = IPROA
IZRES = IPROZ
IISRES = IPROM
CALL STISBM ( IARES, IZRES, IISRES )
IJHION = IPROZ * 1000 + IPROA
IJHION = IJHION * 100 + KXHEAV
IONID = IJHION
CALL DCDION ( IONID )
CALL SETION ( IONID )
* |
* +-----*
* | Heavy ion:
ELSE IF ( IJBEAM .EQ. -2 ) THEN
CUMUL(0) = ZERZER
SIGMA = EXP(0.00553*U+2.1386)
SIGMA1 = 0.5 *5.6
SIGMA2 = 5.6
IA1 = 141
IA2 = 92
IAINI= 235
IAMEZ=235/2
c AMEZZI =INT(AMEZ)

```

```

IAHS=(IA1+IA2)/2
c IAHS=INT(AH1S)
* AMEZZI=235./2
* AHS=(A1+A2)/2
* Take A/2=120 FOR 241Am
DO I=0, 235
ASYM(I) = EXP ( -((FLOAT(I-IAMEZ)**2))/(2.*(SIGMA**2)))
ANSYM(I) = EXP(-((FLOAT(I-IA2)**2)/(2.*SIGMA2**2)) +
& EXP(-((FLOAT(I-(IAINI-IA2)))**2)/(2.*SIGMA2**2)) + HLFHLF *
& (EXP(-((FLOAT(I-IA1)**2)/(2.*SIGMA1**2)) +
& EXP(-((FLOAT(I-(IAINI-IA1)))**2)/(2.*SIGMA1**2)) )
* WRITE (lnuout,*) ASYM(I), ANSYM(I)
END DO
W = ((WA - ANSYM(IAMEZ))/(1-WA*(ASYM(IAHS))))
DO I=0,235
ADIST(I)= ANSYM(I) + W*ANSYM(I)
END DO
* Calculate the cumulative function (simple trapezium integration)
DO I = 1, 235
CUMUL(I) = CUMUL(I-1) + HLFHLF*(ADIST(I)+ADIST(I-1))
END DO
SUM = CUMUL(235)
DO I = 1, 235
CUMUL(I)=CUMUL(I)/SUM
END DO
* Sample from the mass distribution
XI = FLRNDM(DUMMY)
* WRITE(lnuout,*) XI
DO 1 I=1, 234
IF (CUMUL(I) .GE. XI) THEN
IMASS = I
GO TO 2
END IF
1 CONTINUE
2 CONTINUE
MASS = IMASS
IPROA = MASS
IF (MASS .GE. 134) THEN
DELTAZ= -0.45
END IF

```

```

IF ((MASS .GT. 101).AND.(MASS .LT. 134)) THEN
DELTAZ = -0.45*FLOAT(MASS -117)/FLOAT(134-117)
END IF
IF (MASS .LE. 101) THEN
DELTAZ = 0.45
END IF
ZPEAK = FLOAT(IMASS) * 92./235. + DELTAZ
CALL FLNRRN(RGAUSS)
CALL FLNRRN(RGAUSS)
IZ = INT(ZPEAK - 0.6*RGAUSS)
IPROZ = IZ
IJHION = IPROZ * 1000 + IPROA
IJHION = IJHION * 100 + KXHEAV
IONID = IJHION
CALL DCDION ( IONID )
CALL SETION ( IONID )
ILOFLK (NPFLKA) = IJHION
* | Flag this is prompt radiation
LRADDC (NPFLKA) = .FALSE.
* |
* +-----*
* | Normal hadron:
ELSE
IONID = IJBEAM
ILOFLK (NPFLKA) = IJBEAM
* | Flag this is prompt radiation
LRADDC (NPFLKA) = .FALSE.
END IF
* |
* +-----*
* From this point ....
. * Particle generation (1 for primaries)
LOFLK (NPFLKA) = 1
* User dependent flag:
LOUSE (NPFLKA) = 0
* User dependent spare variables:
DO 100 ISPR = 1, MKBMX1
SPAREK (ISPR,NPFLKA) = ZERZER
100 CONTINUE
* User dependent spare flags:

```

```

DO 200 ISPR = 1, MKBMX2
ISPARK (ISPR,NPFLKA) = 0
200 CONTINUE
* Save the track number of the stack particle:
ISPARK (MKBMX2,NPFLKA) = NPFLKA
NPARMA = NPARMA + 1
NUMPAR (NPFLKA) = NPARMA
NEVENT (NPFLKA) = 0
DFNEAR (NPFLKA) = +ZERZER
* ... to this point: don't change anything
* Particle age (s)
AGESTK (NPFLKA) = +ZERZER
AKNSHR (NPFLKA) = -TWOTWO
* Group number for "low" energy neutrons, set to 0 anyway
IGROUP (NPFLKA) = 0
*_____*
* *
* Kinetic energy of the FFs (GeV/nucleons) *
* *
*_____*
*
*
* The total kinetic energy of the fragments is about 80% * (Q +T)
* You have to take into account that fission in this case is
* induced by neutrons with energy up to 1 GeV!!!
* scrivi anche il Q della reazione...
* TMAX = TNEUTENE + 200.0
TMAX = TNEUTENE *0.8+ 167.37
* TMAX = 167.37
TTOT=TMAX*FLOAT(IAINI-MASS)/FLOAT(IAINI)
CALL FLNRRN(RGAUSS)
IF (MASS.LE.117) THEN
ENE = TTOT - RGAUSS* 5.33
END IF
IF (MASS.GT.117) THEN
ENE = TTOT - RGAUSS* 6.66
END IF
ENE = ENE *0.001
TKEFLK (NPFLKA) = ENE
WRITE (LNUOUT,*) MASS,' ',IZ,' ',TNEUTENE,' ',ENE

```

```

* Particle momentum
* PMOFLK (NPFLKA) = PBEAM
PMOFLK (NPFLKA) = SQRT ( TKEFLK (NPFLKA) * ( TKEFLK
(NPFLKA)
& + TWOTWO * AM (IONID) ) )
*
* *
* Cosines (tx,ty,tz)
* You want a 4PI isotropi angular distribution
COSTH = ONEONE -2.D0 * FLRNDM (RRRR)
IF (COSTH.GT.ONEONE) COSTH = ONEONE
IF (COSTH.LT.-ONEONE) COSTH = -ONEONE
ANG = TWOPIP * FLRNDM (SSSS)
UBEAM=SQRT( ONEONE - COSTH * COSTH) * COS(ANG)
VBEAM=SQRT( ONEONE - COSTH * COSTH) * SIN(ANG)
WBEAM=COSTH
TXFLK (NPFLKA) = UBEAM
TYFLK (NPFLKA) = VBEAM
TZFLK (NPFLKA) = WBEAM
* TZFLK (NPFLKA) = SQRT ( ONEONE - TXFLK (NPFLKA)**2
* & - TYFLK (NPFLKA)**2 )
* Polarization cosines:
TXPOL (NPFLKA) = -TWOTWO
TYPOL (NPFLKA) = +ZERZER
TZPOL (NPFLKA) = +ZERZER
* Particle coordinates
99 X1 = 0.D0
X2 = 4.D0
XFLK (NPFLKA) = -X2 + FLRNDM(XXXX)*TWOTWO *X2
Y1 = 0.D0
Y2 = 4.D0
YFLK (NPFLKA) = -Y2 + FLRNDM(XXXX)*TWOTWO *Y2
CHECK = YFLK (NPFLKA)**2 + XFLK (NPFLKA)**2
IF (CHECK.GT.16.0) GO TO 99
Z1 = 0.D0
Z2 = 4.2635E-5
ZFLK (NPFLKA) = ( Z2 -Z1 ) * FLRNDM(ZZZZ)
* Calculate the total kinetic energy of the primaries: don't change
IF ( ILOFLK (NPFLKA) .EQ. -2 .OR. ILOFLK (NPFLKA) .GT. 100000 )
& THEN

```

```

TKESUM = TKESUM + TKEFLK (NPFLKA) * WTFLK (NPFLKA)
ELSE IF ( ILOFLK (NPFLKA) .NE. 0 ) THEN
TKESUM = TKESUM + ( TKEFLK (NPFLKA) + AMDISC (ILOFLK(NPFLKA))
)
& * WTFLK (NPFLKA)
ELSE
TKESUM = TKESUM + TKEFLK (NPFLKA) * WTFLK (NPFLKA)
END IF
RADDLY (NPFLKA) = ZERZER
* Here we ask for the region number of the hitting point.
* NREG (NPFLKA) = ..
. * The following line makes the starting region search much more
* robust if particles are starting very close to a boundary:
CALL GEOCRS ( TXFLK (NPFLKA), TYFLK (NPFLKA), TZFLK (NPFLKA) )
CALL GEOREG ( XFLK (NPFLKA), YFLK (NPFLKA), ZFLK (NPFLKA),
& NRGFLK(NPFLKA), IDISC )
* Do not change these cards:
CALL GEOHSM ( NHSPNT (NPFLKA), 1, -11, MLATTC )
NLATTC (NPFLKA) = MLATTC
CMPATH (NPFLKA) = ZERZER
CALL SOEVSU
RETURN
*==== End of subroutine Source =====*
END

```



# List of Figures

|    |   |    |
|----|---|----|
| 1  | WORLD MARKETED ENERGY CONSUMPTION. YELLOW DATA (HISTORY) FROM [7], ORANGE DATA (PROJECTION) FROM [8]. . . . .   | 3  |
| 2  | ELECTRICITY GENERATION BY FUEL IN 2008. DATA TAKEN FROM [9] AND REVISED IN A PIE GRAPH. . . . .   | 3  |
| 3  | TH/U FUEL CYCLE. PICTURE TAKEN FROM [14]. . . . .   | 11 |
| 4  | PS COMPLEX. PICTURE TAKEN FROM [20]. . . . .  | 18 |
| 5  | SCHEMATIC REPRESENTATION OF A SPALLATION PROCESS CAUSED BY 1 GeV INCIDENT PROTON. THE SOLID ARROWS REFER TO INTRANUCLEAR CASCADE, WHILE DOTTED ARROWS TO INTERNUCLEAR CASCADE [24]. . . . . | 20 |
| 6  | NUMBER OF NEUTRONS PER INCIDENT PROTON AS A FUNCTION OF THE PROTON ENERGY [25]. . . . .   | 21 |
| 7  | LEAD TARGET. . . . .  | 22 |
| 8  | PICTURE OF THE TARGET ZONE. . . . .   | 23 |
| 9  | NEUTRON BEAM LINE . . . . .   | 24 |
| 10 | SWEEPING MAGNET. . . . .  | 25 |
| 11 | INSTANTENOUS NEUTRON FLUX AT DIFFERENT FACILITIES. . . . .  | 27 |
| 12 | AVERAGED NEUTRON FLUX AT DIFFERENT FACILITIES. . . . .  | 28 |
| 13 | MEASURED AND MONTE CARLO SIMULATED NEUTRON FLUX IN THE EXPERIMENTAL AREA. . . . .   | 29 |
| 14 | RELATIVE ENERGY UNCERTAINTY DUE TO THE PROTON BEAM TIME SPREAD. . . . .   | 30 |
| 15 | RELATIVE ENERGY UNCERTAINTY DUE TO MODERATION PATH AND BEAM TIME SPREAD. . . . .  | 31 |
| 16 | SCHEMATIC LAYOUT OF 4 FIC 1 CELLS. . . . .  | 34 |
| 17 | NEUTRON FLUX ATTENUATION AT DIFFERENT POSITIONS INSIDE FIC (FLUKA SIMULATION). . . . .  | 38 |
| 18 | FIC 1 SIGNAL PICK-UP. . . . .   | 39 |
| 19 | FIC 1 Front-end electronics. Layout copied from the n_TOF web-site  | 40 |
| 20 | DATA FLOW FROM DETECTORS TO TAPES. PICTURE TAKEN FROM [47].   | 42 |

|    |  |    |
|----|--|----|
| 21 | MATCHING OF WAVE FUNCTIONS AT THE BOUNDARY OF A SQUARE POTENTIAL WELL. (A) FAR FROM RESONANCE THE EXTERIOR AND INTERIOR WAVE FUNCTIONS MATCH BADLY, AND LITTLE PENETRATION OF THE NUCLEUS OCCURS. (B) AS THE MATCHING IMPROVES, THE PENETRATION GETS HIGHER. (C) THE INCIDENT PARTICLE HAS A HIGH PENETRATION PROBABILITY AND THE CROSS SECTION SHOWS A MAXIMUM. THIS IS THE RESONANT CONDITION. (PICTURE TAKEN FROM [KRA87].) . . . . . | 44 |
| 22 | RAW DATA. . . . .  | 46 |
| 23 | TIME SCHEME OF THE RECORDED SIGNAL. . . . .  | 47 |
| 24 | RECORDED RAW SIGNALS FROM NEIGHBORING ELECTRODES. . . . .  | 48 |
| 25 | SIGNALS AFTER SUBTRACTION OF $\gamma$ -FLASH. . . . .  | 48 |
| 26 | PULSE HEIGHT DISTRIBUTION OF $^{235}\text{U}$ FISSION EVENTS. THE DISCRIMINATION THRESHOLD SET ON THE CDF IS ALSO VISIBLE. PICTURE TAKEN FROM [27]. . . . .  | 49 |
| 27 | GEOMETRY CONSIDERED IN EACH FLUKA [42] SIMULATION. . . . .   | 52 |
| 28 | MASS DISTRIBUTION OF FFs GENERATED IN NEUTRON INDUCED FISSION OF $^{235}\text{U}$ . . . . .  | 52 |
| 29 | KINETIC ENERGY DISTRIBUTION OF FFs GENERATED IN NEUTRON INDUCED FISSION OF $^{235}\text{U}$ . . . . .  | 52 |
| 30 | ENERGY DEPOSITED IN 0.5 CM OF $\text{ARCF}_4$ BY <i>light</i> FFs GENERATED IN NEUTRON INDUCED FISSION OF $^{235}\text{U}$ . . . . .   | 53 |
| 31 | ENERGY DEPOSITED IN 0.5 CM OR $\text{ARCF}_4$ BY <i>heavy</i> FFs GENERATED IN NEUTRON INDUCED FISSION OF $^{235}\text{U}$ . . . . .   | 53 |
| 32 | ENERGY DEPOSITED IN 7 CM OR $\text{ARCF}_4$ BY THE FFs GENERATED IN NEUTRON INDUCED FISSION OF $^{235}\text{U}$ . . . . .  | 53 |
| 33 | SIMULATION OF THE ENERGY DEPOSITED BY FISSION FRAGMENTS IN THE FIC FOLDED WITH AN ENERGY RESOLUTION OF 15% AND NORMALIZED TO THE MEASURED PULSE HEIGHT SPECTRUM. THE THRESHOLD AT CHANNEL 35 CORRESPONDS TO A DEPOSITED ENERGY OF ABOUT 18 MEV. . . . .  | 53 |
| 34 | SIMULATED BEAM PROFILE FOR NEUTRON ENERGY BETWEEN 100 KEV AND 100 MEV FOR TWO TARGETS SPACED BY 16 CM. . . . .   | 58 |
| 35 | EXPERIMENTAL CORRELATION BETWEEN AMPLITUDE OF DETECTED DIGNSLS AND ENERGY OF THE INCIDENT NEUTRONS FOR $^{235}\text{U}$ CASE. SMALL AMPLITUDE PULSES IN THE HIGH NEUTRON ENERGY REGION ARE DUE TO FRAGMENTATION. . . . .   | 60 |
| 36 | EXPERIMENTAL AMPLITUDE DISTRIBUTION FOR $^{235}\text{U}$ . SIGNALS WITH AN AMPLITUDE HIGHER THAN 35 CHANNELS ARE DUE TO IONIZATION OF THE FIC GAS BY FISSION FRAGMENTS. . . . .  | 60 |

|    |   |    |
|----|---|----|
| 37 | EXPERIMENTAL DISTRIBUTION OF THE CHARGE TO AMPLITUDE RATIO VERSUS AMPLITUDE FOR $^{235}\text{U}$ . EVENTS BELOW THE DOT LINE CORRESPOND TO VIRTUAL SIGNALS. A THRESHOLD OF 35 CHANNELS ON AMPLITUDE IS APPLIED. . . . .   | 61 |
| 38 | EXPERIMENTAL DISTRIBUTION OF THE NUMBER OF DETECTED FISSION EVENTS AS A FUNCTION OF THE ENERGY OF THE NEUTRON INDUCING IT. A THRESHOLD OF 35 CHANNELS ON AMPLITUDE IS APPLIED AND EVENTS WITH A CHARGE TO AMPLITUDE RATIO SMALLER THAN 8 ARE DISCARDED. . . . . | 62 |
| 39 | DEAD TIME CORRECTION FACTOR. . . . .  | 62 |
| 40 | EXPERIMENTAL CHARGE DISTRIBUTION FOR $^{235}\text{U}$ ISOTOPE. . . . .  | 63 |
| 41 | SIMULATED ENERGY DEPOSITION FOR $^{235}\text{U}$ ISOTOPE. . . . .   | 63 |
| 42 | CALIBRATION CURVE. A LINEAR RELATION IS VISIBLE. . . . .  | 65 |
| 43 | SIMULATED ENERGY DEPOSITION (10% ENERGY RESOLUTION IS APPLIED) CALIBRATED ON THE EXPERIMENTAL HISTOGRAM OF AMPLITUDES. . . . .  | 65 |
| 44 | EXPERIMENTAL AMPLITUDE DISTRIBUTION FOR $^{238}\text{U}$ . SIGNALS WITH AN AMPLITUDE HIGHER THAN 35 CHANNELS ARE DUE TO IONIZATION OF THE FIC GAS BY FISSION FRAGMENTS. . . . .   | 67 |
| 45 | EXPERIMENTAL DISTRIBUTION OF THE CHARGE TO AMPLITUDE RATIO VERSUS AMPLITUDE FOR $^{238}\text{U}$ . EVENTS BELOW THE DOT LINE CORRESPOND TO VIRTUAL SIGNALS. A THRESHOLD OF 35 CHANNELS ON AMPLITUDE IS APPLIED. . . . .   | 67 |
| 46 | EXPERIMENTAL DISTRIBUTION OF THE NUMBER OF DETECTED FISSION EVENTS AS A FUNCTION OF THE ENERGY OF THE NEUTRON INDUCING IT. A THRESHOLD OF 35 CHANNELS ON AMPLITUDE IS APPLIED AND EVENTS WITH A CHARGE TO AMPLITUDE RATIO SMALLER THAN 8 ARE DISCARDED. . . . . | 68 |
| 47 | DEAD TIME CORRECTION FACTOR. . . . .  | 69 |
| 48 | CALIBRATION CURVE. A LINEAR RELATION IS VISIBLE. . . . .  | 69 |
| 49 | SIMULATED ENERGY DEPOSITION (11.95% ENERGY RESOLUTION IS APPLIED) CALIBRATED ON THE EXPERIMENTAL HISTOGRAM OF AMPLITUDES. . . . .   | 69 |
| 50 | CALIBRAZIONE. . . . .   | 70 |
| 51 | COMPARISON BETWEEN N_TOF (20 BINS/DECADE) $^{238}\text{U}$ (N,F) EXPERIMENTAL CROSS SECTIONS AND DIFFERENT EVALUATIONS. . . . .   | 72 |
| 52 | COMPARISON BETWEEN N_TOF (20 BINS/DECADE) $^{238}\text{U}$ (N,F) EXPERIMENTAL CROSS SECTIONS AND DIFFERENT EVALUATIONS. . . . .   | 72 |
| 53 | COMPARISON BETWEEN N_TOF (20 BINS/DECADE) $^{238}\text{U}$ (N,F) EXPERIMENTAL CROSS SECTIONS AND PREVIOUS EXPERIMENTAL DATA. . . . .  | 73 |

|    |   |    |
|----|---|----|
| 54 | COMPARISON BETWEEN N_TOF (20 BINS/DECADE) <sup>238</sup> U (N,F) EXPERIMENTAL CROSS SECTIONS AND PREVIOUS EXPERIMENTAL DATA.  | 73 |
| 55 | EXPERIMENTAL AMPLITUDE DISTRIBUTION READ BY THE TWO ELECTRODES OF <sup>233</sup> U SEPARATELY, NORMALIZED FOR THE VALUE OF THE SAMPLE MASS.   | 75 |
| 56 | EXPERIMENTAL DISTRIBUTION OF THE CHARGE TO AMPLITUDE RATIO VERSUS AMPLITUDE FOR <sup>233</sup> U. EVENTS BELOW THE DOT LINE CORRESPOND TO VIRTUAL SIGNALS. A THRESHOLD OF 35 CHANNELS ON AMPLITUDE IS APPLIED.    | 76 |
| 57 | EXPERIMENTAL DISTRIBUTION OF DETECTED FISSION EVENTS FOR UNIT MASS AS A FUNCTION OF THE NEUTRON ENERGY. THE COMPATIBILITY BETWEEN THE TWO HISTOGRAMS IS USED AS A CROSS CHECK ON THE VALUES OF THE SAMPLE MASSES. | 77 |
| 58 | TOTAL DEAD TIME CORRECTION FACTOR TO BE APPLIED TO THE ANALYSIS OF THE <sup>233</sup> U ISOTOPE.  | 78 |
| 59 | SIMULATED ENERGY DEPOSITION (14.5% ENERGY RESOLUTION IS APPLIED) CALIBRATED ON THE EXPERIMENTAL HISTOGRAM OF AMPLITUDES FOR ELECTRODE # 13.   | 78 |
| 60 | SIMULATED ENERGY DEPOSITION (17.6% ENERGY RESOLUTION IS APPLIED) CALIBRATED ON THE EXPERIMENTAL HISTOGRAM OF AMPLITUDES FOR ELECTRODE # 16.   | 78 |
| 61 | COMPARISON BETWEEN N_TOF (20 BINS/DECADE) AND ENDFB-VII.0 $\sigma_{(n,f)}$ .  | 79 |
| 62 | COMPARISON BETWEEN N_TOF (20 BINS/DECADE) <sup>233</sup> U (N,F) EXPERIMENTAL CROSS SECTIONS AND DIFFERENT EVALUATIONS.   | 80 |
| 63 | COMPARISON BETWEEN N_TOF (20 BINS/DECADE) <sup>233</sup> U (N,F) CROSS SECTIONS AND PREVIOUS EXPERIMENTAL DATA.   | 80 |
| 64 | COMPARISON BETWEEN N_TOF (20 BINS/DECADE) <sup>233</sup> U (N,F) CROSS SECTIONS AND DIFFERENT EXPERIMENTAL DATA.  | 82 |
| 65 | COMPARISON BETWEEN N_TOF (20 BINS/DECADE) <sup>233</sup> U (N,F) EXPERIMENTAL CROSS SECTIONS AND DIFFERENT EXPERIMENTAL DATA.   | 82 |
| 66 | COMPARISON BETWEEN N_TOF (100 BINS/DECADE) <sup>233</sup> U (N,F) EXPERIMENTAL CROSS SECTIONS OBTAINED IN THE HIGH AND LOW ENERGY ANALYSIS. ENDF/B-VII.0 AND ENDF/B-VI.8 ARE REPORTED AS REFERENCE.               | 83 |
| 67 | COMPARISON BETWEEN N_TOF (20 BINS/DECADE) <sup>233</sup> U (N,F) EXPERIMENTAL CROSS SECTIONS OBTAINED IN THE HIGH ENERGY ANALYSIS OF FIC DATA WITH $\sigma_{(n,f)}$ EXTRACTED BY PPAC ANALYSIS.                   | 83 |

|    |   |    |
|----|---|----|
| 68 | EXPERIMENTAL AMPLITUDE DISTRIBUTION READ BY THE THREE ELECTRODES OF $^{243}\text{Am}$ SEPARATED, NORMALIZED FOR THE VALUE OF THE MASS SAMPLE. AN OFFSET OF 10 CHANNELS IS VISIBLE FOR ELECTRODE # 8. . . . .                              | 86 |
| 69 | EXPERIMENTAL AMPLITUDE DISTRIBUTION READ BY THE THREE ELECTRODES OF $^{243}\text{Am}$ SEPARATED, NORMALIZED FOR THE VALUE OF THE MASS SAMPLE. THE AMPLITUDES OF SIGNALS SEEN BY ELECTRODE # 8 ARE CORRECTED FOR THE OFFSET. . . . .       | 86 |
| 70 | EXPERIMENTAL DISTRIBUTION OF THE CHARGE TO AMPLITUDE RATIO VERSUS AMPLITUDE FOR ALL $^{243}\text{Am}$ SAMPLES. EVENTS BELOW THE DOT LINE CORRESPOND TO VIRTUAL SIGNALS. . . . .   | 87 |
| 71 | EXPERIMENTAL DISTRIBUTION OF DETECTED FISSION EVENTS FOR UNIT MASS AS A FUNCTION OF THE NEUTRON ENERGY. THE COMPATIBILITY AMONG THE THREE HISTOGRAMS IS USED AS A CROSS CHECK ON THE VALUES OF THE SAMPLE MASSES. . . . .                 | 88 |
| 72 | TOTAL DEAD TIME CORRECTION FACTOR TO BE APPLIED TO THE ANALYSIS OF THE $^{243}\text{Am}$ ISOTOPE. . . . .   | 89 |
| 73 | COMPARISON BETWEEN N_TOF (20 BINS/DECADE) AND ENDFB-VII.0 $\sigma_{(n,f)}$ . . . . .  | 90 |
| 74 | COMPARISON BETWEEN N_TOF (20 BINS/DECADE) $^{243}\text{Am}$ (N,F) EXPERIMENTAL CROSS SECTIONS AND DIFFERENT EVALUATIONS. . . . .  | 91 |
| 75 | COMPARISON BETWEEN N_TOF (20 BINS/DECADE) $^{243}\text{Am}$ (N,F) EXPERIMENTAL CROSS SECTIONS AND DIFFERENT EVALUATIONS. . . . .  | 91 |
| 76 | COMPARISON BETWEEN N_TOF (20 BINS/DECADE) $^{243}\text{Am}$ (N,F) CROSS SECTIONS AND PREVIOUS EXPERIMENTAL DATA. . . . .  | 93 |
| 77 | COMPARISON BETWEEN N_TOF (20 BINS/DECADE) $^{243}\text{Am}$ (N,F) CROSS SECTIONS AND PREVIOUS EXPERIMENTAL DATA. . . . .  | 93 |
| 78 | COMPARISON BETWEEN N_TOF (80 BINS/DECADE) $^{243}\text{Am}$ (N,F) CROSS SECTIONS OBTAINED IN THE HIGH AND LOW ENERGY ANALYSIS. . . . .  | 94 |
| 79 | EXPERIMENTAL AMPLITUDE DISTRIBUTION READ BY THE THREE ELECTRODES OF $^{241}\text{Am}$ SEPARATED AND NORMALIZED FOR THE VALUE OF THE MASS SAMPLE. . . . .  | 96 |
| 80 | EXPERIMENTAL DISTRIBUTION OF THE CHARGE TO AMPLITUDE RATIO VERSUS AMPLITUDE FOR ELECTRODE # 1 OF THE ISOTOPE $^{241}\text{Am}$ . ONLY AMP $\geq 58$ WERE CONSIDERED. EVENTS BELOW THE DOTTED LINE CORRESPONDS TO VIRTUAL SIGNALS. . . . . | 96 |
| 81 | EXPERIMENTAL DISTRIBUTION OF THE CHARGE TO AMPLITUDE RATIO VERSUS AMPLITUDE FOR ELECTRODE # 2 OF THE ISOTOPE $^{241}\text{Am}$ . ONLY AMP $\geq 58$ WERE CONSIDERED. EVENTS BELOW THE DOTTED LINE CORRESPONDS TO VIRTUAL SIGNALS. . . . . | 97 |

|    |  |     |
|----|--|-----|
| 82 | EXPERIMENTAL DISTRIBUTION OF THE CHARGE TO AMPLITUDE RATIO VERSUS AMPLITUDE FOR ELECTRODE # 3 OF THE ISOTOPE $^{241}\text{Am}$ . ONLY $\text{AMP} \geq 58$ WERE CONSIDERED. EVENTS BELOW THE DOTTED LINE CORRESPONDS TO VIRTUAL SIGNALS. . . . . | 97  |
| 83 | EXPERIMENTAL AMPLITUDE DISTRIBUTION OF SIGNALS READ BY ELECTRODE # 1. CONDITIONS DERIVED FROM PULSE SHAPE ANALYSIS HAVE BEEN APPLIED. . . . .  | 98  |
| 84 | EXPERIMENTAL DISTRIBUTION OF THE CHARGE TO AMPLITUDE RATIO VERSUS AMPLITUDE FOR $^{233}\text{U}$ SIGNALS COLLECTED BY ELECTRODE NUMBER 13. . . . .   | 99  |
| 85 | EXPERIMENTAL DISTRIBUTION OF THE CHARGE TO AMPLITUDE RATIO VERSUS AMPLITUDE FOR $^{241}\text{Am}$ SIGNALS COLLECTED BY ELECTRODE NUMBER 1. . . . .   | 99  |
| 86 | EXPERIMENTAL DISTRIBUTION OF THE CHARGE TO AMPLITUDE RATIO VERSUS AMPLITUDE FOR $^{233}\text{U}$ SIGNALS COLLECTED BY ELECTRODE NUMBER 13. . . . .   | 100 |
| 87 | EXPERIMENTAL DISTRIBUTION OF THE CHARGE TO AMPLITUDE RATIO VERSUS AMPLITUDE FOR $^{241}\text{Am}$ SIGNALS COLLECTED BY ELECTRODE NUMBER 1. . . . .   | 100 |
| 88 | EXPERIMENTAL DISTRIBUTION OF DETECTED FISSION EVENTS AS A FUNCTION OF THE NEUTRON ENERGY. AS SHOWN PULSE SHAPE ANALYSIS CAN BE PERFORMED ON CHARGE OR AMPLITUDE DISTRIBUTION EQUIVALENTLY. . . . .   | 101 |
| 89 | EXPERIMENTAL DISTRIBUTION OF THE CHARGE TO AMPLITUDE RATIO CORRECTED FOR THE OFFSET VALUE VERSUS AMPLITUDE FOR $^{233}\text{U}$ SIGNALS COLLECTED BY ELECTRODE NUMBER 13. . . . .  | 102 |
| 90 | EXPERIMENTAL DISTRIBUTION OF THE CHARGE TO AMPLITUDE RATIO CORRECTED FOR THE OFFSET VALUE VERSUS AMPLITUDE FOR $^{241}\text{Am}$ SIGNALS COLLECTED BY ELECTRODE NUMBER 1. . . . .  | 102 |
| 91 | EXPERIMENTAL CHARGE DISTRIBUTION OF SIGNALS VERSUS THEIR AMPLITUDES FOR $^{235}\text{U}$ SAMPLE. A LINEAR RELATION IS VISIBLE. . . . .   | 104 |
| 92 | EXPERIMENTAL DISTRIBUTION OF THE CHARGE TO AMPLITUDE RATIO VERSUS AMPLITUDE FOR $^{235}\text{U}$ . A DISTORSION AT LOW AMPLITUDES IS VISIBLE. . . . .  | 105 |
| 93 | EXPERIMENTAL DISTRIBUTION OF THE CHARGE TO AMPLITUDE RATIO CORRECTED FOR THE OFFSET VALUE VERSUS AMPLITUDE FOR $^{235}\text{U}$ . . . . .  | 105 |
| 94 | LINEAR FIT OF THE PEAK OF THE AMPLITUDE DISTRIBUTION DUE TO FFs AND $\alpha$ PARTICLES. . . . .  | 105 |

|     |   |     |
|-----|---|-----|
| 95  | EXPERIMENTAL CHARGE DISTRIBUTION OF SIGNALS VERSUS THEIR AMPLITUDES. A LINEAR RELATION IS VISIBLE. . . . .  | 106 |
| 96  | EXPERIMENTAL DISTRIBUTION OF THE CHARGE TO AMPLITUDE RATIO VERSUS AMPLITUDE FOR ELECTRODE #1. . . . .   | 106 |
| 97  | EXPERIMENTAL DISTRIBUTION OF THE CHARGE TO AMPLITUDE RATIO CORRECTED FOR THE OFFSET VALUE VERSUS AMPLITUDE FOR ELECTRODE #1 OF $^{241}\text{Am}$ . . . . .                                    | 106 |
| 98  | EXPERIMENTAL CHARGE DISTRIBUTION OF SIGNALS VERSUS THEIR AMPLITUDES. A LINEAR RELATION IS VISIBLE. . . . .  | 107 |
| 99  | EXPERIMENTAL CHARGE DISTRIBUTION OF SIGNALS VERSUS THEIR AMPLITUDES. A LINEAR RELATION IS VISIBLE. . . . .  | 108 |
| 100 | EXPERIMENTAL DISTRIBUTION OF THE CHARGE TO AMPLITUDE RATIO VERSUS AMPLITUDE FOR ELECTRODE # 3 OF $^{241}\text{Am}$ . . . . .  | 108 |
| 101 | EXPERIMENTAL DISTRIBUTION OF THE CHARGE TO AMPLITUDE RATIO CORRECTED FOR THE OFFSET VALUE VERSUS AMPLITUDE FOR ELECTRODE #3 OF $^{241}\text{Am}$ . . . . .                                    | 108 |
| 102 | EXPERIMENTAL DISTRIBUTION OF CHARGE TO AMPLITUDE RATIO CORRECTED FOR THE OFFSET. . . . .  | 109 |
| 103 | EXPERIMENTAL DISTRIBUTION OF CHARGE TO AMPLITUDE RATIO CORRECTED FOR THE OFFSET FOR ELECTRODE # 1 OF $^{241}\text{Am}$ . . .  | 110 |
| 104 | EXPERIMENTAL DISTRIBUTION OF CHARGE TO AMPLITUDE RATIO CORRECTED FOR THE OFFSET FOR ELECTRODE # 2 OF $^{241}\text{Am}$ . . .  | 111 |
| 105 | EXPERIMENTAL DISTRIBUTION OF CHARGE TO AMPLITUDE RATIO CORRECTED FOR THE OFFSET FOR ELECTRODE # 3 OF $^{241}\text{Am}$ . . .  | 111 |
| 106 | EXPERIMENTAL DISTRIBUTION OF CHARGE FOR $^{235}\text{U}$ AND FOR ELECTRODE # 1 OF $^{241}\text{Am}$ . THIS LAST WAS CORRECTED FOR THE RATIO OF THE GAUSSIAN CENTROIDS. TAILS OVERLAP. . . . . | 112 |
| 107 | SIMULATED ENERGY DEPOSITION (10% ENERGY RESOLUTION IS APPLIED) CALIBRATED ON THE EXPERIMENTAL HISTOGRAM OF AMPLITUDES FOR $^{235}\text{U}$ . . . . .  | 114 |
| 108 | COMPARISON AMONG $^{241}\text{Am}$ $\sigma_{(n,f)}$ EXTRACTED BY SELECTING DIFFERENT PORTIONS OF ALL AVAILABLE DATA. . . . .  | 115 |
| 109 | COMPARISON BETWEEN N_TOF (VARIABLE BINNING) AND ENDFB-VII.0 $\sigma_{(n,f)}$ . . . . .  | 116 |
| 110 | COMPARISON BETWEEN N_TOF (VARIABLE BINNING) $^{241}\text{Am}$ (N,F) EXPERIMENTAL CROSS SECTIONS AND DIFFERENT EVALUATIONS. .  | 118 |
| 111 | COMPARISON BETWEEN N_TOF (VARIABLE BINNING) $^{241}\text{Am}$ (N,F) EXPERIMENTAL CROSS SECTIONS AND DIFFERENT EVALUATIONS. .  | 118 |
| 112 | COMPARISON BETWEEN N_TOF (VARIABLE BINNING) $^{241}\text{Am}$ (N,F) CROSS SECTIONS AND PREVIOUS EXPERIMENTAL DATA. . . . .  | 119 |

|     |   |     |
|-----|---|-----|
| 113 | COMPARISON BETWEEN n_TOF (VARIABLE BINNING) <sup>241</sup> AM (N,F) CROSS SECTIONS AND PREVIOUS EXPERIMENTAL DATA. . . . .  | 119 |
| 114 | ISOTOPIC COMPOSITION OF THE CM SAMPLES HOUSED IN FIC. THE SPECTROSCOPIC ANALYSIS WAS PERFORMED IN DUBNA (JINR, RUSSIAN FEDERATION). . . . .   | 122 |
| 115 | LINEAR FIT OF THE PEAK OF THE AMPLITUDE DISTRIBUTION DUE TO FF'S AND $\alpha$ PARTICLES.) . . . . .   | 122 |
| 116 | EXPERIMENTAL CHARGE DISTRIBUTION OF SIGNALS VERSUS THEIR AMPLITUDES. A LINEAR RELATION IS VISIBLE. . . . .  | 123 |
| 117 | EXPERIMENTAL CHARGE DISTRIBUTION OF SIGNALS VERSUS THEIR AMPLITUDES. . . . .  | 124 |
| 118 | EXPERIMENTAL CHARGE DISTRIBUTION OF SIGNALS VERSUS THEIR AMPLITUDES. . . . .  | 124 |
| 119 | EXPERIMENTAL CHARGE DISTRIBUTION OF SIGNALS VERSUS THEIR AMPLITUDES. . . . .  | 125 |
| 120 | EXPERIMENTAL DISTRIBUTION OF DETECTED FISSION EVENTS AS A FUNCTION OF THE NEUTRON ENERGY. THE EQUIVALENCE BETWEEN PERFORMING AN ANALYSIS ON THE CHARGE OF SIGNALS OR ON THEIR AMPLITUDE IS EVIDENT. . . . . | 126 |
| 121 | EXPERIMENTAL DISTRIBUTION OF DETECTED FISSION EVENTS AS A FUNCTION OF THE NEUTRON ENERGY. THE EQUIVALENCE BETWEEN PERFORMING AN ANALYSIS ON THE CHARGE OF SIGNALS OR ON THEIR AMPLITUDE IS EVIDENT. . . . . | 126 |
| 122 | COMPARISON BETWEEN n_TOF (VARIABLE BINNING) AND ENDFB-VII.0 $\sigma_{(n,f)}$ . . . . .  | 128 |
| 123 | Comparison between n_TOF (variable binning) and different evaluations   | 129 |
| 124 | COMPARISON BETWEEN n_TOF (VARIABLE BINNING) AND PREVIOUS EXPERIMENTAL DATA. . . . .   | 130 |
| 125 | COMPARISON OF NEUTRON SPECTRA FROM THERMAL AND FAST BREEDER REACTORS [104]. . . . .   | 135 |
| 126 | FUSION NEUTRON ENERGY SPECTRA [105]. . . . .  | 135 |

# List of Tables

|    |  |     |
|----|--|-----|
| 1  | HEAT CONVERSION VALUES. DATA FROM [6; 10; 11]. . . . .   | 4   |
| 2  | sidewaystable . . . . .  | 6   |
| 3  | TARGET ACCURACIES. . . . .   | 15  |
| 4  | COLLIMATOR PARAMETERS. . . . .   | 25  |
| 5  | CHARACTERISTICS OF THE N_TOF FACILITY. . . . .   | 32  |
| 6  | FIC 1 SAMPLES. . . . .   | 35  |
| 7  | FIC 1 WORKING PARAMETERS. . . . .  | 35  |
| 8  | ELECTRON DRIFT VELOCITY IN DIFFERENT GAS MIXTURES IN MM/ $\mu$ S<br>[46]. . . . .  | 37  |
| 9  | FIC 1 MASS UNCERTAINTIES.MASS VALUES REFER TO THE RA-<br>DIOACTIVE ISOTOPE CONTAINED IN THE SAMPLE. . . . .  | 57  |
| 10 | $^{235}\text{U}$ SAMPLE CHARACTERISTICS. . . . .   | 59  |
| 11 | CORRESPONDENCE BETWEEN THE AMPLITUDE OF SIGNALS DETECTED<br>IN FISSION OF $^{235}\text{U}$ AND THE SIMILUTED ENERGY DEPOSITED IN THE<br>GAS CELL BY FFs COMING FROM $^{235}\text{U}$ SAMPLE. . . . . | 64  |
| 12 | $^{238}\text{U}$ SAMPLE CHARACTERISTICS. . . . .   | 66  |
| 13 | $^{238}\text{U}$ SUMMARY. . . . .  | 74  |
| 14 | $^{233}\text{U}$ SAMPLE CHARACTERISTICS. . . . .   | 75  |
| 15 | $^{233}\text{U}$ SUMMARY. . . . .  | 84  |
| 16 | $^{243}\text{Am}$ SAMPLE CHARACTERISTICS. . . . .  | 85  |
| 17 | CHANNEL DISCRIMINATING BETWEEN FFs AND $\alpha$ PARTICLES. . . .   | 85  |
| 18 | $^{243}\text{U}$ SUMMARY. . . . .  | 94  |
| 19 | $^{241}\text{Am}$ SAMPLE CHARACTERISTICS. . . . .  | 95  |
| 20 | CHANNEL DISCRIMINATING BETWEEN FFs AND $\alpha$ PARTICLES. . . .   | 95  |
| 21 | AMPLITUDES CHOSEN AS THRESHOLD DISCRIMINATING BETWEEN<br>FFs AND $^4\text{He}$ NUCLEI AFTER $\alpha$ PILE-UP CONSIDERATION. . . . .  | 104 |
| 22 | $^{241}\text{Am}$ SUMMARY. . . . .   | 120 |
| 23 | $^{245}\text{Cm}$ SAMPLE CHARACTERISTICS. . . . .  | 121 |
| 24 | CHANNEL DISCRIMINATING BETWEEN FFs AND $\alpha$ PARTICLES. . . .   | 123 |
| 25 | PARAMETERS OBTAINED BY THE GAUSSIAN FITS OF THE CHARGE<br>TO AMPLITUDE DISTRIBUTIONS (OFFSET CORRECTION APPLIED). . .  | 127 |
| 26 | COMPARISON OF NEUTRON YIELDS OBTAINED WITH DIFFERENT RE-<br>ACTIONS [106]. . . . .   | 134 |

# References

- [1] United Nations (Department of Economics and Social Affairs, Population Division), *World Population to 2300*, ST/ESA/SER.A/236, New York (2004).
- [2] J. Ritch, *It's all about People: the Future of Nuclear*, American Nuclear Society Annual Meeting (2007).
- [3] World Resources Institute, in collaboration with the United Nations Environment Programme and the United Nations Development Programme, *A Guide to the Global Environment*, New York, Oxford University Press (1994).
- [4] IEA (International Energy Agency), *The Developing World and the Electricity Challenge*, January 2005.
- [5] M. Schneider *et al.*, *The world nuclear industry status report 2007*, (2008).
- [6] Data taken from the World Nuclear Association website.
- [7] Energy Information Administration (EIA), *International Energy Annual 2006*, June-December 2008.
- [8] Energy Information Administration (EIA), *Energy Projections Plus* (2009).
- [9] IEA Energy Statistics, OECD/IEA 2008.
- [10] U.S. Department of Energy, *Lower and Higher Heating Values of Hydrogen and Fuels Hydrogen Analysis Resource Center*. [http://hydrogen.pnl.gov/cocoon/morf/projects/hydrogen/datasheets/lower\\_and\\_higher\\_heating\\_values.xls](http://hydrogen.pnl.gov/cocoon/morf/projects/hydrogen/datasheets/lower_and_higher_heating_values.xls).
- [11] [http://www.chemeurope.com/lexikon/e/Heating\\_value/#\\_note-NIST/](http://www.chemeurope.com/lexikon/e/Heating_value/#_note-NIST/).
- [12] IAEA, *Thorium fuel cycle - Potential benefits and challenges* IAEA-TECDOC-1450 (2005).
- [13] U.S. DOE Nuclear Energy Research Advisory Committee and the Generation IV International Forum, *A technology roadmap for Generation IV nuclear energy systems*, GIF-002-00 (December 2002).
- [14] C. Grosjean, *Mesure de la section efficace de fission induite par neutrons rapides des noyaux  $^{232}\text{Th}/^{233}\text{U}$  dans le cadre des cycles des combustibles innovants*, PhD thesis (2005).
- [15] International Atomic Energy Agency, "Classification of Radioactive Waste", Vienna, 1994.

- [16] International Evaluation Co.operation, *Uncertainty and target accuracy assessment for innovative systems using recent covariance data evaluations*, ISBN 978-92-64-99053-1.
- [17] All documents describing the facility are available at <http://www.cern.ch/ntof>.
- [18] C. Rubbia *et al.*, *Tech. Rep.* CERN/LHC/98-02, CERN (1998).
- [19] <http://linac2.home.cern.ch/linac2/sources/source.htm>.
- [20] M.Giovanozzi *et al.*, *The proton beams for the time-of-flight neutron facility at the CERN-PS*, CERN-PS/2000-009 (AE).
- [21] Private communications.
- [22] Private communications.
- [23] J. Carpenter, *Experience with spallation sources*, Frederic Joliot-Otto Hahn Summer School 2002, Cadarache, France, 2002. Lectures.
- [24] A. J. Koning, *Review of Intermediate energy nuclear reaction models for accelerator-based nuclear energy applications*, Proceedings of the 8<sup>th</sup> Journées de Saturne Saclay, 1995.
- [25] W. Gudowski, *Why accelerator-driven transmutation of wastes enables future nuclear power?*, Royal Institute of Technology, Stockholm, Sweden.
- [26] A. Abánades *et al.*, *Results from the TARC experiment: spallation neutron phenomenology in lead and neutron-driven nuclear transmutation by adiabatic resonance crossing*, Nuclear Instruments and Methods in Physics Research, A **478** (2002) 577-730.
- [27] n\_TOF Collaboration, *Perf. Rep.*, CERN/INT-O-011 INTC-2002-037.
- [28] J. L. Tain, V. Vlachoudis, *n\_TOF new target commissioning and beam characterization*, CERN-INTC-2008-035.
- [29] F. Gunsing *et al.*, *Neutron resonance spectroscopy at n\_TOF at CERN*, in Nuclear Data for Science and Technology, eds. O. Bersillon *et al.* (EDP Sciences, Les Ulis, 2007) 537.
- [30] S. Marrone *et al.*, *A low-mass neutron flux monitor for the n\_TOF facility at CERN*, Nuclear Instruments and Methods in Physics Research, A **517**, 389 (2004).
- [31] J. Pancin *et al.*, *Measurement of the n\_TOF beam profile with a Micromegas detector*, Nuclear Instruments and Methods in Physics Research, A **524** (2004) 102-114.

- [32] D. B. Gayther, *International intercomparison of fast neutron flux-rate measurements using fission chamber transfer instruments*, Metrologia **27**, 221-231, (1990).
- [33] <http://www.cern.ch/MEDIPIX>.
- [34] K. Wisshak and F. Käppeler, *Large barium fluoride detectors*, Nuclear Instruments and Methods in Physics Research, A **227** (1984) 91.
- [35] R. Plag *et al.*, *An optimized C<sub>6</sub>D<sub>6</sub> detector for studies of resonance-dominated (n,γ) cross-sections*, Nuclear Instruments and Methods in Physics Research, A **496**, 425 (2003).
- [36] C. Stephan *et al.*, *Neutron induced fission cross section measurements*, J. Nuclear Science and Technology Supplement 2, (2002),276.
- [37] M. Calviani *et al.*, *A fast ionization chamber for fission cross-section measurements at n\_TOF*, Nuclear Instruments and Methods in Physics Research, A **594**, 220 (2008).
- [38] *A Detailed Study of the Hyperdeformed States of Uranium in the <sup>234</sup>U(n,f) Reaction*. The n\_TOF collaboration, CERN/INTC 2002-022, INTC/P145 Add. 1 (2002).
- [39] I. Savvidis *et al.*, *n\_TOF experiment: neutron beam profile and fast neutron background determination, using CR-39 passive neutron detector*, Radiation Measurements, Volume 42, Issue 9, October 2007, Pages 1492-1498.
- [40] <http://lansce.lanl.gov/>.
- [41] [http://www.irmm.jrc.be/html/about\\_IRMM/laboratories/GELINA\\_neutron\\_time\\_of\\_flight\\_facility.htm](http://www.irmm.jrc.be/html/about_IRMM/laboratories/GELINA_neutron_time_of_flight_facility.htm).
- [42] A. Ferrari, P. R. Sala, A. Fassó, J. Ranft *FLUKA: a multi-particle transport code*, CERN-2005-010.
- [43] H. G. Hughes, *MCNPX for Neutron-Proton Transport*, Mathematical and Computation Topical Meeting, American Nuclear Society, Madrid, Spain (27-30 September 1999).
- [44] Y. Kadi *et al.*, *The EA-MC Monte Carlo Code Package*, Proc. of the 5<sup>th</sup> meeting on Shielding Aspects of Accelerators, Targets and Irradiation Facilities (SATIF5), Paris (18-21 July 2000).
- [45] A. Ferrari *et al.*, *A comprehensive study of the n\_TOF background*, n\_TOF Note 211009.
- [46] [http://www.kayelaby.npl.co.uk/atomic\\_and\\_nuclear\\_physics/4\\_4/4\\_4\\_2.html](http://www.kayelaby.npl.co.uk/atomic_and_nuclear_physics/4_4/4_4_2.html).

- [47] n\_TOF Collaboration, *The data acquisition system of the neutron time of flight facility n\_TOF at CERN*, Nuclear Instruments and Methods in Physics Research, A **538**, 692 (2005).
- [48] <http://castor.web.cern.ch/castor/>.
- [49] G. Lorusso *et al.*, *Time-energy relation of the n\_TOF neutron beam: energy standards revisited*, Nuclear Instruments and Methods in Physics Research, A **532**, 622-630 (2004).
- [50] N.Colonna, M. Calviani *et al.*, Nuclear Instruments and Methods in Physics Research, A, in preparation.
- [51] G. D. Adeev *et al.*, *Preprint INR 816/93*, Moscow (1993).
- [52] <http://www.nndc.bnl.gov/exfor/endl00.jsp>.
- [53] <http://www.nndc.bnl.gov/exfor/servlet/E4sGetIntSection?SectID=57069&req=10828>.
- [54] <http://pceet075.cern.ch/Tools/Profile/profile.r>.
- [55] L. Tassant-Got and V. Ketlerov, *Final Report on WP14 Activities on the n\_TOF-ND-ADS Projects*, FIKW-CT2000-00107 (2006).
- [56] Working party on International Evaluation Co-operation, *Nuclear Data Standards*, NEA/WPEC-7 (2006).
- [57] K. Kanda *et al.*, *Measurement of fast neutron induced fission cross section*, JAERI-M Reports, No 85,035 p.220 (1985).
- [58] A. Goverdovskij *et al.*, *Measurement of the fission cross section ratios  $^{238}\text{U}/^{235}\text{U}$  for fast neutrons*, Atomnaya Energiya, Vol 56, Issue 3, pag 162 (1983).
- [59] J. Behrens *et al.*, *Measurement of the neutron induced fission cross sections of  $^{234}\text{U}$ ,  $^{236}\text{U}$  and  $^{238}\text{U}$  relative to  $^{235}\text{U}$  from 0.1 to 30 MeV*, Nuclear Science and Engineering, Vol. 63, p. 250 (1977).
- [60] B. Fursov *et al.*, *Ratio fission cross section measurement for  $^{238}\text{U}$  and  $^{235}\text{U}$  in neutron energy range 1-7 MeV*, Atomnaya Energiya, Vol 43, Issue 3, pag 181 (1977).
- [61] P. Lisowski *et al.*, *Fission cross section ratios for  $^{233}\text{U}$ ,  $^{234}\text{U}$ ,  $^{236}\text{U}$  relative to  $^{235}\text{U}$  from 0.5 to 40 MeV*, Conference on Nuclear Data for Science and Technology, Juelich (Germany) p. 732 (1991).
- [62] P. Lisowski *et al.*, *Neutron induced fission cross section ratios for  $^{232}\text{Th}$ ,  $^{235}\text{U}$ ,  $^{238}\text{U}$ ,  $^{232}\text{Th}$ ,  $^{239}\text{Pu}$  from 1 to 400 MeV*, Conference on Nuclear Data for Science and Technology, Mito (Japan), p. 97 (1988).

- [63] O. A Shcherbakov *et al.*, *Neutron-induced fission of  $^{233}\text{U}$ ,  $^{238}\text{U}$ ,  $^{232}\text{Th}$ ,  $^{239}\text{Pu}$ ,  $^{237}\text{Np}$ ,  $^{\text{nat}}\text{Pb}$  and  $^{209}\text{Bi}$  relative to  $^{235}\text{U}$  in the energy range 1-200 MeV*, Nuclear Science and Technology, Supplement Vol. 2, Issue 1, p. 268.
- [64] J. Kanda *et al.*, *Measurement of fast neutron induced fission cross sections of  $^{232}\text{Th}$ ,  $^{233}\text{U}$  and  $^{234}\text{U}$  relative to  $^{235}\text{U}$* , Radiation Effects, **93** 233 (1986).
- [65] J. Meadows *et al.*, *The Ratio of the Uranium-233 to Uranium-235 Fission Cross Section*, Nuclear Science and Engineering, **54** 317(1974).
- [66] J. Meadows *et al.*, *The fission cross sections of  $^{230}\text{Th}$ ,  $^{232}\text{Th}$ ,  $^{233}\text{U}$ ,  $^{234}\text{U}$ ,  $^{236}\text{U}$ ,  $^{238}\text{U}$ ,  $^{237}\text{Np}$ ,  $^{239}\text{Pu}$ ,  $^{242}\text{Pu}$  relative to  $^{235}\text{U}$  at 14.74 MeV neutron energy*, Annals of Nuclear Energy Vol.15, p.421.
- [67] P.W. Lisowski *et al.*, *Fission cross section ratios for  $^{233,234,236}\text{U}$  relative to  $^{235}\text{U}$  from 0.5 to 400 MeV*, Conference on Nuclear Data for Science and Technology, p. 737, Juelich (1991).
- [68] ENDF descriptive comments.
- [69] B. I. Fursov *et al.*, *Fission cross-section measurement for  $^{233}\text{U}$  and  $^{241}\text{Pu}$  relative to  $^{235}\text{U}$  fission cross-section in the energy range 0.024 - 7.4 MeV*, Atomnaya Energiya, Vol.44, Issue.3, p.236.
- [70] G. W. Carlson *et al.*, *Uranium-233 and Plutonium-239 Relative to Uranium-235 from 1 keV to 30 MeV.*, Nuclear Science and Engineering Vol.66, p.205 (1978).
- [71] O. Scherbakov *et al.*, *Neutron-induced fission of  $^{233}\text{U}$ ,  $^{238}\text{U}$ ,  $^{232}\text{Th}$ ,  $^{239}\text{Pu}$ ,  $^{237}\text{Np}$ ,  $^{\text{nat}}\text{Pb}$  and  $^{209}\text{Bi}$  relative to  $^{235}\text{U}$  in the energy range 1-200 MeV*, Journal of Nuclear science and Technology, Supplement 2, p. 230-233 (August 2002).
- [72] F. Tovesson *et al.*, *Neutron-induced fission cross section of  $^{233}\text{Pa}$  and  $^{233}\text{U}$  between 1.0 and 8.5 MeV*, Nuclear Physics, A **733**, 3-19 (2004).
- [73] C. Grosjean *et al.*, Private communications.
- [74] L. Tassant-Got *et al.*, Private communications.
- [75] M. Aiche *et al.*, *Quasi-absolute neutron-induced fission cross section of  $^{243}\text{Am}$* , Conference on Nuclear Data for Science and Technology, p.186(473), Nice 2007.
- [76] P.A. Seeger, *Fission cross sections from Pommard*, Los Alamos Scientific Lab. Reports No. 4420, p. 138 (1970)
- [77] B. I. Fursov *et al.*, *Fission cross-sections measurements for  $^{231}\text{Pa}$  and  $^{243}\text{Am}$  by fast neutrons*, : Atomnaya Energiya Vol.59, p.339.
- [78] A. B. Laptev *et al.*, *Neutron-Induced Fission Cross Sections of  $^{240}\text{Pu}$ ,  $^{243}\text{Am}$  and*

- Nat W in the Energy Range 1-200 MeV.*, Nuclear Physics, Section A Vol.734, Issue.1, p.45.
- [79] J. W. Behrens *et al.*, *Measurement of the Neutron-Induced Fission Cross Sections of  $^{241}\text{Am}$  and  $^{243}\text{Am}$  Relative to  $^{235}\text{U}$  from 0.2 to 30 MeV*, Nuclear Science and Engineering, Vol.77, p.444.
- [80] A. V. Fomichev *et al.*, *Neutron Induced Fission Cross Sections For  $^{240}\text{Pu}$ ,  $^{243}\text{Am}$ ,  $^{209}\text{Bi}$ , *Nat W Measured Relative to  $^{235}\text{U}$  in The Energy Range 1-350 MeV*, Khlopin Radium Institute, Leningrad Reports No.262.*
- [81] A. A. Goverdovskiy *et al.*, *Cross-section ratio measurement for  $^{243}\text{Am}/^{235}\text{U}$  by neutrons in the energy range 5 - 10.5 MeV*, Atomnaya Energiya Vol.67, Issue.1, p.30.
- [82] D.W.Sweet, report AEEW-R-1090 (1977).
- [83] ENDF/B-VII.0 Descriptive Comments.
- [84] H. A. Bethe, *Annual Physik*, **5** (1930) 325.
- [85] P. M. Milazzo, Private communications.
- [86] ENDF/B-VII.O descriptive comments.
- [87] J. W. Behrens *et al.*, *Measurement of the Neutron-Induced Fission Cross Sections of  $^{241}\text{Am}$  and  $^{243}\text{Am}$  Relative to  $^{235}\text{U}$  from 0.2 to 30 MeV*, Nuclear Science and Engineering Vol.77, p.444.
- [88] H. Knitter *et al.*, *Measurement of the neutron induced fission cross-section of  $^{241}\text{Am}$  from 100 eV to 5.3 MeV*, Nuclear Instrum.and Methods in Physics Res. Vol.78, p.1.
- [89] E. Fomushkin *et al.*, *Cross sections and angular distributions of fragments from fission of  $^{238}\text{Pu}$ ,  $^{242}\text{Pu}$  and  $^{241}\text{Am}$  by neutrons with energies from 0.45 up to 3.6 MeV*, Yadernaya Fizika, Vol.10, Issue.5, p.917.
- [90] J. Dabbs *et a.*, *Measurement of the  $^{241}\text{Am}$  neutron fission cross section*, Nuclear Science and Engineering Vol.83, p.22.
- [91] D. Shpak *et al.*, *On under barrier fission of  $^{241}_{95}\text{Am}$  with neutrons*, Yaderno-Fizicheskie Issledovaniya Reports, No.8, p.4.
- [92] M. Cance *et al.*, *Absolute measurement of the neutron induced fission cross section of  $^{241}\text{Am}$  with neutrons in the energy range 0.5 to 3 MeV*, All Union Conference on Neutron Physics ,Kiev,9-13 Jun 1975, Vol.5, p.363.
- [93] R. Nobles *et al.*, *Neutron-induced fission curve for  $^{241}\text{Am}$* , Physical Review Vol.99, p.616(CA2).

- [94] Descriptive comments.
- [95] B. Fursov *et al.*, *Fission cross sections measurements for some minor actinides*, Conference on Nuclear Data for Science and Technology, Trieste 1997, Vol.1, p.488.
- [96] M. Moore *et al.*, *Analysis of the fission and capture cross section of the curium isotopes*, Physical Review, Part C, Nuclear Physics Vol.3, p.1656.
- [97] I. Ivanin *et al.*, *Measurements of Fission Cross Sections For Curium Isotopes*, Conference on Nuclear Data for Science and Technology, Trieste 1997.
- [98] R. White *et al.*, *Neutron-Induced Fission Cross Section Measurements and Calculations of Selected Transplutonic Isotopes*, Conference on Nuclear Data for Science and Technology, Antwerp 1982, p.218.
- [99] B. Gokhberg *et al.*, *Fission cross-section of  $^{245}\text{Cm}$  by fast neutrons and angular distribution of fragments*, Yadernaya Fizika Vol.16, p.665.
- [100] E. Fomushkin *et al.*,  *$^{245}\text{Cm}$  fast neutron fission cross-section energy dependence measurements*, Atomnaya Energiya Vol.63, Issue.4, p.242.
- [101] E. Fomushkin *et al.*, *Measurement of Highly Active Isotope Fission Cross-Sections with Nuclear Explosion Neutrons*, Conference on Nuclear Data for Science and Technology, Juelich 1991 p.439.
- [102] <http://www.world-nuclear-news.org/newsarticle.aspx?id=24606>.
- [103] <http://www.dw-world.de/dw/article/0,,4829136,00.html>.
- [104] DEO FUNDAMENTAL HANDBOOK, *Nuclear physics and reactor theory*, DOE-HDBK-1019/1/93, January 1993.
- [105] K.N. Leung *et al.*, *Compact neutron generator development and application*, Proceedings of 16<sup>th</sup> world conference on nondestructive testing Montreal Canada, 30<sup>th</sup> August - 3<sup>rd</sup> September (2004).
- [106] Y. Kadi *et al.*, *Design of an accelerator-Driven System for the destruction of Nuclear waste*, Lectures given at the Workshop on Hybrid Nuclear Systems for Energy Production, Utilisation of Actinides & Transmutation of Long-Lived Radioactive Waste, Trieste, Italy, 3 September 2001 [http://www.ictp.trieste.it/~pub\\_off/lectures/lns012/Kadi\\_002.pdf](http://www.ictp.trieste.it/~pub_off/lectures/lns012/Kadi_002.pdf).

# Bibliography

- [Bar01] John R. Lamarch; Anthony J. Baratta, *Introduction to nuclear engineering*, Prentice Hall, Upper Saddle River, New Jersey, 2001.
- [Erb97] P.E. Hodgson; E. Gadioli; E. Gadioli Erba; E. Gadioli Erba, *Introductory nuclear physics*, Oxford University Press, Oxford, 1997.
- [Kno79] Glenn F. Knoll, *Radiation detection and measurements*, John Wiley, New York, 1979.
- [Kra87] Kenneth S. Krane, *Introductory nuclear physics*, John Wiley, New York, 1987.